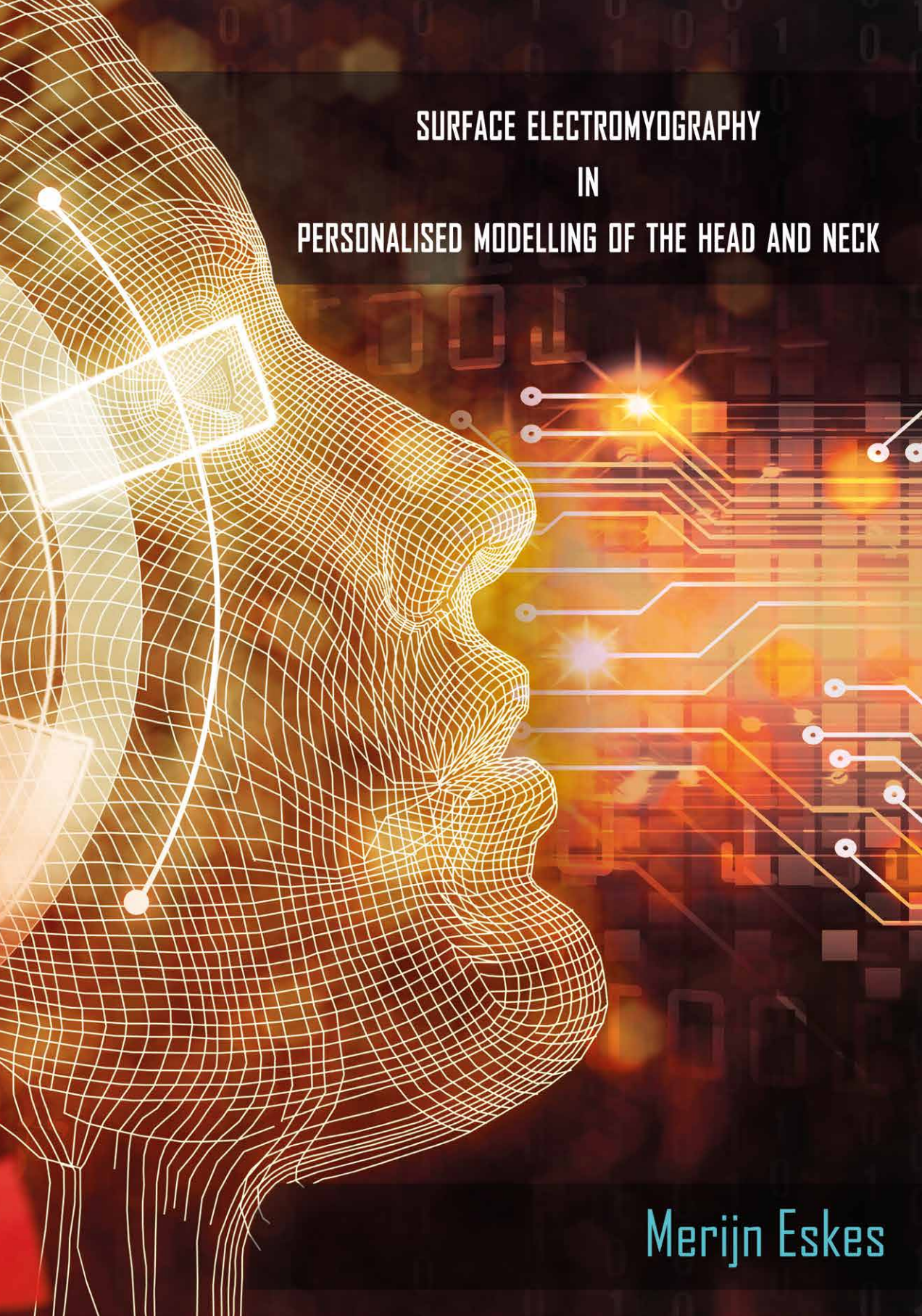
SURFACE ELECTROMYOGRAPHY
IN
PERSONALISED MODELLING OF THE HEAD AND NECK
Merijn Eskes

SURFACE ELECTROMYOGRAPHY IN PERSONALISED MODELLING OF THE HEAD AND NECK

Merijn Eskes

The work described in this thesis was performed at the Netherlands Cancer Institute – Antoni van Leeuwenhoek, Amsterdam, the Netherlands, and at the Robotics and Mechatronics group within the MIRA Institute for Biomedical Technology and Technical Medicine at the University of Twente, Enschede, the Netherlands.

Cover design:	Amanda Kelle and Merijn Eskes
Lay-out:	Drukkerij Westerlaan and Merijn Eskes
Printed by:	Drukkerij Westerlaan in Lichtenvoorde
ISBN:	978-90-365-4447-4
DOI:	10.3990/1.9789036544474

Printing of this thesis was financially supported by:

State of Art Menswear, Delsys Europe,
Atos Medical Nederland, TMSi, ChipSoft, Lesli,
Netherlands Cancer Institute (Oncology Graduate School),
University of Twente (Robotics and Mechatronics group).

SURFACE ELECTROMYOGRAPHY IN PERSONALISED MODELLING OF THE HEAD AND NECK

DISSERTATION

to obtain
the degree of doctor at the University of Twente,
on the authority of the rector magnificus,
prof. dr. T.T.M. Palstra,
on account of the decision of the graduation committee,
to be publicly defended
on the 13th of December 2017 at 10.45 hours

by

Merijn Eskes

Born on the 1st of September 1987
in Winterswijk, the Netherlands

This dissertation has been approved by:

Supervisors Prof. dr. ir. C.H. Slump
Prof. dr. A.J.M. Balm

Co-supervisor Dr. ir. F. van der Heijden

Dissertation committee

Chairman and secretary	
Prof. dr. P.M.G. Apers	University of Twente
Supervisors	
Prof. dr. ir. C.H. Slump	University of Twente
Prof. dr. A.J.M. Balm	University of Amsterdam
Co-supervisor	
Dr. ir. F. van der Heijden	University of Twente
Internal members	
Prof. dr. ir. H.J. Hermens	University of Twente
Prof. dr. ir. H.F.J.M. Koopman	University of Twente
Prof. dr. ir. G.J.M. Krijnen	University of Twente
External members	
Prof. dr. M.W.M. van den Brekel	University of Amsterdam
Prof. dr. L.E. Smeele	University of Amsterdam
Referee	
Dr. M.J.A. van Alphen	Netherlands Cancer Institute

Paranymphs
T. Eskes
J.J.W. Eskes

Contents

PART I

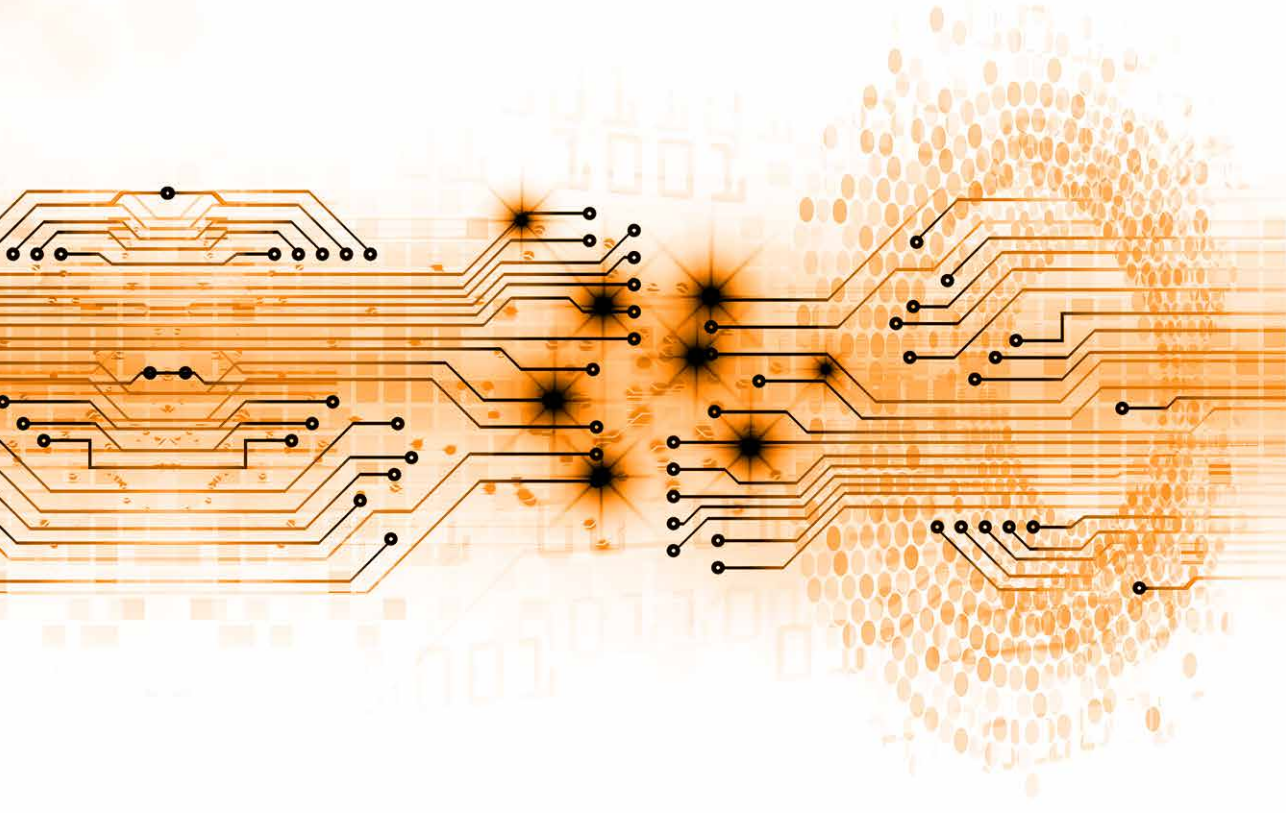

PROBLEM STATEMENT AND CLINICAL BACKGROUND

1.1. Introduction

1.1.1. Functional Inoperability

Cancer treatment could have serious functional consequences due to multiple vital functions in the head and neck region, for example; swallowing, speech and mastication. The clinical decision-making process relies strongly on both limitations created by vital anatomical structures (anatomical inoperability) and the expected function loss after treatment. The last aspect still remains a difficult estimation. To set the borders for inoperability in the functional domain, the term functional inoperability was coined [1], which designates tumours that lead to too severe consequences on vital function if surgically removed. A worldwide survey was conducted among head and neck specialists to see to what extent this term is used in clinical practice and whether it influences their daily clinical practice. Unfortunately, no clear picture emerged from these studies. Instead, a great difference in estimating functional inoperability was found [1,2]. Although these studies were published in 2009 and 2011, estimating functional inoperability still is subjective and thus remains a major issue.

Nevertheless, the prediction of function loss after treatment is becoming increasingly important in the weighing between surgical treatment and organ sparing (chemotherapy and) radiotherapy or photodynamic therapy [3,4]. In case of anatomical inoperability, the assessment is obvious and most specialists will agree on the matter. Examples of anatomical inoperability are tumours that surround the carotid artery, or tumours that invade the skull base. However, assessing functional inoperability is far more difficult. As found by Kreeft et al. worldwide specialists in the field of head and neck oncology have a whole other judgment whether tumours are to be surgical resected and the consequences of the surgery on vital functions, like speech and swallowing [2]. Especially in the United States of America professionals will often opt for surgery, despite the reasonable possibility of severe loss of function.

On the other side of the coin is the patient and his or her treatment preference, which is based on social and professional commitments and life expectancy. These personal aspects might play a role in quitting surgical options and choosing for an organ sparing alternative like radiotherapy, chemotherapy or chemoradiotherapy which can lead to other side effects but with the chance of preservation of speech[1].

As the term, functional inoperability is relatively new and the application of it is still subjective and not evidence based, it is an interesting and important field of research where a lot of improvement can be made. To indicate the limited usage, we applied Google trends to discover usage across the world but this led to zero results due to insufficient search queries over the past decades. In fact, when inserting a quick exact phrase "functional inoperability" in Google search only 650 search results – or hits – emerged on September 12th, 2017 (and only 162 hits in Google Scholar, see Figure 1.1).

[1] The subtle definition differences between voice, speech, and language can be found here: https://www.nidcd.nih.gov/health/what-is-voice-speech-language

We also tried a quick Bing search (584) together with a search on Microsoft Academic (only 6 hits, of which were 3 relevant). The first authors to appear in the list that mentioned functional inoperability were Fryjordet and Klevmark in 1971. These authors evaluated the operability in 515 patients with bronchial carcinoma based on electronic data [5]. Although major surgery has an enormous impact on vital functions, so far minor scientific attention from the perspective of functional inoperability can be found in the literature. This leaves a major challenge for the improvement of healthcare.

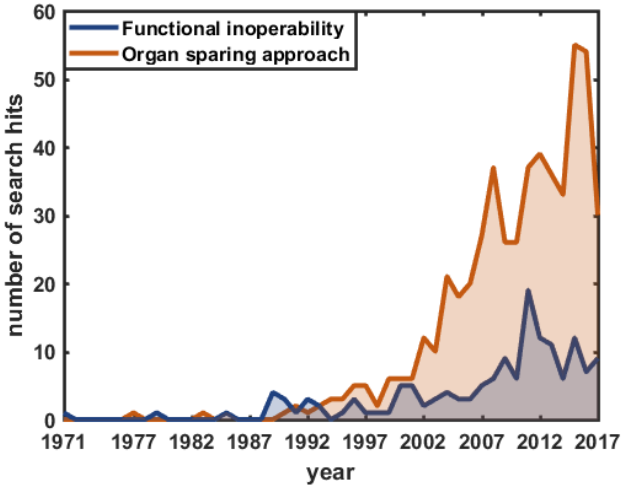

Figure 1.1 The trend of the search terms: "functional inoperability" and "organ sparing approach" in the search engine of Google Scholar on September 12th, 2017.

1.1.2. Virtual Therapy Group

Introduction

The Virtual Therapy Group (VTG) started with an explorative internship into functional inoperability and possibilities to predict postoperative function loss in 2009. Hitherto, this led to the start of six doctoral theses of which two are already completed and a steady flow of technical medicine students pursuing their clinical research internships. The group formulated the following mission statement in 2015 [6]:

"Medical cancer treatments can have serious side effects which under circumstance can be debilitating. When tumour board members discuss possible treatments, they often have to make important decisions with little insight into the extent of such consequences. As a result, patients and physicians have to rely on *personal experience and intuition* when selecting between possible (surgical) interventions.

To give evidence-based foundations to such choices, we will construct a *personalised, detailed, high resolution functional digital model of each individual patient, a genuine virtual lookalike.* This virtual patient will combine data obtained from medical imaging and other biomechanical technologies in one functional model. High quality 3D animations incorporate the anatomy, physiology, and neuron-musculature of the virtual patient.

Physicians will "apply" the curative treatment options to this virtual patient to realise *an audio-visual dynamic representation of the functional sequelae of treatment.* The virtual patient will simulate the effect on important functions, e.g., mastication, swallowing, and audible speech in head and neck cancer. This gives the tumour board and the patient direct access to the use of a functional predictive tool, to realise evidence based decisions on treatment proposals. Furthermore, it enables tailoring of the proposed treatment to the individual patient, to improve functional outcome and decide on additional pre- and post-treatment therapy. It will also clarify the individual functional consequences of the proposed treatment in an audio-visual manner during the counselling procedure.

In ten years, we want to be able to construct a digital model not only for head and neck cancer patients, but for each cancer patient where treatments could impair mechanical functions.

These digital models will store all medical images, physiological data, and all state-of-the-art knowledge of therapy consequences and functional side effects. High quality 3D animations will visualise the likely outcomes of treatments, and their development over time, to the tumour board and patients. Before treatment, these visualisations will guide important decisions about treatment options and selection."

Proposed solution

The proposed solution in assessing functional outcome is the development of a digital doppelgänger, which could be incorporated in the multidisciplinary decision making and counselling of the patient. Figure 1.2 shows the current workflow in blue and the proposed addition to improve the clinical care in orange.

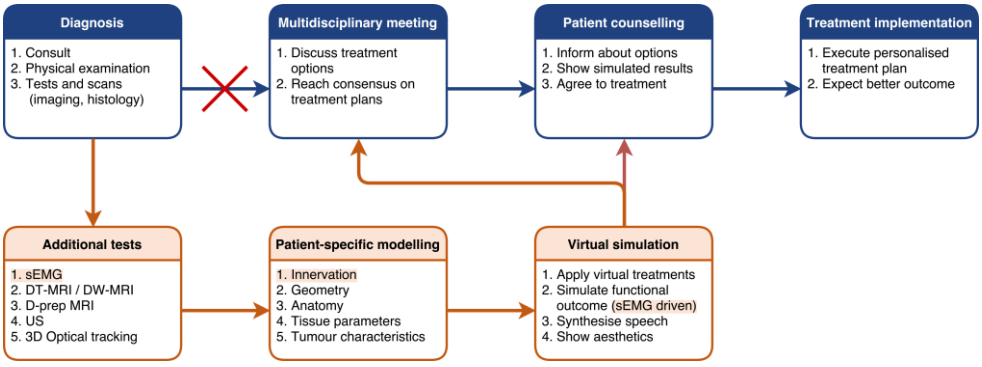

Figure 1.2 Flow chart of proposed clinical work flow including patient-specific modelling and virtual treatment simulation. Accentuated orange texts show the importance of this work.

1.1.3. Why does a digital doppelgänger require perioral muscles and their activations patterns?

While the lips are important for speech and facial expressions, most tumours and resection of these tumours usually do not result in severe function loss because reasonable function can be restored with various surgical techniques [7–10]. The main focus of lip reconstruction on function is to conserve intraoral mucosal lining and retain the surface area of the oral aperture [10]. In addition, the aesthetic outcome is of great importance.

The main purpose of the experiments in this thesis is to demonstrate the feasibility of such methods in an easy-to-access environment so they can be extrapolated to more complex environments. 3D tracking measurements of the lips and lip motion is easily done using stereo-camera or multi-camera set-ups. Surface electromyography (sEMG) recordings to register an estimation of the muscle activation patterns of facial muscles is a bit more complex because of the overlapping and intertwining structure of the facial musculature [11,12]. Also, the small size of these facial muscles makes it more difficult to measure than for instance the biceps brachii and triceps brachii muscles. Despite these challenges, it is relatively easy in comparison to intraoral EMG measurements of the tongue and in particular the surface EMG measurements. Secondly, it is important to be able to simulate the appearance of patients and their remaining function as it can improve patient counselling.

1.1.4. Facial anatomy and characteristics

The face, itself, gives us our identity and it plays a major role in communication, as it is the interface between individuals. The underlying facial muscles carry out some of the most important functions of everyday life, yet they are often overlooked. In fact, people only realise the importance when they are faced with negative effects caused by genetical defects, disease, surgical treatment, radiotherapy, chemotherapy, or the aging process. The importance was already reflected by Cicero who considered facial expressions as "Imago Animi Vultus", the image of the soul [13].

The facial muscles are also known as the mimetic muscles (Greek: μίμησις or mimesis, imitation) [12]. It is an important group of striated skeletal muscles and they are innervated by the facial nerve (cranial nerve VII). The facial nerve branches off extracranially into five important facial branches (Figure 1.3) [12,14]: 1. temporal branch, 2. zygomatic branch, 3. buccal branch, 4. marginal branch, and 5. cervical branch.

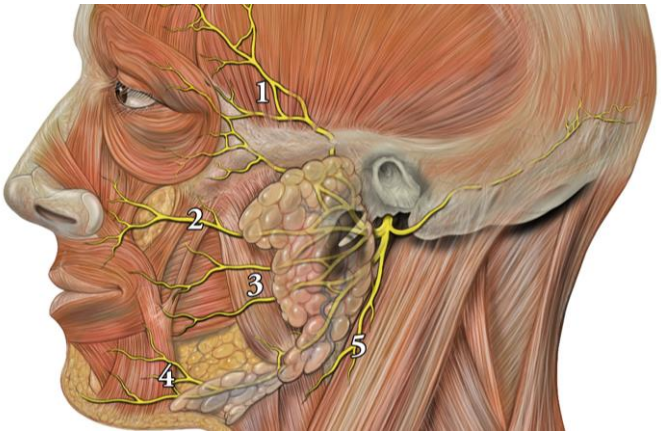

Figure 1.3 The facial nerve (CNVII) and its branches (yellow) located below the parotid gland (semi-transparent). 1: temporal branch, 2. zygomatic branch, 3. buccal branch, 4. marginal branch, 5. cervical branch. Adapted from [15]. Image created by Patrick Lynch.

Besides facial muscle control, taste sensations of the anterior two-thirds of the tongue are received by branches of the facial nerve [14]. The origin, insertion, innervation, and function of relevant facial muscles are denoted in Table 1.1.

Table 1.1 Origin, insertion, innervation, and function of relevant facial muscles, adapted from [14]

Muscle	Origin	Insertion	Innervation	Function
LLS	Inferior orbital margin	Skin and muscle of the upper lip	Zygomatic branch facial nerve	Elevates and everts upper lip
LLSan	Upper part of the frontal process of the maxilla	Skin of lateral nostril and upper lip	Buccal branch facial nerve	Dilates nostril and elevates upper lip
ZYG	Lateral aspect of zygomatic bone	Modiolus	Zygomatic and buccal branches of facial nerve	Elevates the corners of the mouth in lateral direction
ZYGm	Anterior aspect of zygomatic bone	Skin and muscle of the upper lip	Buccal branch of facial nerve	Elevates and everts upper lip
LAO	Canine fossa (maxilla)	Modiolus	Buccal branch of facial nerve	Draws the corners of the mouth upwards
RIS	Deep fascia of face and parotid	Modiolus and skin at angle of mouth	Buccal branch of facial nerve	Retracts angle of mouth
BUC	Alveolar processes of the maximallary bone, mandible, temporo-mandibular joint	Mucous membrane of the cheeks, modiolus, orbicularis oris	Buccal branch of facial nerve	Compresses cheek against the teeth and gums
DAO	Anterolateral base of mandible	Modiolus	Mandibular branch of facial nerve	Draws the corners of the mouth downwards and laterally
DLI	Platysma and anterolateral body of the mandible	Muscular tissue and mucosa of the lower lip	Mandibular branch of facial nerve	Helps to depress and/or evert the lower lip
MEN	Anterior mandible	Skin of the chin (mentolabial sulcus)	Mandibular branch of facial nerve	Elevates and protrudes lower lip, elevates skin of chin
PLA	subcutaneous tissue of infraclavicular and supraclavicular regions	base of mandible; skin of cheek and lower lip; modiolus; orbicularis oris	Cervical branch facial nerve	Draws the corners of the mouth inferiorly and widens it.

Table 1.1 (continued) Origin, insertion, innervation, and function of relevant facial muscles, adapted from [14]

Muscle	Origin	Insertion	Innervation	Function
OOI and OOS	Maxilla and mandible, deep surface of perioral skin, modiolus	Mucous membrane of the lips	Buccal branch facial nerve	Narrows orifice of mouth, purses lips and puckers lip edges
TEM	Temporal lines on the parietal bone of skull superior temporal surface of sphenoid bone	Coronoid process of the mandible	Deep temporal nerves, anterior branches of mandibular nerve	Elevation and retraction of mandible
MAS	Zygomatic arch and zygomatic process of maxilla	Lateral surface of angle and lower ramus of mandible	Mandibular nerve	Elevates mandible
DIG	Mastoid notch (digastric fossa)	Hyoid bone	mandibular division (V_3) of the trigeminal (CN V) via mylohyoid nerve	Depresses mandible, opening mouth, and/or elevates larynx
DIGp	mastoid process of temporal bone	Hyoid bone	facial nerve (CN VII)	Depresses mandible, opening mouth

Apart from the important function in everyday life and their small sizes, the facial muscles are known to be special. They have a unique anatomical architecture. Normal skeletal muscles have tendons that attach to bony parts, while the facial muscles also have nontendinous attachments to soft tissue of the skin or other muscles. Some facial muscles even have both their origin and insertion to nontendinous attachments [11,14]. Another aspect is the absence of muscle spindles and fasciae [11,16]. The facial muscles also overlap and intertwine more drastically than other skeletal muscles [12,14].

There is a high inter- and intra-individual variability of facial muscle locations and their morphology. For example, Shimada and Gasser described the variations in arrangement of the muscles that insert in the vicinity of the mouth angle, which is called the modiolus, in relation to the angle of the mouth [17]. Classical text books describe the modiolus being the point lateral to the mouth's angle where several facial muscles converge. However, Shimada and Gasser found three distinctive groups: convergence point is lateral to the mouth's angle, convergence point is above the mouth's angle, and convergence point is below the mouth's angle. The latter two being most present in their 147 studied cadavers [17]. Others described the variations in risorius and zygomatic minor muscles, sometimes being completely absent or having only a few fibres [18,19].

Their motor nucleus is the largest among all motor nuclei of the human brain stem [13]. Additionally, histochemical studies showed that the facial muscles have multiple myoneural junctions distributed in round or oval-shaped clusters over the muscle's region, and in contrast to classic motor unit structure where only a few are located near the centre of the muscle fibre and distributed within a narrow band in the muscles [20].

The neural command of facial muscles can be distinguished in two groups: voluntary and emotional involuntary control. Morecraft et al. found a potential anatomical substrate that may contribute to the clinical dissociation of emotional and voluntary facial movement [21]. When examining the motor control of facial muscles using electromyography, isolated muscle contractions of these muscles is very difficult probably because they lack practice as the orofacial functions require an orchestra of activating multiple muscles simultaneously. These recruitment patterns differ from person to person [22], like other functional movements in humans, such as in locomotion [23].

The facial acting coding system (FACS) is an extensive tool developed for the field of neuropsychology [24]. FACS uses action units (AU) that describe the contraction or relaxation of one or more muscles to systematically categorise different facial expressions. This is also very useful in facial animation, because a virtual model can be controlled using these AUs producing the whole spectrum of facial expressions by only defining the AUs and place them in a sequence. Subsequently, Lapatki extensively described the visual examination of facial muscle contractions [11].

Perioral Muscles

The perioral muscles are the muscles surrounding the buccal orifice (Figure 1.4). According to Lapatki these muscles can be functionally divided into three groups that control the shape of the buccal orifice [11]:

1. Retractors of the upper lip
    a. levator labii superioris alaeque nasi (LLSAN)
    b. levator labii superioris (LLS)
    c. zygomaticus minor (ZYGm)
2. Closure and sealing of the oral commissure
    a. levator anguli oris (LAO)
    b. zygomaticus major (ZYG)
    c. buccinator (BUC)
    d. depressor anguli oris (DAO)
    e. orbicularis oris region (OOR) muscles
3. Retractor and elevator of the lower lip
    a. depressor labii inferioris (DLI)
    b. mentalis (MEN)

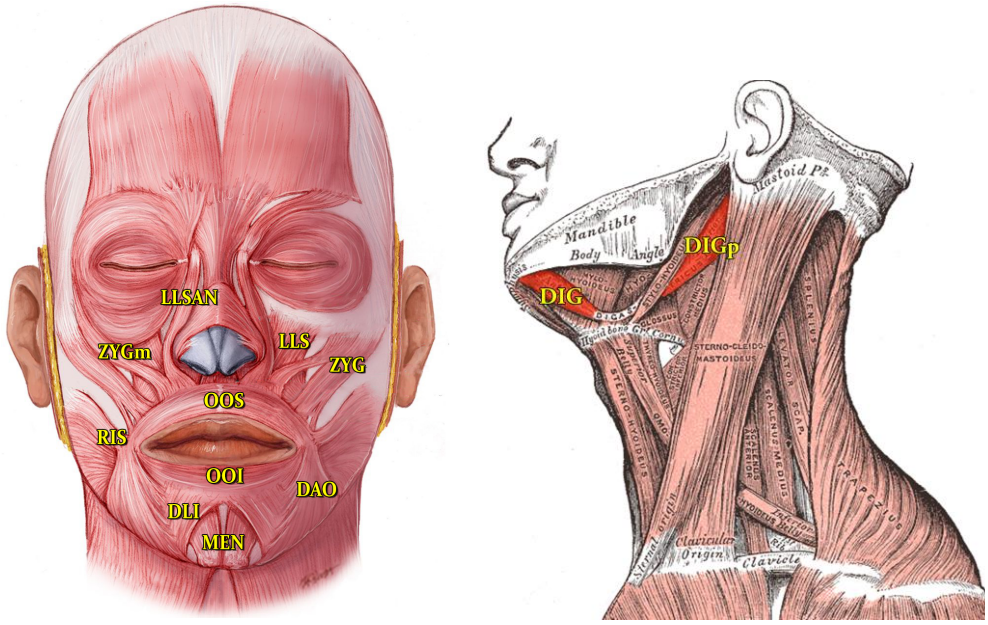

Figure 1.4 The facial muscles (left, adapted from [27]. Original image ©201é 3Đ0É Î ÇÅ0Ç and digastric muscle (right, adapted from [28]) with its anterior and posterior part.

The other perioral muscles are: the risorius, the platysma, and the muscles in the orbicularis oris region. The latter muscles are addressed differently in various studies. orbicularis oris superior (OOS) and inferior (OOI), or as subdivision of orbicularis oris peripheralis (OOP) [25], marginalis (OOM) [25], and having tangential fibres (OOT) [26], and the incisivus labii superioris (ILS) and inferioris (ILI) [11].

Other involved muscles

The anterior belly of the digastric muscle (DIG) is important for opening of the mouth and was therefore taken into account. The posterior belly of the digastric muscle (DIGp), the temporalis (TEM) and masseter (MAS) muscles are important for chewing and not directly involved in facial movements.

To conclude, the facial musculature is an intriguing and complex subject. For the experiments described in this thesis the following muscles were considered relevant and as such were included in the measurements: OOS, OOI, LLSAN, DAO, RIS, ZYG, MEN, and DIG.

1.2. References

1. Kreeft A, Tan IB, van den Brekel MWM, Hilgers FJ, Balm AJM. The surgical dilemma of "functional inoperability" in oral and oropharyngeal cancer: current consensus on operability with regard to functional results. Clin Otolaryngol. 2009;34: 140–146. doi:10.1111/j.1749-4486.2009.01884.x

2. Kreeft AM, Tan IB, Leemans CR, Balm AJM. The surgical dilemma in advanced oral and oropharyngeal cancer: how we do it. Clin Otolaryngol. 2011;36: 260–266. doi:10.1111/j.1749-4486.2011.02299.x

3. Dirix P, Nuyts S. Evidence-based organ-sparing radiotherapy in head and neck cancer. Lancet Oncol. 2010;11: 85–91. doi:10.1016/S1470-2045(09)70231-1

4. Karakullukcu B, van Oudenaarde K, Copper MP, Klop WMC, van Veen R, Wildeman M, Bing Tan I. Photodynamic therapy of early stage oral cavity and oropharynx neoplasms: an outcome analysis of 170 patients. Eur Arch Oto-Rhino-Laryngology. 2011;268: 281–288. doi:10.1007/s00405-010-1361-5

5. Fryjordet A, Klevmark B. Investigations of Operability in Cases of Bronchial Carcinoma: Evaluation of 515 Patients. Scand J Thorac Cardiovasc Surg. 1971;5: 97–102. doi:10.3109/14017437109135539

6. Balm AJM, van der Heijden F. Virtual Therapy. In: Mission [Internet]. 2015 [cited 1 Sep 2017] p. 1. Available: http://www.virtualtherapy.nl/mission/

7. Baumann D, Robb G. Lip Reconstruction. Semin Plast Surg. 2008;22: 269–280. doi:10.1055/s-0028-1095886

8. Rapidis AD, Valsamis S, Anterriotis DA, Skouteris CA. Functional and aesthetic results of various lip-splitting incisions: A clinical analysis of 60 cases. J Oral Maxillofac Surg. 2001;59: 1292–1296. doi:10.1053/joms.2001.27517

9. Dziegielewski PT, O'Connell DA, Rieger J, Harris JR, Seikaly H. The lip-splitting mandibulotomy: Aesthetic and functional outcomes. Oral Oncol. 2010;46: 612–617. doi:10.1016/j.oraloncology.2010.05.006

10. Raschke GF, Rieger UM, Bader R-D, Schultze-Mosgau S. Lip reconstruction: an anthropometric and functional analysis of surgical outcomes. Int J Oral Maxillofac Surg. 2012;41: 744–750. doi:10.1016/j.ijom.2012.02.005

11. Lapatki BG. The Facial Musculature: Characterisation at a Motor Unit Level. Radboud University Nijmegen. 2010.

12. Prendergast PM. Anatomy of the face and neck. In: Shiffman MA, Di Giuseppe A, editors. Cosmetic Surgery Art and techniques. 2013. p. 36. doi:10.1007/978-3-642-21837-8

13. Müri RM. Cortical control of facial expression. J Comp Neurol. 2016;524: 1578–1585. doi:10.1002/cne.23908

14. Moore KL, Dalley AF, Agur AMR. Clinically oriented anatomy. Lippincott Williams & Wilkins. 2013.

15. Lynch P. Facial nerve branches. In: Wikimedia Commons contributors [Internet]. 2006 [cited 1 Sep 2017] p. 1. Available: https://commons.wikimedia.org/wiki/File:Head_facial_nerve_branches.jpg

16. Stål P. Characterization of human oro-facial and masticatory muscles with respect to fibre types, myosins and capillaries. Morphological, enzyme-histochemical, immuno-histochemical and biochemical investigations. Swed Dent J Suppl. 1994;98: 1–55.

17. Shimada K, Gasser RF. Variations in the facial muscles at the angle of the mouth. Clin Anat. 1989;2: 129–134. doi:10.1002/ca.980020302

18. Sato S. Statistical studies on the exceptional muscles of the Kyushu-Japanese. Kurume Med J. 1968;15: 69–82. doi:10.2739/kurumemedj.15.69

19. Farahvash MR, Abianeh SH, Farahvash B, Farahvash Y, Yagoobi A, Nazparvar B. Anatomic Variations of Midfacial Muscles and Nasolabial Crease: A Survey on 52 Hemifacial Dissections in Fresh Persian Cadavers. Aesthetic Surg J. 2010;30: 17–21. doi:10.1177/1090820X09360703

20. Happak W, Liu J, Burggasser G, Flowers A, Gruber H, Freilinger G. Human facial muscles: dimensions, motor endplate distribution, and presence of muscle fibers with multiple motor endplates. Anat Rec. 1997;249: 276–84. doi:10.1002/(SICI)1097-0185(199710)249:2<276::AID-AR15>3.0.CO;2-L

21. Morecraft RJ, Louie JL, Herrick JL, Stilwell-Morecraft KS. Cortical innervation of the facial nucleus in the non-human primate. Brain. 2001;124: 176–208. doi:10.1093/brain/124.1.176

22. Schumann NP, Bongers K, Guntinas-Lichius O, Scholle HC. Facial muscle activation patterns in healthy male humans: A multi-channel surface EMG study. J Neurosci Methods. 2010;187: 120–128. doi:10.1016/j.jneumeth.2009.12.019

23. Ivanenko YP, Poppele RE, Lacquaniti F. Five basic muscle activation patterns account for muscle activity during human locomotion. J Physiol. 2004;556: 267–282. doi:10.1113/jphysiol.2003.057174

24. Ekman P, Friesen WV, Hager JC. The Facial Action Coding System (FACS): A technique for the measurement of facial action. Consulting Psychologists Press, Inc. 1978.

25. Wu J, Yin N. Detailed Anatomy of the Nasolabial Muscle in Human Fetuses as Determined by Micro-CT Combined With Iodine Staining. Ann Plast Surg. 2016;76: 111–6. doi:10.1097/SAP.0000000000000219

26. Blair C. Interdigitating Muscle Fibers Throughout Orbicularis Oris Inferior. J Speech Lang Hear Res. 1986;29: 266. doi:10.1044/jshr.2902.266

27. Prendergast PM. Anatomy of the Face and Neck. In: Shiffman MA, Di Giuseppe A, editors. Cosmetic Surgery. Art and techniques. 1st ed. 2013. p. 36.

28. Gray H. Digastric muscle. In: Wikimedia Commons contributors [Internet]. 2007 [cited 1 Sep 2017] p. 1. Available: https://en.wikipedia.org/wiki/File:Digastricus.png

TECHNICAL BACKGROUND AND OUTLINE

2.1. Electromyography

2.1.1. A brief history [1]

Francesco Redi (February 18th, 1626 – March 1st, 1697) discovered a highly specialised muscle in the electric eel that generates electricity. His experiments are widely recognised as the first documented EMG experiments [1]. Luigi Aloisio Galvani (September 9th, 1737 – December 4th, 1798) demonstrated the relationship between electricity and muscle contraction [2]. Decades later, Emil du Bois-Reymond (November 7th, 1818 – December 26th, 1896) discovered the nerve action potential and pioneered the possibility of measuring electrical activity during voluntary muscle contraction in humans [3]. It was Étienne-Jules Marey (March 5th, 1830 – May 15th, 1904) who performed the first actual recordings, and he was the one who in 1890 called this measurement technique 'Electromyography' [4]. The technique was adopted by many research groups around the world with all kinds of scientific advancements. In 1965, the International Society of Electrophysiological Kinesiology (ISEK) was founded, which still exists today. The advancements also led to the first clinical use of surface EMG (sEMG), designed by Hardyck et al. in 1966 [5]. In the early 1980s, Cram and Steger created a sEMG sensing device for use in the clinic to scan a variety of muscles. A couple of years later, a normative database with data from 104 healthy volunteers was built by Cram and Engstrom [6]. The database functions as a source of reference values to compare to clinical experiments and is still in use today. Although multichannel sEMG measurements were already proposed in 1979 by Nishizono et al. to measure conduction velocity [7], the advances in computing power, analysis techniques, and electrode fabrication allowed for the introduction of high-density surface electrodes with minuscule electrodes and very small interelectrode distances. Many more scientists have contributed to the history of electromyography – too many to acknowledge them all. However, Carlo John De Luca (1943 – July 20th, 2016) and colleagues of the NeuroMuscular Research Center (NMRC) deserve special attention, as they were pivotal for the understanding of muscle physiology and measuring methods, especially for spectral analysis of the sEMG signals in relation to muscle fatigue [8]. A few of the aforementioned contributing persons are pictured in Figure 2.1.

Figure 2.1 Some important persons in the history of electromyography. Figures adopted from [9–13].

[1] The history template is based on Cram's introduction to surface electromyography [4].

2.1.2. Principles of electromyography

Origin of bioelectrical activity

A muscle cell at rest has a steady-state equilibrium of ion concentrations: a high concentration of potassium on the inside and a low concentration of potassium on the outside of the cell. For sodium, it is the opposite: a low concentration on the inside and a high concentration on the outside. This steady state results in a corresponding membrane potential of about -80 to -90 mV, whereas for neural cells, this resting membrane potential is in the range of -60 to -70 mV. Differences exist between species but are also observed in the same animal in different tissues, as well as in the same tissue under different environmental conditions. The resting potential can be calculated using the Nernst equation or, more accurately, using the Goldman-Hodgkin-Katz equation:

$$E = \frac{RT}{F} \ln\left(\frac{P_K[K]_o + P_{Na}[Na]_o + P_{Cl}[Cl]_i}{P_K[K]_i + P_{Na}[Na]_i + P_{Cl}[Cl]_o}\right) \tag{2.1}$$

Where E is the equilibrium transmembrane resting potential when the net current through the membrane is zero [14], R is the universal gas constant: $8.31\,J/mol\,K$. T is the absolute temperature in K. F is the Faraday constant: $96500\,C/equivalent$. P_M describes the permeability of the membrane for ionic types M. $[\,]_o$ and $[\,]_i$ are the extracellular and intracellular ion concentrations in mol/L [14].

The muscle cell membrane or sarcolemma contains a sodium-potassium pump (the Na^+/K^+ ATP-ase pump, which pumps 3 Na^+ ions out of the cell for every 2 K^+ ions pumped into the cell at the cost of ATP), a voltage-gated potassium pump, and a voltage-gated sodium pump (Figure 2.2).

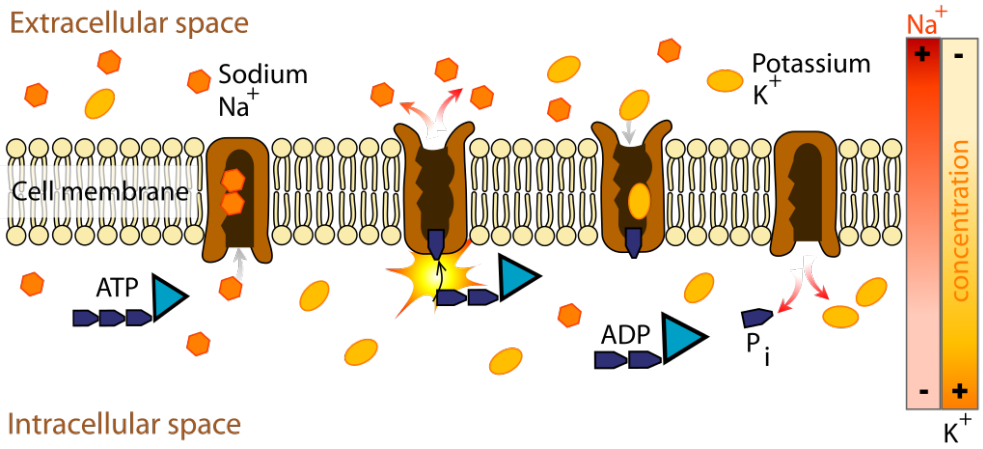

Figure 2.2 Schematic illustration of the sodium-potassium pump. From left to right: three sodium ions are transported from the intracellular space to the extracellular space at the cost of ATP, with two potassium ions transported in exchange from the extracellular space to the intracellular space, adopted from [15].

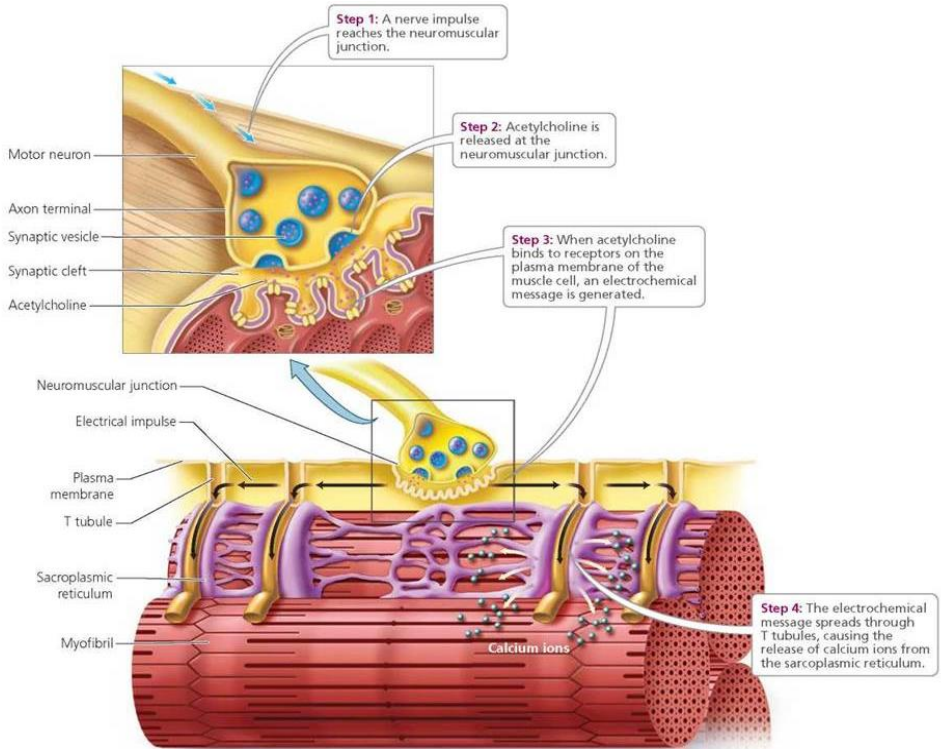

Figure 2.3 The neuromuscular junction and the delivery of a neural command from the nerve cells to the muscle cells, adopted from [16].

Neural impulses or so-called action potentials travel via the motor neuron to the neuromuscular junction. The neuromuscular junction allows for the transition of neural command via nerve cells to muscle cells (Figure 2.3). In this junction, the neuron releases the neurotransmitter acetylcholine, which binds to receptors. This binding process results in depolarisation of the muscle fibre membrane, causing the voltage-gated sodium pump to open and allowing a rapid influx of sodium ions, which further increases the potential. The sodium pump then closes, and the potassium pump opens. Sodium can no longer flow into the cell, and potassium exits the cell, effectuating repolarisation.

At this point, the initial ion concentrations are restored by the Na^+/K^+ ATP-ase pump, and the cell prepares for a new action potential. This recovery time is called the 'refractory period', which is divided into an absolute and a relative part (Figure 2.4). In the absolute part, no stimuli can generate a new action potential, whereas in the relative part, only intense stimuli may generate a new action potential. The electrical impulse travels down the transverse tubules of the muscle fibres. Because of this depolarisation wave, L-type voltage-gated calcium channels in the transverse tubule membrane open and release calcium stores in the sarcoplasmic reticulum. Calcium ions then trigger muscle contraction. This process of depolarisation and repolarisation over the muscle fibres is the origin of the EMG signal [14].

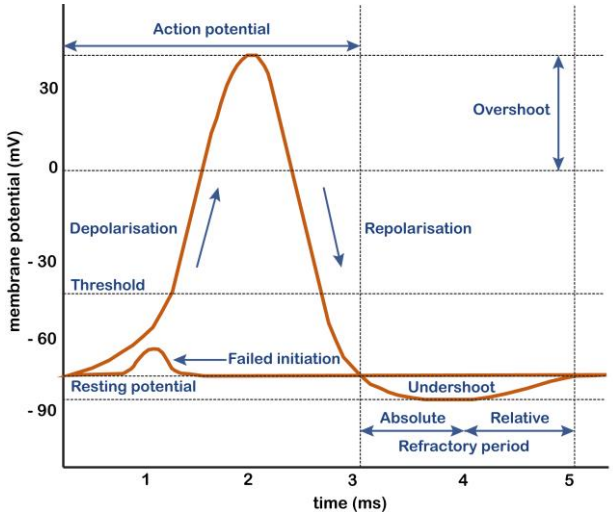

Figure 2.4 **A schematic display of the action potential, adapted from [26].**

The ensuing muscle contraction can be described by the "sliding filament theory" first proposed by two independent research teams [17,18]. Huxley called it the 'swinging cross-bridge theory' [19]. Sliding occurs by cyclic attachment and detachment of myosin on actin filaments. Contraction takes place when the myosin pulls the actin filament towards the centre. It detaches from an actin molecule and creates a force (stroke) to bind to the next actin molecule, which is possible in the presence of calcium ions because then these binding sites on the actin molecule are available. When calcium ions are actively pumped back into the sarcoplasmic reticulum, the binding sites on the actin molecule become blocked again, and contraction ceases. Over the years, improvements have transformed the swinging cross-bridge theory into the swinging lever arm model [20–22].

From the origin of the EMG signal to the electromyogram

The origin of motion starts in the brain in the motor cortex. The motor cortex is responsible for planning, control, and execution of voluntary movement. Motor axons originating from the motor neurons innervate single or multiple muscle fibres, forming the smallest functional units, called 'motor units' (MUs) (Figure 2.5).

The MU action potentials (MUAPs) detected by the electrodes have typical triphasic patterns, reflecting the superposed signal of the entire MU (Figure 2.7) [23,24].

The electric dipole model explains why a single muscle fibre depolarisation is measured as a bipolar signal by monopolar electrodes (Figure 2.7).

Muscle force is produced by activating MUAPs. To increase force, one can recruit more MUAPs, increase the firing rate of the recruited MUAPs, or both. The retained muscle contraction is established by so-called MUAP trains (MUAPT) (Figure 2.7). The MUAPT can be denoted mathematically as a series of Dirac impulses $\delta(t)$: $\sum_{k=1}^{K}\delta(t-t_k)$, convoluted with a filter that resembles the MUAP's shape (Figure 2.7) [25].

Thus, the MUAPT can be expressed as:

$$u_i(t) = \sum_{k=1}^{K} h_i(t - t_k)$$
$$t_k = \sum_{l=1}^{k} \Delta t_l \qquad for \;\; k = 1, 2, \cdots, n \tag{2.2}$$

Where h_i is the impulse response of the filter, t_k are the points in time at which the MUAPs occur. Δt contains the interpulse intervals, i is the i^{th} particular MU and K is the total number of interpulse intervals in a MUAPT. The integer k denotes a specific event (Figure 2.7).

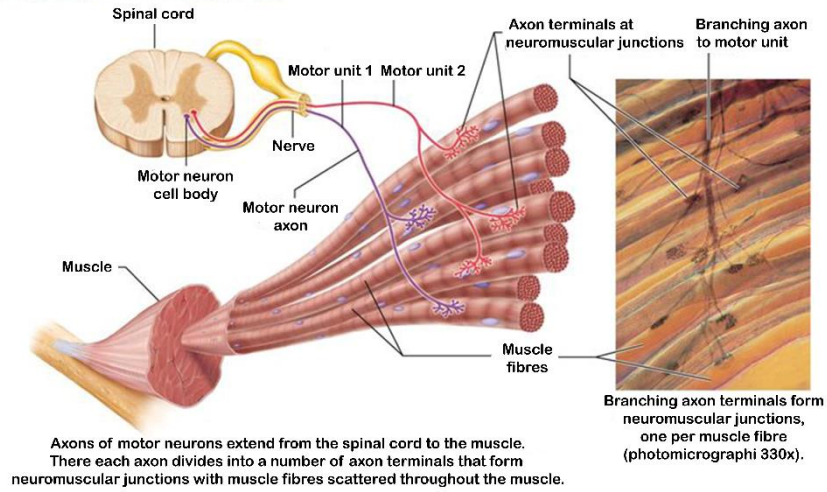

Figure 2.5 Illustration of a motor unit, adopted from [27] with permission of Pearson Education, Inc. ©2013 Pearson Education, Inc.

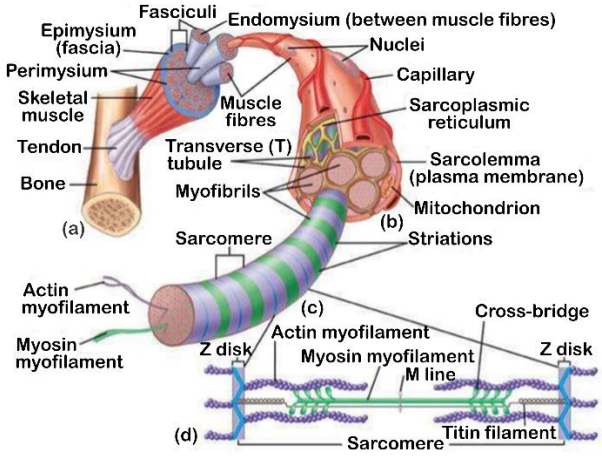

Figure 2.6 Architecture of a skeletal muscle, adopted from [28] with permission of The McGraw-Hill Companies, Inc. ©2003 The McGraw-Hill Companies, Inc.

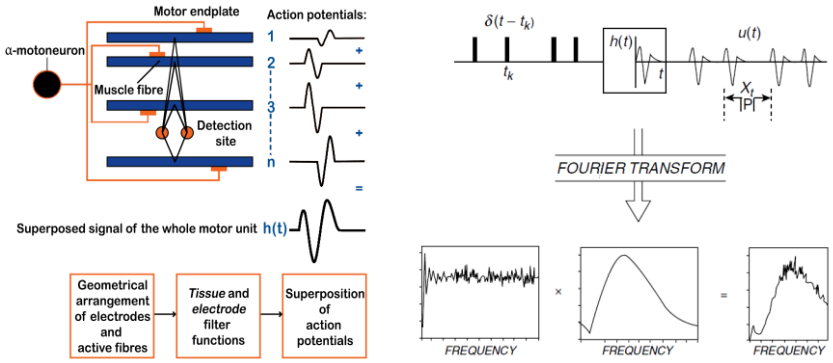

Figure 2.7 Left: Schematic representation of the generation of the motor unit action potential. Right: Model for a motor unit action potential train (MUAPT) and the corresponding Fourier transform of the interpulse intervals (IPIs), the motor unit actions potentials (MUAP), and the MUAPT. Adapted from [25]. Original image ©2006 John Wiley & Sons, Inc.

A model of the EMG signal s may be described as a linear summation of MUAPTs (Figure 2.7), where p is the number of total MUs contributing to the potential field, $n(t)$ is the measurement noise [25]:

$$s(t) = \left(\sum_{i=1}^{p} u_i(t) \right) + n(t) \tag{2.3}$$

The filtering properties of the recording electrodes are accommodated in h_i. The generated force depends on the firing rate and recruited MUs. Thus, it depends on the statistics of the interpulse intervals Δt_l. The technique of sEMG uses surface electrodes that are placed on top of the skin, ideally above the centre of the muscle belly. They acquire signals of the underlying muscles. In contrast to intramuscular electrodes, sEMG is noninvasive and easy to use but measures individual muscles less selectively, is more prone to artefacts, and it has a relatively low signal-to-noise ratio (SNR). These are the two different ways of acquiring signals from muscle action potentials. The surface electrodes are available in all kinds of dimensions and materials, whereas intramuscular electrodes can be fine wire or needle electrodes that are inserted into the muscle using a guiding needle. The intramuscular electrodes measure activity in their direct surroundings, usually the activity of a few sarcomeres. The two types of electrodes and their advantages and disadvantages are presented in Table 2.1.

Factors influencing the surface electromyogram and measurement standards

The sEMG signal is a crude estimate of neural command because many factors influence the relationship between motor control innervation and the measured sEMG signal. Farina et al. and De Luca et al. extensively described these intrinsic and extrinsic factors [29–31]. Because of these factors, the ISEK endorsed Merletti's proposed standards on how to report on EMG data to minimise the differences when replicating the experiments of others in 1999 [32]. Farina et al. listed these factors that affect the measured signals as shown in Table 2.2.

Table 2.1 Comparison of the advantages and disadvantages of surface and intramuscular electrodes. Adapted from [33].

Electrode type	Advantages	Disadvantages
Surface electrodes	Easy to use	Can only measure the surface muscle EMG
	Noninvasive	Low SNR
	Safer	Poor selectivity of muscles and MUAPs
	Large recording region	More prone to artefacts
	Less hinder of movement	
Intramuscular electrodes	Capable of detecting MUAP	Difficult to use
	Better selectivity of muscles and MUAPs	Invasive
	High SNR	Movement obstructing
	Able to measure deep muscles	Hazardous

In the next paragraphs, several muscle properties are described that are essential for modelling: force-amplitude relationship, force-velocity relationship, and length-tension relationship.

Force-Amplitude relationship

With so many contributing factors (as listed above in Table 2.2), sEMG amplitude is not simply equivalent to force. Nevertheless, there is some correlation between increased force and increased sEMG amplitude. This is illustrated in Figure 2.8 for the normalised forces produced by the biceps, deltoid, and first dorsal interosseous (FDI) muscles and corresponding normalised values of the sEMG feature extractor. The three muscles all show a different transfer function from sEMG feature extractor to produced force. The FDI muscle has the most linear curve, whereas the biceps muscle shows a more nonlinear relationship. This is because muscles that predominantly contain one fibre type possess a more linear relationship than muscles with mixed fibre types. As in the case of the biceps muscle, these relationships are more curvilinear with their breaking point at around 50% MVC [4]. Unfortunately, constructing similar curves for facial muscles is difficult because lifting predetermined weights with isolated muscle contractions is cumbersome. However, using displacements and e.g. finite-element models, internal forces may be calculated.

Muscle fatigue and sEMG changes

Muscle fatigue, or the inability to sustain or generate force, can be the result of two underlying factors: metabolic fatigue and neural fatigue. Metabolic fatigue is caused by a shortage of fuel, such as ATP, glycogen, and creatine phosphate, or the pollution within a muscle fibre by substrates that interfere with the calcium ions [34,35]. Neural fatigue is inadequate motor command in the motor cortex [34]. The effect of muscle fatigue on sEMG was first noticed by Piper, who noticed a 'slowing' of surface myoelectric signals during static contraction [35,36]. Nowadays, high-density sEMG is used to decompose the underlying MUs from the superposed sEMG signal. High-density sEMG is defined as: "a non-invasive technique to measure electrical muscle activity with multiple (more than two) closely spaced electrodes overlying a restricted area of the skin" by Drost et al. [37].

It can measure both spatial and temporal activity. Farina and Holobar demonstrated the muscle fatigue characteristics using the high-density sEMG technique (Figure 2.9) [35,38]. The main findings show a decrease in conduction velocity and a change in MU shape.

Table 2.2 Factors that influence the surface EMG. Adopted from [29].

Type	Subtype	Source
Non-physiological	Anatomic	Shape of the volume conductor
		Thickness of the subcutaneous tissue layers
		Tissue inhomogeneities
		Distribution of the motor unit territories in the muscle
		Size of the motor unit territories
		Distribution and number of fibres in the motor unit territories
		Length of the fibres
		Spread of the endplates and tendon junctions within the motor units
		Spread of the innervation zones and tendon regions among motor units
		Presence of more than one pinnation angle
	Detection system	Skin-electrode contact (impedance, noise)
		Spatial filter for signal detection
		Electrode size and shape
		Inclination of the detection system relative to muscle fibre orientation
		Location of the electrodes over the muscle
	Geometrical	Muscle fibre shortening
		Shift of the muscle relative to the detection system
	Physical	Conductivities of the tissues
		Amount of crosstalk from nearby muscles
Physiological	Fibre membrane properties	Average muscle fibre conduction velocity
		Distribution of motor unit conduction velocities
		Distribution of conduction velocities of the fibres within the motor units
		Shape of the intracellular action potentials
	Motor unit properties	Number of recruited motor units
		Distribution of motor unit discharge rates
		Statistics and coefficient of variation for discharge rate
		Motor unit synchronisation

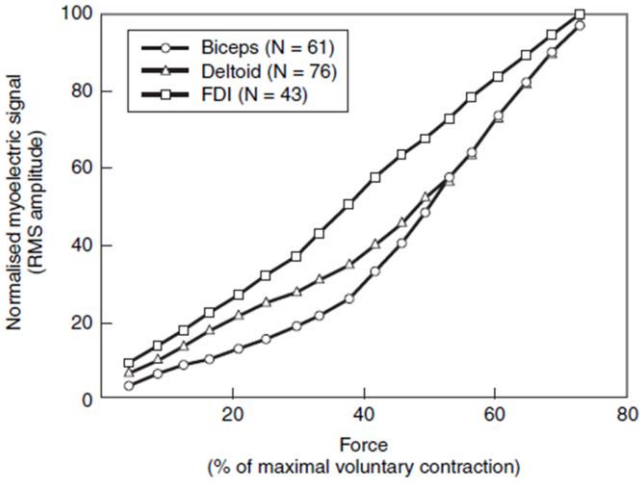

Figure 2.8 Effects of muscle on sEMG signal-force relationship. FDI: first dorsal interosseous muscle. N = average number of isometric contractions for each muscle group. Adopted from Lawrence and De Luca [39].

Electrode configuration

Detection of sEMG signals can be performed in various electrode placement configurations. The ideal placement of the surface electrodes is at the midline of the muscle belly, parallel to the muscle fibres. Laptaki et al. investigated the optimal placement of surface electrodes in the lower face using high-density sEMG grids [40], which can serve as a guideline. The main distinct configurations are: monopolar, bipolar, and tripolar. In all cases, a common ground reference electrode is placed at an electrically neutral site (usually a bony part). The monopolar configuration is the optimal configuration for sEMG acquisition since, in this configuration, the signal will contain all information that can be recorded from the detection volume [41]. However, it is more prone to artefacts and crosstalk; the bipolar configuration, therefore, is widely used. With the upcoming use of high-density sEMG, the choice of configuration has become less relevant, because multiple electrode deductions can be made. In this way, the optimal configuration can be obtained [41,42].

2.1.3. EMG processing: from sEMG signals to muscle activation signals

Adequate sEMG recording requires proper skin preparation, the right choice of electrodes, and accurate electrode positioning. Abrasive gel and alcohol are used to remove hair and dead skin cells. Smaller electrodes will increase spatial resolution and decrease crosstalk, but they will also increase the skin-electrode impedance values. The electrodes measure the unamplified EMG signal, which typically is in the range between a few μV and 2-3 mV. As stated by Nyquist, the signal should be sampled at at least twice its maximum frequency. SENIAM, the European initiative on surface electromyography noninvasive assessment of muscles, has given important recommendations to standardise these facets (Tale 2.3) [43].

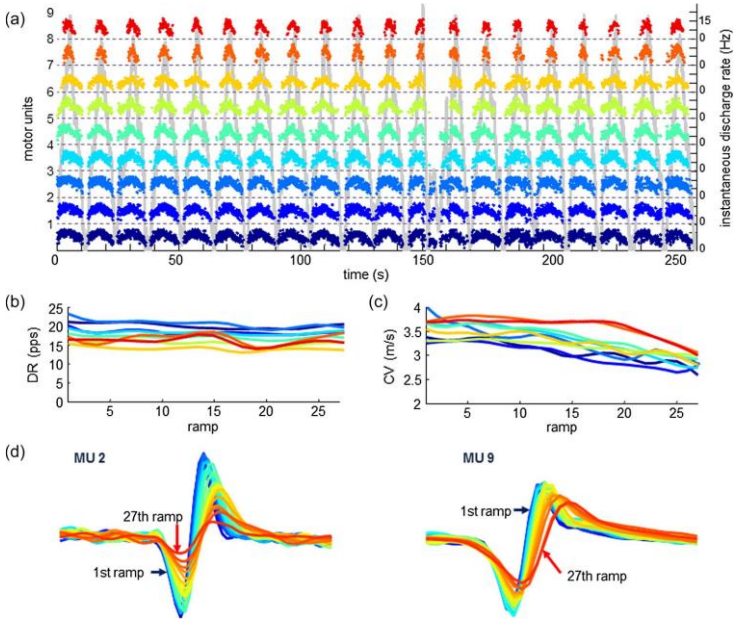

Figure 2.9 Discharge patterns of nine motor units identified by convolution kernel compensation decomposition from 64-channel surface EMG of the abductor pollicis brevis muscle during 27 repetitions of isometric linearly increasing and decreasing contractions (with force ranging from 0% to 10% of the maximum). In this example, ischemia was induced in the hand with a cuff around the forearm inflated at 180 mmHg to increase fatigue. Each dot indicates a single motor unit discharge at a given instant, whereas its relative vertical displacement codes the instantaneous motor unit discharge rate. Different motor units are depicted in different colors and are active for different proportions of time. Thus, they demonstrate different levels of fatigue. Motor units 1 to 7 gradually decrease their average conduction velocity (CV) across different contractions, whereas motor units 8 and 9 maintain the initial conduction velocity from the first to the 18th contraction, but then their conduction velocity decreases after the 18th contraction. Average motor unit discharge rates per contraction (DR) do not vary significantly over time [panel (b)]. The MUAPs of motor units 1 to 7 change significantly over the 27 contractions, while much smaller changes are observed for motor units 8 and 9. Corresponding colours in panels (a), (b), and (c) represent the results of the individual motor units. In panel (d), the various colours represent distinct contractions. Adopted from [38] with permission of IEEE. ©2016 IEEE.

Feature Extraction

To obtain useful information from the measured surface electromyographic signals, a mathematical process called 'feature extraction' is required. Thirty-seven time domain and frequency domain features were investigated by Phinyomark et al. [44]. They found that most were redundant and could be classified into four main groups according to their mathematical properties: energy and complexity, frequency, prediction model, and time-dependence [44]. Despite root mean square being the most well-known feature, the mean absolute value proved to be the recommendation for the energy information method. The wavelength feature was recommended for the complexity information

method, the Willison amplitude for the frequency information group, autoregressive coefficients performed best for the prediction model methods, and, lastly, MAVS for the time-dependency method. The frequency domain features proved inferior in sEMG signal classification. Table 2.4 presents the equations of the above winners per mathematical class.

Tale 2.3 SENIAM recommendations. Adapted from [45].

Part	Parameter	Recommendation
Electrodes	Material	Ag/AgCl with pre-gelled surface
	Size and shape	Circular electrodes with a diameter < 10mm
	Interelectrode distance (IED)	< 20mm or < ¼ of muscle length, whichever is smaller
	Location	
	Longitudinal	Halfway the distal motor endplate zone and the distal tendon
	Transversal	Maximise geometrical distance to other muscles
	Bipolar configuration	Parallel to muscle fibres
	Reference electrode location	Wrist, ankle, spinous process of C7, or other electrically inactive areas
Amplifier	High-pass filter	
	For EMG spectral analysis	< 10 Hz
	For movement analysis only	~ 20 Hz
	Low-pass filter	
	For general applications	~ 500 Hz (sampling frequency> 1000 samples/s)
	For wideband applications	~ 1000 Hz (sampling frequency> 2000 samples/s)
	Input referred voltage noise level (IRVNL)	< 1 μV_{RMS} (bandwidth 10 – 500 Hz)
	Input referred current noise level (IRCNL)	< 10 pA_{RMS} (bandwidth 10 – 500 Hz)
	Input impedance	
	Conventional electrodes	> 100 MΩ
	Pasteless 'dry' pin electrodes	> 1000 MΩ
	Gain	Suitable to bring the signal into the input range of the A/D converter with desired input resolution
Sampler and A/D converter	Sampling frequency (f_s)	> 1000 Hz (general applications > 2000 Hz (wideband applications)
	N bits of A/D	12 (requires amplifier with variable gain) 16 (fixed gain amplifiers may be used)

Normalising the sEMG features

For most applications in biomechanical modelling, the sEMG features have to be normalised to obtain values between zero and one. Halaki and Ginn extensively described the normalisation of EMG signals, as will be briefly discussed below [46]:

1. Maximum (peak) activation levels during maximum contractions: this is the most common method. The EMG recorded during the maximum voluntary isometric contraction (MVIC) task is used as the 100% reference value. Sometimes, the EMG during the task produces higher EMG than the MVIC.

To prevent this from occluding the results, researchers used the task under investigation performed at maximum effort as the 100% reference value. Unfortunately, as individuals complete tasks with different motor control schemes, this method does not allow for comparison between volunteers.

2. Peak or mean activation levels obtained during the task under investigation: using the peak or mean activation levels obtained during the task under investigation as the reference value.
3. Activation levels during submaximal isometric contractions: this was suggested as an alternative to the MVIC because volunteers are often unable to mobilise maximum potential. Other limiting factors were the increased risk of injury and pain. Unfortunately, comparison between individuals is, again, impossible.
4. Peak-to-peak amplitude of the maximum M-wave (M-max): an M-wave can be recorded after stimulation of a peripheral motor nerve. To obtain maximum M-wave, we can increase the stimulus amplitude until the M-wave peak-to-peak amplitude increases no further. Despite the potential, repeatability is still questionable.

Table 2.4 Mathematical definitions of different EMG feature extractions: MAV: mean absolute value, RMS: root mean square, WL: wavelength, WAMP: Willison amplitude, AR: autoregressive coefficients, MAVS: mean absolute value slope.

Feature	Formula
RMS	$y_i = \sqrt{\frac{1}{N}\sum_{j=0}^{N-1} x_{i-j}^2}$
MAV	$y_i = \frac{1}{N}\sum_{j=0}^{N-1} \lvert x_{i-j} \rvert$
WL	$y_i = \sum_{j=1}^{N-1} \lvert x_{i-j+1} - x_{i-j} \rvert$
WAMP	$y_i = \sum_{j=1}^{N-1} \left[f\left(\lvert x_{i-j+1} - x_{i-j} \rvert \right) \right]$ $f(x) = \begin{cases} 1 \; if \; x \geq x_{\lim} \\ 0 \; if \; x < x_{\lim} \end{cases}$
AR	$y_i = \sum_{p=1}^{P} a_P y_{i-p} + x_i$ suggested order $P = 4$
MAVS	$y_{i,k} = \mathrm{MAV}_{i+k} - \mathrm{MAV}_k$ difference between adjacent MAVs $\mathrm{MAV}_i = \frac{1}{N}\sum_{j=0}^{N-1} \lvert x_{i-j} \rvert$ $k = 1, \ldots, K-1$ K = number of segments, covering the signal suggested $K = 3$

2.2. Biomechanical Modelling

2.2.1. A brief history [2]

De Motu Animalium (On the Movement of Animals), written by Aristotle (384–322 BC) in ±350 B.C., can be seen as the first written history of the study of biomechanics [47]. The term 'biomechanics' (1899 A.C. [48]) comes from the ancient Greek words βίος (bios) and μηχανική (mēchanikē), which respectively mean life and mechanics. Biomechanics is the study of structure and function of biological systems using methods of mechanics. Leonardo di ser Piero Da Vinci (April 15th, 1452 – May 2nd, 1519), the ultimate universal genius (Homo Universalis), was also interested in biomechanics. He studied joint function and analysed the forces on muscle tendons from origins to insertions. He applied animal concepts into his inventions, e.g., a bird's flight anatomy for his well-known flying machines [54]. René Descartes (March 31st, 1596 – February 11th, 1650; Cogito ergo sum – *Je pense, que je suis* – I think therefore I am) was a notable French intellectual in the Dutch Golden Age, who stated that we are all mere machines governed by mechanical laws, with the exception of our soul [55]. Giovanni Alfonso Borelli (January 28th, 1608 – December 31st, 1679), encouraged by this idea, studied all kinds of movement using mechanics [56]. Isaac Newton January 4th, 1643 – March 31st, 1727[3]) published his book "*Philosophiæ Naturalis Principia Mathematica*" in 1687, which lay the foundations for classical mechanics [57]. The generally known equations of motion also play an important part in this dissertation. Ernst Heinrich Weber (June 24th, 1795 – January 26th, 1878) and Wilhelm Eduard Weber (October 24th, 1804 – June 23rd, 1891) published their work "*Mechanik der menslichen Gehwerkzeuge*" in 1836 [58]. However, modern motion analysis was first applied by Étienne-Jules Marey (March 5th, 1830 – May 16th, 1904), who used cinematography to investigate locomotion and correlated this to ground reaction forces. He published "*Du mouvement dans les fonctions de la vie*" in 1868 and "*Le Mouvement*" in 1894 [59,60].

Figure 2.10 Some important persons in the history of biomechanics. Figures adopted from [49–53].

[2] The history template is based on the presidential lecture given by Martin at the 23rd annual conference of the American society of biomechanics [102].
[3] The British Empire adopted the Gregorian calendar in 1752 in favour of the Julian calendar. The Julian calendar dates are: December 25th 1642 and March 20th 1727.

Research in human gait analysis (and thus biomechanics) was taken to a higher level by Christian Wilhelm Braune (July 17th, 1831 – April 29th, 1892), who published "*Der Gang des Menschen"* together with Otto Fisher (1861 - 1917) in 1895 [61].

The field of computational biomechanics has grown with the increase of computing power since the 1940s. Nowadays, the finite-element method is widely used in modern technological and medical research, with future applications in daily clinical practice [62–68].

2.2.2. From statistical modelling towards biomechanical modelling

Statistical models are great for modelling relationships and representing real-world data in rather straightforward mathematical equations. There are so-called black-box models, in which the model's internal workings are unknown, and grey-box models, in which the model's internal workings are known but the real-world physical workings are not represented. In our case, we want to look at the relationship between sEMG features and 3D lip positions, velocities, and accelerations. If these relationships exist, biomechanical models that incorporate physiological features could be utilised to provide an anatomical and physiological realistic model. This would be a so-called white-box model because we know the internal workings of the model, e.g., equations of motion, the muscle activation and contraction dynamics, et cetera.

The statistical models described in this dissertation use principal component analysis (PCA) and an extended version of the generalised regression neural network (GRNN). PCA was first described by Pearson in 1901, whereas GRNN was proposed by Specht in 1999 [69,70]. After first obtaining information on a static relationship, we must prove this relationship for a dynamic case, too, incorporating dynamics into the model by using state-space representation. We optionally applied a Kalman filter[4] [71–73].

Upon accepting the existence of a plausible relationship between dynamic 3D lip movement and sEMG features, we can move on to more complex biomechanical models that better represent real-world physiological processes. The biomechanical models can be divided into modelling subparts: rigid bodies (i.e., bones), deformable tissues (i.e., soft tissues), and muscles (i.e., active parts which produce forces). These parts can all be presented with simple or more complex mathematical descriptions. Models can be either static or dynamic. Static models disregard effects over time. Surgery planning in maxillofacial surgery as described by Mollemans et al. is one example of using a static model [74].

Dynamic simulations are models in which forces that act on the model are time-dependent. One such model was developed by Chabanas et al. [65,75] and Gladilin et al.

[4] The Kalman filter's first implementation was in the Apollo navigation computer. Stanley F. Schmidt realised that the filter could be divided into two distinct parts: one part for time periods when no sensor outputs are available and another part when sensor outputs are available to incorporate the measurements. This partitioning of the estimation problem was advantageous for the Apollo mission because hours could elapse between sensor outputs. [103]

[76,77], who resected the bones of their digital model, and reconstructed the jaw at the optimal location. They then visualised the effects of the new bone structure on outer appearance by simulating the effects of bone reposition on soft tissues. They also defined the facial muscles and through dynamic simulation assessed the effects of muscle activation on soft tissues [65,75]. The facial muscles can be activated with simulated (arbitrary) muscle activation patterns, or they can be supplied with an approximation of the real muscle activation patterns, with the use of sEMG features as derivations of the muscle activity. This is called 'forward dynamics' or 'forward modelling'. In our case, forward modelling will drive a model with sEMG features that can accurately describe the measured 3D lip movement. Forward modelling will be essential for our future application because it will show the 3D movement when using patient-specific muscle activation patterns. If the model is accurate enough, this will result in similar movement as the captured movement. Also, when the model is adjusted virtually to incorporate surgical changes, forward modelling with an adjusted model and patient-specific muscle activation patterns may show us potential limitations in the form of the expected functional problems. Biomechanical modelling may also be used to track the outputs, the 3D lip movements, in order to obtain the muscle activation patterns required to establish such movements. This is called 'inverse dynamics' or 'inverse modelling'. Inverse modelling plays a major role as it may unravel the possible compensatory mechanisms for vital functional movements. By applying inverse modelling – tracking the movements that produce a vital function and calculating which muscle activation patterns are involved – we could make the model account for resected or damaged muscles. This may be valuable in assessing which nerves and muscles must be spared to maintain the vital functions.

Figure 2.11 Schematic representation of forward and inverse modelling with muscle activations and 3D movement.

2.2.3. Muscle modelling

Zajac rigorously described the mathematical modelling of a muscle and its tendon in 1989 [78]. His text is based on the classical work of Hill, now commonly known as the Hill's muscle model [79]. The Hill-type muscle is shown in Figure 2.12.

In the next paragraphs, two muscle properties are described, which are essential for modelling: force-velocity relationship and length-tension relationship. These can also be found in Zajac's extensive overview. The exerted muscle force depends on the activation levels, the aforementioned force-generation properties, and the tendon properties [78].

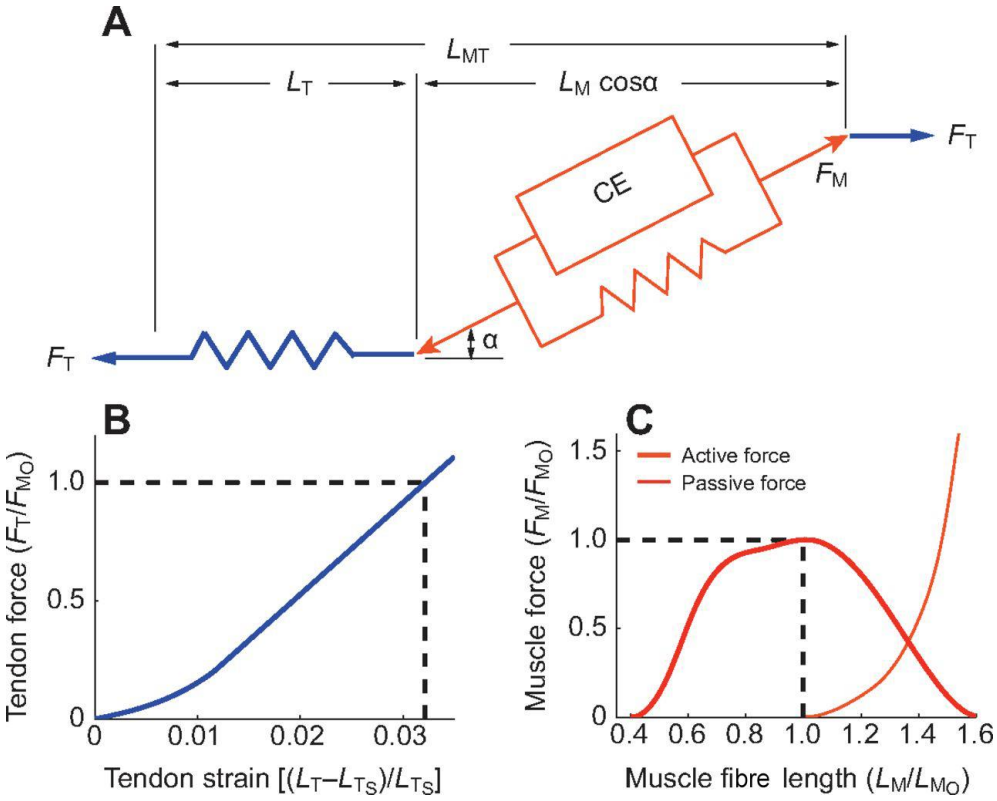

Figure 2.12 **Hill-type muscle model. (A) The muscle model consists of a contractile element (CE) arranged in parallel with an elastic element (PE), which primarily represent the mechanical properties of the muscle fibres. Both of these elements are in series with another elastic element (SE), primarily representing the mechanical properties of the tendon. (B) Tendon force depends nonlinearly on tendon length and is related to muscle force according to the formula: $F_T=F_M \cos\alpha$, where F_T is tendon force, F_M is muscle force, and α is pennation angle. (C) Isometric muscle force is taken to be equal to the sum of passive force and active force, both of which depend nonlinearly on muscle length. Muscle length and tendon length are related to total musculotendon length according to the formula: $L_{MT}=L_T+L_M \cos\alpha$, where L_{MT} is musculotendon length, L_T is tendon length, and L_M is muscle length. L_{MO}, optimal muscle length; L_{TS}, tendon slack length; F_{MO}, peak isometric muscle force. Adopted from [80], who adapted it from [81] with permission of IEEE and The Company of Biologists Ltd. ©1990 IEEE and ©2013 The Company of Biologists Ltd.**

Force-Velocity relationship

Exerted muscle force (or, more specifically, active tension) also depends on contraction velocity (Figure 2.13). The contraction velocity, in turn, depends on the cross-bridging of sarcomeres. During concentric (muscle actively shortening) actions and when velocity is high, forming the necessary cross-bridges is more difficult because of the sliding filaments cycle time, whereas in low-velocity circumstances there is more time to form more cross-bridges and thus more force. In eccentric (muscle actively lengthening) actions, muscle force is high where velocity is high, and muscle force is low where velocity is low.

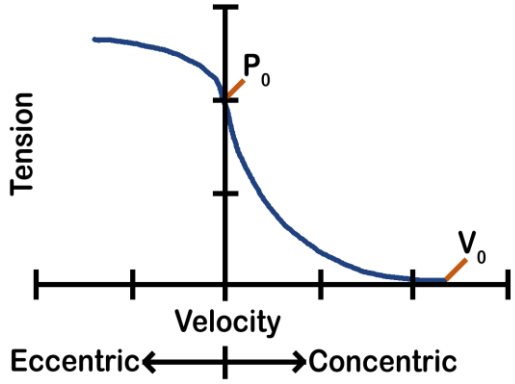

Figure 2.13 Velocity-active tension relationship for muscle. P_0 describes the force or tension at isometric (muscle actively held at fixed length) and V_0 is the maximum velocity under zero tension. Adapted from [82].

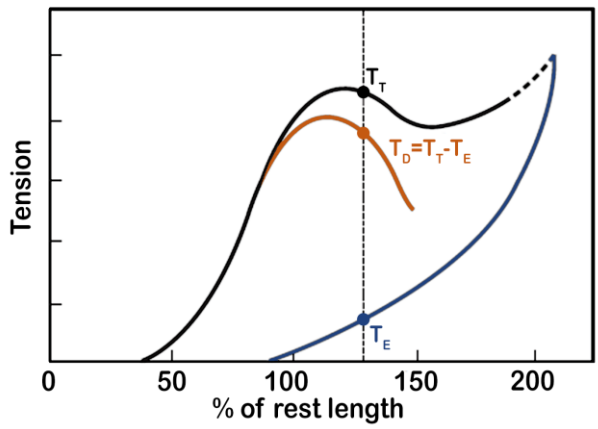

Figure 2.14 Tension-length curves for isolated muscle. Blue curve: passive elastic tension T_E in a muscle passively stretched to increasing lengths. Black curve: total tension T_T exerted by muscle contracting actively from increasing initial lengths. Orange curve: developed tension T_D calculated by subtracting elastic tension values on curve 1 from the total tension values at equivalent lengths on curve 2 ($T_D = T_T - T_E$). Adapted from [83]. Original image ©1988 Williams & Wilkins.

Length-Tension relationship

Muscle force also depends on the resting length of the muscle. The total tension depends on the active and passive tension in the muscles. The active tension-length relationship describes the degree of overlap of the actin and myosin filaments and thus cross-bridge effectiveness, whereas the passive tension-length relationship describes the exerted force due to passive stretch of the muscles including elastic elements. This is shown in Figure 2.14.

2.2.4. Optimisation techniques

In biomechanical modelling, forces are the central point. Inherently, the equations of motion developed by Newton come into play, in particular Newton's second law [84]:

$$\mathbf{f}(\mathbf{q},\mathbf{u},t) = \mathbf{M}\dot{\mathbf{u}} \tag{2.4}$$

In which, $\mathbf{q}$ is a vector containing positions, $\mathbf{u}$ is a vector with velocities, and t is time. $\mathbf{M}$ is the diagonal matrix containing masses. The force vector $\mathbf{f}(\mathbf{q},\mathbf{u},t)$ can be divided into a passive (muscle stretch, ligaments, scar tissue) and an active part (forces due to muscle activation): $\mathbf{f}(\mathbf{q},\mathbf{u},t) = \mathbf{f}_p(\mathbf{q},\mathbf{u}) + \mathbf{f}_a(\mathbf{q},\mathbf{u},\mathbf{a}(t))$, in which $\mathbf{a}(t)$ contains the muscle activations between 0 and 1. In the Hill-type muscle models, the relationship between activation and force is linear. The relationship between force, length, and shortening velocity is nonlinear. This is described mathematically as:

$$\mathbf{f}_a = \mathbf{\Lambda}(\mathbf{q},\mathbf{u})\mathbf{a} \tag{2.5}$$

The matrix $\mathbf{\Lambda}$ relates the activations in vector $\mathbf{a}$ to the system forces. Because of these basic equations, the forward and inverse problems can be solved using optimisation techniques. Erdemir et al. provided an extensive work on model-based estimation of muscle forces [85]. Because the human body has many joints, and multiple muscles act on these joints, estimating the muscle forces distributed over these muscles is difficult. Moreover, distinct muscle activation patterns can achieve the same movement of the joint. This so-called 'muscle redundancy' or 'load-sharing problem' can be solved by minimising a cost or objective function. Unfortunately, the choice of the objective function or cost terms will determine the outcome of estimated muscle forces, which will often differ from the measured indication of active muscles. The various optimisation techniques that can be used to solve the optimisation problem can be grouped into the following strategies [85]: a) inverse dynamics-based static optimisation, b) forward dynamics assisted data tracking, c) optimal control, and d) other strategies.

2.3. Aim and outline

This dissertation aims to demonstrate the feasibility and importance of muscle activation signals calculated from sEMG recordings in biomechanical models of the face, for application in a virtual therapy toolkit. Much research has been conducted into biomechanical modelling with sEMG of the lower and upper limbs (see Erdemir et al. [85]). Studies of the facial muscles, face models, and EMG, however, are scarce. Research describing facial EMG measurements has been performed in the context of speech interfaces – mostly silent-speech interface [86] and multi-modal speech synthesis [87] – lipreading [88], human machine interfaces [89,90], psychophysiology [91,92], and medical assessments [93,94]. Few studies reported on the estimation of lip shapes or lip movement incorporating EMG [95,96], while facial models are widely present [76,97–101].

Part II describes the statistical exploration into the practical use of sEMG as a predictor or estimator of facial expressions and visemes, which are groups of speech sounds that visually look the same: e.g., mama and papa. Chapter 3 classifies 3D lip shapes with sEMG, essentially indicating that sEMG of the facial muscles can convey enough information to create personalised 3D lip models. Chapter 4 extends this work towards dynamic movements and also incorporates dynamics into the statistical model.

In Part III, sEMG applicability is further explored in biomechanical models. In Chapter 5, facial expressions are simulated with a biomechanical face model that uses sEMG signals as a derivative of the person-specific activation signals. The opposite procedure, inverse modelling to obtain realistic person-specific activations signals, is performed in Chapter 6. This chapter evaluates whether sEMG could help in solving the ambiguity problem that occurs in inverse modelling, as described above. As inverse-modelling in a finite-element model will be a rather time-consuming approach, Chapter 7 evaluates different methods with a simplified model of the arm with two degrees of freedom. This chapter aims to give us an indication of which algorithms can be best pursued in the more complex models of the face and tongue. The performance assessment of two inverse-modelling algorithms, with and without sEMG assistance, may serve as a first indicator.

Finally, Part IV wraps up the work by presenting a short summary per chapter, general conclusions, a general discussion, and future perspectives in Chapter 8. A general summary in English and in Dutch follow in Chapters 9 and 10.

The appendices have been accommodated in Part V.

2.4. References

1. Redi F. Esperienze intorno a diverse cose naturali, e particolarmente a quelle, che ci son portate dall'Indie. 1617. pp. 47–51.
2. Galvani L. De viribus electricitatis in motu musculari commentarius [Internet]. Accademia delle Scienze. 1791. Available: http://137.204.24.205/cis13b/bsc03/intro_opera.asp?id_opera=23
3. Du Bois-Reymond E. Untersuchungen über thierische elektricität. Teimer-verlag. 1849.
4. Criswell E, editor. Cram's Introduction to Surface Electromyography. Bartlett Publishers. 2010.
5. Hardyck CD, Petrinovich LF, Ellsworth DW. Feedback of Speech Muscle Activity during Silent Reading: Rapid Extinction. Science (80-). 1966;154: 1467–1468. doi:10.1126/science.154.3755.1467
6. Cram JR, Engstrom D. Patterns of neuromuscular activity in pain and nonpain patients. Clin Biofeedback Heal. 1986;9: 106–116.
7. Nishizono H, Saito Y, Miyashita M. The Estimation of Conduction Velocity in Human Skeletal Muscle in situ with Surface Electrodes. Electroencephalogr Clin Neurophysiol. 1979;46: 659–664. doi:10.1016/0013-4694(79)90103-2
8. De Luca CJ. Myoelectrical manifestations of localized muscular fatigue in humans. Crit Rev Biomed Eng. 1984;11: 251–279.
9. Wikimedia Commons contributors. Étienne Jules Marey by Nadar [Internet]. 2016 [cited 1 Sep 2017]. Available: https://commons.wikimedia.org/w/index.php?title=File:Étienne_Jules_Marey_by_Nadar.jpg&oldid=212312669
10. Wikimedia Commons contributors. Francesco Redi [Internet]. 2017 [cited 1 Sep 2017]. Available: https://commons.wikimedia.org/w/index.php?title=File:Francesco_Redi.jpg&oldid=239644513
11. Wikimedia Commons contributors. Luigi Galvani, oil-painting [Internet]. [cited 1 Sep 2017]. Available: https://commons.wikimedia.org/w/index.php?title=File:Luigi_Galvani,_oil-painting.jpg&oldid=251480478
12. Wikimedia Commons contributors. Dubua-Reymon [Internet]. 2016 [cited 1 Sep 2017]. Available: https://commons.wikimedia.org/w/index.php?title=File:Dubua-Reymon.jpg&oldid=223558964
13. Professor Carlo J. De Luca (1943–2016). J Electromyogr Kinesiol. 2017;32: A1 doi:10.1016/j.jelekin.2016.10.007
14. Clark Jr. JW. The origin of biopotentials. In: Webster JG, editor. Medical instrumentation application and design. 4th ed. 2010. pp. 126–146.
15. Wikimedia Commons contributors. Scheme sodium-potassium pump [Internet]. 2017 [cited 1 Sep 2017]. Available: https://commons.wikimedia.org/w/index.php?title=File:Scheme_sodium-potassium_pump-en.svg&oldid=254194406
16. Eugene. The Muscular System - Biology of Humans [Internet]. 2017 [cited 1 Sep 2017]. Available: http://schoolbag.info/biology/humans/7.html
17. Huxley AF, Niedergerke R. Structural Changes in Muscle During Contraction: Interference Microscopy of Living Muscle Fibres. Nature. 1954;173: 971–973. doi:10.1038/173971a0
18. Huxley H, Hanson J. Changes in the Cross-Striations of Muscle during Contraction and Stretch and their Structural Interpretation. Nature. 1954;173: 973–976. doi:10.1038/173973a0
19. Huxley HE. The Mechanism of Muscular Contraction. Science (80-). 1969;164: 1356–1366. doi:10.1126/science.164.3886.1356
20. Spudich JA, Sivaramakrishnan S. Myosin VI: an innovative motor that challenged the swinging lever arm hypothesis. Nat Rev Mol Cell Biol. 2010;11: 128–137. doi:10.1038/nrm2833
21. Holmes KC. The swinging lever-arm hypothesis of muscle contraction. Curr Biol. 1997;7: R112–R118. doi:10.1016/S0960-9822(06)00051-0
22. Batters C, Veigel C, Homsher E, Sellers JR. To understand muscle you must take it apart. Front Physiol. 2014;5: 1–14. doi:10.3389/fphys.2014.00090

23. Winter DA. Biomechanics and Motor Control of Human Movement [Internet]. John Wiley & Sons, Inc. 2009. doi:10.1002/9780470549148

24. Basmajian J V, DeLuca CJ. Muscles alive: their functions revealed by electromyography. Williams & Wilkins. 1985.

25. Webster J. Encyclopedia of Medical Devices and Instrumentation [Internet]. Webster JG, editor. John Wiley & Sons, Inc. 2006. doi:10.1002/0471732877

26. Eskes M. Development of a facial sEMG controlled personalised dynamic 3D lip model. University of Twente. 2013.

27. Marieb EN, Hoehn. Human Anatomy & Physiology. 9th ed. Pearson Education Inc. 2013.

28. Seeley ST. Anatomy & Physiology. 8th ed. The McGraw-Hill Companies, Inc. 2008.

29. Farina D, Merletti R, Enoka RM. The extraction of neural strategies from the surface EMG. J Appl Physiol. 2004;96: 1486–1495. doi:10.1152/japplphysiol.01070.2003

30. Farina D, Merletti R, Enoka RM. The extraction of neural strategies from the surface EMG: an update. J Appl Physiol. 2014;117: 1215–1230. doi:10.1152/japplphysiol.00162.2014

31. De Luca CJ. The Use of Surface Electromyography in Biomechanics. J Appl Biomech. 1997;13: 135–163. doi:10.1123/jab.13.2.135

32. Merletti R. Standards for Reporting EMG Data. J Electromyogr Kinesiol. 2017;35: I–II. doi:10.1016/S1050-6411(17)30219-5

33. Huang C, Chen C, Chung H-Y. The review of applications and measurements in facial electromyography. J Med Biol Eng. 2004;25: 15–20.

34. Enoka RM, Duchateau J. Muscle fatigue: what, why and how it influences muscle function. J Physiol. 2008;586: 11–23. doi:10.1113/jphysiol.2007.139477

35. Cifrek M, Medved V, Tonković S, Ostojić S. Surface EMG based muscle fatigue evaluation in biomechanics. Clin Biomech. 2009;24: 327–340. doi:10.1016/j.clinbiomech.2009.01.010

36. Piper H. Elektrophysiologie menschlicher Muskeln [Internet]. 1st ed. Springer Berlin Heidelberg. 1912. doi:10.1007/978-3-642-50944-5

37. Drost G, Stegeman DF, van Engelen BGM, Zwarts MJ. Clinical applications of high-density surface EMG: a systematic review. J Electromyogr Kinesiol. 2006;16: 586–602. doi:10.1016/j.jelekin.2006.09.005

38. Farina D, Holobar A. Characterization of Human Motor Units From Surface EMG Decomposition. Proc IEEE. 2016;104: 353–373. doi:10.1109/JPROC.2015.2498665

39. Lawrence JH, De Luca CJ. Myoelectric signal versus force relationship in different human muscles. J Appl Physiol. 1983;54: 1653–9. Available: http://www.ncbi.nlm.nih.gov/pubmed/6874489

40. Lapatki BG, Oostenveld R, Van Dijk JP, Jonas IE, Zwarts MJ, Stegeman DF. Optimal placement of bipolar surface EMG electrodes in the face based on single motor unit analysis. Psychophysiology. 2010;47: 299–314. doi:10.1111/j.1469-8986.2009.00935.x

41. Merletti R, Botter A, Troiano A, Merlo E, Minetto MA. Technology and instrumentation for detection and conditioning of the surface electromyographic signal: state of the art. Clin Biomech (Bristol, Avon). 2009;24: 122–34. doi:10.1016/j.clinbiomech.2008.08.006

42. Staudenmann D, Kingma I, Stegeman DF, van Dieën JH. Towards optimal multi-channel EMG electrode configurations in muscle force estimation: a high density EMG study. J Electromyogr Kinesiol. 2005;15: 1–11. doi:10.1016/j.jelekin.2004.06.008

43. Stegeman DF, Hermens HJ. Standards for surface electromyography : the European project " Surface EMG for non-invasive assessment of muscles (SENIAM)." 1999; 108–112.

44. Phinyomark A, Phukpattaranont P, Limsakul C. Feature reduction and selection for EMG signal classification. Expert Syst Appl. 2012;39: 7420–7431. doi:10.1016/j.eswa.2012.01.102

45. Liu C. Prediction of lip shapes based on electromyography measurements. University of Twente. 2010.

46. Halaki M, Gi K. Normalization of EMG Signals: To Normalize or Not to Normalize and What to Normalize to? Computational Intelligence in Electromyography Analysis - A Perspective on Current Applications and Future Challenges. 2012. doi:10.5772/49957

47. Farquharson ASL. On the motion of animals by Aristotle [Internet]. The University of Adelaide. 2015. Available: https://ebooks.adelaide.edu.au/a/aristotle/motion/

48. Merriam-Webster. Biomechanics [Internet]. [cited 1 Sep 2017]. Available: https://www.merriam-webster.com/dictionary/biomechanics

49. Wikimedia Commons contributors. Francesco Hayez 001 [Internet]. 2016 [cited 1 Sep 2017]. Available: https://commons.wikimedia.org/w/index.php?title=File:Francesco_Hayez_001.jpg&oldid=203300306

50. Vinci L da. Biografia di Leonardo da Vinci [Internet]. 2017 [cited 1 Sep 2017]. Available: http://community.pcacademy.it/wp-content/lavori/Urbanetz/bio.html

51. Wikimedia Commons contributors. Frans Hals - Portret van René Descartes [Internet]. 2016.

52. Wikimedia Commons contributors. Giovanni Alfonso Borelli [Internet]. 2014 [cited 1 Sep 2017]. Available: https://commons.wikimedia.org/w/index.php?title=File:Giovanni_Alfonso_Borelli.jpg&oldid=141669929

53. Wikimedia Commons contributors. GodfreyKneller - IsaacNewton [Internet]. 2017 [cited 1 Sep 2017]. Available: https://commons.wikimedia.org/w/index.php?title=File:GodfreyKneller-IsaacNewton-1689.jpg&oldid=253851567

54. Sirén O. Leonardo da Vinci, the artist and the man. New Haven Yale University Press. 1916.

55. Nadler S. The philosopher, the priest, and the painter: a portrait of Descartes. Princeton University Press. 2013.

56. Borelli GA. De motu animalium. Lugduni in Batavis : apud Danielem à Gaesbeeck, Cornelium Boutesteyn, Iohannem de Vivie & Petrum van der Aa. 1685. doi:10.3931/e-rara-28707

57. Newton I. Philosophiae Naturalis Principia Mathematica [Internet]. Jussu Societatis Regiae ac Typis Josephi Streater. 1687. doi:10.3931/e-rara-440

58. Weber W, Weber E. Mechanik der menschlichen Gehwerkzeuge eine anatomisch-physiologische Untersuchung. Dietrich. 1836.

59. Marey E-J. Du mouvement dans les fonctions de la vie. Baillière G, editor. Germer Baillière. 1868.

60. Marey E-J. Le Mouvement. Masson G, editor. Libraire de l'académie de médecine. 1984.

61. Fischer O, Braune CW. Der Gang des Menschen. 1985.

62. Zienkiewicz OC, Taylor RL, Zienkiewicz OC, Taylor RL. The finite element method. McGraw-hill London. 1977.

63. Koch RM, Gross MH, Carls FR, von Büren DF, Fankhauser G, Parish YIH. Simulating facial surgery using finite element models. Proceedings of the 23rd annual conference on Computer graphics and interactive techniques - SIGGRAPH '96. 1996. pp. 421–428. doi:10.1145/237170.237281

64. Nicosia MA. A planar finite element model of bolus containment in the oral cavity. Comput Biol Med. 2007;37: 1472–1478. doi:10.1016/j.compbiomed.2007.01.007

65. Chabanas M, Payan Y. Finite element model of the face soft tissue for computer-assisted maxillofacial surgery. Proceedings of the Fifth International Symposium on Computer Methods in Biomechanics and Biomedical Engineering (CMBBE 2001). 2001. pp. 1–6. Available: http://membres-timc.imag.fr/Yohan.Payan/papers/BBE01_Chabanas.pdf

66. Kopperdahl DL, Aspelund T, Hoffmann PF, Sigurdsson S, Siggeirsdottir K, Harris TB, Gudnason V, Keaveny TM. Assessment of incident spine and hip fractures in women and men using finite element analysis of CT scans. J Bone Miner Res. 2014;29: 570–580. doi:10.1002/jbmr.2069

67. Koch RM, Roth SHM, Gross MH, Zimmermann AP, Sailer HF. A framework for facial surgery simulation. Proceedings of the 18th spring conference on Computer graphics - SCCG '02. 2002. p. 33. doi:10.1145/584458.584464

68. van Alphen MJA, Kreeft AM, van der Heijden F, Smeele LE, Balm AJM. Towards virtual surgery in oral cancer to predict postoperative oral functions preoperatively. Br J Oral Maxillofac Surg. 2013;51: 747–751. doi:10.1016/j.bjoms.2013.06.012

69. Specht DF. A general regression neural network. IEEE Trans Neural Networks. 1991;2: 568–576. doi:10.1109/72.97934

70. Pearson K. LIII. On lines and planes of closest fit to systems of points in space. Philos Mag Ser 6. 1901;2: 559–572. doi:10.1080/14786440109462720

71. Swerling P. First-order error propagation in a stagewise smoothing procedure for satellite observations. 1959.

72. Kalman RE. A New Approach to Linear Filtering and Prediction Problems. J Basic Eng. 1960;82: 35. doi:10.1115/1.3662552

73. Welch G, Bishop G. An introduction to the Kalman filter. SIGGRAPH. 2001. pp. 1–81.

74. Mollemans W, Schutyser F, Nadjmi N, Maes F, Suetens P. Predicting soft tissue deformations for a maxillofacial surgery planning system: from computational strategies to a complete clinical validation. Med Image Anal. 2007;11: 282–301. doi:10.1016/j.media.2007.02.003

75. Chabanas M, Luboz V, Payan Y. Patient specific finite element model of the face soft tissues for computer-assisted maxillofacial surgery. Med Image Anal. 2003;7: 131–151. doi:10.1016/S1361-8415(02)00108-1

76. Gladilin E, Zachow S, Deuflhard P, Hege H. Towards a Realistic Simulation of Individual Facial Mimics. In: Thomas E, Bernd G, Heinrich N, Hans-Peter S, editors. Proceedings of the Vision Modeling and Visualization Conference 2001 (VMW '01). 2001. pp. 129–134.

77. Gladilin E, Zachow S, Deuflhard P, Hege HC. Anatomy- and physics-based facial animation for craniofacial surgery simulations. Med Biol Eng Comput. 2004;42: 167–170. doi:10.1007/BF02344627

78. Zajac FE. Muscle and tendon: properties, models, scaling, and application to biomechanics and motor control. Crit Rev Biomed Eng. 1989;17: 359–411. Available: http://www.ncbi.nlm.nih.gov/pubmed/2676342

79. Hill AV. The Heat of Shortening and the Dynamic Constants of Muscle. Proc R Soc B Biol Sci. 1938;126: 136–195. doi:10.1098/rspb.1938.0050

80. O'Neill MC, Lee L-F, Larson SG, Demes B, Stern JT, Umberger BR. A three-dimensional musculoskeletal model of the chimpanzee (Pan troglodytes) pelvis and hind limb. J Exp Biol. 2013;216: 3709–23. doi:10.1242/jeb.079665

81. Delp SL, Loan JP, Hoy MG, Zajac FE, Topp EL, Rosen JM. An interactive graphics-based model of the lower extremity to study orthopaedic surgical procedures. IEEE Trans Biomed Eng. 1990;37: 757–767. doi:10.1109/10.102791

82. Soderberg GL, others. Selected topics in surface electromyography for use in the occupational setting: expert perspectives. Cincinnati, OH, US Dep Heal Hum Serv. 1992;

83. Gowitzke BA, Milner M. Scientific bases of human movement. Williams & Wilkins. 1988.

84. Stavness IK. Byte Your Tongue. The University of British Columbia. 2010.

85. Erdemir A, Mclean S, Herzog W, van den Bogert AJ. Model-Based Estimation of Muscle Forces Exerted During Movements. Clin Biomech. 2007;22: 131–154. doi:10.1016/j.clinbiomech.2006.09.005

86. Denby B, Schultz T, Honda K, Hueber T, Gilbert JM, Brumberg JS. Silent speech interfaces. Speech Commun. 2010;52: 270–287. doi:10.1016/j.specom.2009.08.002

87. Beskow J. Talking Heads - Models and Applications for Multimodal Speech Synthesis. KTH Royal Institute of Technology. 2003.

88. Wand M, Schmidhuber J. Improving Speaker-Independent Lipreading with Domain-Adversarial Training. 2017; 2–6. Available: http://arxiv.org/abs/1708.01565

89. Science C, Publications S. Surface Electromyography-Based Facial Expression Recognition in Bi-Polar Configuration Mahyar Hamedi , Sh-Hussain Salleh , Tan Tian Swee , and Kamarulafizam Department of Biomedical Instrumentation and Signal Processing , Faculty of Biomedical and Health . 2011;7: 1407–1415.

90. Hamedi M, Salleh S-H, Astaraki M, Noor AM. EMG-based facial gesture recognition through versatile elliptic basis function neural network. Biomed Eng Online. 2013;12: 73. doi:10.1186/1475-925X-12-73

91. Sato W, Fujimura T, Suzuki N. Enhanced facial EMG activity in response to dynamic facial expressions. Int J Psychophysiol. 2008;70: 70–4. doi:10.1016/j.ijpsycho.2008.06.001

92. Rymarczyk K, Biele C, Grabowska A, Majczynski H. EMG activity in response to static and dynamic facial expressions. Int J Psychophysiol. 2011;79: 330–3. doi:10.1016/j.ijpsycho.2010.11.001

93. Takada J, Miyamoto JJ, Sato C, Dei A, Moriyama K. Comparison of EMG activity and blood flow during graded exertion in the orbicularis oris muscle of adult subjects with and without lip incompetence: a cross-sectional survey. Eur J Orthod. 2017; 1–8. doi:10.1093/ejo/cjx061

94. Szyszka-Sommerfeld L, Woźniak K, Matthews-Brzozowska T, Kawala B, Mikulewicz M. Electromyographic analysis of superior orbicularis oris muscle function in children surgically treated for unilateral complete cleft lip and palate. J Cranio-Maxillofacial Surg. 2017; doi:10.1016/j.jcms.2017.06.012

95. Honda K, Kurita T, Kakita Y, Maeda S. Physiology of the lips and modeling of lip gestures. J Phon. 1995; 243–254.

96. Lucero JC, Munhall KG. A model of facial biomechanics for speech production. J Acoust Soc Am. 1999;106: 2834–2842. doi:10.1121/1.428108

97. Lee Y, Terzopoulos D, Waters K. Realistic Modeling for Facial Animation. 1995; 55–62.

98. P KW. A Muscle Model for Animating Three-Dimensional Facial Expression. 1987;21: 17–24.

99. Wu X, Dang J, Stavness I. Iterative method to estimate muscle activation with a physiological articulatory model. Acoust Sci Technol. 2014;35: 201–212. doi:10.1250/ast.35.201

100. Wu T, Hung AP-L, Hunter P, Mithraratne K. Modelling facial expressions: A framework for simulating nonlinear soft tissue deformations using embedded 3D muscles. Finite Elem Anal Des. 2013;76: 63–70. doi:10.1016/j.finel.2013.08.002

101. Flynn C, Stavness I, Lloyd J, Fels S. A finite element model of the face including an orthotropic skin model under in vivo tension. Comput Methods Biomech Biomed Engin. 2015;18: 571–582. doi:10.1080/10255842.2013.820720

102. Martin RB. A genealogy of biomechanics. 23rd Annual Conference of the American Society of Biomechanics. 1999.

103. Grewal M, Andrews A. Applications of Kalman Filtering in Aerospace 1960 to the Present [Historical Perspectives. IEEE Control Syst Mag. 2010;30: 69–78. doi:10.1109/MCS.2010.936465

PART II

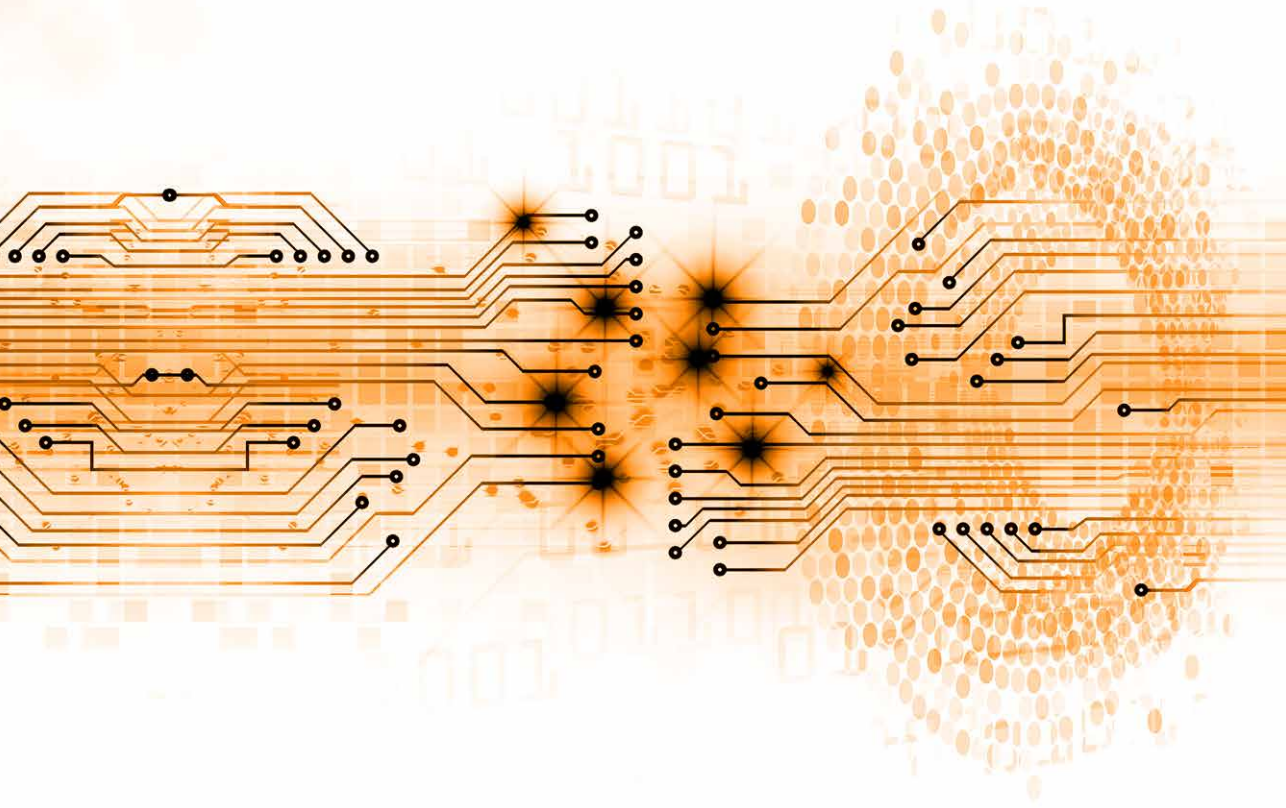

DATA AVAILABLE ONLINE
DOI: 10.17605/OSF.IO/XKJZP

PREDICTING 3D LIP SHAPES USING FACIAL sEMG

This chapter was published in Plubic Library of Science ONE

ESKES M, VAN ALPHEN MJA, BALM AJM, SMEELE LE, BRANDSMA D, VAN DER HEIJDEN F (2017)
PREDICTING 3D LIP SHAPES USING FACIAL SURFACE EMG
PLOS ONE 12(4): E0175025. DOI: 10.1371/JOURNAL.PONE.0175025

Abstract

Aim

The aim of this study is to prove that facial surface electromyography (sEMG) conveys sufficient information to predict 3D lip shapes. High sEMG predictive accuracy implies we could train a neural control model for activation of biomechanical models by simultaneously recording sEMG signals and their associated motions.

Materials and methods

With a stereo-camera set-up, we recorded 3D lip shapes and simultaneously performed sEMG measurements of the facial muscles, applying principal component analysis (PCA) and a modified general regression neural network (GRNN) to link the sEMG measurements to 3D lip shapes. To test reproducibility, we conducted our experiment on five volunteers, evaluating several sEMG features and window lengths in unipolar and bipolar configurations in search of the optimal settings for facial sEMG.

Conclusions

The errors of the two methods were comparable. We managed to predict 3D lip shapes with a mean accuracy of 2.76 mm when using the PCA method and 2.78 mm when using modified GRNN. Whereas performance improved with shorter window lengths, feature type and configuration had little influence.

3.1. Introduction

Treatment choice for oral cavity carcinoma still depends on the subjective judgements of treating physicians and multidisciplinary tumour boards. The primary choice of treatment will normally be surgery, with or without adjuvant radiotherapy [1]. If the functional consequences of surgery would reduce the quality of life to an unacceptable extent, the tumour is considered 'functionally inoperable' [2], and organ-sparing chemoradiation treatment will provide a better alternative. Yet, 'functional inoperability' is a subjective label and as such not very reliable [3].

To predict functional consequences more objectively, we have been developing a virtual-therapy tool that comprises a patient-specific biomechanical model of the oral cavity and oropharynx [4]. To further individualise this model, we proposed implementing electromyographic (EMG) signals to estimate volunteer-specific muscle activations during specific tongue movements. Since surface EMG (sEMG) of the tongue is difficult to perform, we decided first to look at lip shapes, which are easier to capture in 3D images, while their underlying muscle activation patterns are easy to assess with sEMG, yet the facial musculature is still complex enough to prove our concept.

Most research efforts with facial EMG have focussed on speech interfaces, mostly silent-speech interfaces [5] and multimodal speech synthesis models [6]. Their general aim has been to categorise phonemes, words, articulatory features, or gestures by facial and tongue EMG signals [7–14]. Honda et al. [15] and Lucero & Munhall [16] have both published on predicting lip shapes. Honda et al. [15] used video imaging to estimate lip shapes, but the images were in 2D, and their model did not account for jaw movements. Lucero & Munhall's [16] finite-element model (FEM) of the face and lips estimated 3D lip positions, but their lip marker correlation coefficients were relatively low (mean<0.71).

We are now taking a step forward by investigating two methods to estimate 3D lip shapes. Our first objective was to show that facial sEMG can adequately estimate volunteer-specific 3D lip shapes. If sEMG conveys sufficient information to estimate lip shapes, we could use that information together with simultaneous video recordings of the pertaining motions to train a neural control model for the activation of a personalised biomechanical model that in the end will present the effects of treatment in a virtual-therapy environment. Furthermore, this could perhaps bring us closer to solving the load-sharing problem of inverse dynamics [17]. Finally, accurate sEMG-based lip modelling would also be helpful in other fields, such as silent-speech interfaces and multimodal speech synthesis [5,6,11].

Our second objective was to see if we could identify any volunteer-independent settings for sEMG feature extraction, which would greatly benefit our future application: an individualised biomechanical simulation model for lip and oral cancer patients. Not having to optimise the settings per patient would save us a lot of time and effort.

3.2. Materials and methods

3.2.1. Volunteers and data acquisition

To test reproducibility, we recruited five volunteers (four males and one female) aged between 24 and 25. In our recruiting e-mail, we briefly explained about our experiment and on the test day itself, we once again informed them of the procedure and of their rights as volunteers, including the right to withdraw at any moment without stating a reason. All volunteers gave their informed consent and their approval for publication of anonymised results. This experiment was approved by the Medical Research Ethics Committee of the Netherlands Cancer Institute and conducted in accordance with Dutch legislation, including the Agreement on Medical Treatment Act, Personal Data Protection Act, and the Code of Conduct for Responsible Use of the Federa (Dutch Federation of Biomedical Scientific Societies).

With a black skin marker, we marked ten points on the lips for measuring 3D lip positions and six on the face (two infraorbitally, two supraorbitally, and two on the nose) to compensate for head movements, see Figure 3.1. Our camera set-up consisted of two consumer cameras (Casio® EX-FC100), which we calibrated with a 10x10x10 cm wireframe cube with 27 nodes at known positions before placing it in front of the volunteer. To quantify the measurement error of our camera measurement device, we calculated the root mean square (RMS) of the distances between the actual 3D node positions and their 3D positions as calculated from the two stereo images. Using a leave-one-out method, we calibrated with 26 nodes and rotated the remaining node so that we obtained 27 error distances, from which we calculated the RMS measurement error, being 0.63 mm.

Led by human lip anatomy and a paper by Lapatki et al. [19], we decided to perform sEMG measurements of the zygomaticus major (ZYG), the risorius (RIS), the orbicularis oris superior (OOS) and inferior (OOI), the mentalis (MEN), the depressor anguli oris (DAO), and the levator labii superioris alaeque nasi (LLSAN) muscles. We further included the digastric muscle (DIG) to represent jaw opening in our model.

For performing sEMG measurements, we used a Porti-system from TMSi (Oldenzaal, the Netherlands) with sintered disc-shaped sEMG micro-electrodes (1.5 mm diameter, Ag/AgCl) with shielded cables, see Figure 3.1. As the size of the electrodes prohibited interelectrode distances (IEDs) smaller than 10 mm, we used 10-mm IEDs. Because of individual differences in face dimensions, we could not use a ruler to apply the electrodes, so we placed them according to Figure 3.1 and then fine-tuned their positions by searching for maximum sEMG output. Finally, we placed a self-adhesive common ground reference electrode on the left wrist.

3.2.2. Instructions to volunteers

We asked our volunteers to adopt thirteen poses (including a rest pose) by making seven facial expressions (voluntary smiling, pursed lips, raised upper lip, mouth open, depressed mouth corners, blowing, and pouting; see Figure 3.2) and five vowel sounds

(/a/, /e/, /i/, /o/, /u/) for four seconds each, in random order. Between each pose, they were to adopt a rest pose with closed mouth and relaxed muscles to serve as our reference when defining the magnitude of marker position displacements in the other poses, since only displacements can be inferred from sEMG signals.

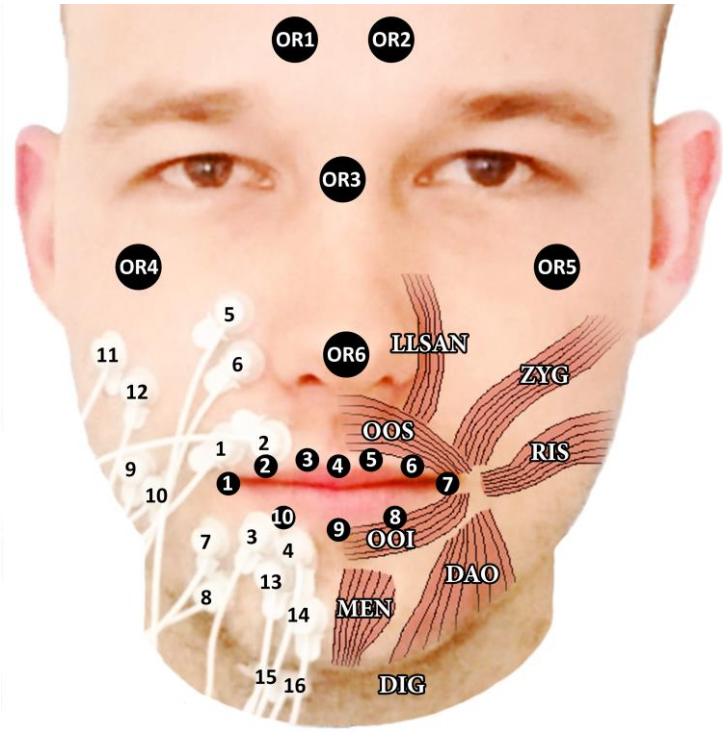

Figure 3.1 Surface electrode and facial marker positions. Volunteer with sEMG electrodes in bipolar configuration placed on the zygomaticus major (ZYG), risorius (RIS), orbicularis oris superior (OOS) and inferior (OOI), mentalis (MEN), depressor anguli oris (DAO), levator labii superioris alaeque nasi (LLSAN), and digastric (DIG) muscles, and showing ten markers on the lips and six infraorbitally, supraorbitally, and on the nose (muscle anatomy adapted from [18]).

Figure 3.2 Rest pose and seven facial expressions as instructed to the volunteers. A: rest, B: voluntary smiling, C: pursed lips, D: raised upper lip, E: mouth open, F: depressed mouth corners, G: blowing, H: pouting.

The seven facial expressions correspond with isolated facial muscle contractions [19]. For nontrained volunteers, it is very difficult to perform the poses without any cocontractions of other muscles. Since multiple variables are involved in model training, these cocontractions are embedded in the model and automatically disentangled during the prediction phase. We took pictures of each pose with both cameras and simultaneously performed sEMG measurements, repeating our data acquisition four times with a pause between repetitions.

3.2.3. Data processing and analysis

After manually selecting the marker positions in the images and coming up with a set of 40 lip pixel coordinates for each pose (ten markers, 2D positions with two cameras), we reconstructed these coordinates into a vector, $\mathbf{X}(p,r) \in \mathbb{R}^{30}$, which held the 30 coordinates of the ten markers in 3D space. Here, $p = 0,\cdots,12$ gives the pose number, and $r = 1,\cdots,5$ the repetition number. Referring to the facial markers, we used them to register all poses to the same reference frame to correct for head motion.

Our manual selection of the image points induced an error. To assess this error, as well as the error induced by imperfect head motion compensation, we estimated the RMS of the differences between two selection runs, the so-called intraobserver error (e_{obs}). Let $x_{m,1}(p), m=1,\cdots,30$ denote the coordinates of the marker position of pose p in the first selection run and $x_{m,2}(p)$ the ones in the second run, then we defined e_{obs} as the RMS of the Euclidean length of the differences, calculating it over the ten markers and thirteen poses (including the rest pose) as follows:

$$e_{obs} = \sqrt{\frac{1}{130}\sum_{p=0}^{12}\sum_{m=1}^{30}\left(x_{m,1}(p) - x_{m,2}(p)\right)^2} \tag{3.1}$$

The RMS intraobserver error turned out to be $e_{obs} = 2.34\,\text{mm}$, which implies that the measurement error ($0.63\,\text{mm}$) will not have had a large impact on our position estimation. After all, the measurement and observer errors are independent. Therefore, the total of errors follows from the root of the sum of squares. Neglecting the measurement error would result in an underestimation of the total error of $\sqrt{\left(2.34^2\right)/\left(0.63^2+2.34^2\right)} = 0.97$. Notably, the intraobserver error involved two selection runs, which implies that the error of a single run would equal $e_{obs}/\sqrt{2}$, with the assumption of uncorrelated errors.

To assess the magnitude of marker position variations, we calculated the RMS of the Euclidean distance between the ten markers of a pose and the corresponding markers in the rest position ($p=0$), which we then averaged over the twelve poses and the five repetitions:

$$d_{RMS} = \sqrt{\frac{1}{600}\sum_{r=1}^{5}\sum_{p=1}^{12}\sum_{m=1}^{30}\left(x_m(p,r) - x_m(0,r)\right)^2} \tag{3.2}$$

Here, $x_m(p,r)$ denotes the m^{th} element from the vector $\mathbf{X}(p,r)$. We also corrected the magnitude of variation (d_{RMS}) for the intraobserver error (e_{obs}) between two selection runs to correct the two selections $x_m(p,r)$ and $x_m(0,r)$ as follows:

$$d_c = \sqrt{{d_{RMS}}^2 - {e_{obs}}^2} \tag{3.3}$$

To estimate lip positions from our sEMG recordings, we used two methods: nonlinear regression with principal component analysis (PCA) and nonlinear regression with a modified version of general regression neural network (GRNN). We have described these methods below. To assess the accuracy of the positions $\hat{\mathbf{X}}(p,r)$ as estimated by both regression methods, we calculated the RMS of the Euclidean length of the differences between marker positions of the estimated pose and the reference pose:

$$e_{RMS} = \sqrt{\frac{1}{600}\sum_{r=1}^{5}\sum_{p=1}^{12}\sum_{m=1}^{30}\left(\hat{x}_m(p,r) - x_m(p,r)\right)^2} \tag{3.4}$$

where $\hat{x}_m(p,r)$ is the m^{th} element of the vector $\hat{\mathbf{X}}(p,r)$. We corrected this e_{RMS} for the manual selection error by applying the factor $e_{obs}/\sqrt{2}$, introducing the factor $1/\sqrt{2}$ because the e_{obs} was based on two manual selections runs, whereas in equation (3.4), we have only one selection run:

$$e_c = \sqrt{{e_{RMS}}^2 - \tfrac{1}{2}{e_{obs}}^2} \tag{3.5}$$

To compare between volunteers, we defined the ratio of the error to position deviation (e_r) as follows:

$$e_r = \frac{e_c}{d_c} \tag{3.6}$$

To compare our results with literature [16], we calculated correlation coefficients between $\hat{x}_m(p,r)$ and $x_m(p,r)$ per volunteer and per coordinate, coming up with a total of 30 correlation coefficients, which we then averaged to find the mean correlation coefficient of each volunteer.

3.2.4. sEMG preprocessing

The sEMG signals were recorded with a sample frequency of 2,048 Hz. We applied a fourth-order Butterworth bandpass filter with 15 and 500 Hz cut-off frequencies. Thanks to the actively shielded electrode cables, which significantly reduced the mains interference and motion artefacts, we found no significant AC power line interference. Therefore, we omitted a 50 Hz notch filter. We recorded the signals in two configurations: unipolar and bipolar, extracting four types of sEMG features: mean absolute value (MAV), root mean square (RMS), waveform length (WL), Willison amplitude (WAMP) with thresholds at $s_{lim} = 10\,\text{mV}$ and $s_{lim} = 20\,\text{mV}$. Table 3.1 shows the equations for all features, which we chose because they had performed well in a recent experiment [20].

We defined the features for six window lengths: 50, 100, 150, 200, 250, and 300 ms and used a sliding window with maximum overlap (all-but-one sample) to calculate the features: if there were n sEMG samples in a record and the window length was p samples, the resulting EMG feature record had $n-p+1$ samples. Our reason for using a maximum overlap was to get a maximum number of feature vectors per record. Notwithstanding the inevitable autocorrelation within the features, maximising the number of features results in better performance of both estimation methods.

We decided to truncate the calculated features of approximately four seconds to three seconds exactly (i.e. 6145 samples) to achieve an equal amount for each feature set $\mathbf{g}(i,p,r)$. There are 60 feature sets $\mathbf{g}(i,p,r)$ containing the features of 8 sEMG channels with i=1, ⋯,6145 (the samples), p=1, ⋯,12 (the poses), and r=1, ⋯,5 (the repetitions).

Table 3.1 sEMG feature types and their equations.

Feature	Equation
MAV	$g(j)=\frac{1}{N}\sum_{i=j-\frac{1}{2}(N-1)}^{j+\frac{1}{2}(N-1)}\lvert s(i)\rvert$
RMS	$g(j)=\sqrt{\frac{1}{N}\sum_{i=j-\frac{1}{2}(N-1)}^{j+\frac{1}{2}(N-1)}s(i)^2}$
WL	$g(j)=\sum_{i=j-\frac{1}{2}(N-1)}^{j+\frac{1}{2}(N-1)-1}\lvert s(i+1)-s(i)\rvert$
WAMP $s_{\lim}=10$ $s_{\lim}=20$	$g(j)=\sum_{i=j-\frac{1}{2}(N-1)}^{j+\frac{1}{2}(N-1)-1}\left[v\left(\lvert s(i+1)-s(i)\rvert\right)\right]$ $v(s)=\begin{cases}1, \text{ if } s\geq s_{\lim}\\ 0, \text{ otherwise}\end{cases}$

3.2.5. Principal component analysis based estimation

We trained our PCA-based regression method using a database that included observed marker positions and associated feature vectors. As we used static poses, we considered the raw sEMG signals to be stationary during each pose. Consequently, the statistics of features calculated for a sliding window were considered constant. Therefore, for each lip position $\mathbf{X}(p,r)$, we needed only one sEMG feature vector rather than the whole set of 6,145 sEMG feature vectors $\mathbf{g}(i,p,r)$, thus avoiding a huge dimension of the measurement space.

We first averaged the vectors in a set over the time samples to yield a single 8D feature vector $\bar{\mathbf{g}}(p,r)$. As we figured we could not perform a linear mapping from this 8D feature space to the 30D position space, we decided to apply nonlinear regression. We did try using linear regression at first, but ended up with large errors. The simplest way of approximating a nonlinear mapping is using a truncated Taylor series expansion of only the quadratic

terms. So, to implement nonlinear regression, we augmented these feature vectors with the ½×8×9=36 quadratic terms that could be formed from the eight elements in $\bar{\mathbf{g}}(p,r)$, thus obtaining a set of 44D data vectors $\bar{\mathbf{g}}_{aug}(p,r)$. Next, we concatenated this vector with the 30 coordinates $\mathbf{X}(p,r)$ of the pose, which gave us the following 74D vector $\mathbf{z}(p,r)$:

$$\mathbf{z}(p,r)=\begin{bmatrix}\mathbf{X}(p,r)\\ \bar{\mathbf{g}}_{aug}(p,r)\end{bmatrix} \text{ with } \begin{matrix} p=1,\cdots,12 \text{ (poses)}\\ r=1,\cdots,5 \text{ (repetitions)}\end{matrix} \tag{3.7}$$

The training of the PCA model was combined with cross-validation to avoid any performance evaluation bias. The PCA model was trained with pooled data from four repetitions of twelve poses each. Testing was done on the remaining repetition. We reiterated this procedure four times while rotating the five repetition sets in the training pool and the test set. Each training pool comprised a 74×48 matrix $\mathbf{Z}_{train}$, the columns of which were vectors $\mathbf{z}(p,r)$, with a corresponding test set comprising a 74×12 matrix $\mathbf{Z}_{test}$.

Before developing the PCA model, we first normalised our data with respect to the mean and variance because there were two different physical dimensions and units. For each of the 74 elements in the training set, the average and sample variance were calculated. These two parameters were used to shift and scale the data such that the average was zero and the variance was one. We also performed this operation on the test set.

The PCA model $\mathbf{Y}$ is a $74\times D$ matrix, containing the D most dominant eigenvectors $\mathbf{y}_d$ that result from $\mathbf{Z}_{train}\mathbf{Z}^T_{train}\mathbf{y}_d=\lambda_d\mathbf{y}_d$, where λ_d are the eigenvalues. We normalised the eigenvectors, i.e. the principal components, to get $\mathbf{YY}^T=\mathbf{I}$ and sorted the eigenvectors $\mathbf{y}_d$ in $\mathbf{Y}=[\mathbf{y}_1,\cdots,\mathbf{y}_d]$ to get the condition $\lambda_d\geq\lambda_{d+1}$ for the corresponding eigenvalues.

PCA is basically an encoding/decoding method. Any data vector from the test set $\mathbf{Z}_{test}$, say $\mathbf{z}_{test}$, could be encoded into a lower *D*-dimensional coefficient vector $\mathbf{b}$:

$$\mathbf{b}=\mathbf{Y}^T\mathbf{z}_{test} \tag{3.8}$$

Decoding from $\mathbf{b}$ uses the same model:

$$\mathbf{z}_{test}\approx\mathbf{Yb} \tag{3.9}$$

Equations (3.8) and (3.9) were not directly helpful in estimating lip positions. In the test set, we wanted to estimate lip positions from the sEMG features, so we could use only that part of the vector $\mathbf{z}_{test}$ that contained the sEMG features. We adapted equation (3.9) accordingly and defined the submatrix $\mathbf{Y}_g$ of $\mathbf{Y}$, which contained the sEMG features only (the lower 44 rows of $\mathbf{Y}$). We then had:

$$\bar{\mathbf{g}}_{aug}=\mathbf{Y}_g\mathbf{b}+\mathbf{v} \tag{3.10}$$

Where $\mathbf{v}$ contained the residuals that represented the approximation error in equation (3.9), and $\bar{\mathbf{g}}_{aug}$ was the part of $\mathbf{z}_{test}$ that contained the 44 sEMG features. We regarded equation (3.10) as a linear observation model of $\mathbf{b}$, $\mathbf{Y}_g$ being the observation matrix and $\mathbf{v}$ the observation noise. Least Square Error (LSE) estimation of $\mathbf{b}$ is then straightforward [21]:

$$\hat{\mathbf{b}}_{LSE} = \left(\mathbf{Y}_g^T \mathbf{Y}_g\right)^{-1} \mathbf{Y}_g^T \bar{\mathbf{g}}_{aug} \tag{3.11}$$

$\hat{\mathbf{b}}_{LSE}$ being the estimated coefficient vector. From that, we could estimate the full vector $\mathbf{z}_{test}$, including the 30 lip position coordinates $\mathbf{X}$ by applying equation (3.9):

$$\hat{\mathbf{z}}_{LSE} = \mathbf{Y}\hat{\mathbf{b}}_{LSE} \tag{3.12}$$

Undoing the normalisation finalised the estimation.

An extension of this estimation of $\mathbf{b}$ is the Minimum Mean Square Error (MMSE) estimation. This method exploits the prior knowledge that the PCA coefficients are uncorrelated, with zero means. The covariance matrix $\mathbf{C}_b$ of $\mathbf{b}$ is diagonal with diagonal elements λ_d. With uncorrelated residuals $\mathbf{v}$, the covariance matrix is proportional to the unity matrix $\mathbf{C}_v = \sigma_v^2 \mathbf{I}$. The unbiased MMSE estimate $\hat{\mathbf{b}}_{MMSE}$, based on the sEMG features, then follows [21]:

$$\hat{\mathbf{b}}_{MMSE} = (\mathbf{Y}_g^T \mathbf{Y}_g + \sigma_v^2 \mathbf{C}_b^{-1})^{-1} \mathbf{Y}_g^T \bar{\mathbf{g}}_{aug} \tag{3.13}$$

Obviously, when σ_v is set to zero, $\hat{\mathbf{b}}_{MMSE}$ equals $\hat{\mathbf{b}}_{LSE}$. So, the MMSE estimate encompasses the LSE estimate, and there is no need to treat it separately.

3.2.6. Extended general regression neural network estimation

The second regression method is an extension of the general regression neural network (GRNN). GRNN is a nonlinear interpolation method based on Parzen kernel density models [22]. We combined the design and evaluation of GRNN with cross-validation in the same way as outlined before. First, we defined a linear index over the poses and repetitions:

$$c \overset{def}{=} 12(r-1) + p$$

Assuming the vectors $\mathbf{X}_c$ and $\bar{\mathbf{g}}_c$ are associated, we had a population of pairs available in a training pool $\{(\mathbf{X}_c, \bar{\mathbf{g}}_c) \,|\, c=1, \cdots, 48\}$. Given a new sEMG vector $\bar{\mathbf{g}}$, GRNN estimates the associated vector $\hat{\mathbf{X}}$ by:

$$\hat{\mathbf{X}} = \sum_{c=1}^{48} w_c \mathbf{X}_c \quad \text{with:} \quad w_c = \frac{s(\bar{\mathbf{g}}, \bar{\mathbf{g}}_c)}{s(\bar{\mathbf{g}}, \bar{\mathbf{g}}_1) + s(\bar{\mathbf{g}}, \bar{\mathbf{g}}_2) + \ldots + s(\bar{\mathbf{g}}, \bar{\mathbf{g}}_{52})} \tag{3.14}$$

where $s(\bar{\mathbf{g}}, \bar{\mathbf{g}}_c)$ is a similarity measure between $\bar{\mathbf{g}}$ and $\bar{\mathbf{g}}_c$ derived from a Parzen estimate of the underlying probability density. We replaced the Parzen kernel that uses isotropic Gaussians based on Euclidean distances with the likelihood function $p(\mathbf{g} \,|\, c)$, assuming

nonisotropic Gaussians with pose-dependent Mahalanobis distances. This alteration of the standard GRNN would induce better adaptations to the feature vectors' statistical properties. We defined all 48 poses in a training pool as individual classes. For each class, a feature set $\mathbf{g}(i,p,r)$ was available, which we used to train the likelihood function $p(\mathbf{g}|c)$. In the assumption of normal distributions for the likelihood function $p(\mathbf{g}|c)=N(\mathbf{g}-\boldsymbol{\mu}_c,\mathbf{C}_c)$, learning boils down to estimating the mean $\boldsymbol{\mu}_c$ and the covariance matrix $\mathbf{C}_c$, as in $\hat{\boldsymbol{\mu}}_c=\bar{\mathbf{g}}_c$. We defined the similarity measures associated with a new vector $\bar{\mathbf{g}}$ as follows:

$$s(\bar{\mathbf{g}},\bar{\mathbf{g}}_c)=N(\bar{\mathbf{g}}-\bar{\mathbf{g}}_c,\alpha^2\mathbf{C}_c+\gamma\mathbf{I}) \tag{3.15}$$

The introduction of factor α^2 improved the generalisation capability. For each pose, only four repetitions in a training pool were available. Therefore, poses were not well populated in the 8-dimensional feature space. By spreading the Gaussian kernels with the factor α^2, we increased the overlap between kernels. We added the term $\gamma\mathbf{I}$ to improve numerical stability, but the choice of γ (around 10^{-6}) was not critical.

For each regression method, we determined the best performing combination of feature type, window length, and configuration (of 60 possible combinations) using the cross-validation technique mentioned before. With the PCA method, we evaluated the parameter σ_v for each combination over the range of $\sigma_v=0,0.05,\cdots,0.3$ and the PCA dimension D over the range of $D=1,2,\cdots,48$. With the GRNN method, we analysed the parameter α over the range of $\alpha=1,2,\cdots,10$.

To estimate the mean optimal settings, we averaged the error values e_c over the five volunteers and looked which settings gave the minimum error:

$$\begin{aligned} e_{c,average}(conf,feat,win,D,\sigma_v) &= \frac{1}{5}\sum_{vol=1}^{5} e_c(vol,conf,feat,win,D,\sigma_v) \\ e_{c,\min} &= \min_{conf,feat,win,D,\sigma_v} e_{c,average}(conf,feat,win,D,\sigma_v) \end{aligned} \tag{3.16}$$

In the GRNN method, we interchanged the parameters D and σ_v with α.

We applied the one-sided paired Student's T-test to check for significant differences between the PCA-based regression methods and to test for significant differences between volunteer-independent and volunteer-specific parameters. After all, since the PCA-LSE is in fact included in the PCA-MMSE at $\sigma_v=0$, it can never be better than the PCA-MMSE. The same holds true for volunteer-specific parameters, which will always outperform or be equivalent to volunteer-independent parameters. We compared the GRNN with the PCA-MMSE using the two-sided paired Student's T-test, because we did not know whether the GRNN method would perform better or worse than the PCA-based regression method. Finally, we performed a repeated-measures ANOVA test to look for statistically significant influences of the various sEMG feature extraction settings and parameters.

3.3. Results

Figure 3.3 gives an idea of the accuracy showing the 3D lip shapes of volunteer 5 with volunteer-specific settings for both PCA-MMSE (in orange) and modified GRNN (in blue). Table 3.2 presents the optimal results of the five individual volunteers for both methods. Table 3.3 shows the results for the mean optimal settings as calculated by equation (3.16). Both with volunteer-specific ($P<<0.01$) and with volunteer-independent settings ($P<<0.01$), the PCA-MMSE method performed significantly better than the PCA-LSE method. However, we found no significant difference between the modified GRNN method and the PCA-MMSE method (volunteer-specific settings: $P \sim 0.17$ and volunteer-independent settings: $P \sim 0.99$), nor did we find any significant difference between the volunteer-specific settings and the volunteer-independent settings (PCA-LSE: $P \sim 0.82$, PCA-MMSE: $P \sim 0.15$, GRNN $P \sim 0.06$). In the PCA-based estimation, dimension D ($P<<0.01$), and parameter σ_v ($P<<0.01$) were both statistically significant, whereas feature type ($P \sim 0.14$), window length ($P \sim 0.06$), and configuration ($P \sim 0.06$) were not. In the modified GRNN-based estimation, parameter α ($P<<0.01$) and window length ($P<<0.01$) were statistically significant, whereas feature type ($P \sim 0.07$) and configuration ($P \sim 0.58$) were not. The averaged data showed somewhat lower error measures e_c and e_r when we used the PCA method. Nevertheless, with volunteer-specific settings, the GRNN method performed better in four volunteers.

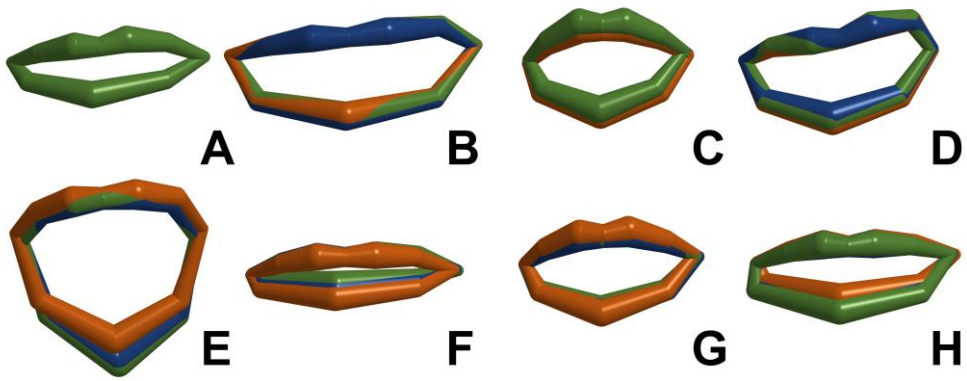

Figure 3.3 Rest pose and seven facial expressions in 3D of volunteer 5 averaged over the five repetitions. Green: lip shapes tracked by 3D image reconstruction using a stereo-camera set-up. Orange: lip shapes estimated by the PCA-based nonlinear regression. Blue: lip shapes estimated by the extended GRNN-based nonlinear regression. A: rest (not estimated), B: voluntary smiling, C: pursed lips, D: raised upper lip, E: mouth open, F: depressed mouth corners, G: blowing, H: pouting.

Table 3.2 **The lowest error values for e_c and e_r by volunteer with the corresponding settings.**

	e_c (mm)		e_r		ρ		Config.[a]		Feat.[b]		Window (ms)		D	σ_v	α
	P	G	P	G	P	G	P	G	P	G	P	G	P		G
1	2.71	2.69	0.24	0.24	0.90	0.90	1	1	1	1	200	200	10	0.05	3
2	3.00	3.12	0.29	0.31	0.88	0.86	2	2	2	3	300	150	17	0.25	5
3	2.41	2.25	0.23	0.22	0.91	0.92	1	1	1	1	300	50	12	0.10	2
4	1.99	1.42	0.23	0.17	0.91	0.94	1	2	1	4	300	50	7	0.05	2
5	2.94	2.39	0.33	0.27	0.87	0.90	1	1	1	5	100	200	6	0.05	3

a. The monopolar configuration is represented by 1 and the bipolar configuration by 2.

b. Optimal features are represented by numbers as follows:
1. WAMP s_{lim} = 10 mV; 2. WAMP s_{lim} = 20 mV; 3. WL; 4. MAV; 5. RMS.

c. The different methods are represented by capitals: P for PCA and G for GRNN

Table 3.3 **The error values for e_c and e_r by volunteer with the mean optimal settings, i.e. volunteer-independent settings (see equation (3.16)).**

	e_{rms} (mm)		e_c (mm)		e_r		ρ	
Volunteer	**PCA[a]**	**GRNN[b]**	**PCA[a]**	**GRNN[b]**	**PCA[a]**	**GRNN[b]**	**PCA[a]**	**GRNN[b]**
1	3.18	3.68	2.71	3.28	0.28	0.33	0.90	0.89
2	3.94	3.58	3.57	3.17	0.36	0.32	0.85	0.85
3	2.95	2.95	2.45	2.44	0.25	0.25	0.91	0.91
4	2.60	2.18	2.01	1.42	0.20	0.14	0.91	0.94
5	3.40	3.80	2.97	3.42	0.30	0.35	0.88	0.86
Averaged	3.21	3.24	2.74	2.75	0.28	0.28	0.89	0.89
Corrected Average	2.76	2.78						

a. PCA settings: configuration = unipolar; feature = WAMP s_{lim} = 10 mV; window length = 300 ms; D = 9; σ_v = 0.05.

b. GRNN settings: configuration = bipolar; feature = MAV; window length = 50 ms; α = 2

We found the lowest mean error in the unipolar configuration when estimating positions with PCA and in the bipolar configuration when using GRNN. However, three volunteers performed better in the unipolar configuration. When we interchanged configurations, the corrected error with mean optimal settings ($e_{c,min}$) became 3.78 mm when using PCA and 3.01 mm when using GRNN. The PCA method showed more consistency with respect to the chosen feature than the GRNN method. In all volunteers, the WAMP feature showed the best results – in four volunteers at $s_{lim} = 10\,\text{mV}$, which also showed the lowest mean error rates, and in one at $s_{lim} = 20\,\text{mV}$. The GRNN method showed a preference for the MAV feature in the averaged results. Two volunteers performed better when we used the WAMP feature at $s_{lim} = 10\,\text{mV}$. In one volunteer, WL gave the best results, and in another, RMS.

Table 3.4 lists the optimal settings for both methods per feature, averaged over the volunteers (see equation (3.16)), with the corresponding error measures. In the PCA method, WAMP at $s_{lim}=10\,\text{mV}$ clearly performed better. The error measures between the different features were much smaller when we used GRNN, showing a maximum difference in e_c of 0.31 mm between MAV and WAMP at $s_{lim}=20\,\text{mV}$. The methods showed differences in preferred window lengths, with 300 ms in the PCA method and 50 ms in GRNN. However, influence of window length appeared much more profound in GRNN than in PCA, producing maximum e_c differences of merely 0.02 mm in PCA and no less than 0.68 mm in GRNN.

In all volunteers, we found good correlation coefficients (ρ). With the PCA method, ρ ranged between 0.87 and 0.91 and with the GRNN method, ρ ranged between 0.86 and 0.94. The mean ρ was 0.89 with both methods (see Table 3.2). Between features, ρ ranged between 0.87 and 0.89.

Table 3.4 The mean optimal results (see equation (3.16)) by feature obtained with PCA and GRNN and the corresponding settings.

	RMS		**MAV**		**WL**		**WAMP** $s_{lim}=10\,\text{mV}$		**WAMP** $s_{lim}=20\,\text{mV}$	
	PCA	GRNN	PCA	GRNN	PCA	GRNN	PCA	GRNN	PCA	GRNN
e_c **mm)**	3.31	2.81	3.33	2.78	3.28	2.88	2.76	2.84	3.27	3.09
e_r	0.34	0.29	0.34	0.28	0.33	0.29	0.28	0.29	0.33	0.31
ρ	0.87	0.89	0.87	0.89	0.87	0.89	0.89	0.89	0.87	0.88
Config.	Mono	Bi	Mono	Bi	Mono	Mono	Mono	Mono	Mono	Mono
Window (ms)	50	50	50	50	50	50	300	150	200	50
D	7	NA	7	NA	9	NA	9	NA	16	NA
σ_v	0.05	NA	0.05	NA	0.05	NA	0.05	NA	0.1	NA
α	NA	2	NA	2	NA	2	NA	3	NA	2

The optimal PCA dimension D ranged between 6 and 17 in our volunteers and showed an optimum in the averaged results at 9. By evaluating the results for all different dimensions, we found that the first four to five principal components had a large influence on shape prediction. When we used eight principal components, the error values reached a plateau, after which only small changes in the errors occurred. When using nine principal components, we found explained variances in the PCA model of 92 to 96% in our volunteers.

We never found the optimal value for σ_v to be zero, which means that the MMSE analysis performed better. We noted a clear trend towards higher e_c values when increasing σ_v. A 0.05 increase of σ_v produced a mean error increase of 0.11 (range: 0.10 to 0.13).

This trend occurred in four of five volunteers; volunteer 2 was the only one to show a small error decrease as σ_v was raised to 0.25.

The averaged results showed the lowest error at parameter $\alpha=2$. Only volunteer 2 clearly deviated with the lowest error at $\alpha=5$. In this volunteer, the error was 0.50 mm larger at $\alpha=2$, with the other settings unchanged.

When comparing volunteers by values in e_r, we found the PCA method to be more consistent than the GRNN method: the former gave a value range of 0.23 to 0.33 and the latter a range of 0.17 and 0.31. Both methods gave a value of 0.28 for e_r with the averaged data.

3.4. Discussion

Our study has shown that it is, indeed, possible to estimate static 3D lip shapes from volunteer-specific sEMG measurements of facial muscles and the digastric muscle. The tested methods, PCA-based nonlinear regression and a modified GRNN, gave comparable results with an average accuracy of about 2.8 mm in five measured volunteers.

In the PCA approach, MMSE performed significantly better than LSE. The MMSE method uses the additional knowledge that the values in the coefficients $\mathbf{b}$ are uncorrelated, with zero means and with variances that are known from the PCA model [21]. Therefore, the growth of the coefficients is controlled, and a higher PCA dimension can be achieved, which will lead to a more accurate estimation. The corrected RMS error of 2.76 mm and correlation coefficient of 0.89 are promising results. The modified GRNN method produced almost identical results. Both models seem generally applicable, but PCA was more consistent between volunteers, whereas in four volunteers, the modified GRNN method produced more accurate position estimates.

A disadvantage of using the modified GRNN method could be the fact that GRNN can be regarded as an interpolation method with a lookup-table that is filled by the training set and probed by the sEMG feature vector of the unknown pose. The method performs well as long as the feature vector probes in the vicinity of feature vectors in the table, as was the case in this study. The results are less predictable if the feature vector probes in a white area of the lookup-table, which can occur when a pose is adopted that is not present in the training set. As PCA behaves smoother in the untrained regions, this method may be of better use for our ultimate goal: to predict post-treatment function loss, we will need maximum accuracy in predicting not only 3D lip shapes, but also functional movements that result from multiple muscle activations, even though we could never create a volunteer-specific training set that includes all possible poses.

Since most models in literature do not give quantitative values, we have difficulty comparing our results with previous findings. Lucero & Munhall's finite-element model of the face and lips uses intramuscular facial EMG measurements (ZYG, LLS, DAO, MEN, OOS, OOI, and the depressor labii inferioris and levator anguli oris muscles) [16].

They placed five markers on the lips and estimated vertical displacements and protrusions of these markers, finding mean correlation coefficients of 0.71 and 0.28 for vertical displacement and protrusion, respectively.

Although our methods performed much better than this finite-element approach, our models could only describe phenomena, whereas a FEM could establish a one-to-one correspondence between anatomy and physiology on the one hand and mathematical structures on the other, which renders it more suitable for a practical application to predict post-treatment function loss. Moreover, the FEM approach can include the (nonlinear) dynamics of anatomy and physiology. Some poses, e.g. the pose adopted when articulating the vowel sounds /a/ and /e/, require little persistent muscle activation. When we disregard the muscle activation patterns (and associated sEMG patterns) that produce these poses, it is much harder to distinguish between them.

We cannot draw any decisive conclusions as to an optimal configuration, feature, or window length for processing sEMG signals. The PCA method showed a preference for unipolar sEMG measurements in combination with the WAMP feature at $s_{lim} = 10\,\mathrm{mV}$ and calculated over longer time windows (on average, 300 ms). The GRNN method performed best in a bipolar configuration with the MAV feature determined over a 50-ms time window. However, the optimal settings varied between volunteers, especially in the GRNN method. In the PCA method, we did not find a single best setting for window length either, but the effects on the error with PCA were marginal – probably because we evaluated static poses only with an sEMG-feature sequence averaged over three seconds. The GRNN method performed significantly better with smaller window lengths than with larger ones, possibly because small windows have more fluctuations in the sEMG features, thus expanding the covariance matrix and leading to a better kernel coverage in the 8-dimensional feature space. For the purpose of this study, a volunteer-specific model coupling sEMG to positions, we did not find it necessary to determine one single best configuration for all volunteers, since the parameters could be fine-tuned during the training process with each volunteer's individual data. Nevertheless, narrowing down the parameter ranges and evaluating only the best performing features would definitely reduce computation time.

Meltzner et al. used a modified Mel-frequency cepstral coefficients (MFCC) algorithm for feature extraction from sEMG [12,13]. MFCCs are frequently used in automatic speech recognition with acoustical signals. Despite the fact that sEMG signals possess different properties than acoustical signals, Meltzner et al. found that an MFCC algorithm tailored to their needs outperformed the other processing algorithms they tested [12,13]. More recently, Längkvist et al. reviewed the applications of deep learning for feature extraction from time series [23], and Wand & Schultz showed the use of deep neural networks in EMG-based speech recognition [24]. These are interesting topics that might improve our results, but we would probably need much more training data. Since the current accuracy

has the same order of magnitude as the observation error, these improvements will be marginal.

Future experiments may benefit from the inclusion of advanced feature extraction algorithms like the ones mentioned before in combination with high-density sEMG grids. Staudenmann et al. showed that these grids improved sEMG-based muscle force estimation by some 30% [25]. Another good thing about these grids is that they eliminate the need for precise microelectrode placement.

When tested on our five volunteers, our methods produced satisfying initial results and our models showed comparable accuracy in all volunteers. Despite our relatively small sample size, our results indicate that sEMG of the perioral muscles conveys sufficient information to estimate 3D lip positions, and we have identified important parameters. A larger sample size might reveal that window length, configuration, and feature type also have significant influence on the RMS errors. On the other hand, a large sample size may produce significant differences of small RMS errors, which do not have any practical meaning.

Despite similar performances, we favour the PCA-based regression model because of the advantages discussed before, the possible disadvantages of modified GRNN, and the computational load of the estimators, which is in favour of the PCA method.

It must be noted that training sets are volunteer-specific and cannot be used for the estimation of lip poses of other volunteers. This problem also occurs in EMG-speech recognition, as described by Schultz & Wand [10]. They showed that generic independent-speaker models might be feasible but at the cost of higher error. Meltzner et al. argue that speaker-dependent systems do have practical applications and that the minimal amount of training data necessary per individual is not too big of a burden [12]. For our ultimate goal, these volunteer-specific models are key, as each patient is unique.

Variance in facial muscle anatomy, small muscles and electrodes hampers the exact identification of muscles and electrode locations, which may cause small differences between volunteers in muscle activation measurements or amount of crosstalk picked up in the signals. Lapatki et al. showed there is a high risk of crosstalk in the facial musculature due to cocontraction of adjacent muscles [26]. Even when using high-density grids, crosstalk remains visible, even if it is reduced. We saw coactivation in all volunteers and all poses in varying degrees. Apparently, either the volunteers were not always able to perform isolated muscle contractions, or crosstalk occurred.

Our most important conclusion is that features extracted from facial sEMG can estimate lip shapes in 3D with high accuracy. This finding is an essential step forward in constructing a virtual-therapy model to predict post-treatment function loss. We found our sEMG processing parameters to be generally applicable and could use them in our

future application for oral and lip cancer patients, so we will not have to optimise our sEMG parameters for each patient individually.

These settings might not only benefit researchers in the field of silent-speech interfaces, but might also be interesting for researchers in the field of human machine interfaces (HMI) – for instance, in projects like Hamedi et al.'s, who used facial sEMG to classify emotions [7,27]. The results of our study seem promising for controlling machines via HMI with support of up to 13 control commands (the thirteen poses). Our models would be able to classify emotions and present them visually in 3D, too. Moreover, as suggested by Honda et al., the models could produce visual output for physiological vocal-tract models in speech production and speech synthesis. Or they could provide visual feedback in EMG-based speech recognition.

For the development of a virtual-therapy model that could predict functional outcome, the current models should be extended to incorporate dynamics as well as unilateral lip movements. Such extension would require video capturing of the lips and bilateral sEMG measurements.

Our recommendation for future research would be to combine FEM with nonlinear regression and apply the estimation techniques to model the neural activation of simulated muscles instead of lip positions, thus separating activation modelling from dynamic modelling. The first step in developing such an activation model of the lips has been taken.

3.5. Conclusion

This study shows that static 3D lip shapes can be estimated from volunteer-specific sEMG measurements of facial muscles and the digastric muscle. The tested methods – PCA-based nonlinear regression and a modified GRNN – gave comparable results with an average accuracy of about 2.8 mm in the five measured volunteers.

3.6. Acknowledgements

We thank R.J.J.H. van Son PhD for the critical review of the manuscript. Also, many thanks to our volunteers for participating in this study.

3.7. Conflict of interest

The authors declare that they have no conflict of interest.

3.8. Funding

No funding was acquired for this research.

3.9. Ethical approval

The described project involved healthy human volunteers. The performed measurements were noninvasive and not stressful. There was no infringement of the (psychological) integrity of the volunteers. Therefore, no ethical approval was required.

The study was performed in accordance with Dutch legislation, including the Agreement on Medical Treatment Act, Personal Data Protection Act, and the Code of Conduct for Responsible Use of the Federa (Dutch Federation of Biomedical Scientific Societies). Approval was given by the Netherlands Cancer Institute Medical Research Ethics Committee.

Volunteers were recruited by e-mail with a short explanation about the study. They also received information on the nature of our experiment and on their rights as volunteers (including the right to opt out at any moment without any need to explain). They all gave their verbal consent to the publication of anonymised results and written consent to the publication of Figure 3.1 and Figure 3.2.

3.10. References

1. Gore SM, Crombie AK, Batstone MD, Clark JR. Concurrent chemoradiotherapy compared with surgery and adjuvant radiotherapy for oral cavity squamous cell carcinoma. Head Neck. 2015;37: 518–523. doi:10.1002/hed.23626
2. Kreeft A, Tan IB, van den Brekel MWM, Hilgers FJ, Balm AJM. The surgical dilemma of "functional inoperability" in oral and oropharyngeal cancer: current consensus on operability with regard to functional results. Clin Otolaryngol. 2009;34: 140–6. doi:10.1111/j.1749-4486.2009.01884.x
3. Kreeft AM, van der Molen L, Hilgers FJ, Balm AJ. Speech and swallowing after surgical treatment of advanced oral and oropharyngeal carcinoma: a systematic review of the literature. Eur Arch Otorhinolaryngol. 2009;266: 1687–1698. doi:10.1007/s00405-009-1089-2
4. van Alphen MJA, Kreeft AM, van der Heijden F, Smeele LE, Balm AJM. Towards virtual surgery in oral cancer to predict postoperative oral functions preoperatively. Br J Oral Maxillofac Surg. 2013;51: 747–751. doi:10.1016/j.bjoms.2013.06.012
5. Denby B, Schultz T, Honda K, Hueber T, Gilbert JM, Brumberg JS. Silent speech interfaces. Speech Commun. 2010;52: 270–287. doi:10.1016/j.specom.2009.08.002
6. Beskow J. Talking Heads - Models and Applications for Multimodal Speech Synthesis. KTH Royal Institute of Technology. 2003.
7. Hamedi M, Salleh S-H, Tan TS, Ismail K, Ali J, Dee-Uam C, Pavaganun C, Yupapin PP. Human facial neural activities and gesture recognition for machine-interfacing applications. Int J Nanomedicine. 2011;6: 3461–3472. doi:10.2147/IJN.S26619
8. Arjunan SP, Weghorn H, Kumar DK, Naik G, Yau WC. Recognition of Human Voice Utterances from Facial Surface EMG without Using Audio Signals. In: Filipe J, Cordeiro J, Cardoso J, editors. Enterprise Information Systems: 9th International Conference, ICEIS 2007, Funchal, Madeira, June 12-16, 2007, Revised Selected Papers. 2008. pp. 366–378. doi:10.1007/978-3-540-88710-2_29
9. Betts BJ, Binsted K, Jorgensen C. Small-vocabulary speech recognition using surface electromyography. Interact Comput. 2006;18: 1242–1259. doi:10.1016/j.intcom.2006.08.012
10. Schultz T, Wand M. Modeling coarticulation in EMG-based continuous speech recognition. Speech Commun. 2010;52: 341–353. doi:10.1016/j.specom.2009.12.002
11. Brumberg JS, Nieto-Castanon A, Kennedy PR, Guenther FH. Brain-Computer Interfaces for Speech Communication. Speech Commun. 2010;52: 367–379. doi:10.1016/j.specom.2010.01.001
12. Meltzner GS, Sroka J, Heaton JT, Gilmore LD, Colby G, Roy S, Chen N, Luca CJ De. Speech Recognition for Vocalized and Subvocal Modes of Production using Surface EMG Signals from the Neck and Face. 9th Annual Conference of the International Speech Communication Association (INTERSPEECH 2008). 2008. pp. 2667–2670.
13. Meltzner GS, Colby G, Deng Y, Heaton JT. Signal Acquisition and Processing Techniques for sEMG Based Silent Speech Recognition. 33rd Annual International Conference of the IEEE EMBS. 2011. pp. 4848–4851.
14. Jou S-C, Maier-Hein L, Schultz T, Waibel A. Articulatory Feature Classification using Surface Electromyography. 2006 IEEE International Conference on Acoustics, Speech and Signal Processing Proceedings. 2006. p. I-605-I-608. doi:10.1109/ICASSP.2006.1660093
15. Honda K, Kurita T, Kakita Y, Maeda S. Physiology of the lips and modeling of lip gestures. J Phon. 1995;23: 243–254. doi:10.1016/S0095-4470(95)80046-8
16. Lucero JC, Munhall KG. A model of facial biomechanics for speech production. J Acoust Soc Am. 1999;106: 2834–2842. doi:10.1121/1.428108
17. Stavness I, Lloyd JE, Fels S. Automatic prediction of tongue muscle activations using a finite element model. J Biomech. 2012;45: 2841–2848. doi:10.1016/j.jbiomech.2012.08.031
18. Schünke M, Schulte E, Schumacher U. Head. In: Ross LM, Lamperti ED, Taub E, editors. Thieme atlas of anatomy: head and neuroanatomy. 1st ed. 2010. p. 44.

19. Lapatki BG, Stegeman DF, Zwarts MJ. Selective contractions of individual facial muscle subcomponents monitored and trained with high-density surface EMG. In: Beurskens CHG, van Gelder RS, Heymans PG, Manni JJ, Nicolai JA, editors. The Facial Palsies Complementary Approaches. 2005. pp. 89–108. doi:10.1007/s00238-008-0236-0

20. Phinyomark A, Nuidod A, Phukpattaranont P, Limsakul C. Feature Extraction and Reduction of Wavelet Transform Coefficients for EMG Pattern Classification. Electron Electr Eng. 2012;122: 27–32. doi:10.5755/j01.eee.122.6.1816

21. van der Heijden F, Duin RPW, de Ridder D, Tax DMJ. Classification, parameter estimation and state estimation: an engineering approach using MATLAB. John Wiley & Sons. 2005

22. Specht DF. A general regression neural network. IEEE Trans Neural Networks. 1991;2: 568–576. doi:10.1109/72.97934

23. Längkvist M, Karlsson L, Loutfi A. A review of unsupervised feature learning and deep learning for time-series modeling. Pattern Recognit Lett. 2014;42: 11–24. doi:10.1016/j.patrec.2014.01.008

24. Wand M, Schultz T. Pattern learning with deep neural networks in EMG-based speech recognition. 36th Annual International Conference of the IEEE Engineering in Medicine and Biology Society. 2014. pp. 4200–4203. doi:10.1109/EMBC.2014.6944550

25. Staudenmann D, Kingma I, Stegeman DF, van Dieën JH. Towards optimal multi-channel EMG electrode configurations in muscle force estimation: a high density EMG study. J Electromyogr Kinesiol. 2005;15: 1–11. doi:10.1016/j.jelekin.2004.06.008

26. Lapatki BG, Oostenveld R, Van Dijk JP, Jonas IE, Zwarts MJ, Stegeman DF. Optimal placement of bipolar surface EMG electrodes in the face based on single motor unit analysis. Psychophysiology. 2010;47: 299–314. doi:10.1111/j.1469-8986.2009.00935.x

27. Hamedi M, Salleh S-H, Swee TT, Kamarulafizam. Surface Electromyography-Based Facial Expression Recognition in Bi-Polar Configuration. J Comput Sci. 2011;7: 1407–1415. doi:10.3844/jcssp.2011.1407.1415

IV

DATA AVAILABLE ONLINE
DOI: 10.17605/OSF.IO/DUX3W

PREDICTING 3D LIP MOVEMENT USING FACIAL sEMG

This chapter was published in Medical & Biological Engineering & Computing

ESKES M, VAN ALPHEN MJA, SMEELE LE, BRANDSMA D, BALM AJM, VAN DER HEIJDEN F (2017)
PREDICTING 3D LIP MOVEMENT USING FACIAL sEMG:
A FIRST STEP TOWARDS ESTIMATING FUNCTIONAL AND AESTHETIC OUTCOME OF ORAL CANCER SURGERY
MEDICAL & BIOLOGICAL ENGINEERING & COMPUTING, 55(4), 573-583. DOI: 10.1007/S11517-016-1511-Z

Abstract

Aim

In oral cancer, loss of function due to surgery can be unacceptable, designating the tumour as functionally inoperable. Other curative treatments can then be considered. Currently, predictions of these functional consequences are subjective and unreliable. We want to create patient-specific models to improve and objectify these predictions.

Materials and methods

A first step was taken by controlling a 3D lip model with volunteer-specific sEMG activities. We focus on the lips first, because they are essential for speech, oral food transport, and facial mimicry. Besides, they are more accessible to measurements than intraoral organs. 3D lip movement and corresponding sEMG activities are measured in five healthy volunteers, who performed 19 instructions repeatedly, to create a quantitative lip model by establishing the relationship between sEMG activities of eight facial muscles bilaterally on the input side and the corresponding 3D lip displacements on the output side. The relationship between 3D lip movement and sEMG activities was accommodated in a state-space model.

Conclusions

A good relationship between sEMG activities and 3D lip movement was established with an average root mean square error of 2.43 mm for the first-order system and 2.46 mm for the second-order system. This information can be incorporated into biomechanical models to further personalise functional outcome assessment after treatment.

4.1. Introduction

Oral cancer, including that of the lips, is the sixth most common cancer worldwide [1]. Surgery is still standard care [2] and can lead to deterioration of speech, swallowing, and mastication with serious consequences on quality of life [3]. If surgical resection of a tumour results in an unacceptable loss of function, the tumour is designated as functionally inoperable, and other curative treatment options such as chemoradiotherapy or radiotherapy can serve as alternative treatments [4].

Accurate prediction of the functional consequences of surgery is an urgent need to make the right choice of treatment [5]. Functional prediction using virtual surgery is complex and involves several aspects of patient-specific anatomical geometry, biomechanical tissue properties, branching and distribution pattern of the nervous system, and the muscle activation signals that control a particular function. Biomechanical modelling, including the muscular system, in the oral and oropharyngeal region, has been the subject of ongoing research [6–9].

This paper focuses on the lips, since these are essential for speech, oral food transport, and facial mimicry. To create a predictive model, a continuum of 3D lip shapes is needed ultimately to perform virtual surgery on a model. Former research on lip modelling, utilising surface electromyography (sEMG) of facial muscles, is more phonetic in nature and is mainly focused on the categorisation of facial expressions [10], categorisation of vowels [11], and words [12].

To our knowledge, only two studies have described lip shape modelling in combination with quantitative lip pose estimation using facial electromyography (EMG). Honda et al. recorded lip motion in the 2D frontal projection of the face and sEMG signals from only one side [13]. They used a direct linear mapping of EMG to the lip coordinates based on multiple regression analysis. A visual comparison between the measured and modelled lip shapes was made. Lucero and Munhall acquired intramuscular EMG data, using hooked-wire bipolar electrodes, of one side of the face, and simultaneously measured lip and face displacements on the other side [14]. The relationship between EMG activity and marker displacements was based on a facial finite element model and the connection between EMG feature and the steady-state force generated by the corresponding muscle was presumed to be linear. The quantitative evaluation was expressed in terms of cross-correlation between model-predicted and measured displacements of the individual markers. For markers on the lips, these cross-correlations were rather low (mean values: 0.0 - 0.91) with very low cross-correlation for protrusion. The instructions in these studies differed, Honda et al. used five Japanese vowels, and the subject in the study of Lucero and Munhall was asked to produce an English sentence. Both models were tested on one volunteer.

The goal of this study is twofold. First, we want to demonstrate that sEMG signals contain enough information for controlling 3D dynamic models of facial expressions, particularly lip movements. The second goal is to establish the optimal processing configuration to extract information from facial sEMG data. To avoid the complexity and pitfalls of detailed

biomechanical models, we first focus on an empirical model. If the results of this empirical model are promising, the premise is justified that sEMG signals are very useful to solve the ambiguity problems in inverse dynamic modelling [15]. In addition, our study also should reveal which sEMG processing configuration, e.g. sEMG feature type and time window, is most promising for sEMG-based inverse modelling. The ambiguity problem of inverse dynamic modelling stems from the fact that a desired movement can be accomplished in various ways [15]. The activation pattern that causes the desired movement is not unique. The addition of the sEMG could provide further information about a patient-specific activation pattern.

4.2. Methods

4.2.1. Volunteers and data acquisition

Data were obtained from five healthy volunteers ($k = 1, \cdots, 5$) consisting of two males and three females, age ranging from 21 to 30. The recording sites of the skin were cleansed with NuPrep abrasive gel and alcohol. The sEMG signals were recorded using a TMSi® Porti™ system (TMSi ®, Oldenzaal, the Netherlands). The micro-sEMG sintered disc-shaped surface electrodes (1.5 mm diameter, Ag/AgCl, with shielded cables) were placed above eight muscles on both sides of the face ($n = 1, \cdots, 16$), as shown in Figure 4.1. The locations were chosen based on human lip anatomy and a study of Lapatki et al. showing the effects on lip shapes [16]. Additionally, a common ground reference electrode was applied with a self-adhesive button electrode on the left wrist. In Table 4.1 the measured muscles, their functions and electrode number, corresponding to the numbering in Figure 4.1 are given. Sixteen facial markers were defined using a skin marker. Ten markers covered the lip contour ($m = 1, \cdots, 10$). The other six markers ($m_{OR} = 1, \cdots, 6$) were located on the face (cheeks, nose and forehead; see Figure 4.1) and were used to compensate for head movement. The volunteers were positioned in front of a triple-camera set-up consisting of three cameras (Basler avA1000-100gc), which recorded the lip movement at 100 frames per second.

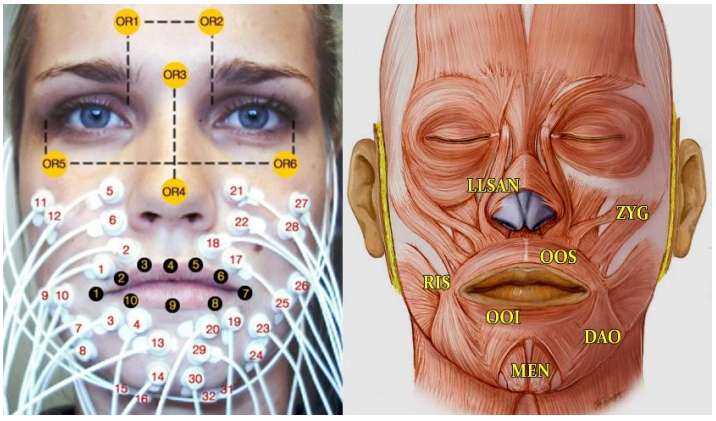

Figure 4.1 Left: Locations of electrodes, orientation markers, lip markers, and facial markers. Right: Measured facial muscles (excluding the digastric muscle), adapted from [17], with permission of Springer. ©2012 Springer-Verlag Berlin Heidelberg.

Table 4.1 **Muscle, muscle function, and corresponding electrode number.**

Muscle	Function	Electrodes number (right/left)
Zygomaticus major (ZYG)	Elevates the corners of the mouth in lateral direction	11, 12 / 27,28
Risorius (RIS)	Retracts angle of mouth	9, 10 / 25, 26
Orbicularis oris superior (OOS)	Narrows orifice of mouth, purses lips and puckers lip edges	1, 2 / 17, 18
Orbicularis oris inferior (OOI)	Narrows orifice of mouth, purses lips and puckers lip edges	3, 4 / 19, 20
Mentalis (MEN)	Draws up the skin of the chin and causes the lower lip to protrude	13, 14 / 29, 30
Depressor anguli oris (DAO)	Draws the corners of the mouth downwards and laterally	7, 8 / 23, 24
Levator labii superioris aleaque nasi (LLSAN)	Elevates and everts upper lip	5, 6 / 21, 22
Digastricus (DIG)	Depresses mandible, opening mouth, and/or elevates larynx	15, 16 / 31, 32

4.2.2. Instructions to volunteers

A study of van Son et al., showed that Dutch (experienced) lip readers were able to recognise five consonantal and five vowel visemes [18]. Visemes are groups of speech sounds that are visually indistinguishable. These Dutch viseme instructions were used in this study. Besides these visemes, six facial expressions that maximised independent contraction of the measured muscles were included. These selected expressions were based on the work of Lapatki et al. [16]. Lastly, two asymmetric motions were performed from left to right to left with closed lips, and with open lips, and one dynamic motion transfer between two expressions; purse lips to smiling to purse lips. Each volunteer was asked to repeat the 19 instructions ($i = 1, \cdots, 19$) five times ($r = 1, \cdots, 5$). The instructions are shown Table 4.2.

4.3. Data processing and analysis

4.3.1. sEMG preprocessing

The sEMG signals $s_n(t,i,r)$ were recorded in bipolar configuration with a sample frequency of 2,048 Hz. Here, t is the time index, i is the instruction and r is the repetition number. All recorded signals were bandpass filtered with a high- and low-pass fourth-order Butterworth filter with cut-off frequencies of, respectively, 15 and 500 Hz, in accordance with van Boxtel [19].

Many different sEMG feature types have been proposed in the literature. Based on the results of Phinyomark et al., who examined 37 feature types, and our results of a preliminary experiment, we chose to investigate four feature types given in Table 4.3 [20]. Thresholds for the WAMP feature (x_{lim}) were set to 10 and 20 mV. With all 16 sEMG channels stacked in a vector the result is denoted: $\mathbf{g}_f(t,i,r) \in \mathbb{R}^{16}$,

with $f = 1, \cdots, 5$ the feature type. Features were calculated over a sliding window with maximum overlap. The different window lengths examined were: 50, 100, 150, 200, 250, and 300 ms.

Table 4.2 Instructions: visemes (1-10), facial expressions (11-17), and asymmetric movements (18-19).

#	Viseme	Phonemes	Description/Location	Instruction
1	1	[p], [b], [m]	Bilabial consonants	APA
2	2	[f], [v], [ʋ]	Labiodental consonants	AVA
3	3	[s], [z], [ʃ]	Nonlabial front fricatives	AZA
4	4a	[t], [d], [n], [j], [l]	Other nonlabial front consonants	ATA
5	4b	[k], [χ], [ʁ], [ŋ]	Other nonlabial back consonants	AKA
6	5a	[i], [I], [e], [ɛ]	Close and half-close front vowels (unrounded)	KIEK
7	5b	[ɛi], [a], [o]	Half-open and open vowels (unrounded)	KAK
8	6	[u], [y], [œ], [ɔ]	Short back vowels (rounded)	KOEK
9	7	[Ø], [o]	Long back vowels (rounded)	KOOK
10	8	[au], [œy]	Closing and rounding diphthongs	KAUK

The videos were recorded concurrently with the sEMG. To synchronise the recorded sEMG signals with the video recordings a synchronisation pulse was fed to the TMSi® Porti™ system when the cameras started their recordings. Thereafter the sEMG signals were cut and resampled to 100 Hz, equivalent to the frame rate of the cameras.

Table 4.3 mathematical definitions of the sEMG features.

f	Feature	Formula
1	RMS	$\sqrt{\frac{1}{N}\sum_{i=1}^{N} x_i^2}$
2	MAV	$\frac{1}{N}\sum_{i=1}^{N} \lvert x_i \rvert$
3	WL	$\sum_{i=1}^{N-1} \lvert x_{i+1} - x_i \rvert$
4 $x_{\text{lim}} = 10$ mV	WAMP	$\sum_{i=1}^{N-1} \left[f\left(\lvert x_i - x_{i+1} \rvert \right) \right]$
5 $x_{\text{lim}} = 20$ mV		with $f(x) = \begin{cases} 1 & \text{if } x \geq x_{\text{lim}} \\ 0 & \text{otherwise} \end{cases}$

There is a small time delay between a sEMG activity and the corresponding muscle activation. It is difficult to define a default value for this delay. Honda et al. used 70 ms [13], whereas Vatikiotis et al. used different delays varying from 0 to 100 ms [21]. By minimising the estimation errors of the lip marker positions, we empirically determined a mean muscle activation delay of 30 ms, which we compensated in all records.

4.3.2. Video preprocessing

The facial markers were tracked in the images of the three cameras, and the 2D coordinates were reconstructed to a set of 3D coordinates. The root mean squared (RMS) error of the 3D localisation of markers, obtained via the leave-one-out method, was 0.73 mm. The resulting 3D positions of the ten markers on the lip, corrected for head movement, are denoted by $\mathbf{X}(t,i,r) \in \mathbb{R}^{30}$.

4.3.3. The measurement model

State-space estimation requires the availability of a measurement model that links the sEMG features $\mathbf{g}_f(t,i,r)$ to marker positions $\mathbf{X}(t,i,r)$. The relationship between these quantities is nonlinear, whereas a linear model was preferred. To arrive at a linear approximation, a truncated Taylor series in $\mathbf{g}_f(t,i,r)$ up to order two was used. For this, the $16D$ feature vector $\mathbf{g}_f(t,i,r)$ was augmented with all the 136 quadratic terms and cross products of its elements yielding a $152D$ vector $\underline{\mathbf{g}}_f(t,i,r)$.

To establish the measurement model, first a principal component analysis (PCA) was applied. Suppose that a training set consisting of J observed sEMG features $\underline{\mathbf{g}}(j)$ and corresponding marker positions $\mathbf{X}(j)$, with $j = 1,\cdots,J$, is available. The exact construction of this training set will be explained later. PCA was applied to the concatenation of these vectors:

$$\mathbf{z}(j) \overset{def}{=} \begin{bmatrix} \mathbf{X}(j) \\ \underline{\mathbf{g}}(j) \end{bmatrix} \tag{4.1}$$

The dimension of the vectors $\mathbf{z}(j)$ is 182. The set was normalised with respect to mean and variance of each element before applying the PCA, because the sEMG features and the 3D coordinates present two different physical dimensions. The PCA resulted in a $182D$ dimensional orthogonal matrix $\mathbf{Y}$ containing the first D principal components of the set. Encoding of a vector $\mathbf{z}$ in a D-dimensional coefficient vector $\mathbf{b}$, and subsequent decoding, occurs according to:

$$\begin{aligned} \mathbf{b} &= \mathbf{Y}^T\mathbf{z} \quad \text{(encoding)} \\ \hat{\mathbf{z}} &= \mathbf{Y}\mathbf{b} \quad \text{(decoding)} \end{aligned} \tag{4.2}$$

The mean of the coefficient vector $\mathbf{b}$ is zero, and the covariance matrix $\mathbf{C}_\mathbf{b}$ is diagonal with the elements sorted in descending order.

To arrive at a (pseudo-) linear measurement model, we constructed the matrix $\mathbf{Y}_\mathbf{g}$ from $\mathbf{Y}$ by leaving out the first 30 rows corresponding to the positions $\mathbf{X}$. We then have:

$$\hat{\underline{\mathbf{g}}} = \mathbf{Y}_\mathbf{g}\mathbf{b} \tag{4.3}$$

Suppose that the residuals of $\hat{\underline{\mathbf{g}}}$ are given by $\mathbf{v}$, such that $\underline{\mathbf{g}} = \hat{\underline{\mathbf{g}}} + \mathbf{v}$, then:

$$\underline{\mathbf{g}} = \mathbf{Y}_\mathbf{g}\mathbf{b} + \mathbf{v} \tag{4.4}$$

This can be regarded as a linear measurement model of $\mathbf{b}$ with $\underline{\mathbf{g}}$ the measurement vector, $\mathbf{Y}_\mathbf{g}$ the measurement matrix, and $\mathbf{v}$ the measurement noise. The covariance matrix $\mathbf{C}_\mathbf{v}$ of $\mathbf{v}$ is a 152×152 dimensional matrix which can easily be estimated from the training set. Due to augmentation of $\mathbf{g}$ with quadratic terms, the measurement noise is not guaranteed to be uncorrelated, and the matrix $\mathbf{C}_\mathbf{v}$ might be nondiagonal.

4.3.4. State-space modelling

For dynamic modelling, two state-space models were implemented, a first-order and a second-order system. In the first-order system, a time series $\mathbf{b}(t)$ was modelled dynamically with:

$$\mathbf{b}(t+1) = \mathbf{F}\mathbf{b}(t) + \mathbf{w}(t) \tag{4.5}$$

$\mathbf{b}(t)$ is the D-dimensional state vector, and $\mathbf{F}$ is the $D\times D$ system matrix. The process noise $\mathbf{w}(t)$ was assumed to be zero mean and uncorrelated in time. Its covariance matrix is $\mathbf{C}_\mathbf{w}$. The system matrix $\mathbf{F}$ was estimated from the training set using $\mathrm{E}\left[\mathbf{b}(t+1)\mathbf{b}^T(t)\right] = \mathbf{F}\mathrm{E}\left[\mathbf{b}(t)\mathbf{b}^T(t)\right]$.

Here, $\mathrm{E}[\ ]$ is the expectation operator; hence, $\hat{\mathbf{F}} = \overline{\mathbf{b}(t+1)\mathbf{b}^T(t)}\left(\overline{\mathbf{b}(t)\mathbf{b}^T(t)}\right)^{-1}$.

The covariance matrix $\mathbf{C}_w$ can be estimated from the training set using $\mathbf{w}(t) = \mathbf{b}(t+1) - \mathbf{F}\mathbf{b}(t)$. Preliminary experiments showed that both $\mathbf{F}$ and $\mathbf{C}_w$ are diagonal. This was expected as the PCA decorrelated the coefficients $\mathbf{b}(t)$. In addition, the system matrix $\mathbf{F}$ appeared to approximate the identity matrix $\mathbf{I}$. This was also expected as the sampling period, 10 ms, is rather small compared to the expected time constant of lip motions.

In the second-order system, the state vector was defined as:

$$\mathbf{x}(t) \overset{def}{=} \begin{bmatrix} \mathbf{b}(t-1) \\ \mathbf{b}(t) \end{bmatrix} \tag{4.6}$$

with associated state equation:

$$\mathbf{x}(t+1) = \mathbf{F}\mathbf{x}(t) + \mathbf{w}(t) \quad \text{with} \quad \mathbf{F} = \begin{bmatrix} \mathbf{0} & \mathbf{I} \\ \mathbf{F}_1 & \mathbf{F}_2 \end{bmatrix} \tag{4.7}$$

Preliminary experiments showed that the submatrices $\mathbf{F}_1$ and $\mathbf{F}_2$ are diagonal which again is in line with the uncorrelatedness of the coefficients $\mathbf{b}(t)$. Equation (4.7) models D decoupled second-order autoregressive (AR) models, one for each coefficient $b_n(t)$ in $\mathbf{b}(t)$, i.e.,

$$b_n(t+1) = \alpha_n b_n(t) + \beta_n b_n(t-1) + w_n(t) \quad \text{with} \quad n = 1, \cdots, D \tag{4.8}$$

where α_n is a diagonal element from $\mathbf{F}_2$, and β_n a diagonal element from $\mathbf{F}_1$. The AR models represent second-order differential equations in the continuous time that are characterised by their natural frequencies f_n and relative damping ζ_n given by:

$$f_n = \frac{\sqrt{1-\alpha_n-\beta_n}}{2\pi T} \quad \text{and} \quad \zeta_n = \frac{-\alpha_n - 2}{2\sqrt{1-\alpha_n-\beta_n}} \tag{4.9}$$

where T is the sampling period. The natural frequency determines the bandwidth of the corresponding coefficient. The damping determines the spectrum of the signal around the natural frequency. We used these parameters to fine-tune the state-space model during training.

The process noise $\mathbf{w}(t)$ has zero elements in the first D elements. Thus, the covariance matrix is built as follows:

$$\mathbf{C}_w = \begin{bmatrix} \mathbf{0} & \mathbf{0} \\ \mathbf{0} & \mathbf{C}_{22} \end{bmatrix} \tag{4.10}$$

$\mathbf{C}_{22}$ is a diagonal matrix as the coefficients of a PCA are uncorrelated. Preliminary results showed that this was indeed the case.

To determine the influence of dynamic modelling we also performed static modelling by enforcing the Kalman filter, which is described below, to use only measurements, and to ignore the predictions. This was effectuated by setting the standard deviation of the process noise to almost infinity.

4.3.5. Estimation

The estimation of the coefficients of the PCA was done with a discrete Kalman filter. The dimension of the state vector is in the first-order system D, and in the second-order system $2D$. In practice, D, being the result of the PCA, is much smaller than the dimension of the measurement vector, $\underline{\mathbf{g}}(t)$, which is 152. Therefore, the Kalman filter was used in the following form:

$$\left.\begin{aligned}\hat{\mathbf{x}}(t\,|\,t-1) &= \mathbf{F}\hat{\mathbf{x}}(t-1\,|\,t-1)\\ \mathbf{C}(t\,|\,t-1) &= \mathbf{F}\mathbf{C}(t-1\,|\,t-1)\mathbf{F}^T + \mathbf{C}_w\end{aligned}\right\}\text{prediction}$$

$$\left.\begin{aligned}\mathbf{C}(t\,|\,t) &= \left(\mathbf{C}^{-1}(t\,|\,t-1) + \mathbf{H}^T\mathbf{C}_\mathbf{v}^{-1}\mathbf{H}\right)^{-1}\\ \hat{\mathbf{x}}(t\,|\,t) &= \mathbf{C}(t\,|\,t)\left(\mathbf{C}^{-1}(t\,|\,t-1)\hat{\mathbf{x}}(t\,|\,t-1) + \mathbf{H}^T\mathbf{C}_\mathbf{v}^{-1}\underline{\mathbf{g}}(t)\right)\end{aligned}\right\}\text{updating} \qquad (4.11)$$

This is computationally more efficient than the typical form. In equation (4.11), $\mathbf{H}$ is the measurement matrix, which equals $\mathbf{Y}_\mathbf{g}$ in the first-order system and $\begin{bmatrix}\mathbf{0} & \mathbf{Y}_\mathbf{g}\end{bmatrix}$ in the second-order system.

4.3.6. Training and testing

The algorithm needs training data to find the PCA components $\mathbf{Y}$, the covariance matrices $\mathbf{C}_\mathbf{V}$ and $\mathbf{C}_\mathbf{w}$ and in case of the first-order system the system matrix $\mathbf{F}$ and in case of the second-order system, its submatrices $\mathbf{F}_1$ and $\mathbf{F}_2$. The dimension D of the PCA is a design parameter. Additional design parameters were introduced to fine-tune the models. These were as follows:

- The measurement noise covariance matrix $\mathbf{C}_\mathbf{V}$ was corrected with a regularisation parameter c_v. Instead of $\mathbf{C}_\mathbf{V}$, the matrix $(1-c_v)\mathbf{C}_\mathbf{v} + c_v\overline{\mathbf{C}_\mathbf{v}(\ell,\ell)}\mathbf{I}$, with $\overline{\mathbf{C}_\mathbf{v}(\ell,\ell)}$ the average of the diagonal elements, was used.

- The process noise covariance matrix $\mathbf{C}_\mathbf{w}$ was corrected with a regularisation parameter c_w. That is, the submatrix $\underline{\mathbf{C}_{22}}$, was replaced by the matrix $(1-c_w)\mathbf{C}_{22} + c_w diag(\overline{\mathbf{C}_{22}(\ell,\ell)})$. Here, $diag(\overline{\mathbf{C}_{22}(\ell,\ell)})$ is the diagonal matrix that is built with a smoothed version of the diagonal elements of $\mathbf{C}_{22}$.

- The diagonal matrices $\mathbf{F}_1$ and $\mathbf{F}_2$, which holds the second-order AR parameters α_n and β_n, respectively, were corrected by application of a proportionality constant to the corresponding natural frequencies and damping by constants c_f and c_d. So, instead of f_n and ζ_n, the parameters $c_f f_n$ and $c_d\zeta_n$ were used.

This resulted into three design parameters, D, c_v, and c_w, for the first-order system and five design parameters, D, c_v, c_w, c_f, and c_d, for the second-order system. These parameters were optimised using training data.

We performed cross-validation for training and testing. The procedure is depicted in Figure 4.2. It was applied per volunteer, per feature type, and per window size. Data from the various instructions were pooled by concatenating the data: $\underline{\mathbf{g}}_f(t,r) = \left[\underline{\mathbf{g}}_f(t,1,r) \quad \cdots \quad \underline{\mathbf{g}}_f(t,19,r)\right]$. The data from four repetitions were pooled to get the training data: $\underline{\mathbf{g}}_f(t) = \left[\underline{\mathbf{g}}_f(t,1) \quad \cdots \quad \underline{\mathbf{g}}_f(t,4)\right]$. Testing was performed on the fifth repetition. Cross-validation took place by rotating the repetitions. The final evaluation criterion was defined as the RMS of the error calculated over all marker coordinates and all repetitions. The design parameters were obtained by minimisation of the RMS error by varying these parameters one by one and applying successive parabolic optimisation. The one-sided paired Wilcoxon test was used to test for significant differences between the static and the two dynamic systems. The one-sided test was justified because the static model is in fact included in the dynamic model as a special case, and as such the optimised performance of the dynamic model cannot be less than the static model.

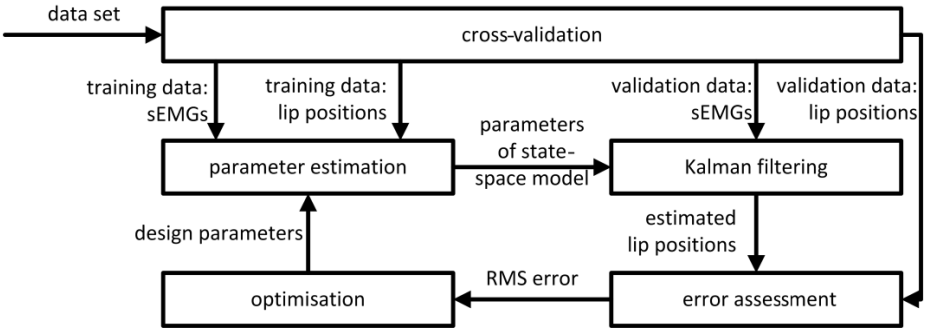

Figure 4.2 The optimisation and evaluation of design parameters using cross-validation.

4.4. Results

The best results for the static, first-order, and second-order state-space models are summarised in Table 4.4 for the individual subjects and on average. The first-order system for state-space modelling performed best on average, with a RMS error of 2.43 mm on average. The first-order and the second-order system showed statistically significant better results than the static system ($p = 0.03$). No significant difference was found between the two dynamic systems. Four subjects showed the best results when the WAMP feature was used. The optimal threshold x_{lim} differed between the subjects. A window length of 200 ms performed best on average. The average RMS error was 2.46 mm for the second-order state-space model, also using the WAMP feature with $x_{\text{lim}} = 10$ mV and a window length of 200 ms. As expected, static modelling showed poorer results, but performed also best when the WAMP feature was used.

Table 4.4 Mean RMS error and standard deviation σ, optimal feature, and window, found per volunteer and on average for the static, first-order, and second-order dynamic model.

Volunteer	1	2	3	4	5	Average
Static						
RMS error (mm)	2.34	2.55	3.02	2.32	2.92	2.70
σ	(0.21)	(0.21)	(0.12)	(0.15)	(0.14)	(0.19)
Feature	WAMP	WAMP	WAMP	WAMP	WAMP	WAMP
	(20mV)	(20 mV)	(20 mV)	(10 mV)	(10 mV)	(10 mV)
Window (ms)	200	200	300	250	300	250
First-order system						
RMS error (mm)	2.10	2.29	2.64	2.10	2.66	2.43
σ	(0.17)	(0.19)	(0.17)	(0.19)	(0.19)	(0.18)
Feature	WAMP	WL	WAMP	WAMP	WAMP	WAMP
	(20 mV)		(20 mV)	(10 mV)	(10 mV)	(10 mV)
Window (ms)	200	200	200	250	250	200
Second-order system						
RMS error (mm)	2.02	2.42	2.58	2.13	2.66	2.46
σ	(0.19)	(0.18)	(0.18)	(0.21)	(0.21)	(0.18)
Feature	WAMP	WL	WAMP	WAMP	WAMP	WAMP
	(20 mV)		(20 mV)	(10 mV)	(10 mV)	(10 mV)
Window (ms)	200	250	150	200	200	200

The RMS errors for the different features for the first-order and second-order system are presented in Table 4.5. It can be seen that for both $x_{\text{lim}} = 10$ mV and $x_{\text{lim}} = 20$ mV the WAMP feature performance was comparable. Regarding the other features, the WL performed slightly worse compared to the WAMP. RMS and MAV showed the poorest results.

Table 4.5 Optimal settings averaged over the volunteers obtained per feature and system order.

	RMS		MAV		WL		WAMP10		WAMP20	
System order	**1st**	**2nd**	**1st**	**2nd**	**1st**	**2nd**	**1st**	**2nd**	**1st**	**2nd**
RMS error (mm)	2.74	2.70	2.67	2.64	2.50	2.50	2.43	2.46	2.45	2.46
Window (ms)	200	200	250	200	200	200	200	200	200	200

The influence of the different parameters and window length on the error in the second-order system can be seen in Figure 4.3. Each graph shows the influence of one parameter on the RMS error while the others are set to values which lead to the optimal results on average. The dimension of the PCA, D, shows a plateau after 20 components. Optimal values of 0.1 and 3.4 were found for c_v and c_f, respectively. The regularisation parameter c_d had the minimum error at a factor of 0.7. The constant c_w showed little influence but had an optimum on average at 0.2.

The window lengths showed a similar trend in all subjects, with the best results for medium length windows. For the first-order system, comparable values were found.

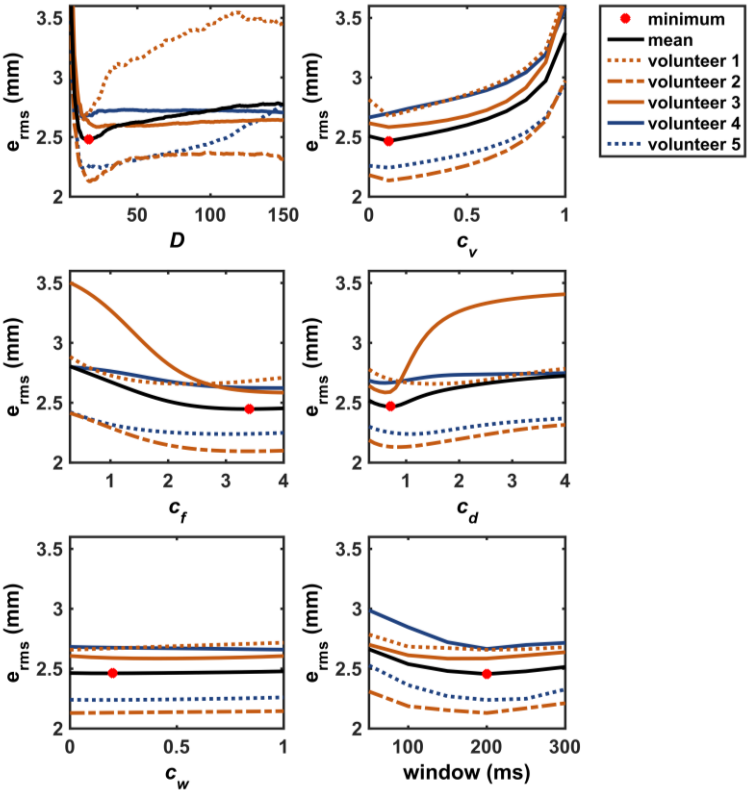

Figure 4.3 The dependence of the RMS error on the various parameters and window length in the second-order system.

4.5. Discussion

For the prediction of the functional and aesthetic consequences of treatment in oral cancer, dynamic models of the lips are required. Biomechanical modelling is physics based and as such the most direct method to predict these consequences. However, finding the patient-specific muscle activation signals needed for the biomechanical models is difficult [22]. sEMG signals may contain information to help in finding these patient-specific activations signals. To find the optimal sEMG processing configuration and to prove that sEMG signals contain sufficient information to do so, the current study describes an empirically derived model that is able to estimate the dynamics of lip displacements with an average RMS error of 2.43 mm.

This empirical model is sEMG driven, which incorporates volunteer-specific information. As far as we know, we are the first who expressed distance errors of lip motion prediction based on sEMG features.

The approach used here, incorporated the dynamics of the system by means of a state-space model. To test whether dynamical modelling was superior to static modelling, we implemented both. As expected, incorporation of dynamics improved the model. In comparison with the static system RMS errors decreased in every volunteer, with an average of 0.27 mm for the first-order system and 0.24 mm for the second-order system. An advantage of a dynamic system is that bandwidth can be sacrificed to improve the signal-to-noise ratio. Apparently, in the current application such a sacrifice pays off, but not drastically.

The difference between the first-order and second-order system is negligible. A higher-order system has more parameters which have to be estimated, making the filter more sensitive for deviations in those parameters to the optimum settings. An optimal equilibrium has to be found between modelling accurate dynamic behaviour for which higher-order systems are beneficial, and confining the impact of errors in the estimated parameters for which a lower-order system is preferred. In this study, the advantages of a second-order system over a first-order system did not outweigh the errors induced by the deviations in the estimated parameters.

The fudging parameters were used to optimise the model per volunteer and hence make it volunteer- specific. Only the regularisation parameter c_w for the process noise covariance matrix $\mathbf{C}_w$ did not have much influence. For each parameter, a similar trend was seen regarding the optimal values, but the level of influence differed per volunteer. The optimal values found in this study can be used to set the limits for future volunteers, thereby decreasing computational time of the parabolic optimisation. The dimension of the PCA reached a plateau at 20, four dimensions more than the original 16 dimensions, suggesting that the cross products of the sEMG provided additional information. Preliminary experiments indicated that leaving out all the nonlinear cross products seriously deteriorated the results. Hence, the nonlinearity of the system is substantial. Finally, window length was optimal at medium lengths. A possible explanation is that short window lengths are prone to noise, whereas longer window lengths smooth the signals too much.

The different features also had a noticeable influence on the RMS error. The WAMP features with $x_{\text{lim}} = 10$ and $x_{\text{lim}} = 20$ mV were most promising. Perhaps that thresholds in-between these values could perform better. One can also think of optimising x_{lim} per muscle channel for optimal results. The widely used RMS feature performed worse. This was also found by Phinyomark et al. [20].

Because of different error assessments, the differences of our model compared to studies in the literature will be discussed qualitatively. The main differences are stated in Table 4.6. The current model showed results for a more extensive set of instructions, including asymmetric movements. Furthermore, more 3D lip markers and more muscles were included. Our model predicts 3D movement of the lips based on measurements on both sides of the face and therefore is more realistic. Honda et al. used a linear statistical approach, which is inadequate for modelling nonlinear soft tissue changes.

Table 4.6 Differences in experimental setup in related studies.

	Current study	Honda et al.	Lucero & Munhall
Dimension	3D	2D	3D
Measurement	Bilateral	Unilateral	Unilateral
Muscles	16	6	7
Lip markers	10	7	5
EMG	Surface	Surface	Hooked-wire
Jaw movement	Digastric muscle	Omitted	Manual
Model	PCA MMSE + Kalman	Multiple regression	FEM
Instructions	Visemes and facial expressions (19)	Japanese vowels (5)	English sentence
Volunteers	5	1	1
Error assessment	RMS distance	Visual	Visual and cross-correlations

To allow the model to cope with nonlinear behaviour, we calculated the cross products of the sEMG signal features to add nonlinearity. The model of Honda et al. did not include the factor of jaw movement, making the estimation of vertical movement prone to errors. Lucero and Munhall controlled jaw movement by tracking an optical marker instead of EMG signals. Nonsurprisingly, the modelled facial tissue followed this movement well. We added sEMG measurements of the digastric muscle to make the prediction of jaw movement possible. Both Honda et al. and Lucero and Munhall measured EMG signals on one side of the face, disregarding asymmetry in facial morphology and lip movement as described by Campbell [23]. The use of hooked-wire, as used by Lucero and Munhall, or needle electrodes is attractive to overcome the problem of crosstalk, but for clinical applications this will be impractical because they are invasive and consequently patient-unfriendly. Therefore, in generating future personalised 3D models controlled by EMG signals, sEMG will have our preference, being easy applicable and patient-friendly. Furthermore, we tested our model in five subjects, indicating it is general applicable.

A limitation of the proposed set-up is the high number of required sEMG electrodes. This makes the current approach time-consuming which is inconvenient in future clinical practice. Monopolar derivations can be used to halve the number of electrodes; however, this configuration does not reduce unwanted noise from the recordings by using the differential amplifier design [24]. Another approach to lessen the number of electrodes is to identify less influential muscle channels for the estimation of motion, and include only those channels that affect motion prediction most.

Another difficulty is the variability in muscle anatomy, and overlying soft tissue, which makes standardisation of the measurements difficult. Additionally, physiological orofacial functions usually require simultaneous contraction of various muscles. These muscles therefore lack training in isolated contractions, resulting in relatively high co-contraction of muscles. Also, volunteers can use different muscle activation patterns to perform the

same instruction. We saw similar results when facial expressions were performed as described by Schumann et al. [25]. Most volunteers were able to selectively activate the LLSAN, whereas most volunteers had difficulty in pulling their lip corners down (DAO). Purse lips, pout, and voluntary smiling all induced multiple muscle activations, showing the difficulty in selective muscle activation of facial muscles.

The two main pillars of our study were to demonstrate that sEMG signals contain sufficient information to control 3D dynamic models of lip movements and to determine the best sEMG processing configuration for this purpose. These two steps are necessary for our ultimate goal to enable inverse biomechanical modelling of the lips, oral cavity, and tongue, in order to retrieve patient-specific muscle activation signals inducing oral functions. These activation signals are needed to enable prediction of functional consequences after surgery. Besides patient-specific activation signals, patient-specific anatomical information and tissue parameters are required for simulating treatment effects. The current model does not account for these aspects yet. However, a biomechanical model should incorporate this physical relationship and patient-specific parameters before mimicking performed treatments. The simulated activations controlling the biomechanical model should be similar to the actual muscular control of the patient. sEMG is an instrument to provide the information for these simulated activations. Unfortunately, sEMG is a rough estimate, because of a nonlinear relationship, crosstalk, misplacement of electrodes, and other artefacts. We showed that the relationship between 3D lip motion and sEMG can be accurately described by a statistical model. So it can be expected that with our approach the ambiguity problem of inverse modelling can be solved. Our next studies will focus on the relationship between activation signals and sEMG in biomechanical models.

4.6. Conclusion

This study presented a next step towards the personalisation of the functional outcome assessment after treatment of oral cancer. The two dynamic modelling methods proved that a continuum of 3D lip positions can be predicted based on volunteer-specific sEMG features. The discrete Kalman filter with a first-order state estimation performs slightly better than a second-order system, with a mean RMS error of 2.43 mm. The optimal sEMG processing configuration was found to be the WAMP feature with x_{lim} = 10 mV and a window length of 200 ms. In future studies, this method may be used to solve the problems concerning inverse modelling in biomechanical models, by reduction of the solution space and including patient-specific information.

4.7. Acknowledgements

The authors gratefully acknowledge I. Jacobi, PhD for assisting in developing the instruction list and R.J.J.H van Son, PhD for his critical review of the manuscript. Furthermore, they acknowledge the volunteers for participating in this research. Lastly, the authors gratefully acknowledge the Maurits en Anna de Kock Foundation (www.mauritsenannadekockstichting.nl) for funding the triple-camera set-up and the Porti EMG system.

4.8. Conflict of interest

The authors declare that they have no conflict of interest.

4.9. Funding

No funding was acquired for this research.

4.10. Ethical approval

Although this research involved healthy human volunteers, no ethical approval was required as the study did not infringe the (psychological) integrity of the volunteers. Measurements were noninvasive and not stressful. The study was performed within the Dutch legislation regarding the Agreement on Medical Treatment Act, Personal Data Protection Act, and the Code of Conduct for Responsible Use of the Federa (Dutch Federation of Biomedical Scientific Societies). Verbal information and consent is obtained. Furthermore, verbal consent is obtained for publishing the photographs in Figure 4.1 and Table 4.2.

4.11. References

1. Siegel R, Naishadham D, Jemal A. Cancer statistics, 2012. CA Cancer J Clin. 2012;62: 10–29. doi:10.3322/caac.20138

2. Shah JP, Gil Z. Current concepts in management of oral cancer-surgery. Oral Oncol. 2009;45: 394–401. doi:10.1016/j.oraloncology.2008.05.017

3. Kreeft A, Tan IB, van den Brekel MWM, Hilgers FJ, Balm AJM. The surgical dilemma of "functional inoperability" in oral and oropharyngeal cancer: current consensus on operability with regard to functional results. Clin Otolaryngol. 2009;34: 140–6. doi:10.1111/j.1749-4486.2009.01884.x

4. Kreeft AM, Tan IB, Leemans CR, Balm AJM. The surgical dilemma in advanced oral and oropharyngeal cancer: how we do it. Clin Otolaryngol. 2011;36: 260–266. doi:10.1111/j.1749-4486.2011.02299.x

5. van Alphen MJA, Kreeft AM, van der Heijden F, Smeele LE, Balm AJM. Towards virtual surgery in oral cancer to predict postoperative oral functions preoperatively. Br J Oral Maxillofac Surg. 2013;51: 747–751. doi:10.1016/j.bjoms.2013.06.012

6. Stavness I, Nazari MA, Perrier P, Demolin D, Payan Y. A biomechanical modeling study of the effects of the orbicularis oris muscle and jaw posture on lip shape. J speech, Lang Hear Res. 2013;56: 878–890. doi:10.1044/1092-4388(2012/12-0200)

7. Stavness I, Gick B, Derrick D, Fels S. Biomechanical modeling of English /r/ variants. J Acoust Soc Am. 2012;131: EL355-360. doi:10.1121/1.3695407

8. Pelteret J-P V, Reddy BD. Development of a computational biomechanical model of the human upper-airway soft-tissues toward simulating obstructive sleep apnea. Clin Anat. 2014;27: 182–200. doi:10.1002/ca.22313

9. Vogt F, Lloyd JE, Perrier P. Efficient 3D Finite Element Modeling of a Muscle-Activated Tongue. In: Harders M, Székely G, editors. Biomedical Simulation. 2006. pp. 19–28.

10. Hamedi M, Salleh S-H, Swee TT, Kamarulafizam. Surface Electromyography-Based Facial Expression Recognition in Bi-Polar Configuration. J Comput Sci. 2011;7: 1407–1415. doi:10.3844/jcssp.2011.1407.1415

11. Arjunan SP, Kumar DK, Yau WC, Weghorn H. Unvoiced speech control based on vowels detected by facial surface electromyogram. In: Isaías P, McPherson M, Bannister F, editors. Proceedings of the IADIS International Conference on e-Society. 2006. pp. 381–388.

12. Betts BJ, Binsted K, Jorgensen C. Small-vocabulary speech recognition using surface electromyography. Interact Comput. 2006;18: 1242–1259. doi:10.1016/j.intcom.2006.08.012

13. Honda K, Kurita T, Kakita Y, Maeda S. Physiology of the lips and modeling of lip gestures. J Phon. 1995;23: 243–254. doi:10.1016/S0095-4470(95)80046-8

14. Lucero JC, Munhall KG. A model of facial biomechanics for speech production. J Acoust Soc Am. 1999;106: 2834–2842. doi:10.1121/1.428108

15. Stavness I, Lloyd JE, Fels S. Automatic prediction of tongue muscle activations using a finite element model. J Biomech. 2012;45: 2841–2848. doi:10.1016/j.jbiomech.2012.08.031

16. Lapatki BG, Stegeman DF, Zwarts MJ. Selective contractions of individual facial muscle subcomponents monitored and trained with high-density surface EMG. In: Beurskens CHG, van Gelder RS, Heymans PG, Manni JJ, Nicolai JA, editors. The Facial Palsies Complementary Approaches. 2005. pp. 89–108. doi:10.1007/s00238-008-0236-0

17. Prendergast PM. Anatomy of the face and neck. In: Shiffman MA, Di Giuseppe A, editors. Cosmetic Surgery Art and techniques. 2013. p. 36. doi:10.1007/978-3-642-21837-8

18. van Son N, Huiskamp TMI, Bosman AJ, Smoorenburg GF. Viseme classifications of Dutch consonants and vowels. J Acoust Soc Am. 1994;96: 1341–1355. doi:10.1121/1.411324

19. van Boxtel A. Optimal signal bandwidth for the recording of surface EMG activity of facial, jaw, oral, and neck muscles. Psychophysiology. 2001;38: 22–34. doi:10.1111/1469-8986.3810022

20. Phinyomark A, Phukpattaranont P, Limsakul C. Feature reduction and selection for EMG signal classification. Expert Syst Appl. 2012;39: 7420–7431. doi:10.1016/j.eswa.2012.01.102

21. Vatikiotis-Bateson E, Munhall KG, Hirayama M, Lee YV, Terzopoulos D. The Dynamics of Audiovisual Behavior in Speech. In: Stork DG, Hennecke ME, editors. Speechreading by Humans and Machines. 1996. pp. 221–232. doi:10.1007/978-3-662-13015-5

22. Wu X, Dang J, Stavness I. Iterative method to estimate muscle activation with a physiological articulatory model. Acoust Sci Technol. 2014;35: 201–212. doi:10.1250/ast.35.201

23. Campbell R. Asymmetries in moving faces. Br J Psychol. 1982;73: 95–103. doi:10.1111/j.2044-8295.1982.tb01794.x

24. Robertson LD, Mustain EH, Maurer K, Evans E, Calderwood S, Sexton J. EMG instrumentation. In: Kamen G, Gabriel D, editors. Essentials of Electromyography. 1st ed. 2009. p. 66.

25. Schumann NP, Bongers K, Guntinas-Lichius O, Scholle HC. Facial muscle activation patterns in healthy male humans: A multi-channel surface EMG study. J Neurosci Methods. 2010;187: 120–128. doi:10.1016/j.jneumeth.2009.12.019

PART III

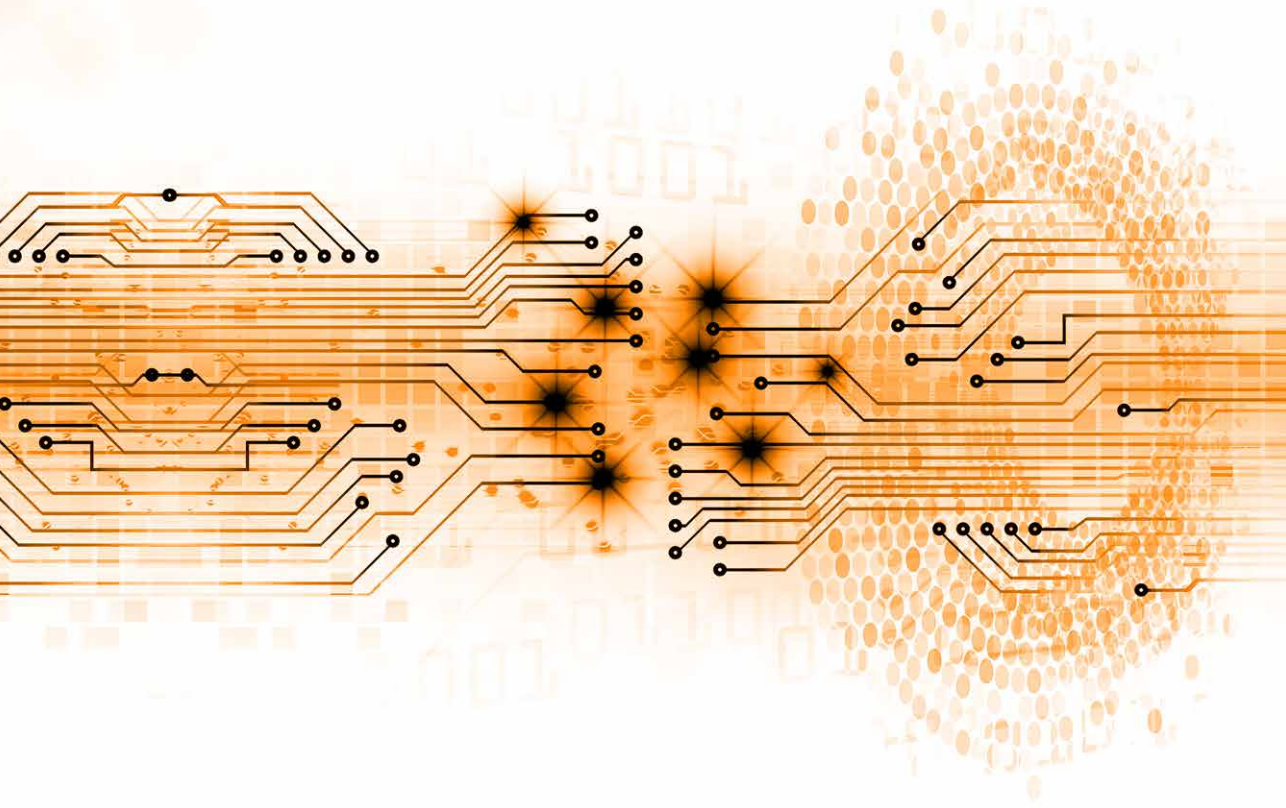

V

DATA AVAILABLE ONLINE
DOI: 10.17605/OSF.IO/DUX3W

FORWARD MODELLING OF 3D LIP MOVEMENT

This chapter was published in International Journal of Computer Assisted Radiology and Surgery

ESKES M, BALM AJM, VAN ALPHEN MJA, SMEELE LE, STAVNESS I, VAN DER HEIJDEN F (2017)
SIMULATION OF FACIAL EXPRESSIONS USING PERSON-SPECIFIC sEMG SIGNALS CONTROLLING
A BIOMECHANICAL FACE MODEL
INTERNATIONAL JOURNAL OF COMPUTER ASSISTED RADIOLOGY AND SURGERY, 1-13. DOI: 10.1007/S11548-017-1659-5

Abstract

Aim

Functional inoperability in advanced oral cancer is difficult to assess preoperatively. To assess functions of lips and tongue, biomechanical models are required. Apart from adjusting generic models to individual anatomy, muscle activation patterns (MAPs) driving patient-specific functional movements are necessary to predict remaining functional outcome. We aim to evaluate how volunteer-specific MAPs derived from surface electromyographic (sEMG) signals control a biomechanical face model.

Materials and methods

Muscle activity of seven facial muscles in six volunteers was measured bilaterally with sEMG. A triple-camera set-up recorded 3D lip movement. The generic face model in ArtiSynth was adapted to our needs. We controlled the model using the volunteer-specific MAPs. Three activation strategies were tested: activating all muscles (act_{all}), selecting the three muscles showing highest muscle activity bilaterally (act_3) – this was calculated by taking the mean of left and right muscles and then selecting the three with highest variance – and activating the muscles considered most relevant per instruction (act_{rel}), bilaterally. The model's lip movement was compared to the actual lip movement performed by the volunteers, using 3D correlation coefficients (ρ).

Conclusion

The correlation coefficient between simulations and measurements with act_{rel} resulted in a median ρ of 0.77. act_3 had a median ρ of 0.78, whereas with act_{all} the median ρ decreased to 0.45. We demonstrated that MAPs derived from noninvasive sEMG measurements can control movement of the lips in a generic finite element face model with a median ρ of 0.78. Ultimately, this is important to show the patient-specific residual movement using the patient's own MAPs. When the required treatment tools and personalisation techniques for geometry and anatomy become available, this may enable surgeons to test the functional results of wedge excisions for lip cancer in a virtual environment and to weigh surgery versus organ-sparing radiotherapy or photodynamic therapy.

5.1. Introduction

Surgical treatment in advanced head and neck cancer can lead to severe function loss, including chewing deficits, dysphagia, and speech impairment. If this function loss is expected to be unacceptable, then other treatments, like radiotherapy, chemotherapy, and photodynamic therapy, can be considered [1]. Although alternative curative treatments like radiotherapy have their own effects on functional outcome, in the future we will focus on surgical effects first by developing a virtual surgery tool because these are relatively easier to model. Unfortunately, it is difficult to predict functional outcome of the aforementioned treatments accurately. In fact, the prediction depends heavily on the subjective judgements by members of the multidisciplinary tumour board and therefore can differ greatly among specialists [2].

To tackle the problem of preoperative prediction of surgical outcome, biomechanical models are preferred as these models can be adjusted to represent the actual anatomy and pathological anatomical changes and they can simulate physical processes. Biomechanical models of the head and neck region have been developed. In particular, in the field of animation and facial surgery planning [3–7], these models mainly predicted aesthetic outcome. A couple of those models also predicted functional outcome, like effects of scar tissue on tongue mobility [8,9], intraoral swallowing effects [10], and facial expressions after maxillofacial surgery [11].

The models can be controlled by simulated muscle activation patterns. These activation patterns contract the models' muscles (elements) resulting in a visible movement. This process is called forward modelling: the determination of motion calculated from known forces. Each person learns to perform functional tasks (e.g. mastication, speech, and swallowing) with a specific motor control strategy. These strategies differ per person. Moreover, muscular compensatory mechanisms might be used after impairment.

Forward modelling is a prerequisite for prediction of functional consequences after surgery using biomechanical models. When a tumour is virtually resected in a model, forward modelling may give insight in residual movement when controlling the adapted model with the patient's muscle activation strategies, whereas inverse modelling (calculating the required muscle activation patterns from known movement) may give insight in compensatory possibilities. This residual movement can then be addressed by the multidisciplinary medical team, and function loss may be estimated.

Modelling of the perioral region is of interest because it is easily accessible and can serve as a proof of principle for more complex organs like the tongue. Besides, surgery of the lips could lead to both cosmetic and function deficits. Lip cancers are surgically treated by wedge excision and primary closure with consequences for pursing the lips and opening the mouth. Larger defects require reconstruction with local or free flaps. In those last cases, function preservation is even more at stake.

The obtained information on function loss with the use of our future models may deliver patient and physician an overview of the possible cosmetic and function deficits of the different treatment options, both surgical and nonsurgical curative alternatives such as radiotherapy or photodynamic therapy. This also increases the quality of patient counselling. In other words, it makes objective and more informed choices in treatment options possible.

Biomechanical models have been created for many parts of the human body: upper and lower limb, shoulder, elbow, and wrist (see Erdemir et al. for an overview [12]). These models are commonly used for calculating forces on regions of interest. The models are controlled by muscle activation patterns, which can also be derived from electromyographic (EMG) signals. Research in EMG-controlled biomechanical models of the perioral region is still a subject of ongoing research [13–18]. Lucero and Munhall used intramuscular EMG as input for standard Hill-type muscles in their biomechanical face model with a multilayer deformable mesh [18]. Although reasonably good correlation coefficients were obtained between the model's movement and measured movement in general, markers around the lips performed poor in anterior-posterior direction. Flynn et al. developed a model of the face with a complex anisotropic multilayer skin with in vivo tension [17]. They, and others, tested their model by manually activating facial muscles to obtain simulated facial expressions [13,19,20].

Before embarking on complex personalised biomechanical models including the patient's as well as the tumour's geometry and anatomy, we investigated in this study whether we could supply such models with patient-specific motor control by means of sEMG measurements.

In previous research we demonstrated that noninvasive surface EMG (sEMG) conveys sufficient information to predict static facial expressions and volunteer-specific lip motion [21,22]. However, these statistical models lack the physiological relationship required to predict surgical outcomes. Therefore, we aim to demonstrate that a biomechanical 3D lip model can be controlled by muscle activation patterns derived from volunteer-specific sEMG signals of facial muscles to simulate facial expressions.

These principles will be applicable in our future projects in which we will add a virtual surgery tool and in which we plan to take the step towards intraoral sEMG measurements of the tongue muscles to make tongue models more patient specific. The results demonstrated in this study may not only be of interest in speech research or in facial animation but also in biomechanics research with an important prelude for our virtual surgery models. Demonstrating the feasibility of driving biomechanical face models via individual sEMG measurements is important because it forms the basis for affected function by patient-specific motor control. When a virtual surgery tool or radiotherapy tool becomes available, it will show the movement in the affected situation based on personalised innervation signals.

5.2. Methods

5.2.1. Volunteers and data acquisition

For detailed information regarding the data acquisition, we refer to Eskes et al. (Chapter 4) [22]. Here follows a summary: six healthy volunteers participated, three males and three females, ages ranging from 21 to 30. We measured sEMG signals (s_m, signal per muscle channel m) with the TMSi® Porti™ system (TMSi®, Oldenzaal, the Netherlands) of seven facial muscles bilaterally (see Figure 5.1). A common ground self-adhesive reference electrode was placed on the left wrist. Six optical face markers – for head orientation – and ten optical lip markers – to follow lip movement – were drawn using a skin marker (Figure 5.1) and tracked at 100 frames per second with our triple-camera set-up [22,23]. The Medical Research Ethics Committee of the Netherlands Cancer Institute approved this study, and the volunteers gave their informed consent.

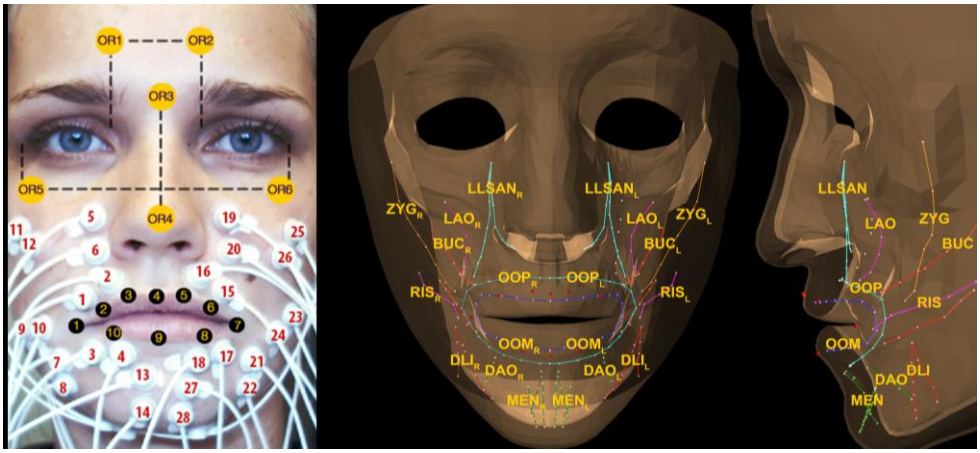

Figure 5.1 Left: Surface electrode locations, orientation markers, and lip markers. Right: Anterior-posterior view and lateral view of the model and the model's muscle bundles and lip markers. The muscles are abbreviated as follows: zygomaticus major (ZYG), risorius (RIS), levator labii superioris alaeque nasi (LLSAN), levator anguli oris (LAO), buccinator (BUC), orbicularis oris peripheralis (OOP) and marginalis (OOM), depressor labii inferior (DLI), depressor anguli oris (DAO), and mentalis (MEN), subscript L for ten left-sided muscles and subscript R for ten right-sided muscles.

5.2.2. Instructions to volunteers

Volunteers performed four facial expressions to maximise independent muscle contraction of the recorded muscles: A. purse lips, B. raise upper lip, C. depress mouth corners, and D. voluntary smile, an asymmetric motion: E. left-right-left with closed lips, and a combination of two expressions: F. purse lips and closed mouth smile (Figure 5.2). These facial expressions were based on the work of Lapatki et al. and Schumann et al. [24,25]. At the start of the experiment the instructions were shown to the volunteer in combination with a live demonstration by the experimenter. Oral feedback on the volunteer's performance was given, while he or she was repeating the instructions four times with two seconds rest in between.

Figure 5.2 Instructions to volunteers: A. purse lips, B. raise upper lip, C. depress mouth corners, D. voluntary smile, E. left-right-left with closed mouth, F. purse lips-closed mouth smile-purse lips.

5.2.3. Finite element face model

We used the reference finite element face model in ArtiSynth that was originally developed with ANSYS® software at the ICP/GIPSA and TIMC-IMAG laboratories in Grenoble [15,16,26–28]. It is described in detail in Nazari et al. [14]. The most important details are as follows. The soft tissues of the face are represented by three layers of elements and includes 6,342 elements (6,024 linear hexahedral and 318 linear wedge) and 8,720 nodes. The epidermis and dermis are contained in the outer layer of about 1.5 mm thick. The hypodermis comprises the inner and centre layers that vary between 4 and 11 mm in thickness. All layers were given the same passive tissue properties, including tissue density of $1{,}040\ \mathrm{kg/m^3}$, and material stiffness specified as a Mooney – Rivlin constitutive equation given by:

$$W = C_{10}(\tilde{I}_1 - 3) + C_{20}(\tilde{I}_1 - 3)^2 + \frac{\kappa}{2}(\ln J)^2 \tag{5.1}$$

where W is the stress energy, and $C_{10} = 2.5\ \mathrm{kPa}$, $C_{20} = 1.175\ \mathrm{kPa}$, and $\kappa = 25\ \mathrm{kPa}$ are the material parameters. The left Cauchy – Green tensor: $\tilde{\mathbf{B}} = \tilde{\mathbf{F}}\tilde{\mathbf{F}}^T$ is used to calculate $\tilde{I}_1 = \mathrm{trace}(\tilde{\mathbf{B}})$, and $J = \det(\mathbf{F})$. The distortional part of the deformation gradient $\mathbf{F}$ is described by $\tilde{\mathbf{F}} = j^{-1/3}\mathbf{F}$.

The facial muscles were represented by muscle fibres within the finite element mesh, and they are organised into 20 muscle groups (Figure 5.1). During simulations finite element muscles were used in which the elements surrounding the fibres were assigned as muscle

elements with transversely isotropic material properties described by Blemker et al. [29]. Elements that were within a radius of 5 mm of the muscle fibres were considered a muscle element. In the case of the orbicularis oris peripheralis (OOP) and marginalis (OOM) muscle elements were manually assigned.

Common muscle model parameters were used across volunteers. They are based on values from the literature [17]: maximum stretch $\lambda^* = 1.4$, where the force-stretch relationship becomes linear, exponential stress coefficient $P_1 = 0.05$, and uncrimping factor $P_2 = 6.6$. The maximum stress of the muscle elements σ_{max}, as exception, was optimised per volunteer by decreasing the maximum stress with 10 % each time inverted elements occurred, starting at 300 kPa.

The mandible and maxilla underlying the face tissue model were represented as rigid bodies. Gravity acted on the model with acceleration set to -9.8 m/s² in vertical direction.

5.2.4. Boundary conditions, collision behaviour, and incompressibility

Nodes on the inner surface of the finite element face model were attached to the underlying mandible and maxilla (similar to the attachments shown in Stavness et al. Figure 3 [28]). The nodes of the centre and the outer layer were dynamic. Contact of elements, which is especially important when pressing the lips together, is handled with the mesh-based collision behaviour in ArtiSynth. Interpenetration of the upper and lower lip surfaces is detected; node penetrations are corrected with impulse-based contact constraints [30]. The friction coefficient for contacts was set to zero. Instead of constraint-based soft tissue incompressibility, we used nodal soft incompressibility with a quadratic bulk potential and a bulk modulus of 25 kPa. Soft incompressibility tries to ensure that the volume of the finite element model remains locally constant by generating a restoring pressure based on a potential field.

5.2.5. sEMG to normalised model activations

sEMG measures the total contribution from motor units beneath the electrodes as well as contributions from neighbouring motor units. sEMG is, by its nature, indiscriminate, and therefore crosstalk is inevitable. Moreover, in the complex face region muscles overlap and intertwine. A monopolar measurement configuration is more prone to crosstalk as it measures the deeper and surrounding muscle signals, whereas in a bipolar configuration, the acquisition depth and pickup of crosstalk depend on the interelectrode distance. Therefore, we recorded sEMG signals in bipolar configuration with a sample frequency of 2048 Hz. A fourth-order Butterworth bandpass filter with a high- and low-pass cut-off frequency of 15 and 500 Hz was used to filter the recorded sEMG signals, as recommended by Van Boxtel [31]. The placement of our microelectrodes was done by considering the generic facial muscle anatomy and the optimal placement as described by Lapatki et al. [32]. A limiting factor was the face dimension of the volunteers and the corresponding availability of skin to place the electrodes, which was usually directly adjacent to each other (Figure 5.1). Occasionally, no signal was sensed because of the tiny surface of the electrodes and the small surface of the underlying muscle belly. This occurred mainly when acquiring signals of the risorius muscle.

In these cases, replacements of the microelectrode over 1-2 mm yielded good signal-to-noise ratios. Thus, a ruler-based placement strategy appeared to be impractical.

To generate input for the activation patterns of the ArtiSynth model, a transformation function was required that converted the sEMG signals from our seven bilaterally measured muscles into usable activations for ten bilateral muscles of the model. The design of this transformation was based on the study of Schumann et al. describing monopolar sEMG profiles of 30 healthy males for various instructions and on the activation patterns described by Flynn et al. [17,25].

The measured muscles are: the orbicularis oris superior (OOS, electrodes 1, 2, 15, 16), the orbicularis oris inferior (OOI, electrodes 3, 4, 17, 18), the risorius (RIS, electrodes 9, 10, 23, 24), the zygomaticus major (ZYG, electrodes 11, 12, 25, 26), the levator labii superioris alaeque nasi (LLSAN, electrodes 5 , 6, 19, 20), the depressor anguli oris (DAO electrodes 7, 8, 21, 22), and the mentalis (MEN, electrodes 13, 14, 27, 28). The missing muscle activations were determined as follows:

$$s_{OOP} = 0.50\,(s_{OOS} + s_{OOI}) \tag{5.2}$$

$$s_{OOM} = 0.10\,(s_{OOP} + s_{OOI}) \tag{5.3}$$

$$s_{BUC} = 0.50\,(s_{RIS} + s_{ZYG}) \tag{5.4}$$

$$s_{LAO} = 0.75\,s_{LSSAN} \tag{5.5}$$

$$s_{DLI} = 0.75\,s_{DAO} \tag{5.6}$$

In the ArtiSynth model, the orbicularis oris muscles are defined as peripheralis (OOP) and marginalis (OOM). Therefore, a combination of OOS and OOI was used for the OOP (equation (5.2)). Based on Flynn et al. [17], a fifth of the OOP was used for the OOM (equation (5.3)). The electrodes associated with the RIS were probably also influenced by the buccinator (BUC). Presumably, the electrodes of the ZYG were also influenced by the BUC. Therefore, we set BUC as a combination of ZYG and RIS activity (equation (5.4)). The levator anguli oris (LAO) is close to the LLSAN. Thus, the LAO was set to 75% of LLSAN (equation (5.5)). The depressor labii inferior (DLI) is adjacent to the DAO, which is why we chose 75% of the DAO as DLI activation (equation (5.6)). The MEN, ZYG, RIS, DAO, and LLSAN muscles were set to their corresponding measurements.

In previous research in which we used statistical models [21,22], the best performing sEMG feature extractor was Willison amplitude (WAMP) with a threshold $s_{\text{lim}} = 10$ mV and a sliding window of 200 ms with maximum overlap. In preliminary experiments for the current study we also tested the transfer function described by Buchanan et al. [33]. Eventually, the WAMP feature again proved to be best and therefore this feature was used for all the experiments described in this study. It can be calculated as follows for all sliding windows:

$$g_m(t,i,r) = \sum_{n=1}^{N-1}\left[f\left(\left|s_m(t+n-1) - s_m(t+n)\right|\right)\right] \tag{5.7}$$

$$\text{with} \quad f(s_m) = \begin{cases} 1 & \text{if} \quad s_m \geq s_{\text{lim}} \\ 0 & \text{otherwise} \end{cases} \qquad \begin{array}{l} i \text{ is instruction index} \\ r \text{ is repetition index} \end{array}$$

$s_m(t)$ is the measured sEMG of muscle m, and t is the time index. n is the running time index within each sliding window consisting of N samples. There were six instructions: $i = 1,\cdots,6$. Each instruction was repeated four times: $r = 1,\cdots,5$. As there are ten muscles on both sides of the face, the muscle index runs from 1 to 10 (left) and 11 to 20 (right).

We tested three different activation strategies:

- act_{all} : all the muscles in the model are activated.
- act_3 : only the three muscles that were most active measured bilaterally according to:

  1. Muscle feature, averaged bilaterally: $\bar{g}_m(t,i,r) = \frac{1}{2}(g_m(t,i,r) + g_{m+10}(t,i,r))$
  2. Variance: $V_m(i,r) = \text{Var}\left[\bar{g}_m(t,i,r)\right]$
  3. Sort: for each i,r: determine m_j such that $V_{m_j}(i,r) \geq V_{m_{j+1}}(i,r)$
  4. Select largest three: m_1, m_2, and m_3

- act_{rel} : the muscles that are considered most relevant for an instruction (Table 5.1).

Table 5.1 The muscles used with the relevant muscle strategy per instruction.

Instruction		Relevant muscles (act_{rel})
A.	**Purse lips**	OOP, OOM, BUC
B.	**Raise upper lip**	LLSAN
C.	**Depress mouth corners**	DAO, MEN
D.	**Voluntary smile**	LLSAN, RIS, ZYG, LAO, DAO, DLI
E.	**Left-right-left with closed mouth**	OOP, OOM, LLSAN, RIS, ZYG, LAO, BUC
F.	**Purse lips – closed mouth smile – purse lips**	OOP, OOM, LLSAN, RIS, ZYG, LAO, BUC

The model's activation range is from zero to one. Therefore, min-max normalisation was applied over the time index. It linearly transformed the data from original minimum and maximum to data between zero and one.

$$g_{norm,m}(t,i,r) = \frac{g_m(t,i,r) - \min\limits_t(g_m(t,i,r))}{\max\limits_t(g_m(t,i,r)) - \min\limits_t(g_m(t,i,r))} \tag{5.8}$$

5.2.6. Synchronisation of repetitions and model output

As volunteers performed the repetitions with different speed and because the model's output showed a different timing, a time shift and time scaling were performed. First, to create equally sized time series, we resampled the measurements (i.e. positions and features) in order to have them matched to the ArtiSynth sampling period. To synchronise the measurements, for each instruction and each repetition a principal component analysis (PCA) was applied to reduce the 30D space (ten 3D markers) to a 1D space. This was done both for the model-predicted positions and for the measured positions.

The PCA was implemented using singular value decomposition (SVD) of the $30\times T$ matrix $\mathbf{X}$ containing in each column the *X*-, *Y*-, and *Z*-coordinates of the 10 markers. The number T of columns equals the number of time samples. Application of SVD yields:

$$\mathbf{X} = \mathbf{U}\mathbf{\Sigma}\mathbf{V}^T \tag{5.9}$$

The matrix $\mathbf{U} \in \mathbb{R}^{30\times 30}$ contains the principal components. The squares σ_j^2 of the diagonal of the matrix $\mathbf{\Sigma}$ contain the variances of the principal components. These variances are sorted, $\sigma_j^2 \geq \sigma_{j+1}^2$. A coefficient vector $\mathbf{b} \in \mathbb{R}^{\mathrm{T}}$ was determined from the first principal component $\mathbf{u}_1 \in \mathbb{R}^{30}$ from $\mathbf{U}$:

$$\mathbf{b} = \mathbf{u}_1^T \mathbf{X} \tag{5.10}$$

We obtained $\mathbf{b}_{est}$ and $\mathbf{b}_{meas}$ the coefficient vectors for the model-predicted positions and the measured ones, respectively. The maximisation of the cross-correlation function $\rho(t)$ between $\mathbf{b}_{est}$ and $\mathbf{b}_{meas}$ gave the synchronisation difference at $\arg\max \rho(t)$. The procedure was repeated for each instruction and repetition. Figure 5.3 shows the synchronisation process of two repetitions of one volunteer. The optimal shifting determined in the PCA domain was applied on the resampled data.

5.2.7. Performance measures

Figure 5.5 and the online videos provide a qualitative visual impression. Quantitative performance measures are given by correlation coefficients for 3D quantities as provided by Pitermann and Munhall [34]:

$$\vec{\mu}_v = \left(\frac{1}{n}\sum_{i=1}^{n} x_i, \frac{1}{n}\sum_{i=1}^{n} y_i, \frac{1}{n}\sum_{i=1}^{n} z_i \right) \tag{5.11}$$

$$\sigma_v = \sqrt{\frac{1}{n-1}\sum_{i=1}^{n} \left\| \vec{v}_i - \vec{\mu}_v \right\|^2} \tag{5.12}$$

$$\rho_{\vec{v}\vec{w}} = \frac{\frac{1}{n}\sum_{i=1}^{n} \vec{v}_i{}^T \vec{w}_i - \vec{\mu}_v{}^T \vec{\mu}_w}{\sigma_v \sigma_w} \tag{5.13}$$

Equation (5.11) gives the mean position $\vec{\mu}_v$ of a 3D landmark trajectory of samples $\vec{v}_i = (x_i, y_i, v_i)$. The standard deviation σ_v of the 3D node trajectory $\vec{v}_i$ is given by equation (5.12). $\rho_{\vec{v}\vec{w}}$ is the 3D correlation coefficient between 3D landmark trajectories $\vec{v}_i$ and $\vec{w}_i$, and is calculated with equation (5.13).

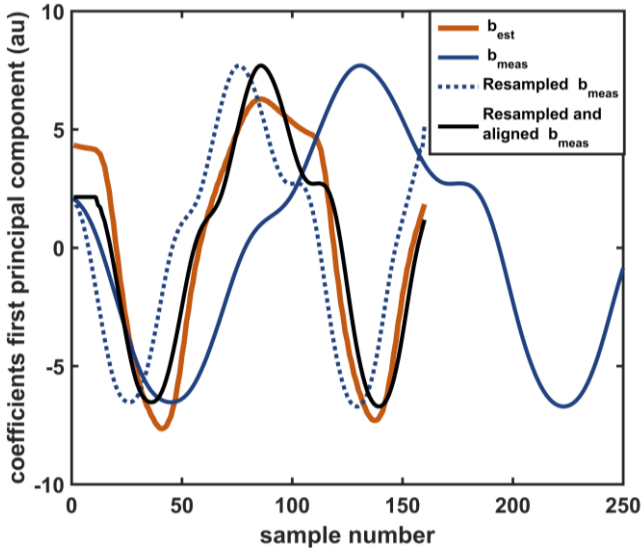

Figure 5.3 Synchronisation example. The first principal component coefficient vectors of the measurement $\mathbf{b}_{meas}$ and the model output $\mathbf{b}_{est}$ are shown. Together with the resampled coefficient vector, and the resampled and aligned coefficient vector.

5.3. Results

Fair performance for all activation strategies was seen in qualitative assessment (in Figure 5.5 visuals are given for volunteer 2). Comparable results were obtained in all datasets (online videos show the performance of all volunteers). Activating the relevant facial muscles gave visual results that best matched the intended instructions. In general, the amplitude of the model's movement was less than the volunteer's movement. The three highest activated muscles differed among volunteers and sometimes also within repetitive measurements within one volunteer. This can be derived from Figure 5.4 that gives the distribution of activation patterns of the symmetric instructions A – D. Instruction B (raise upper lip) showed the most selective contraction followed by instruction A (purse lips). Instruction C (depress mouth corners) showed a lot of cocontraction of the risorius muscle. Instruction D (voluntary smile) showed that indeed a lot of facial muscles come into play when producing voluntary smiles.

In all cases, at least one of the most important muscles (act_3) was also present in the relevant muscle strategy. Comparing the model's movements with those of the volunteers visually, the most difficult instruction was 'pursed lips to closed mouth smile to pursed lips' resulting in small displacements of the model. The easiest instruction was 'raise upper lip'. Selectively depressing the lip corners was difficult to perform for most volunteers inducing a lot of cocontraction in the perioral region.

Pursing the lips (A) with act_3 resulted in a small opening between the lips in all volunteers, whereas act_{all} only had a minuscule opening in volunteer 2 and volunteer 3. act_{rel} had no opening between the pursed lips.

Raising the upper lip (B) with act_{all} showed less pronounced results, but more compressed lips drawn upwards in volunteers 2, 4, and 5.

Depressing the mouth corners (C) was difficult for the volunteers, but also to simulate with the model. Only act_{rel} gave visual satisfying results. act_3 had fair results in volunteers 2, 3, 5, and 6, though with an opening between the lips.

Voluntary smile (D) showing an open mouth smile was only possible with act_{rel}, while act_{all} and act_3 resulted in closed mouth smiles except in volunteer 4 which had a modest open smile with act_3.

The instruction left-right-left with closed lips (E) in general showed modest displacements, but recognisable instructions with all activation strategies.

The instruction purse lips-closed mouth smile-purse lips (F) with act_{all} showed a small opening during closed mouth smile in volunteers 2, 4, 5, and 6, while in all volunteers act_3 induced a small opening between the pursed lips in the model.

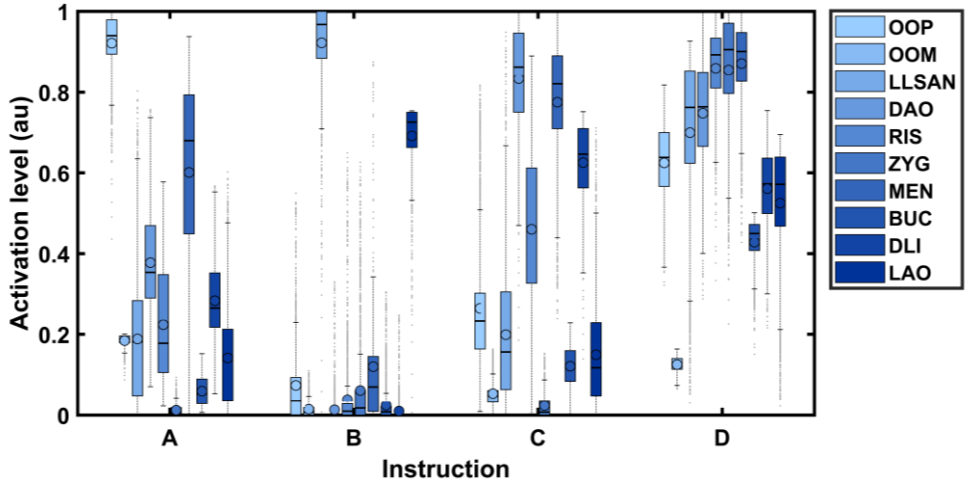

Figure 5.4 Boxplot of normalised sEMG features per instruction and per muscle including data of all volunteers and repetitions. High standard deviations indicate the volunteer-specific differences in activation strategies. The median is shown with a horizontal line and the mean with a dot. The median is shown with a horizontal line and the mean with a dot. The boxes give first to third quartiles and the outer horizontal lines reflect minimum and maximum values. ('au' is for 'arbitrary units').

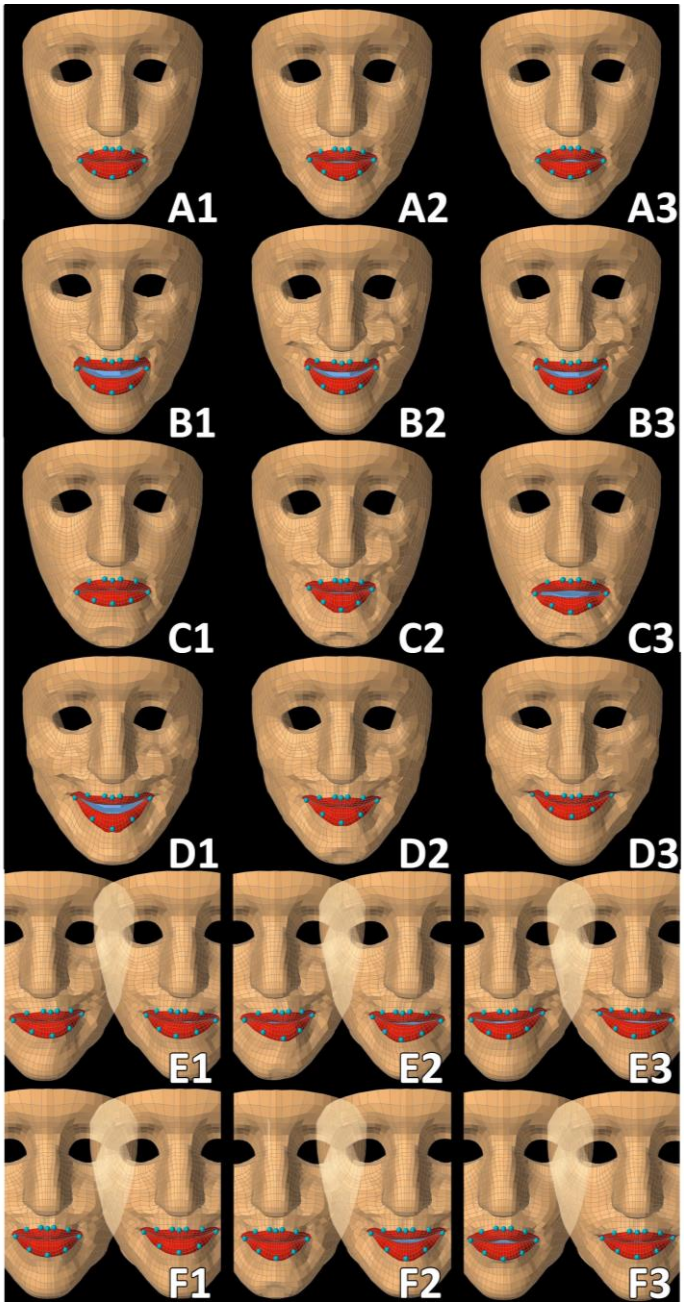

Figure 5.5
Qualitative simulation results for volunteer 2. The different instructions are represented by the capitals:
A. purse lips,
B. raise upper lip,
C. depress mouth corners,
D. voluntary smile,
E. left-right-left with closed lips (left-right is shown),
F. purse lips-closed mouth smile-purse lips (purse lips-closed mouth smile is shown).
The three different activating strategies are given by the numbers:
1. act_{rel} ,
2. act_{all} ,
3. act_3 .
The ten cyan dots on the model's lips are the nodes that are being compared to the volunteers' tracked lip markers as shown in Figure 5.1.
For performance of all volunteers, scan the QR-code to go to the online videos.

The boxplots in Figure 5.6 show the distribution of correlation coefficients between volunteers, instructions, and markers. Here, we have the following observations:

The performance between volunteers differed, especially using act_{all}. act_3 and act_{rel} had similar results.

Although visually assessed instruction B was best executed by the volunteers, the corresponding correlation coefficients were not maximal. Instead, instructions E and F showed the best correlations. Again, act_{all} performed worst and act_3 and act_{rel} had similar results except for instruction C.

The distribution of correlation coefficients between markers had a clear pattern: lateral markers showed higher correlations than centre markers, and upper lip markers had better results than lower lip markers in general. The overall mean values were: $\bar{\rho}_{act_{all}} = 0.26$, $\bar{\rho}_{act_3} = 0.55$, $\bar{\rho}_{act_{rel}} = 0.53$, with overall standard deviations: $\sigma_{act_{all}} = 0.63$, $\sigma_{act_3} = 0.51$, and $\sigma_{act_{rel}} = 0.52$, respectively. The medians were: $\rho^{median}_{act_{all}} = 0.45$, $\rho^{median}_{act_3} = 0.78$, and $\rho^{median}_{act_{rel}} = 0.77$.

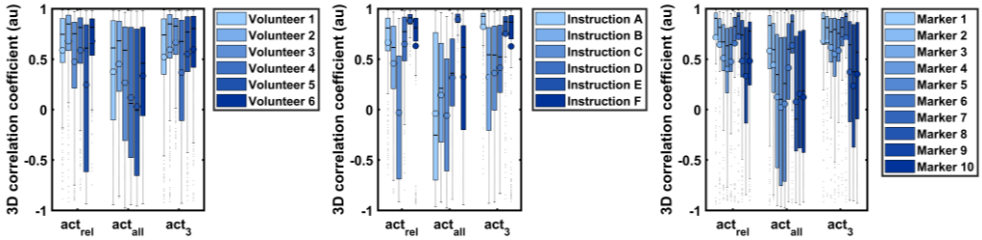

Figure 5.6 Boxplots of correlation coefficients per volunteer, per instruction, and per marker for the three activation strategies.

5.4. Discussion

To our knowledge, this is the first study demonstrating that volunteer-specific activation patterns calculated from sEMG measurements can be used to control a generic biomechanical model to generate asymmetric facial expressions with qualitative fair results. When visually assessed, the performance looked best when only the subset act_{rel} of all muscles was activated. These muscles were assumed to be most relevant for the specific instruction. Visual performance seemed to be less when activating all muscles act_{all}, which should be the ideal situation containing all measured information. This loss of generality can be caused by different limitations of the method: (a) occurrence of cocontraction of pairs of muscles, (b) crosstalk in the sEMG signals, (c) shortcomings in the transfer function from sEMG feature to activation signal, and (d) shortcomings in the biomechanical model, e.g. deviations from its optimal parameter setting, and deviation from the geometry.

The quantitative results: the correlation coefficients, showed a large standard deviation also caused by the limitations as mentioned above. Predicted mobility of the 3D lip markers was less than measured in volunteers.

This can be explained by inaccuracies in the tissue parameters (e.g. soft versus stiff skin parameters) and the resolution of the finite element model. Increasing the temporal step size and the number of elements will probably improve the accuracy. Improving the stability of the model for large deformations (possibly through model remeshing) is also essential. Lip shapes and thus the corresponding lip markers differed in volunteers. Subsequently, they did not match the generic face model's geometry completely. This inaccuracy contributes to the mediocre values and high standard deviation of the correlation coefficients. Besides, instead of using an isotropic skin – all three layers had the same tissue parameters – a more sophisticated approach might be superior. This might be accomplished by giving each layer, or even regions within layers, specific material properties. This anisotropic skin model was first demonstrated by Flynn et al. [17].

The sEMG to muscle activation and finally muscle contraction is governed by a complex process. During recordings crosstalk is inevitable. A solution could be the use of the crosstalk equation of Lapatki et al. to determine whether an electrode is flooded with neighbouring signals [35]. Crosstalk of adjacent muscles can explain why the model activated the OOP and OOM in all instructions. OOS and OOI electrodes 1, 2, 3, 4, 15, 16, 17, and 18, used to calculate OOP and OOM, could measure activity from e.g. MEN, DAO, and LLSAN during those specific instructions. This results in OOP and OOM activity in the model. Intramuscular or needle EMG electrodes are more selective and are able to measure contributions of the single muscle, with less crosstalk and reducing false input activity. However, we feel that a patient-friendly method and a less time-consuming method is preferred. Especially when aiming at future preoperative modelling of patients to predict functional postoperative risk. sEMG crosstalk problems might further be minimised by using high-density sEMG (HD-sEMG) [35]. Another point of attention is the arbitrary composition of the BUC, the DLI, and the LAO, out of neighbouring muscles. This induces an additional error. A future increase of bipolar or HD-sEMG measurements should compensate for this problem too.

Also, the muscle models may be improved. Instead of spherical muscles containing the surrounding elements within a radius of 5 mm of the muscle fibre, this radius can be optimised per muscle. Possibly by obtaining literature values or using patient-specific sizes to be determined in MRI scans of the patient, furthermore, one can manually assign elements or even improve the muscle representation using more than one muscle fibre, as was done by Wu et al. [20]. Another activation strategy option instead of act_3 is to determine the muscle channels showing activity that exceeds a certain threshold. The choice of three recruited muscles is arbitrarily, and the number of active muscles definitively differs per instruction and per person.

This is demonstrated in the high standard deviations in the sEMG results of our experiments (Figure 5.4) as well as the performance of act_{rel} versus act_3 (Figure 5.6).

Although trivial we showed that asymmetric movement is possible in our modelling experiments, in contrast to previous research [18], creating unique opportunities for visualising possible consequences of surgery with a 3D render of the patient to get objective patient-specific information. This is particularly important as people never perform perfect symmetric movements, as is described by Campbell [36].

Many articles address the issue of facial surgery planning with a common goal of predicting aesthetics after facial surgery [5,7,37,38]. Typically, surgical alteration (resection or replacement) of the bony structures underlying the face is applied to a virtual model and the resulting passive effects on soft tissues are then simulated. These principles of surgical alteration in static and dynamic situation and of rigid structures are important and will be addressed in our future models. A virtual surgery tool that can be used to simulate tumour resection in soft tissues is currently being developed in our institute. The tumour will be extracted from segmented MRI data before insertion into the model. Thereafter, the surgeon is able to perform a virtual resection of lip cancer followed by simulation of wound closure. The patient-specific sEMG measurements can then be used to control the adapted model to show residual movement after treatment, which is an essential part of the personalisation of the model. The promising results of our sEMG experiments are an important step in this process. We will first focus on the prediction of dynamic functions which are established by movement. Therefore, incorporating motor control strategies into the model as well as methods to assess motor control is essential. This is why we investigated the use of sEMG.

The results we created with forward dynamics took about five seconds per time step; each instruction was normalised to 160 time steps resulting in 800 s (13 min and 20 s) on a workstation with an Intel Xeon processor (3.40 Ghz). Guidelines in head and neck cancer care suggest 30 days from diagnosis to treatment [39]. Considering this time frame and the possibility of 24/7 runs of the analyses, we think the approach is definitively feasible within the given time. Even with the current set-up and without optimisation the analysis can be performed within the waiting time to treatment.

In the current workflow (Figure 5.7), a patient is diagnosed and undergoes all kinds of scans and tests (imaging and histology). The case is presented to the multidisciplinary team to agree upon treatment. The proposed treatment plan is then explained to the patient. If the patient agrees, treatment is started.

In the future workflow (Figure 5.7), after patient diagnosis and the standard imaging are performed several additional tests are done to obtain information on the specific patient. With all these data, a patient-specific model is built. Specific treatment modalities are tested, and the functional outcome (swallowing, speech, aesthetics, etc.) is simulated.

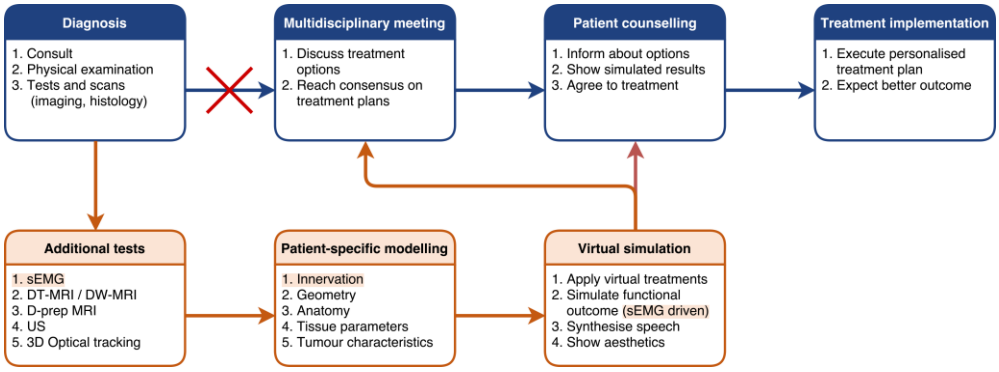

Figure 5.7 The top blue flow chart resembles the current workflow in clinical practice. The bottom orange flow chart shows the additional steps implementing virtual therapy to personalise and optimise the treatment per patient. The orange accentuated text shows the importance of the current study.

The patient is again discussed at the multidisciplinary team meeting using the patient-specific modelling and simulations as objective aid. Next, the patient is informed about various treatment options considering survival, appearance, and functional outcome.

These outcomes are made visible to the patient, who is also able to hear the post-treatment voice, if relevant. Together with the treating physician the patient decides which treatment is best suited for his/her expectations.

Our future experiments can be improved by using volunteer-specific biomechanical models. Recently, Bucki et al. have described a method to adapt a model to volunteer-specific anatomy using personal imaging data and a Mesh-Match-and-Repair algorithm [40], while earlier Chabanas proposed a mesh correction algorithm after a mesh-matching procedure [11]. Additionally, we set the friction coefficient to zero as was done in previous models [14]. However, there is usually some amount of friction between the lips despite saliva, etc. Hence, this is probably not the best option. Future studies on simulation of facial expressions or bilabial and plosive speech articulations may benefit inclusion of a nonzero friction coefficient, though it should be investigated what the optimal value should be.

Patient-specific anatomy of in vivo muscle bundles may be extracted using diffusion tensor magnetic resonance imaging (DT-MRI), as suggested by Wu et al. [13]. Also, appropriate selection of most relevant personal parameters for inclusion in the model's elements could be optimised per volunteer, such as tissue stiffness (which also depends on age), and muscle properties such as shortening.

Future experiments should also focus on inverse modelling. A known issue in biomechanical modelling is the ambiguity problem when sharing forces among a redundant set of muscles. In the case of multiple inverse solutions for the same motions, the resulting solution is based on mathematical properties instead of patient-specific factors. Using inverse modelling the required muscle activation patterns are calculated based on measured movement. It might be expected that incorporation of sEMG signals in the cost term, used to solve the inverse algorithm, contributes to the solution of the ambiguity problem [41]. Inverse modelling is also essential if one wants to incorporate compensatory muscle activity, which is important for the final functional result after surgery, and thus of importance in virtual therapy.

Other challenges concern preventive and rehabilitation exercises. Kraaijenga et al. showed that senior healthy subjects are able to significantly increase swallowing muscle strength and muscle volume after a six-week training period [42]. Van der Molen et al. demonstrated beneficial effect of preventive swallowing exercises in patients undergoing chemoradiotherapy for advanced head and neck cancer [43]. Given these facts, preventive and rehabilitation therapies can influence the functional outcome and thus the prediction of functional outcome. In the future, we hope to add decision support to point out the patients that benefit from pre- and postoperative speech, swallowing or other physical therapies. Besides, a virtual surgery tool and other treatment tools like radiotherapy should be implemented by utilising radiotherapy planning fields to determine which anatomical structures will be affected and to what extent.

To conclude, the use of sEMG opens new ways for patient-specific facial modelling, finally, enabling us to predict the functional and cosmetic outcome after surgery. We applied a novel method to register two time sequences of vectors using the first principal components of these two vectors. Our experiments serve as a proof of principle for other opportunities as modelling of the oral cavity and tongue to predict function deficits after oral surgery, e.g. partial glossectomy, considering personalised muscle activation patterns. Although the extraction of muscle activation signals from tongue muscles is challenging, the epidermal electrodes described by Kim et al. could be a promising option [44].

5.5. Conclusion

Simulation of facial expressions using a biomechanical face model controlled by muscle activation signals estimated from volunteer-specific sEMG signals of facial muscles is feasible and may be useful for simulating function losses in the individual patient. Further experiments should focus on personalising the anatomical geometry of the model using MRI, CT, and DT-MRI, and development of methods to minimise crosstalk between neighbouring muscles using HD-sEMG and advanced data processing techniques. Finally, these models can be expanded to other subsites of the head and neck like tongue, oropharynx, and larynx, while incorporating a virtual surgery tool and other treatments like photodynamic therapy, radiotherapy, and preventive and rehabilitation exercises.

5.6. Acknowledgements

The authors gratefully acknowledge all technical medicine students for their good contributions (www.virtualtherapy.nl/publications). They also thank all volunteers for participating in this study. We thank John Lloyd, Sidney Fels, and the ArtiSynth team for providing the simulation platform for this work www.artisynth.org). In particular, the authors would like to express their gratitude to the Maurits en Anna de Kock foundation (www.mauritsenannadekockstichting.nl) for funding the triple-camera set-up and the Porti EMG system. Lastly, we thank the reviewers for their constructive feedback that helped us to significantly improve the manuscript.

5.7. Conflict of interest

The authors declare that they have no conflict of interest.

5.8. Funding

No funding was acquired for this research.

5.9. Ethical approval

All volunteers were informed about the experiment and about their rights. Written consent was obtained for publishing the photographs in Figure 5.1 and Figure 5.2. The Medical Research Ethics Committee (MREC) of the Netherlands Cancer Institute determined that the study did not fall under the scope of the Medical Research Involving Human Subjects Act (WMO), because the study did not infringe the (psychological) integrity of the volunteers. The measurements were noninvasive and not stressful. Thus, prior review by an accredited MREC was not required. The study was performed within the Dutch legislation regarding the Agreement on Medical Treatment Act, Personal Data Protection Act, and the Code of Conduct for Responsible Use of the Federa (Dutch Federation of Biomedical Scientific Societies).

5.10. References

1. Kreeft A, Tan IB, van den Brekel MWM, Hilgers FJ, Balm AJM. The surgical dilemma of "functional inoperability" in oral and oropharyngeal cancer: current consensus on operability with regard to functional results. Clin Otolaryngol. 2009;34: 140–6. doi:10.1111/j.1749-4486.2009.01884.x

2. Kreeft AM, Tan IB, Leemans CR, Balm AJM. The surgical dilemma in advanced oral and oropharyngeal cancer: how we do it. Clin Otolaryngol. 2011;36: 260–266. doi:10.1111/j.1749-4486.2011.02299.x

3. Gladilin E, Zachow S, Deuflhard P, Hege HC. Anatomy- and physics-based facial animation for craniofacial surgery simulations. Med Biol Eng Comput. 2004;42: 167–170. doi:10.1007/BF02344627

4. Gladilin E, Zachow S, Deuflhard P, Hege H. Towards a Realistic Simulation of Individual Facial Mimics. In: Thomas E, Bernd G, Heinrich N, Hans-Peter S, editors. Proceedings of the Vision Modeling and Visualization Conference 2001 (VMW '01). 2001. pp. 129–134.

5. Koch RM, Roth SHM, Gross MH, Zimmermann AP, Sailer HF. A framework for facial surgery simulation. Proceedings of the 18th spring conference on Computer graphics - SCCG '02. 2002. p. 33. doi:10.1145/584458.584464

6. Koch RM, Gross MH, Bosshard AA. Emotion Editing using Finite Elements. Comput Graph Forum. 1998;17: 295–302. doi:10.1111/1467-8659.00276

7. Chabanas M, Payan Y. Finite element model of the face soft tissue for computer-assisted maxillofacial surgery. Proceedings of the Fifth International Symposium on Computer Methods in Biomechanics and Biomedical Engineering (CMBBE 2001). 2001. pp. 1–6. Available: http://membres-timc.imag.fr/Yohan.Payan/papers/BBE01_Chabanas.pdf

8. van Alphen MJA, Kreeft AM, van der Heijden F, Smeele LE, Balm AJM. Towards virtual surgery in oral cancer to predict postoperative oral functions preoperatively. Br J Oral Maxillofac Surg. 2013;51: 747–751. doi:10.1016/j.bjoms.2013.06.012

9. Buchaillard S, Brix M, Perrier P, Payan Y. Simulations of the consequences of tongue surgery on tongue mobility: implications for speech production in post-surgery conditions. Int J Med Robot Comput Assist Surg. 2007;3: 252–261. doi:10.1002/rcs.142

10. Ho AK, Tsou L, Green S, Fels S. A 3D swallowing simulation using smoothed particle hydrodynamics. Comput Methods Biomech Biomed Eng Imaging Vis. 2014;2: 237–244. doi:10.1080/21681163.2013.862862

11. Chabanas M, Luboz V, Payan Y. Patient specific finite element model of the face soft tissues for computer-assisted maxillofacial surgery. Med Image Anal. 2003;7: 131–151. doi:10.1016/S1361-8415(02)00108-1

12. Erdemir A, Mclean S, Herzog W, van den Bogert AJ. Model-Based Estimation of Muscle Forces Exerted During Movements. Clin Biomech. 2007;22: 131–154 . doi:10.1016/j.clinbiomech.2006.09.005

13. Wu T, Hung AP-L, Hunter P, Mithraratne K. Modelling facial expressions: A framework for simulating nonlinear soft tissue deformations using embedded 3D muscles. Finite Elem Anal Des. 2013;76: 63–70. doi:10.1016/j.finel.2013.08.002

14. Nazari MA, Perrier P, Chabanas M, Payan Y. Simulation of dynamic orofacial movements using a constitutive law varying with muscle activation. Comput Methods Biomech Biomed Engin. 2010;13: 469–482. doi:10.1080/10255840903505147

15. Groleau J, Chabanas M, Marécaux C, Payrard N, Segaud B, Rochette M, Perrier P, Payan Y. A biomechanical model of the face including muscles for the prediction of deformations during speech production. In: Manfredi C, editor. 5th International Workshop on Models and Analysis of Vocal Emissions for Biomedical Applications, MAVEBA'2007. 2007. pp. 173–176. Available: http://www.fupress.com/catalogo/models-and-analysis-of-vocal-emissions-for-biomedical-applications-5th-international-workshop-december-13-15-2007-firenze-italy/1005

16. Nazari MA, Payan Y, Perrier P, Chabanas M, Lobos C. A Continuous Biomechanical Model of the Face : A Study of Muscle Coordination for Speech Lip Gestures. In: Sock R, Fuchs S, Laprie Y, editors. 8th International Seminar on Speech Production. 2008. pp. 321–324. Available : http://issp2008.loria.fr/proceedings.html

17. Flynn C, Stavness I, Lloyd J, Fels S. A finite element model of the face including an orthotropic skin model under in vivo tension. Comput Methods Biomech Biomed Engin. 2015;18: 571–582. doi:10.1080/10255842.2013.820720

18. Lucero JC, Munhall KG. A model of facial biomechanics for speech production. J Acoust Soc Am. 1999;106: 2834–2842. doi:10.1121/1.428108

19. Wu T, Martens H, Hunter P, Mithraratne K. Estimating muscle activation patterns using a surrogate model of facial biomechanics. 2013 35th Annual International Conference of the IEEE Engineering in Medicine and Biology Society (EMBC). 2013. pp. 7172–7175. doi:10.1109/EMBC.2013.6611212

20. Wu T, Hung A, Mithraratne K. Generating facial expressions using an anatomically accurate biomechanical model. IEEE Trans Vis Comput Graph. 2014;20: 1519–1529 . doi:10.1109/TVCG.2014.2339835.1

21. Eskes M, van Alphen MJA, Balm AJM, Smeele LE, Brandsma D, van der Heijden F. Predicting 3D lip shapes using facial surface EMG. Zhang Y, editor. PLoS One. 2017;12: e0175025 . doi:10.1371/journal.pone.0175025

22. Eskes M, van Alphen MJA, Smeele LE, Brandsma D, Balm AJM, van der Heijden F. Predicting 3D lip movement using facial sEMG: a first step towards estimating functional and aesthetic outcome of oral cancer surgery. Med Biol Eng Comput. 2017;55: 573–583. doi:10.1007/s11517-016-1511-z

23. van Dijk S, van Alphen MJA, Jacobi I, Smeele LE, van der Heijden F, Balm AJM. A New Accurate 3D Measurement Tool to Assess the Range of Motion of the Tongue in Oral Cancer Patients: A Standardized Model. Dysphagia. 2016;31: 97–103. doi:10.1007/s00455-015-9665-7

24. Lapatki BG, Stegeman DF, Zwarts MJ. Selective contractions of individual facial muscle subcomponents monitored and trained with high-density surface EMG. In: Beurskens CHG, van Gelder RS, Heymans PG, Manni JJ, Nicolai JA, editors. The Facial Palsies Complementary Approaches. 2005. pp. 89–108. doi:10.1007/s00238-008-0236-0

25. Schumann NP, Bongers K, Guntinas-Lichius O, Scholle HC. Facial muscle activation patterns in healthy male humans: A multi-channel surface EMG study. J Neurosci Methods. 2010;187: 120–128. doi:10.1016/j.jneumeth.2009.12.019

26. Lloyd JE, Stavness I, Fels S. ArtiSynth: A Fast Interactive Biomechanical Modeling Toolkit Combining Multibody and Finite Element Simulation. In: Payan Y, editor. Soft Tissue Biomechanical Modeling for Computer Assisted Surgery. 1st ed. 2012. pp. 355–394. doi:10.1007/8415_2012_126

27. Nazari MA, Perrier P, Chabanas M, Payan Y. Shaping by stiffening: a modeling study for lips. Motor Control. 2011;15: 141–168. Available: http://www.ncbi.nlm.nih.gov/pubmed/21339518

28. Stavness I, Nazari MA, Perrier P, Demolin D, Payan Y. A biomechanical modeling study of the effects of the orbicularis oris muscle and jaw posture on lip shape. J speech, Lang Hear Res. 2013;56: 878–890. doi:10.1044/1092-4388(2012/12-0200)

29. Blemker SS, Pinsky PM, Delp SL. A 3D model of muscle reveals the causes of nonuniform strains in the biceps brachii. J Biomech. 2005;38: 657–665. doi:10.1016/j.jbiomech.2004.04.009

30. Stavness I, Lloyd JE, Payan Y, Fels S. Coupled hard-soft tissue simulation with contact and constraints applied to jaw-tongue-hyoid dynamics. Int j numer method biomed eng. 2011;27: 367–390. doi:10.1002/cnm.1423

31. van Boxtel A. Optimal signal bandwidth for the recording of surface EMG activity of facial, jaw, oral, and neck muscles. Psychophysiology. 2001;38: 22–34. doi:10.1111/1469-8986.3810022

32. Lapatki BG, Oostenveld R, Van Dijk JP, Jonas IE, Zwarts MJ, Stegeman DF. Optimal placement of bipolar surface EMG electrodes in the face based on single motor unit analysis. Psychophysiology. 2010;47: 299–314. doi:10.1111/j.1469-8986.2009.00935.x

33. Buchanan TS, Lloyd DG, Manal K, Besier TF. Neuromusculoskeletal Modeling: Estimation of Muscle Forces and Joint Moments and Movements From Measurements of Neural Command. J Appl Biomech. 2004;20: 367–395. Available: https://www.ncbi.nlm.nih.gov/pmc/articles/PMC1357215/

34. Pitermann M, Munhall KG. An inverse dynamics approach to face animation. J Acoust Soc Am. 2001;110: 1570. doi:10.1121/1.1391240

35. Lapatki BG. The Facial Musculature: Characterisation at a Motor Unit Level. Radboud University Nijmegen. 2010.

36. Campbell R. Asymmetries in moving faces. Br J Psychol. 1982;73: 95–103. doi:10.1111/j.2044-8295.1982.tb01794.x

37. Koch RM, Gross MH, Carls FR, von Büren DF, Fankhauser G, Parish YIH. Simulating facial surgery using finite element models. Proceedings of the 23rd annual conference on Computer graphics and interactive techniques - SIGGRAPH '96. 1996. pp. 421–428. doi:10.1145/237170.237281

38. Sarti A, Gori R, Lamberti C. A physically based model to simulate maxillo-facial surgery from 3d ct images. J Futur Gener Comput Syst. 1999;15: 217–221.

39. van Harten MC, de Ridder M, Hamming-Vrieze O, Smeele LE, Balm AJM, van den Brekel MWM. The association of treatment delay and prognosis in head and neck squamous cell carcinoma (HNSCC) patients in a Dutch comprehensive cancer center. Oral Oncol. 2014;50: 282–290 . doi:10.1016/j.oraloncology.2013.12.018

40. Bucki M, Nazari MA, Payan Y. Finite element speaker-specific face model generation for the study of speech production. Comput Methods Biomech Biomed Engin. 2010;13: 459–67 . doi:10.1080/10255840903505139

41. Pizzolato C, Lloyd DG, Sartori M, Ceseracciu E, Besier TF, Fregly BJ, Reggiani M. CEINMS: A toolbox to investigate the influence of different neural control solutions on the prediction of muscle excitation and joint moments during dynamic motor tasks. J Biomech. 2015;48: 3929–3936 . doi:10.1016/j.jbiomech.2015.09.021

42. Kraaijenga SAC, van der Molen L, Stuiver MM, Teertstra HJ, Hilgers FJM, van den Brekel MWM. Effects of Strengthening Exercises on Swallowing Musculature and Function in Senior Healthy Subjects: a Prospective Effectiveness and Feasibility Study. Dysphagia. 2015;30: 392–403 . doi:10.1007/s00455-015-9611-8

43. van der Molen L, van Rossum MA, Rasch CRN, Smeele LE, Hilgers FJM. Two-year results of a prospective preventive swallowing rehabilitation trial in patients treated with chemoradiation for advanced head and neck cancer. Eur Arch Oto-Rhino-Laryngology. 2014;271: 1257–1270 . doi:10.1007/s00405-013-2640-8

44. Kim D-H et al. Epidermal electronics. Science. 2011;333: 838–843. doi:10.1126/science.1206157

VI

DATA AVAILABLE ONLINE
DOI: 10.17605/OSF.IO/G26KX

sEMG - ASSISTED INVERSE MODELLING OF 3D LIP MOVEMENT

This chapter was accepted for publication in Scientific Reports by Nature

ESKES M, BALM AJM, VAN ALPHEN MJA, SMEELE LE, STAVNESS I, VAN DER HEIJDEN F (2017)
sEMG-ASSISTED INVERSE MODELLING OF 3D LIP MOVEMENT:
A FEASIBILITY STUDY TOWARDS PERSON-SPECIFIC MODELLING
SCIENTIFIC REPORTS - NATURE

Abstract

Aim

We propose a surface-electromyographic (sEMG) assisted inverse-modelling (IM) approach for a biomechanical model of the face to obtain realistic person-specific muscle activations (MA) by tracking movements as well as innervation trajectories.

Materials and methods

We obtained sEMG data of facial muscles and 3D positions of lip markers in six volunteers and, using a generic finite-element (FE) face model in ArtiSynth, performed inverse static optimisation with and without sEMG tracking on both simulation data and experimental data.

Conclusions

IM with simulated data and experimental data without sEMG data showed good correlations of tracked positions (0.93 and 0.67) and poor correlations of MA (0.27 and 0.20). When utilising the sEMG-assisted IM approach, MA correlations increased drastically (0.83 and 0.59) without sacrificing performance in position correlations (0.92 and 0.70). RMS errors show similar trends with an error of 0.15 in MA and of 1.10 mm in position.

Therefore, we conclude that we were able to demonstrate the feasibility of an sEMG-assisted inverse modelling algorithm for the perioral region. This approach may help to solve the ambiguity problem in inverse modelling and may be useful, for instance, in future applications for preoperatively predicting treatment-related function loss.

6.1. Introduction

Biomechanical modelling aims to represent human body dynamics as accurately as possible with mathematical equations, simulating and evaluating human movement and motor control while estimating the resulting internal and external forces. This can be useful in preoperative decision making. For instance, in children with cerebral palsy, Lofterød et al. evaluated the effect of providing 3D gait analysis information on preoperative surgical planning, finding that in the majority of cases surgical planning had been modified to incorporate important gait analysis data [1].

Similar models are urgently needed in the field of Head and Neck Surgery, as well. Modelling of the perioral region may improve treatment and counselling of head and neck cancer patients, particularly by assessing functional inoperability, when surgical resection of a tumour will lead to unwanted severe loss of function [2], and other organ-sparing treatments should be considered instead, e.g. chemotherapy, radiotherapy, photodynamic therapy, or any combination thereof. Human estimation of post-surgical function loss is by nature subjective and unreliable [3]. Therefore, there is urgent clinical need for tools that can predict patient-specific function loss objectively and quantitatively [4–8]. Promising results have been obtained with patient-specific biomechanical models of the face [9–11], oral cavity [12,13] and tongue [4,14,15] , including models that can simulate pharyngeal bolus transport [13,16]. Adding patient-specific neural control to such models by means of surface EMG (sEMG)-assisted inverse dynamics will be an essential step forward, as this will provide insight into pathophysiological dynamics and potential compensatory mechanisms after virtual resection of specific muscles.

There are two main types of modelling dynamics in biomechanics. Forward modelling, or forward-dynamics simulation, is the process of controlling a biomechanical model with given (muscle) activation signals, calculating the resulting forces with the equations of motion to ultimately obtain the corresponding functional movement. Inverse modelling, or inverse-dynamics simulation, is the opposite process, estimating the underlying muscle activation signals from measured actual forces or movements by using a biomechanical model with a mathematical optimisation criterion.

Inverse problems in biomechanical modelling are often mathematically ill-posed because of muscle redundancy: similar functional movements can be performed by different sets of muscles. This so-called load-sharing problem [17,18] poses a significant challenge: to predict a patient's motor behaviour accurately, the simulations must "share" muscle activations in the same way the patient does.

Literature reports various strategies to tackle the load-sharing problem, but these generally apply to models of the arms or legs. A recent paper by Yamasaki et al. shows that higher-order derivatives in static optimisation and forward-inverse dynamics can improve the estimation of muscle activation in highly dynamic motions within a simple musculoskeletal model that includes a one-degree-of-freedom (1DOF) hinge joint [19]. Some authors enforced co-contraction of antagonistic muscles using 1DOF hinge joint

models [20–22] or multi-body models [23], while others used energy-based load-sharing cost terms [24,25]. Hybrid models have combined forward and inverse modelling by using algorithms that can derive neural activation strategy information from the muscle activation signals obtained with EMG. Such so-called EMG-assisted, EMG-informed, EMG-calibrated, or EMG-tracking algorithms were successfully applied in biomechanical models of the trunk [26–28], shoulder and arm [29], and legs [30,31]. Another feat has been the creation of a toolbox for calibrated EMG-informed neuro-musculoskeletal modelling (CEINMS)[32]. Reports on inverse modelling of the perioral region are scarce [33–35], and only few involve EMG measurements [36].

This paper aims to establish an sEMG-assisted inverse-modelling method that can be applied to 3D lip movements. We hypothesise that the addition of sEMG will allow for realistic inverse modelling solutions incorporating patient-specific activation strategies. If true, an sEMG-based model will be able to show the immediate functional outcome of surgery and also, if patients prove unable to relearn their functions, the final outcome. The proposed method is an adaptation of the so-called tracking-based inverse controller in ArtiSynth created by Stavness et al. [15]. This paper has been organised as follows. Section 2 summarises the static optimisation algorithm and introduces our adaptations. Section 3 describes the acquisition of experimental data and the pre-processing required. Section 4 reports on the use of these data in three experiments conducted to test the algorithm. Section 5 contains the discussion. The paper ends with our conclusion.

6.2. EMG-assisted static optimisation

Our EMG-assisted inverse modelling algorithm is based on the inverse tracking controller in ArtiSynth developed by Stavness et al. [15]. They used a combined movement target term and an l^2-norm regularisation term, which resulted in a quadratic programming problem. In the current paper, we stacked the position coordinates of a set of ten tracked 3D marker points on the lips in a $30D$ vector $\mathbf{z}_t(k)$ where k is the discrete time index. For brevity, we shall use the notation $\mathbf{z}_t$ instead of $\mathbf{z}_t(k)$. The model-predicted positions $\mathbf{z}(k)$ depend on $\mathbf{a}(k-1)$, which is the vector of muscle activations at time $k-1$, and on the previous state $\mathbf{z}(k-1)$. This is denoted by $\mathbf{z}(k)=\mathbf{f}_{\mathrm{m}}\left(\mathbf{a}(k-1),\mathbf{z}(k-1)\right)$, where $\mathbf{f}_{\mathrm{m}}()$ is a state-space description representing the biomechanical model. For brevity, we shall write $\mathbf{a}$ instead of $\mathbf{a}(k-1)$ and $\mathbf{f}_{\mathrm{m}}(\mathbf{a})$ instead of $\mathbf{f}_{\mathrm{m}}\left(\mathbf{a}(k-1),\mathbf{z}(k-1)\right)$. Note also that the elements of $\mathbf{a}$ are limited to the interval $[0,1]$. The technology of sEMG provides indirect measurements of the innervation of each muscle. These measurements provide quantitative indications of the activations and are therefore denoted by $\mathbf{a}_t$, which gives rise to the following quadratic cost function:

$$J(\mathbf{a})=\frac{1}{2}\left(\mathbf{f}_{\mathrm{m}}(\mathbf{a})-\mathbf{z}_t\right)^{\mathrm{T}}\mathbf{M}\left(\mathbf{f}_{\mathrm{m}}(\mathbf{a})-\mathbf{z}_t\right)+\frac{1}{2}\mathbf{a}^{\mathrm{T}}\mathbf{A}\mathbf{a}+\frac{1}{2}\left(\mathbf{a}-\mathbf{a}_{prev}\right)^{\mathrm{T}}\mathbf{D}\left(\mathbf{a}-\mathbf{a}_{prev}\right)+\frac{1}{2}\left(\mathbf{a}-\mathbf{a}_t\right)^{\mathrm{T}}\mathbf{E}\left(\mathbf{a}-\mathbf{a}_t\right) \tag{6.1}$$

With $\mathbf{a}_{prev} = \mathbf{a}(k-2)$. The matrices $\mathbf{M}$, $\mathbf{A}$, $\mathbf{D}$, and $\mathbf{E}$ are matrices that weigh different cost aspects. The term with $\mathbf{M}$ assures that model positions are close to measured positions. The term with $\mathbf{A}$ is a regulation term to tame the found activation signals. The term with $\mathbf{D}$ prevents large fluctuations of the found activations. Finally, the term with $\mathbf{E}$ assures that the estimated activations are consistent with the measured sEMG signals. In our experiments, the numerical values of the matrices were as follows: $\mathbf{M} = diag(1)$, $\mathbf{A} = diag(0.05)$, $\mathbf{D} = diag(0.005)$, and $\mathbf{E} = diag(emg_{val})$ or $\mathbf{E} = diag(0)$ in case inverse modelling is performed without sEMG tracking. emg_{val} was determined during the experiments.

To minimise the cost function in equation (6.1), the expression was worked out to a form:

$$\hat{\mathbf{a}} = \arg\min_{\mathbf{a}\in[0,1]} \left\{ \frac{1}{2}\mathbf{a}^{\mathrm{T}}\mathbf{H}^{\mathrm{T}}\mathbf{H}\mathbf{a} - \mathbf{a}^{\mathrm{T}}\mathbf{H}^{\mathrm{T}}\mathbf{b} \right\} \tag{6.2}$$

in which irrelevant terms in equation (6.1) were dropped, and a linearised approximation of the state-space model was used based on Taylor series expansion. Equation (6.2) is recognised as a quadratic programming problem for which stable, numerical solutions are available. The seed for the inversion was always set to the estimated muscle activity of the previous frame. The initial frame's seed was always set to zero muscle activity.

6.2.1. Data acquisition and pre-processing

Volunteers and data acquisition

To perform inverse modelling experiments, we used data of six healthy volunteers (three males, three females), with a mean age of 25 years (range 21 to 30 years), whom we had recruited for our previous studies [6,7]. For details, see Eskes et al. (Chapter 4) [6]. Essentials are summarised below. The data are available on the Open Science Framework [37]. Written consent was obtained for publishing the photograph in Figure 6.1.

sEMG signals s_m (m muscle channels) were recorded with the TMSi® Porti™ system (TMSi ®, Oldenzaal, the Netherlands) and micro-sEMG electrodes (1.5 mm diameter, Ag/AgCl, disc-shaped, with actively shielded cables). The following muscles were measured in bipolar configuration according to the optimal placement described by Lapatki et al. [38]: the orbicularis oris superior (OOS), the orbicularis oris inferior (OOI), the depressor anguli oris (DAO), the mentalis (MEN), the risorius (RIS), the zygomaticus major (ZYG), and the levator labii superioris alaeque nasi (LLSAN) (Figure 6.1). The sEMG signals were bandpass filtered with high-pass and low-pass cut-off frequencies of 15 and 500 Hz, respectively.

To acquire 3D lip movements, we tracked six optical face markers ($\mathbf{X}_{OR} \in \mathbb{R}^{18}$) for head orientation and ten optical lip markers ($\mathbf{X} \in \mathbb{R}^{30}$) at 100 frames per second using a triple-camera set-up (avA1000-100gc, Basler AG, Ahrensburg, Germany), which we had developed for assessing tongue mobility and capturing tongue movement after hypoglossal nerve stimulation [8,39] (Figure 6.1).

We asked the volunteers to perform six different instructions once: A. purse lips, B. raise upper lip, C. depress mouth corners, D. voluntary smile, E. draw mouth corner to the left, then to the right, and again to the left, and F. purse lips to closed-mouth smile to purse lips (Eskes et al. [7], Chapter 5, Figure 5.2). The experiments were approved by the Medical Research Ethics Committee of the Netherlands Cancer Institute and all volunteers gave written informed consent.

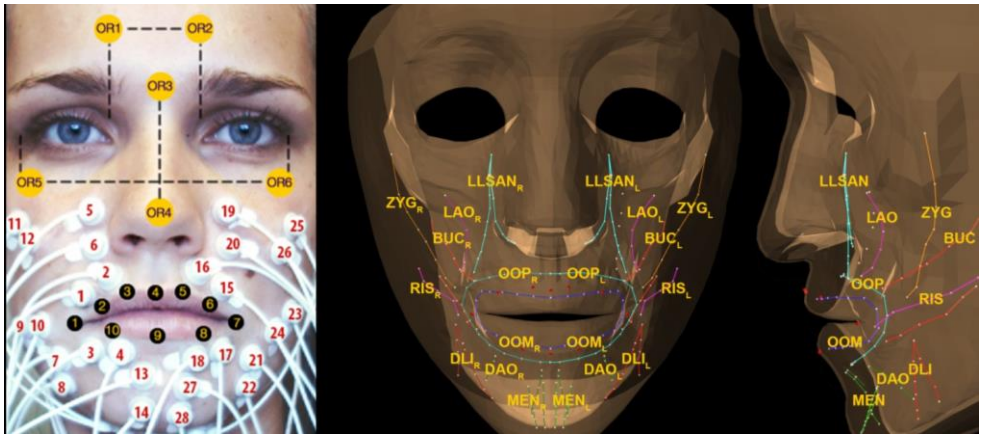

Figure 6.1 Left: Surface electrode locations, orientation markers, and lip markers. Right: Anterior-posterior view and lateral view of the model and the model's muscle bundles and lip markers. The muscles are abbreviated as follows: zygomaticus major (ZYG), risorius (RIS), levator labii superioris alaeque nasi (LLSAN), levator anguli oris (LAO), buccinator (BUC), orbicularis oris peripheralis (OOP) and marginalis (OOM), depressor labii inferior (DLI), depressor anguli oris (DAO), and mentalis (MEN). Subscript L is for left side and subscript R for right side. Adopted from Eskes et al. [7].

Finite-element face model

We performed inverse modelling on the generic face model (Figure 6.1) used in Eskes et al. (Chapter 5) [7], which was based on the work performed at ICP/GIPSA and TIMC-IMAG laboratories in Grenoble [40,41], with details published by Nazari et al. [42]. Their ANSYS® model was ported to ArtiSynth and was named the reference face model [43–45]. With soft tissues represented in three layers of elements, this model had 6,342 elements (6,024 linear hexahedral and 318 linear wedge) and 8,720 nodes. Fourteen muscle groups were available as muscle fibres. We created finite-element muscles, which were defined as the elements surrounding the muscle fibres within a radius of 5 mm. The elements of the orbicularis oris muscles were manually assigned. All these muscle elements were given muscle properties as described by Blemker et al. [46]. The bony parts, the mandible and maxilla, were modelled as rigid bodies. We used literature-based common muscle model parameters for all volunteers [7,11], with the exception of maximum muscle stress (σ_{max}). We optimised the stress parameter per volunteer starting at 300 kPa and gradually decreased σ_{max} repeatedly with 10 percent until the simulation ran smoothly without creating inverted elements. Simulations were performed on two workstations with intel Xeon core and one laptop computer with an intel i7 core.

sEMG to normalised model activations

The model used orbicularis oris peripheralis (OOP) and marginalis (OOM) definitions. Therefore, these activations were constructed from the measured OOS and OOI activations, taking into account the information about activation patterns described by Flynn et al. [11]. The buccinator (BUC), the depressor labii inferior (DLI), and the levator anguli oris (LAO) were not directly measured but derived from the measured muscles as follows:

$$s_{OOP} = 0.50\ (s_{OOS} + s_{OOI}) \tag{6.3}$$

$$s_{OOM} = 0.10\ (s_{OOP} + s_{OOI}) \tag{6.4}$$

$$s_{BUC} = 0.50\ (s_{RIS} + s_{ZYG}) \tag{6.5}$$

$$s_{LAO} = 0.75\ s_{LSSAN} \tag{6.6}$$

$$s_{DLI} = 0.75\ s_{DAO} \tag{6.7}$$

For the different instructions, the following muscles were considered relevant [7,11]:

A. OOP, OOM, and BUC
B. LLSAN
C. DAO and MEN
D. ZYG, RIS, LAO, LLSAN, DAO, and DLI
E. OOP, OOM, LLSAN, RIS, ZYG, BUC, and LAO
F. OOP, OOM, LLSAN, RIS, ZYG, BUC, and LAO

In previous research, we found the following procedure to be optimal for transforming measured sEMG signals into normalised muscle activations [5–7]. We first calculated the Willison Amplitude with $s_{\lim} = 10$ mV over sliding windows of 200 ms with maximum overlap:

$$g_m(t,i,r) = \sum_{n=1}^{N-1} \left[f\left(\left| s_m(t+n-1) - s_m(t+n) \right| \right) \right] \tag{6.8}$$

$$\text{with} \quad f(s_m) = \begin{cases} 1 & \text{if} \quad s_m \geq s_{\lim} \\ 0 & \text{otherwise} \end{cases} \qquad \begin{array}{l} i \text{ is instruction index} \\ r \text{ is repetition index} \end{array}$$

The feature $g_m(t,i,r)$ was calculated from the measured sEMG $s_m(t)$ of muscle m, where t was the time index of the EMG signals, and n the running time index within each sliding window consisting of N samples. This was done for all instructions i and repetitions r (in this case $r = 1$). The feature $g_m(t,i,r)$ was normalised according to:

$$g_{norm,m}(t,i,r) = \frac{g_m(t,i,r) - \min\limits_t(g_m(t,i,r))}{\max\limits_t(g_m(t,i,r)) - \min\limits_t(g_m(t,i,r))} \tag{6.9}$$

Registration of measured 3D lip markers to generic face model

As each face has unique dimensions, we had to apply a registration to allow for movement tracking and root mean square (RMS) error comparison of the generic face model's lip markers with the measured lip markers. We registered each measured coordinate according to equation (6.10):

$$Z_d^{norm}(k) = \left(Z_d(k) - \mu_d^Z\right)\left(\frac{\sigma_d^X}{\sigma_d^Z}\right) + \mu_d^X \tag{6.10}$$

$Z_d(k)$ is the $d-th$ element from the original measured position vector $\mathbf{z}_t(k)$. The normalised measured positions are denoted by $Z_d^{norm}(k)$. In equation (6.10), μ_d^Z is the mean of the measured position coordinates, and μ_d^X the mean of the model's position coordinates. The standard deviation of the model's position coordinates is denoted by σ_d^X , whereas the standard deviation of the measured position coordinates is given by σ_d^Z .

Performance measures

To perform quantitative evaluation, we used the RMS error, e_{pos} , that was calculated over time and over the markers via:

$$e_{pos} = \sqrt{\frac{\sum_{k=1}^{K}\left(\sum_{d=1}^{D}\left(Z_d^{norm}(k) - Z_d(k)\right)^2\right)}{KD}}\sqrt{3} \tag{6.11}$$

With k being the discrete time index, K the number of time samples, and $Z_d(k)$ the model's lip marker position coordinates. $D = 30$ reflects the dimensions, i.e. 10 markers with 3 coordinates each. The factor $\sqrt{3}$ was introduced because we wanted to express the RMS in terms of distances, rather than in terms of coordinates.

The 3D correlation coefficients were calculated as described by Pitermann et al. [36]. The mean position $\boldsymbol{\mu}_Z$ of a 3D lip marker trajectory, with samples $\mathbf{Z}_t = (x_t, y_t, v_t)$, was calculated with equation (6.12):

$$\boldsymbol{\mu}_Z = \left(\frac{1}{T}\sum_{t=1}^{T} x_t, \frac{1}{T}\sum_{t=1}^{T} y_t, \frac{1}{T}\sum_{t=1}^{T} v_t\right) \tag{6.12}$$

The standard deviation $\boldsymbol{\sigma}_Z$ of $\mathbf{Z}_t$ was calculated with equation (6.13):

$$\boldsymbol{\sigma}_Z = \sqrt{\frac{1}{T-1}\sum_{t=1}^{T}\left\|\mathbf{Z}_t - \boldsymbol{\mu}_Z\right\|^2} \tag{6.13}$$

The 3D correlation coefficient ρ_{3D} between 3D landmark trajectories $\mathbf{Z}_t$ and $\mathbf{X}_t$ was calculated with equation (6.14):

$$\rho_{3D} = \frac{\frac{1}{T}\sum_{t=1}^{T}\mathbf{Z}_t{}^T\mathbf{X}_t - \boldsymbol{\mu}_Z{}^T\boldsymbol{\mu}_X}{\boldsymbol{\sigma}_Z\boldsymbol{\sigma}_X} \tag{6.14}$$

The RMS error was also calculated for the activations (e_{act}) according to equation (6.15) with $\mathbf{g}(t)$ being the normalised feature values and $\mathbf{a}(t)$ the inverse calculated activation values, whereas Pearson's correlation coefficient was used as an activation correlation measure.

$$e_{act} = \sqrt{\frac{\sum_{t=1}^{T}\left(\mathbf{g}(t) - \mathbf{a}(t)\right)^2}{T}} \tag{6.15}$$

For all experiments, we compared the inverse calculated activation signals with the original sEMG features using the RMS error and Pearson's correlation coefficient. Also, the movement tracking errors (e_{pos} and ρ_{3D}) were calculated for all experiments. Together, these measures give an indication of performance.

6.3. Experiments

In this study, we performed three different experiments to investigate the added value of sEMG-assisted inverse modelling:

I. A simple muscle contraction to test feasibility of the model and implementation of the inverse methods
II. Inverse simulations with synthetic data produced by the sEMG-driven forward model. Inverse modelling was guided by 3 different sEMG constraints: no constraint, using all muscles (act_{all}), and using relevant muscles (act_{rel}). By comparing the results of these three constraints, we could test our method for feasibility inside the mathematical universe of the face model.
III. Inverse simulations with measurement data containing 3D position data of ten lip markers and sEMG data of fourteen facial muscles. This experiment was conducted to assess the contribution of sEMG in a realistic situation.

6.3.1. Experiment I: Test Cost term implementation by means of a simple point-mass system

Goal and experimental set-up

To test our implementation of the cost function, we first created a simulated muscle activation pattern, contracting the north-north-east, north-east, and east-north-east muscle bundles of the point-mass system as shown in Figure 6.3 [47]. It should be noted that the muscles have different maximum isometric forces, the thick muscles being more powerful than the thinner muscles. Next, inverse modelling was performed, first alternating the cost terms and finally using all cost terms at once. We expected to find that IM with each cost-term alone would not result in calculated IM activations that were similar to the simulated activation patterns, except for IM with the sEMG term, which would probably mimic the forward simulation. When using all cost terms together, we expected there would be a trade-off between the different cost terms, which would likely cause a result that was less perfect but more usable in the real application. In line with logic, when testing a cost term alone, we set its weighing factor at one. When testing all cost-terms together, we set the various weighing factors as described in section 2: $\mathbf{M} = diag(1)$, $\mathbf{A} = diag(0.05)$, $\mathbf{D} = diag(0.005)$, and $\mathbf{E} = diag(emg_{val})$ with in this case $emgval = 0.05$.

Results

For the point-mass system, movement tracking errors were similar in all simulations, whereas activation patterns differed greatly. Using the motion term alone produced a very stiff system, whereas the l^2-norm distributed the forces over the different muscles in the same way the damping term did. Including only the sEMG term showed minimal differences between the inverse calculated activation and the simulated activation and resulted in a good forward solution (e_{pos}). When using all cost terms together, including our sEMG term, we found that muscle activation patterns were still good (Figure 6.2) while used muscle activation strategies improved considerably over performance with individual cost terms or all cost terms combined with exclusion of the sEMG term. However, it should be noted that the solution depends on the weighing factors of the cost terms, e.g. when too much sEMG information is used, the result will mimic the forward solution.

The results were not perfect because of the other cost terms in the objective function and because of integration, which adds noise. Even when we activated only the sEMG target term, there was still a small error between the inverse calculated activations and the simulated sEMG pattern used in forward modelling. Larger errors occurred when we applied all cost terms in the inverse modelling of the point-mass model, which is a direct consequence of taking into account all cost terms, where the sum of all terms should be small, instead of only minimising the sEMG term.

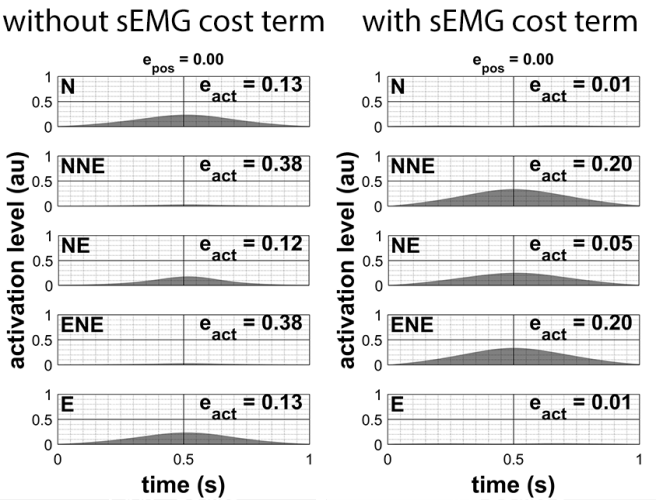

Figure 6.2 Inverse modelling with all cost terms active except for the sEMG term. Left: the estimated activations when not using the sEMG term. Right: estimated activations when using all cost terms including the sEMG term ('au' is for 'arbitrary units').

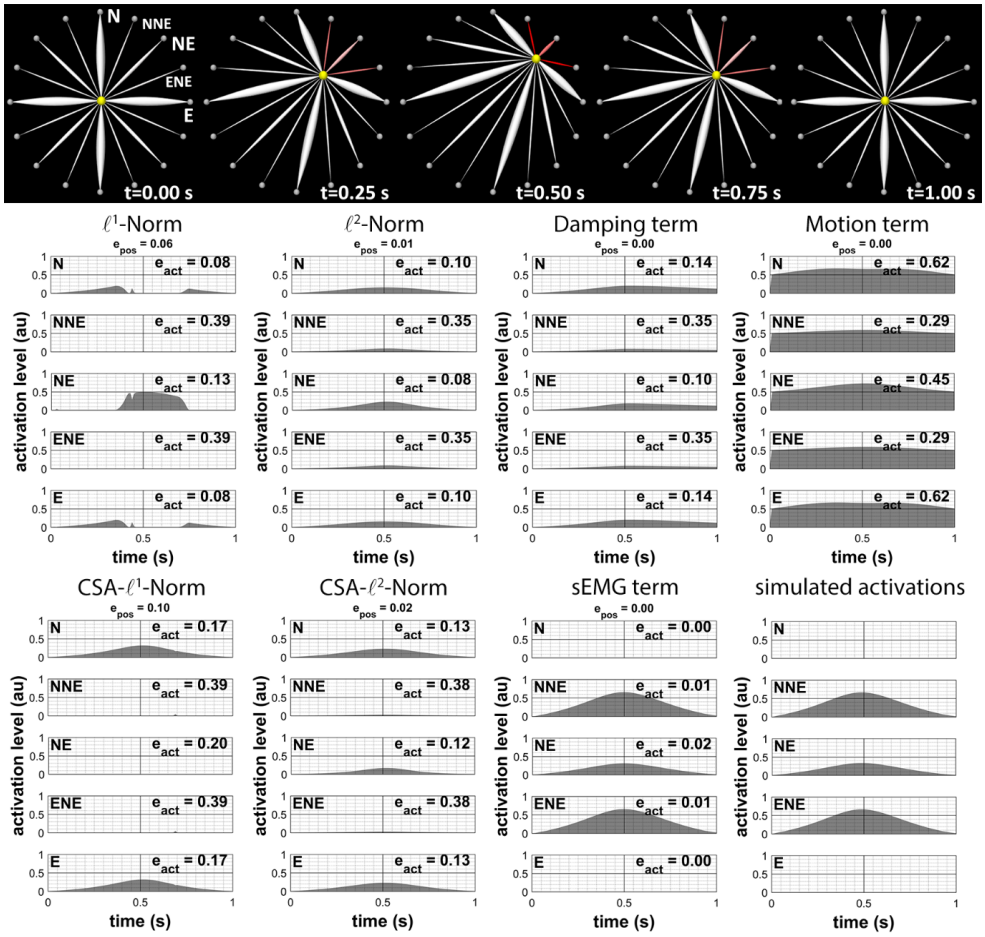

Figure 6.3 The top row shows the point-mass model with simulated forward movement to the northeast corner. The muscles' red colour intensities illustrate the extent of activation. The eight graphs below show the influence of the different cost terms on the estimated muscle activations of five muscles during inverse modelling. The original simulated activations are given in the lower right corner ('au' is for 'arbitrary units').

Conclusion

To conclude, these experiments justified our approach and showed that sacrificing only a little performance in movement tracking resulted in major improvement in muscle activation tracking. Neither the use of any original cost term by itself nor any combined use of cost terms resulted in the correct muscle activation strategy. Incorporation of the sEMG cost term greatly improved the estimated muscle activations while keeping movement tracking orders in the same range. The weighing factors influence the result and should be determined experimentally for the next experiments.

6.3.2. Experiment II: Inverse modelling using simulated data

Goal and experimental set-up

To test the inverse modelling approach within the mathematical universe of the face and assess its feasibility, we started with a standard inverse-modelling approach [15]. To first evaluate this approach in a simple situation, we used our forward-modelling results as motion targets for this experiment [7]. After activating the relevant muscles per instruction (act_{rel}), the forward simulation produced 3D trajectory data of the lip markers. Since this movement lies within the range of the model (position, acceleration) there is no need for registration, which could induce error, and the movement can function as a first indicator of feasibility. Figure 6.4 depicts the mean activations and their standard deviations based on all volunteers for the measured muscles. For use as input for the forward model, they were adjusted with equations (6.3) to (6.7). In this experiment, we used three constraints for the IM sEMG term: no sEMG, including all muscle activations (act_{all}), and including relevant muscle activations (act_{rel}). Thus, the sEMG term's penalty matrix $\mathbf{E}$ was set to zero if no activation targets were used, while we experimentally obtained the optimal value using three different values for emg_{val} to get an idea of the influence of the sEMG term: 5×10^{-5}, 5×10^{-4}, and 5×10^{-3}. Now, a trade-off between muscle activation tracking and movement tracking will be made. In this experiment, all muscles were used (act_{all}). After obtaining the optimal emg_{val}, the constraints act_{all} and act_{rel} were tested.

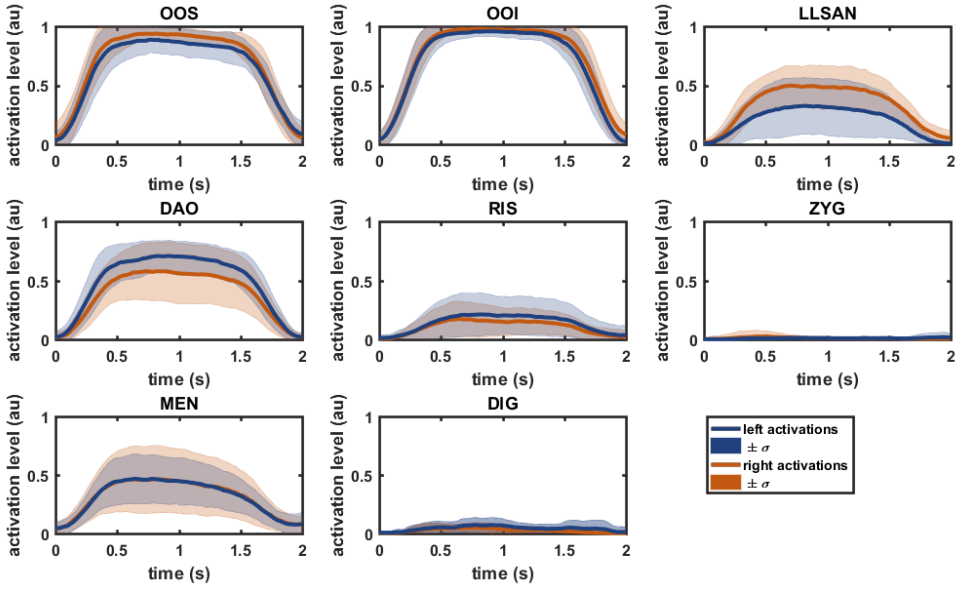

Figure 6.4 Muscle activation patterns calculated from sEMG features of the instruction 'purse lips' as input for forward modelling. The mean and standard deviations of all volunteers are shown for all measured muscles. High standard deviations show the volunteer-specific activations, with asymmetry in the DAO and LLSAN muscles, in particular. ('au' is for 'arbitrary units').

Results

The influence of the sEMG cost term and thus the optimal weighing factor can be derived from Figure 6.5. All volunteers show the same pattern: a weighing factor of 5×10^{-3} actually results in forward modelling as it depends too much on the muscle activations patterns, whereas 5×10^{-4} appears to be the optimal value of all tested factors.

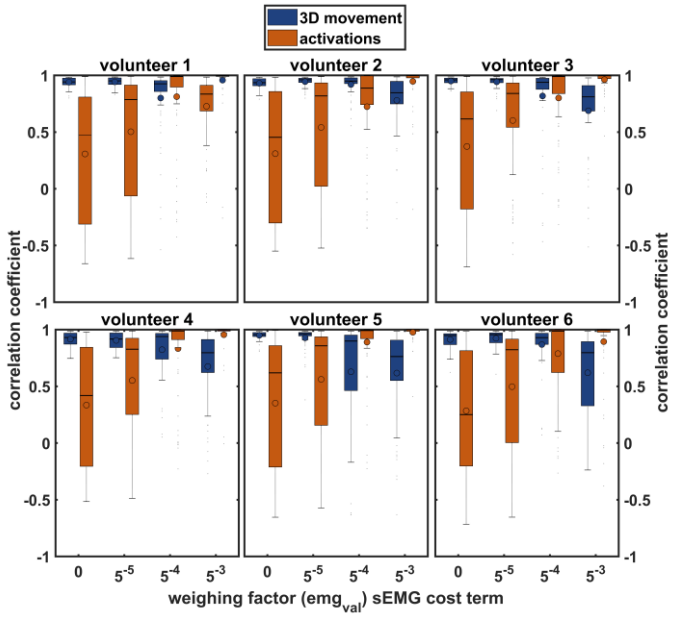

Figure 6.5 Influence of the sEMG cost weighing factor on the 3D correlation coefficients of movement and on Pearson's correlation coefficients of calculated muscle activations and sEMG features. The median is shown with a horizontal line and the mean with a dot. The boxes give first to third quartiles and the outer horizontal lines reflect minimum and maximum values.

Table 6.1 gives the RMS error between the target lip markers and the models' lip markers e_{pos} averaged over all instructions and volunteers for experiments II and III, as well as the e_{act} between the models' calculated activations and measured muscle activations. Similarly, Table 6.2 shows the 3D correlation coefficients ρ_{3D} between model markers and measurement markers and Pearson's correlation coefficients ρ between calculated model activations and measured muscle activations.

As we evaluate these experiments, some comments have to be made. The experiments confirm the load-sharing problem: three different activation strategies showed similar performances in 3D lip movement tracking with a mean ρ_{3D} of 0.93 (no constraint), 0.93 (act_{all}), and 0.92 (act_{rel}), while the correlation with the normalised sEMG features varied: 0.27 (no constraint), 0.44 (act_{all}), and 0.83 (act_{rel}), respectively, illustrating different activation strategies. The forward solution was created with act_{rel}, leading to good correlations in the experiment with act_{rel} constraint (mean $\rho = 0.83$). Like in experiment I, the correlations were not perfect because of the other cost terms in the objective function and because of the noise added by integration.

Table 6.1 Root mean square errors. The mean (μ) and standard deviation (σ) of the e_{pos} for the ten lip markers and e_{act} for the ten muscles left and right over all volunteers and all instructions.

Marker # / Muscle	1 OOM	2 OOP	3 LLSAN	4 DAO	5 RIS	6 ZYG	7 MEN	8 BUC	9 DLI	10 LAO	Average
EXPERIMENT II											
Without sEMG	**μ (σ)**	**μ (σ)**	**μ (σ)**	**μ (σ)**	**μ (σ)**	**μ (σ)**	**μ (σ)**	**μ (σ)**	**μ (σ)**	**μ (σ)**	**μ (σ)**
Lip markers	0.84 (0.35)	0.34 (0.13)	0.28 (0.11)	0.27 (0.13)	0.29 (0.11)	0.36 (0.14)	0.89 (0.40)	0.40 (0.23)	0.41 (0.35)	0.40 (0.23)	**0.45 (0.35)**
Left muscles	0.08 (0.05)	0.32 (0.18)	0.22 (0.13)	0.36 (0.23)	0.16 (0.14)	0.14 (0.14)	0.37 (0.22)	0.12 (0.10)	0.27 (0.16)	0.28 (0.15)	**0.23 (0.15)**
Right muscles	0.08 (0.05)	0.31 (0.17)	0.19 (0.12)	0.42 (0.23)	0.16 (0.14)	0.14 (0.15)	0.36 (0.20)	0.12 (0.11)	0.31 (0.16)	0.26 (0.16)	**0.23 (0.15)**
With sEMG act_{all}	**μ (σ)**	**μ (σ)**	**μ (σ)**	**μ (σ)**	**μ (σ)**	**μ (σ)**	**μ (σ)**	**μ (σ)**	**μ (σ)**	**μ (σ)**	**μ (σ)**
Lip markers	0.81 (0.35)	0.31 (0.10)	0.29 (0.09)	0.29 (0.11)	0.30 (0.09)	0.33 (0.10)	0.84 (0.39)	0.39 (0.20)	0.46 (0.32)	0.39 (0.21)	**0.44 (0.20)**
Left muscles	0.10 (0.07)	0.35 (0.18)	0.19 (0.13)	0.29 (0.21)	0.14 (0.14)	0.10 (0.10)	0.33 (0.23)	0.08 (0.07)	0.25 (0.19)	0.31 (0.16)	**0.21 (0.15)**
Right muscles	0.10 (0.07)	0.33 (0.18)	0.16 (0.12)	0.32 (0.19)	0.14 (0.14)	0.11 (0.10)	0.32 (0.21)	0.09 (0.08)	0.30 (0.18)	0.26 (0.18)	**0.21 (0.15)**
With sEMG act_{rel}	**μ (σ)**	**μ (σ)**	**μ (σ)**	**μ (σ)**	**μ (σ)**	**μ (σ)**	**μ (σ)**	**μ (σ)**	**μ (σ)**	**μ (σ)**	**μ (σ)**
Lip markers	1.07 (0.55)	0.50 (0.25)	0.50 (0.27)	0.51 (0.27)	0.51 (0.27)	0.53 (0.26)	1.11 (0.57)	0.62 (0.33)	0.65 (0.34)	0.63 (0.36)	**0.66 (0.55)**
Left muscles	0.27 (0.30)	0.10 (0.10)	0.08 (0.06)	0.04 (0.06)	0.06 (0.06)	0.05 (0.06)	0.02 (0.04)	0.20 (0.19)	0.02 (0.05)	0.16 (0.15)	**0.10 (0.11)**
Right muscles	0.27 (0.28)	0.10 (0.09)	0.08 (0.07)	0.04 (0.06)	0.06 (0.07)	0.06 (0.07)	0.02 (0.04)	0.19 (0.19)	0.03 (0.05)	0.12 (0.14)	**0.10 (0.11)**
EXPERIMENT III											
Without sEMG	**μ (σ)**	**μ (σ)**	**μ (σ)**	**μ (σ)**	**μ (σ)**	**μ (σ)**	**μ (σ)**	**μ (σ)**	**μ (σ)**	**μ (σ)**	**μ (σ)**
Lip markers	1.83 (1.61)	1.32 (0.79)	1.26 (0.78)	1.20 (0.77)	1.21 (0.81)	1.45 (1.00)	1.91 (1.56)	1.24 (0.98)	1.23 (0.91)	1.32 (1.17)	**1.40 (1.61)**
Left muscles	0.16 (0.19)	0.33 (0.19)	0.30 (0.17)	0.48 (0.22)	0.22 (0.16)	0.15 (0.16)	0.37 (0.23)	0.19 (0.14)	0.33 (0.16)	0.29 (0.15)	**0.28 (0.18)**
Right muscles	0.12 (0.15)	0.34 (0.19)	0.30 (0.14)	0.42 (0.22)	0.24 (0.20)	0.17 (0.18)	0.37 (0.23)	0.20 (0.17)	0.30 (0.16)	0.30 (0.16)	**0.28 (0.18)**
With sEMG act_{all}	**μ (σ)**	**μ (σ)**	**μ (σ)**	**μ (σ)**	**μ (σ)**	**μ (σ)**	**μ (σ)**	**μ (σ)**	**μ (σ)**	**μ (σ)**	**μ (σ)**
Lip markers	1.33 (0.66)	1.05 (0.46)	1.02 (0.49)	1.02 (0.44)	1.03 (0.48)	1.10 (0.53)	1.52 (0.77)	0.97 (0.62)	1.01 (0.74)	0.95 (0.51)	**1.10 (0.66)**
Left muscles	0.08 (0.06)	0.20 (0.16)	0.09 (0.06)	0.07 (0.03)	0.07 (0.04)	0.02 (0.02)	0.10 (0.11)	0.23 (0.18)	0.31 (0.14)	0.31 (0.15)	**0.15 (0.10)**
Right muscles	0.06 (0.03)	0.21 (0.16)	0.08 (0.07)	0.06 (0.03)	0.07 (0.04)	0.02 (0.02)	0.10 (0.11)	0.21 (0.15)	0.28 (0.15)	0.29 (0.15)	**0.14 (0.09)**

Table 6.2 3D and 2D correlations. The mean (μ) and standard deviations (σ) of the 3D correlations for the ten lip markers and the Pearson's correlation coefficients of the facial muscles bilaterally overall for all volunteers and all instructions

Marker # / Muscle	1 OOM	2 OOP	3 LLSAN	4 DAO	5 RIS	6 ZYG	7 MEN	8 BUC	9 DLI	10 LAO	Average
EXPERIMENT II											
Without sEMG	**μ (σ) [ρ]**	**μ (σ) [ρ]**	**μ (σ) [ρ]**	**μ (σ) [ρ]**	**μ (σ) [ρ]**	**μ (σ) [ρ]**	**μ (σ) [ρ]**	**μ (σ) [ρ]**	**μ (σ) [ρ]**	**μ (σ) [ρ]**	**μ (σ) [ρ]**
Lip markers	0.92 (0.07)	0.94 (0.05)	0.94 (0.05)	0.94 (0.05)	0.94 (0.04)	0.93 (0.04)	0.92 (0.06)	0.93 (0.04)	0.94 (0.05)	0.93 (0.05)	**0.93 (0.07)**
Left muscles	0.41 (0.47)	0.46 (0.41)	0.50 (0.52)	-0.19 (0.48)	0.37 (0.60)	0.52 (0.51)	0.29 (0.46)	0.38 (0.57)	-0.07 (0.47)	0.02 (0.51)	**0.27 (0.50)**
Right muscles	0.42 (0.49)	0.41 (0.44)	0.52 (0.48)	-0.20 (0.50)	0.31 (0.59)	0.44 (0.53)	0.32 (0.46)	0.39 (0.55)	-0.09 (0.47)	0.11 (0.55)	**0.26 (0.51)**
With sEMG act_{all}	**μ (σ) [ρ]**	**μ (σ) [ρ]**	**μ (σ) [ρ]**	**μ (σ) [ρ]**	**μ (σ) [ρ]**	**μ (σ) [ρ]**	**μ (σ) [ρ]**	**μ (σ) [ρ]**	**μ (σ) [ρ]**	**μ (σ) [ρ]**	**μ (σ) [ρ]**
Lip markers	0.94 (0.05)	0.94 (0.05)	0.93 (0.07)	0.92 (0.07)	0.93 (0.05)	0.94 (0.05)	0.94 (0.04)	0.94 (0.05)	0.90 (0.13)	0.93 (0.06)	**0.93 (0.05)**
Left muscles	0.39 (0.44)	0.49 (0.39)	0.64 (0.53)	0.57 (0.48)	0.45 (0.60)	0.59 (0.52)	0.59 (0.47)	0.41 (0.57)	0.19 (0.47)	0.00 (0.53)	**0.43 (0.50)**
Right muscles	0.40 (0.45)	0.44 (0.41)	0.68 (0.46)	0.63 (0.38)	0.40 (0.60)	0.51 (0.53)	0.60 (0.43)	0.39 (0.57)	0.16 (0.47)	0.16 (0.57)	**0.44 (0.49)**
With sEMG act_{rel}	**μ (σ) [ρ]**	**μ (σ) [ρ]**	**μ (σ) [ρ]**	**μ (σ) [ρ]**	**μ (σ) [ρ]**	**μ (σ) [ρ]**	**μ (σ) [ρ]**	**μ (σ) [ρ]**	**μ (σ) [ρ]**	**μ (σ) [ρ]**	**μ (σ) [ρ]**
Lip markers	0.93 (0.06)	0.94 (0.04)	0.91 (0.09)	0.90 (0.11)	0.90 (0.12)	0.93 (0.05)	0.93 (0.06)	0.93 (0.05)	0.89 (0.12)	0.92 (0.05)	**0.92 (0.06)**
Left muscles	0.85 (0.11)	0.85 (0.11)	0.91 (0.07)	0.96 (0.02)	0.95 (0.04)	0.96 (0.04)	0.93 (0.08)	0.56 (0.45)	0.90 (0.10)	0.29 (0.49)	**0.82 (0.15)**
Right muscles	0.85 (0.10)	0.86 (0.10)	0.90 (0.08)	0.96 (0.01)	0.92 (0.06)	0.93 (0.07)	0.93 (0.07)	0.60 (0.39)	0.89 (0.09)	0.60 (0.22)	**0.84 (0.12)**
EXPERIMENT III											
Without sEMG	**μ (σ) [ρ]**	**μ (σ) [ρ]**	**μ (σ) [ρ]**	**μ (σ) [ρ]**	**μ (σ) [ρ]**	**μ (σ) [ρ]**	**μ (σ) [ρ]**	**μ (σ) [ρ]**	**μ (σ) [ρ]**	**μ (σ) [ρ]**	**μ (σ) [ρ]**
Lip markers	0.74 (0.23)	0.68 (0.25)	0.65 (0.21)	0.58 (0.24)	0.61 (0.23)	0.70 (0.23)	0.80 (0.16)	0.65 (0.35)	0.64 (0.26)	0.68 (0.31)	**0.67 (0.23)**
Left muscles	0.05 (0.47)	0.20 (0.55)	0.50 (0.41)	-0.11 (0.52)	0.22 (0.64)	0.42 (0.57)	0.00 (0.50)	0.40 (0.56)	0.05 (0.49)	0.15 (0.55)	**0.19 (0.53)**
Right muscles	0.05 (0.43)	0.20 (0.52)	0.43 (0.51)	-0.10 (0.48)	0.18 (0.60)	0.53 (0.51)	-0.04 (0.53)	0.40 (0.52)	0.09 (0.49)	0.33 (0.44)	**0.21 (0.50)**
With sEMG act_{all}	**μ (σ) [ρ]**	**μ (σ) [ρ]**	**μ (σ) [ρ]**	**μ (σ) [ρ]**	**μ (σ) [ρ]**	**μ (σ) [ρ]**	**μ (σ) [ρ]**	**μ (σ) [ρ]**	**μ (σ) [ρ]**	**μ (σ) [ρ]**	**μ (σ) [ρ]**
Lip markers	0.77 (0.21)	0.74 (0.17)	0.65 (0.19)	0.62 (0.26)	0.67 (0.21)	0.75 (0.19)	0.73 (0.25)	0.68 (0.36)	0.66 (0.32)	0.69 (0.34)	**0.70 (0.21)**
Left muscles	-0.00 (0.49)	0.64 (0.43)	0.90 (0.28)	0.97 (0.09)	0.77 (0.41)	0.79 (0.38)	0.92 (0.21)	0.41 (0.51)	0.31 (0.47)	0.04 (0.52)	**0.57 (0.38)**
Right muscles	-0.00 (0.49)	0.63 (0.43)	0.91 (0.29)	0.94 (0.24)	0.79 (0.35)	0.82 (0.34)	0.89 (0.26)	0.39 (0.49)	0.33 (0.45)	0.29 (0.47)	**0.60 (0.38)**

Although we cannot perform statistical tests that will be reliable because of our small data set, some clear trends can be seen. Looking at the RMS errors, we note that the e_{pos} of no sEMG constraint was about the same as with act_{all} constraint, whereas for act_{rel} the e_{pos} was always higher than the other two. The activations errors e_{act} were always lower for act_{rel} constraint than the other two constraint, except for OOM and BUC. More surprisingly, the act_{rel} constraint resulted in a higher e_{pos}, while we had expected the most accurate results from the use of act_{rel} as it was used in the forward simulation. Presumably, the influences of other cost terms and integration and the optimisation of muscle stress must have caused inaccuracies that resulted in better (though not perfect) estimated activations, sacrificing a little in motion tracking performance.

Conclusion

The ideal $emg_{val} = 5 \times 10^{-4}$ enabled a reasonable sEMG-assisted IM appraoch. The sEMG cost term improved the correlations of activations as well as RMS errors while sacrificing only little in motion tracking performance.

6.3.3. Experiment III: Inverse modelling using measured data

Goal and experimental set-up

The goal of experiment III was to apply our new sEMG-assisted IM approach on real data and test its performance. To do so, we used measurement data obtained from healthy volunteers. The motion targets were obtained from recorded position data registered to the generic face model with equation (6.10). The sEMG term's penalty matrix $\mathbf{E}$ was set to $emg_{val} = 0$ in case of no sEMG constraint and to $emg_{val} = 5 \times 10^{-4}$ in case of the sEMG constraint act_{all} (as determined during the previous experiment, see Figure 6.4).

Results

Table 6.1 and Table 6.2 show the RMS errors and the correlation coefficients, respectively. Congruence between measured muscle activations and calculated activations via inverse modelling was similar between volunteers, showing huge standard deviations and a mean around zero in correlations when using no sEMG constraint and reasonable to high correlations using act_{all} (Figure 6.6). 3D movement correlations were similar, too. Remarkably, when using no constraint we found that volunteer 6 showed a deviating higher error in the movement e_{pos} (Figure 6.6). The ρ_{3D} s of lip movement were always equal or higher compared to no constraint. Except for the marker 7. The mean ρ_{3D} s showed a moderate to good correlation ($\rho \sim 0.7$). The e_{pos} was always lower in the sEMG-assisted approach, suggesting that the IM without constraint got stuck in a local minimum.

Calculating correlation coefficients for lip marker performance, we found that the lateral lip markers 1, 2, 6, and 7 performed better than the centre markers, similarly to the forward modelling results [7]. This can be explained by the fact that the volunteers' centre markers moved notably, whereas the model's centre markers only slightly deviated from their original position due to symmetry in the model.

However, when we compare the e_{pos} for all lip markers we observe the opposite effect: the RMS errors are higher for the lateral markers than for the centre markers. This may also be explained by the fact that more movement allows for greater error due to a larger possible distance.

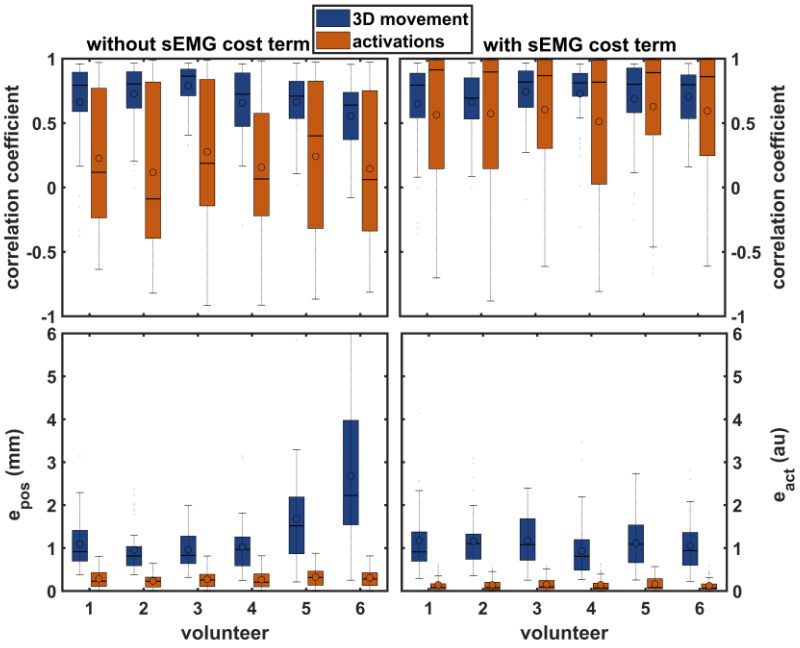

Figure 6.6 RMS errors and 3D correlation coefficients (movement) and Pearson's correlation coefficients (activations) of the different volunteers for experiment III with and without sEMG cost term. The median is shown with a horizontal line and the mean with a dot. The boxes give first to third quartiles and the outer horizontal lines reflect minimum and maximum values ('au' is for 'arbitrary units').

There was a lack of correlation without the sEMG constraint for the activations, caused by too many degrees of freedom in the muscle space. The sEMG-assisted inverse-modelling approach showed clear tendency of producing better, realistic and consistent muscle activations patterns.

Zooming in on the errors and correlation coefficients of the activations, those muscles whose activations were derived from measured muscles (DLI, BUC, LAO) performed worse than the muscles that were measured directly. This helps to explain why our forward model showed lower correlation coefficients in previous studies [7]. The OOP and OOM, derived from OOS and OOI measurements, also showed lower correlations (values), $\rho \sim 0.5$ versus $\rho \sim 0.7$. This is actually an interesting result, suggesting that the measurements do contribute a lot and can provide useful information. It would be interesting to look into the effects of only tracking the measured muscles instead of using derived muscle activations as we did here and to compare the results with experiments in which the DLI, BUC, and LAO are also measured directly.

Conclusion

In conclusion, adding sEMG tracking does not reduce 3D movement tracking accuracy, whilst giving better solutions in muscle activation tracking, as we already expected after experiments I and II. In essence, adding sEMG tracking tailors the inverse solution to a personalised activation strategy with equal performance. Apparently, surface EMG is sufficiently accurate without requiring any invasive needle approaches. However, challenges remain, as the inversion without constraint gave some questionable results, suggesting that the inversion may have got stuck in a local minimum. This would mean that including the sEMG constraint would be a way to avoid the inversion getting stuck in that miminum. However, it also hampers the general goal of seeking compensatory mechanisms by means of other muscle activation strategies. Also, because of a small data set no statistical test could be performed. However, clear trends were observed and should be confirmed by future experiments.

6.4. General results

Muscle stress varied per volunteer, per instruction, and per experiment (Table 6.3). Variation was highest between instructions and between experiments. The required computational time varied across simulations. Experiment III without the sEMG constraint may serve as a good example for computational times, as it was run completely on one workstation whereas the other experiments were distributed over the two workstations and the laptop computer, requiring longer computational times per simulation.

Table 6.3 Maximum muscle stress and computational times.

	sEMG constraint	Maximum muscle stress μ (σ) [kPa]		Computational time μ (σ)	
EXPERIMENT II	Without	6.5×10^4	(5.1×10^4)	06h 06m 55s	(00h 57m 09s)
	act_{all}	3.2×10^4	(2.6×10^4)	11h 04m 17s	(05h 57m 01s)
	act_{rel}	6.8×10^4	(5.7×10^4)	07h 41m 32s	(4h 02m 17s)
EXPERIMENT III	Without	3.3×10^4	(2.5×10^4)	05h 31m 15s	(06h 45m 46s)
	act_{all}	3.3×10^4	(2.7×10^4)	07h 24m 35s	(04h 46m 19s)

6.5. General discussion

To our knowledge, this is the first study to describe the feasibility of sEMG-assisted inverse modelling of 3D lip movements using a biomechanical model of the face and lips. We have shown that implementing a simple sEMG cost term can direct the calculated muscle activations towards the derived muscle activations calculated from sEMG measurements. Adding the sEMG cost term showed a clear trend towards superior overall performance with regard to 3D lip marker trajectories as well as muscle activation patterns when compared with regular inverse modelling.

Our inverse-modelling approach has inherited the limitations of the model described by Eskes et al. (Chapter 5) [7]. First and foremost, the generic model does not account for individual physical geometry. Although our volunteers' measurements were entered into the model initially, inaccuracies could build up during simulations due to mismatches in patient and model morphology. To account for individual geometry and anatomy, our future models should use the mismatch-and-repair algorithm or similar methods [48,49], including diffusion-tensor magnetic resonance imaging (DT-MRI) to reveal muscle fibres and their trajectories [50]. Such combined approach may yield better approximation of muscle dimensions, orientations, and trajectories.

Furthermore, we may improve our simple skin model by introducing anisotropicity and viscoelasticity. Although the simplified soft representation does induce inaccuracies, these are negligible in the light of the larger errors caused by suboptimal registration and sEMG to force mapping. Our conclusions would probably not change if we would use more advanced models with anisotropic and viscoelastic properties.

Inverse modelling without sEMG tracking resulted in estimated activation patterns that totally lacked any correlation with the sEMG signals measured. It may even got stuck in a local minimum. Future experiments to address this could use the sEMGs as starting point and from there calculate the inverse activations. As expected, adding sEMG tracking gave calculated muscle activation patterns that resembled the measurements more closely. Pitermann et al. already highlighted the load-sharing problem by demonstrating that their calculated muscle activations patterns did not show any correlation with the measured intra-muscular rectified and integrated EMG patterns [36]. Varying the initial conditions resulted in different solutions to the inverse problem, including solutions with negative muscle activity. To address this issue, they restricted the inverted EMG to positive values, only, but they found no significant difference in performance between the methods with and without this positive constraint. This illustrates the difficulty of getting volunteer-specific muscle activation patterns when muscle redundancy causes an ill-posed inverse-dynamics problem. Nevertheless, they produced good correlation coefficients for 3D lip marker coordinates [36], even when they applied a volunteer-specific face model to a different volunteer and restricted registration to general linear scaling.

These promising results encouraged us to make the step towards patient-friendly measurements. Pitermann's team measured intramuscular EMG using invasive needle electrodes, but we chose to acquire muscle activation signals with the noninvasive technique of sEMG. Another improvement we made in the experimental set-up was measuring sEMG and 3D lip markers bilaterally. Pitermann et al. measured EMG on the left and facial movement on the right side, which may have induced errors as volunteers may not have performed each instruction with perfect symmetry. Our results suggest that surface EMG is sufficiently accurate to replace the invasive technique of intramuscular EMG with intramuscular needle placement.

Terzopoulos & Waters created one of the first physics-based face models using discrete mass-spring systems to estimate muscle activity from video employing interactive deformable contours (snakes) [33]. They were able to resynthesize facial expression from estimated muscle activity using a simple, yet powerful algorithm, which called for further research in this direction. Where they mapped static facial expression to muscle activity in 2D, our results relate to 3D musculature. Incorporating improved tissue biomechanics, the ArtiSynth model uses a continuum mechanics based FE formulation as well as an advanced orbicularis oris muscle, in contrast to the two fiducial points used in Terzopoulos & Waters' model. Furthermore, we increased the number of perioral muscles to 20, where Terzopoulos & Waters studied merely 4.

Kim & Gomi and Kim et al. created a discrete model of lumped nodal masses connected via viscoelastic elements [34,35]. Despite much lower computational costs, a major drawback of their set-up is the simplified representation of reality provided by their continuum-based finite-element model. Moreover, their inverse-modelling approach involved a gradient descent search with optimisation per trial instead of per sample and without quantitative reporting. However, if sufficiently accurate, such model may be a useful addition to our virtual-therapy toolbox for rapidly simulating new inverse solutions. Our computational times, were quite high, especially when simulating the instruction set proposed in Eskes et al. for all essential functional movements [6].

To exert similar force on the elements in the model across experimental conditions, maximum muscle stress had to be variable. Although muscle stress differed per volunteer and per instruction, we found that mean muscle stress was similar in experiments II and III, at 3.3×10^4 kPa. The variance can be explained by the fact that muscle activation amplitudes differed, as did the extent of co-contraction. The different amplitudes may be explained by sEMG-technical issues. Signal amplitude may have been affected by numerous factors including sensor placement [51]: inaccurate sensor placement will inevitably contribute to crosstalk.

Another important paper by Hirayama et al. [52] reports on inverse dynamics of articulatory trajectories. Using a supervised-learning algorithm, they followed the direct inverse-modelling approach as described by Jordan & Rumelhart [53]. However, theirs was a statistical model, while we prefer biomechanical models that also account for physical laws to simulate the effects of surgical interventions.

All of the above publications confirm the difficulty of validating computed muscle activations with the actual muscle activation strategy. Most researchers have used EMG data as reference values to test algorithm performance. This method is even less reliable when EMG information is used to best track the muscle activation patterns. Recently, Nikooyan et al. reported on a new method to validate forces (and activation levels) in patients with shoulder prostheses, measuring the glenohumeral-joint reaction forces in vivo [29]. Similar data obtained with knee prostheses were made available for the "Grand Challenge Competition to Predict In Vivo Knee Loads" [54,55]. Unfortunately, this type of direct-force data cannot be obtained for facial muscles.

Despite these challenges, we were able to demonstrate that performance in 3D movement tracking did not decrease drastically - in fact, it had a tendency towards improvement - while the activation tracking improved. We think this will open new ways of obtaining realistic person-specific activation strategies.

6.6. Conclusion

We have demonstrated the feasibility of an sEMG-assisted inverse-modelling algorithm for the perioral region. Our method means an important step in the development of a virtual-surgery toolkit for the preoperative estimation of function loss after lip and oral cavity cancer surgery.

6.7. Acknowledgements

The authors thank all volunteers for participating in this study. We thank John Lloyd, Sidney Fels, and the ArtiSynth team for providing the simulation platform for this work (www.artisynth.org). In particular the authors would like to express their gratitude to the Maurits en Anna de Kock foundation (www.mauritsenannadekockstichting.nl) for funding the triple-camera set-up and the Porti EMG system.

6.8. Conflict of interest

The authors declare that they have no conflict of interest.

6.9. Funding

No funding was acquired for this research.

6.10. Ethical approval

All volunteers were informed about the experiment and about their rights. Written consent was obtained for publishing the photograph in Figure 6.1. The Medical Research Ethics Committee (MREC) of the Netherlands Cancer Institute determined that the study did not fall under the scope of the Medical Research Involving Human Subjects Act (WMO), because the study did not infringe the (psychological) integrity of the volunteers. The measurements were noninvasive and not stressful. Thus, prior review by an accredited MREC was not required. The study was performed within the Dutch legislation regarding the Agreement on Medical Treatment Act, Personal Data Protection Act, and the Code of Conduct for Responsible Use of the Federa (Dutch Federation of Biomedical Scientific Societies). Written informed consent was obtained.

6.11. References

1. Lofterød B, Terjesen T, Skaaret I, Huse A-B, Jahnsen R. Preoperative gait analysis has a substantial effect on orthopedic decision making in children with cerebral palsy: comparison between clinical evaluation and gait analysis in 60 patients. Acta Orthop. 2007;78: 74–80. doi:10.1080/17453670610013448

2. Kreeft A, Tan IB, van den Brekel MWM, Hilgers FJ, Balm AJM. The surgical dilemma of "functional inoperability" in oral and oropharyngeal cancer: current consensus on operability with regard to functional results. Clin Otolaryngol. 2009;34: 140–146. doi:10.1111/j.1749-4486.2009.01884.x

3. Kreeft AM, Tan IB, Leemans CR, Balm AJM. The surgical dilemma in advanced oral and oropharyngeal cancer: how we do it. Clin Otolaryngol. 2011;36: 260–266. doi:10.1111/j.1749-4486.2011.02299.x

4. van Alphen MJA, Kreeft AM, van der Heijden F, Smeele LE, Balm AJM. Towards virtual surgery in oral cancer to predict postoperative oral functions preoperatively. Br J Oral Maxillofac Surg. 2013;51: 747–751. doi:10.1016/j.bjoms.2013.06.012

5. Eskes M, van Alphen MJA, Balm AJM, Smeele LE, Brandsma D, van der Heijden F. Predicting 3D lip shapes using facial surface EMG. Zhang Y, editor. PLoS One. 2017;12: e0175025. doi:10.1371/journal.pone.0175025

6. Eskes M, van Alphen MJA, Smeele LE, Brandsma D, Balm AJM, van der Heijden F. Predicting 3D lip movement using facial sEMG: a first step towards estimating functional and aesthetic outcome of oral cancer surgery. Med Biol Eng Comput. 2017;55: 573–583. doi:10.1007/s11517-016-1511-z

7. Eskes M, Balm AJM, van Alphen MJA, Smeele LE, Stavness I, van der Heijden F. Simulation of facial expressions using person-specific sEMG signals controlling a biomechanical face model. Int J Comput Assist Radiol Surg. 2017; doi:10.1007/s11548-017-1659-5

8. van Dijk S, van Alphen MJA, Jacobi I, Smeele LE, van der Heijden F, Balm AJM. A New Accurate 3D Measurement Tool to Assess the Range of Motion of the Tongue in Oral Cancer Patients: A Standardized Model. Dysphagia. 2016;31: 97–103. doi:10.1007/s00455-015-9665-7

9. Lucero JC, Munhall KG. A model of facial biomechanics for speech production. J Acoust Soc Am. 1999;106: 2834–2842. doi:10.1121/1.428108

10. Barbarino GG, Jabareen M, Trzewik J, Nkengne a, Stamatas G, Mazza E. Development and validation of a three-dimensional finite element model of the face. J Biomech Eng. 2009;131: 41006. doi:10.1115/1.3049857

11. Flynn C, Stavness I, Lloyd J, Fels S. A finite element model of the face including an orthotropic skin model under in vivo tension. Comput Methods Biomech Biomed Engin. 2015;18: 571–582. doi:10.1080/10255842.2013.820720

12. Nicosia MA. A planar finite element model of bolus containment in the oral cavity. Comput Biol Med. 2007;37: 1472–1478. doi:10.1016/j.compbiomed.2007.01.007

13. Ho AK, Tsou L, Green S, Fels S. A 3D swallowing simulation using smoothed particle hydrodynamics. Comput Methods Biomech Biomed Eng Imaging Vis. 2014;2: 237–244. doi:10.1080/21681163.2013.862862

14. Buchaillard S, Brix M, Perrier P, Payan Y. Simulations of the consequences of tongue surgery on tongue mobility: implications for speech production in post-surgery conditions. Int J Med Robot Comput Assist Surg. 2007;3: 252–261. doi:10.1002/rcs.142

15. Stavness I, Lloyd JE, Fels S. Automatic prediction of tongue muscle activations using a finite element model. J Biomech. 2012;45: 2841–2848. doi:10.1016/j.jbiomech.2012.08.031

16. Meng Y, Rao MA, Datta AK. Computer Simulation of the Pharyngeal Bolus Transport of Newtonian and Non-Newtonian Fluids. Food Bioprod Process. 2005;83: 297–305. doi:10.1205/fbp.04209

17. Dul J, Townsend MA, Shiavi R, Johnson GE. Muscular synergism-I. On criteria for load sharing between synergistic muscles. J Biomech. 1984;17: 663–673. doi:10.1016/0021-9290(84)90120-9

18. Dul J, Johnson GE, Shiavi R, Townsend MA. Muscular synergism-II. A minimum-fatigue criterion for load sharing between synergistic muscles. J Biomech. 1984;17: 675–684. doi:10.1016/0021-9290(84)90121-0

19. Yamasaki T, Idehara K, Xin X. Estimation of muscle activity using higher-order derivatives, static optimization, and forward-inverse dynamics. J Biomech. 2016;49: 2015–22. doi:10.1016/j.jbiomech.2016.04.024

20. Forster E, Simon U, Augat P, Claes L. Extension of a state-of-the-art optimization criterion to predict co-contraction. J Biomech. 2004;37: 577–81. doi:10.1016/j.jbiomech.2003.09.003

21. Raikova R. A model of the flexion — Extension motion in the elbow joint — Some problems concerning muscle forces modelling and computation. J Biomech. 1996;29: 763–772. doi:10.1016/0021-9290(95)00072-0

22. Raikova R. About weight factors in the non-linear objective functions used for solving indeterminate problems in biomechanics. 1999;32: 689–694.

23. Shabani M, Stavness I. Simulating the effect of muscle stiffness and co-contraction on postural stability. Comput Methods Biomech Biomed Eng Imaging Vis. 2017;1163: 1–12. doi:10.1080/21681163.2017.1332530

24. Asadi Nikooyan A, Veeger HEJ, Chadwick EKJ, Praagman M, van der Helm FCT. Development of a comprehensive musculoskeletal model of the shoulder and elbow. Med Biol Eng Comput. 2011;49: 1425–1435. doi:10.1007/s11517-011-0839-7

25. Praagman M, Chadwick EKJ, Van Der Helm FCT, Veeger HEJ. The relationship between two different mechanical cost functions and muscle oxygen consumption. J Biomech. 2006;39: 758–765. doi:10.1016/j.jbiomech.2004.11.034

26. Cholewicki J, McGill SM. EMG assisted optimization: a hybrid approach for estimating muscle forces in an indeterminate biomechanical model. J Biomech. 1994;27: 1287–9. Available: http://www.ncbi.nlm.nih.gov/pubmed/7962016

27. Cholewicki J, McGill SM, Norman RW. Comparison of muscle forces and joint load from an optimization and EMG assisted lumbar spine model: Towards development of a hybrid approach. J Biomech. 1995;28: 321–331. doi:10.1016/0021-9290(94)00065-C

28. Mohammadi Y, Arjmand N, Shirazi-Adl A. Comparison of trunk muscle forces, spinal loads and stability estimated by one stability- and three EMG-assisted optimization approaches. Med Eng Phys. 2015;37: 792–800. doi:10.1016/j.medengphy.2015.05.018

29. Nikooyan AA, Veeger HEJ, Westerhoff P, Bolsterlee B, Graichen F, Bergmann G, van der Helm FCT. An EMG-driven musculoskeletal model of the shoulder. Hum Mov Sci. 2012;31: 429–447. doi:10.1016/j.humov.2011.08.006

30. Higginson JS, Ramsay JW, Buchanan TS. Hybrid models of the neuromusculoskeletal system improve subject-specificty. Proc Inst Mech Eng H. 2012;226: 113–119.

31. Sartori M, Farina D, Lloyd DG. Hybrid neuromusculoskeletal modeling to best track joint moments using a balance between muscle excitations derived from electromyograms and optimization. J Biomech. 2014;47: 3613–21. doi:10.1016/j.jbiomech.2014.10.009

32. Pizzolato C, Lloyd DG, Sartori M, Ceseracciu E, Besier TF, Fregly BJ, Reggiani M. CEINMS: A toolbox to investigate the influence of different neural control solutions on the prediction of muscle excitation and joint moments during dynamic motor tasks. J Biomech. 2015;48: 3929–3936. doi:10.1016/j.jbiomech.2015.09.021

33. Terzopoulos D, Waters K. Analysis and synthesis of facial image sequences using physical and anatomical models. IEEE Trans Pattern Anal Mach Intell. 1993;15: 569–579. doi:10.1109/34.216726

34. Kim K, Gomi H. Model-Based Investigation of Control and Dynamics in Human Articulatory Motion. J Syst Des Dyn. 2007;1: 558–569. doi:10.1299/jsdd.1.558

35. Kim K, Ura T, Kashino M, Gomi H. A perioral dynamic model for investigating human speech articulation. Multibody Syst Dyn. 2011;26: 107–134. doi:10.1007/s11044-011-9253-z

36. Pitermann M, Munhall KG. An inverse dynamics approach to face animation. J Acoust Soc Am. 2001;110: 1570. doi:10.1121/1.1391240

37. Eskes M. sEMG-assisted inverse modelling of 3D lip movement: a feasibility study towards person-specific modelling [Internet]. 2017. doi:10.17605/OSF.IO/G26KX

38. Lapatki BG, Oostenveld R, Van Dijk JP, Jonas IE, Zwarts MJ, Stegeman DF. Optimal placement of bipolar surface EMG electrodes in the face based on single motor unit analysis. Psychophysiology. 2010;47: 299–314. doi:10.1111/j.1469-8986.2009.00935.x

39. van Alphen MJA, Eskes M, Smeele LE, Balm AJM, van der Heijden F. In vivo intraoperative hypoglossal nerve stimulation for quantitative tongue motion analysis. Comput Methods Biomech Biomed Eng Imaging Vis. 2015;1163: 1–7. doi:10.1080/21681163.2015.1072056

40. Groleau J, Chabanas M, Marécaux C, Payrard N, Segaud B, Rochette M, Perrier P, Payan Y. A biomechanical model of the face including muscles for the prediction of deformations during speech production. In: Manfredi C, editor. 5th International Workshop on Models and Analysis of Vocal Emissions for Biomedical Applications, MAVEBA'2007. 2007. pp. 173–176. Available: http://www.fupress.com/catalogo/models-and-analysis-of-vocal-emissions-for-biomedical-applications-5th-international-workshop-december-13-15-2007-firenze-italy/1005

41. Nazari MA, Payan Y, Perrier P, Chabanas M, Lobos C. A Continuous Biomechanical Model of the Face : A Study of Muscle Coordination for Speech Lip Gestures. In: Sock R, Fuchs S, Laprie Y, editors. 8th International Seminar on Speech Production. 2008. pp. 321–324. Available: http://issp2008.loria.fr/proceedings.html

42. Nazari MA, Perrier P, Chabanas M, Payan Y. Simulation of dynamic orofacial movements using a constitutive law varying with muscle activation. Comput Methods Biomech Biomed Engin. 2010;13: 469–482. doi:10.1080/10255840903505147

43. Lloyd JE, Stavness I, Fels S. ArtiSynth: A Fast Interactive Biomechanical Modeling Toolkit Combining Multibody and Finite Element Simulation. In: Payan Y, editor. Soft Tissue Biomechanical Modeling for Computer Assisted Surgery. 1st ed. 2012. pp. 355–394. doi:10.1007/8415_2012_126

44. Nazari MA, Perrier P, Chabanas M, Payan Y. Shaping by stiffening: a modeling study for lips. Motor Control. 2011;15: 141–168. Available: http://www.ncbi.nlm.nih.gov/pubmed/21339518

45. Stavness I, Nazari MA, Perrier P, Demolin D, Payan Y. A biomechanical modeling study of the effects of the orbicularis oris muscle and jaw posture on lip shape. J speech, Lang Hear Res. 2013;56: 878–890. doi:10.1044/1092-4388(2012/12-0200)

46. Blemker SS, Pinsky PM, Delp SL. A 3D model of muscle reveals the causes of nonuniform strains in the biceps brachii. J Biomech. 2005;38: 657–665. doi:10.1016/j.jbiomech.2004.04.009

47. Stavness I. Byte Your Tongue. The University of British Columbia. 2010.

48. Chabanas M, Luboz V, Payan Y. Patient specific finite element model of the face soft tissues for computer-assisted maxillofacial surgery. Med Image Anal. 2003;7: 131–151. doi:10.1016/S1361-8415(02)00108-1

49. Bucki M, Nazari MA, Payan Y. Finite element speaker-specific face model generation for the study of speech production. Comput Methods Biomech Biomed Engin. 2010;13: 459–67. doi:10.1080/10255840903505139

50. Wu T, Hung AP-L, Hunter P, Mithraratne K. Modelling facial expressions: A framework for simulating nonlinear soft tissue deformations using embedded 3D muscles. Finite Elem Anal Des. 2013;76: 63–70. doi:10.1016/j.finel.2013.08.002

51. De Luca CJ. The Use of Surface Electromyography in Biomechanics. J Appl Biomech. 1997;13: 135–163. doi:10.1123/jab.13.2.135

52. Hirayama M, Vatikiotis-Bateson E, Kawato M. Inverse Dynamics of Speech Motor Control. Proceedings of the 6th International Conference on Neural Information Processing Systems. 1993. pp. 1043–1050.

53. Rumelhart MJ and D. Forward Models: Supervised Learning with a Digital Teacher. Cogn Sci. 1992; 307–354.

54. Fregly BJ, Besier TF, Lloyd DG, Delp SL, Banks SA, Pandy MG, D'Lima DD. Grand challenge competition to predict in vivo knee loads. J Orthop Res. 2012;30: 503–513. doi:10.1002/jor.22023

55. Kinney AL, Besier TF, D'Lima DD, Fregly BJ. Update on Grand Challenge Competition to Predict in Vivo Knee Loads. J Biomech Eng. 2013;135: 21012. doi:10.1115/1.4023255

VII

DATA AVAILABLE ONLINE
DOI: 10.17605/OSF.IO/ACB5N

sEMG - ASSISTED INVERSE MODELLING OF 2D ARM MOVEMENT

This chapter is in preparation for publication in Journal of Biomechanics

ESKES M, SCHAFT EV, BALM AJM, SMEELE LE, STAVNESS I, VAN DER HEIJDEN F (2018)
sEMG-ASSISTED INVERSE MODELLING OF 2D LIP MOVEMENT
JOURNAL OF BIOMECHANICS

Abstract

Aim

The eventual goal of our work is to evaluate possible inverse modelling procedures to be used on more complex models of the face, lips, and tongue with the goal of a virtual head and neck therapy tool, which requires both forward and inverse models that resemble physiologically realistic patient-specific motion and muscle activation patterns. As a first step, the purpose of the current chapter is to test which method can be used best in surface electromyography-assisted inverse modelling. The requirements are computational effort, accuracy, and physiologically realistic volunteer-specific solutions.

Materials and methods

We used data of eight healthy volunteers performing two types of biceps curling experiments with different weights: stiff and relaxed flexion of the elbow. Surface electromyography recordings of the biceps brachii and triceps brachii muscles were made. Simultaneously, shoulder, elbow, and wrist positions were tracked in 3D.

With these data different experiments were carried out on a simple 2D arm model. Forward modelling and inverse modelling with and without sEMG assistance were tested. Static optimisation and dynamic optimisation were both evaluated.

Conclusions

The sEMG-assisted approaches taking into account volunteer-specific muscle activation signals improved the estimation of muscle activations with inverse modelling in a simple arm model. The physiological cocontractions as recorded during the measurements were also seen in the sEMG-assisted inverse dynamics experiments but not in the experiments without sEMG tracking. Of the tested methods, the dynamic solution proved most feasible, with adequate results, acceptable computational time, and capability to generalise to higher-order models.

7.1. Introduction

Movement is one of the most important functions in life and is set in motion by neural motor control via electrochemical impulses. One or more motor units (the alpha-neuron and its innervated muscle fibres) are activated and ultimately cause the muscle to contract. A crude estimate of the number of motor units activated is the surface electromyogram (sEMG) , which measures bioelectrical signals generated in the muscles via surface electrodes [1,2]. Unfortunately, the relationship between muscle activation patterns and the measured EMG is highly nonlinear and nondeterministic for mixed type muscle fibres – there are three main types of muscle fibres: type I, slow twitch fibres, type IIA, fast oxidative fibres, and type IIB, fast glycolytic fibres, which may be present as a mixture in various muscles [3] – and for larger muscles with more motor unit recruitment possibilities, such as the biceps and triceps muscles [4]. Nevertheless, sEMG is widely used in musculoskeletal modelling [5–8], which has two classic approaches: forward modelling (FM) [6,9] and inverse modelling (IM) [10,11]. In FM an estimate for muscle activation – usually a form of feature extraction from processed EMG – is used to drive a biomechanical model [12,13], whereas in IM movement and/or forces are measured to estimate the muscle activations that led to the recorded movement [11,14–16]. Hybrid approaches (hybrid modelling, HM) have also been described combining both FM and IM to make use of the advantages of both methods [6,8,10,17–20].

Solving the inverse dynamics problem has inherent difficulties in estimating correct and volunteer-specific muscle activation patterns. Multiple muscles can be responsible for the same movement. This redundancy inherent to the musculoskeletal system plays a major role in many movements. It has been shown that standard IM does not predict cocontractions, whereas these are common in human movement. Therefore, IM may fail to estimate physiological realistic muscle recruitment patterns [21]. This is commonly known as the load-sharing problem [22,23].

Estimating the muscle activation patterns can be done using the approaches described above (FM, IM, and HM) combining various optimisation methods and different cost functions as described by Yamasaki et al. [24], and Erdemir et al. [7]. The estimation of muscle forces requires optimisation when using forward modelling, as well as when using inverse modelling [7,25,26]. Erdemir et al. categorise the force estimation methods as follows [7]:

1. Inverse dynamics static optimisation
2. Forward dynamics assisted data tracking
3. Optimal control
4. Other

The methods 1-2 are static optimisation methods, in which ‘static’ means applying an optimisation of the control input for each time step individually. The third approach is a dynamic optimisation, in which the whole trajectory of the control inputs are optimised as a single entity.

Dynamic optimisation is computationally inefficient: the computational time is more than 1000 times that of static optimisation according to Anderson and Pandy. [27]. This, combined with the fact that static optimisation and dynamic optimisation obtained remarkably similar results in terms of predicted muscles forces and joint contact forces in gait analysis, lends favour to the static optimisation approach [27]. Nevertheless, recently, Morrow et al. performed a comparison between static and dynamic optimisation for the upper extremity during wheelchair propulsion [28]. They found a less profound similarity between static and dynamic optimisation. They concluded that in their case static optimisation is not a direct replacement for dynamic optimisation and they proposed that for motions greatly influenced by muscle activation dynamics or motions with significant cocontraction, dynamic optimisation may be the preferred approach. Because of these contradictory results, we assessed both static and dynamic optimisation methods.

Various EMG-assisted and HM approaches were proposed to overcome the muscle load-sharing problem [18,29]. Buchanan et al. used a forward-inverse dynamics model [6], Lloyd and Besier used a calibrated model for inverse dynamics [19]. Yamasaki et al. proposed a new method using static optimisation and forward-inverse dynamics using higher-order derivatives [24]. These derivatives should account for (a) the forward dynamics problem of activation and contraction dynamics by error correction of their state vectors, (b) inverse dynamics problem of skeletal system, and (c) the load-sharing problem as static optimisation problem of neural excitations [24].

As described in literature [6,7,24,30], dynamics of the musculoskeletal system are usually modelled as three processes: activation dynamics, contraction dynamics and skeletal dynamics. Therefore, Yamasaki et al. argue that estimated muscle activity is inherently associated with estimation of higher-order derivatives of kinematic data [24].

The eventual goal of our work is to evaluate possible inverse modelling procedures to be used on more complex models of the face, lips, and tongue with the goal of a virtual head and neck therapy tool [9,10,31–37], which requires both forward and inverse models that resemble physiologically realistic patient-specific motion and muscle activation patterns. Therefore, we pursue a method that is able to produce these realistic muscle activation patterns.

As a first step, the purpose of the current chapter is to test which method can be used best in sEMG-assisted IM. The requirements are computational effort – which becomes even more important in clinical practice, where time of diagnostics to treatment should not be excessively large –, accuracy, and physiologically realistic volunteer-specific solutions. In contrast to previous hybrid models [8,17], we applied the sEMG information as extra cost term in the objective function, which just recently has been reported by Bélaise et al. [38], and by Eskes et al. (Chapter 6) [10]. To the best of our knowledge, these are the only two studies utilising the approach of marker tracking and sEMG tracking in a cost function in a forward-dynamics assisted data tracking or optimal control approach.

Bélaise et al. used simulated sEMG data in contrast to Eskes et al., who worked with volunteer-specific sEMG measurement data. The dynamic optimisation variant in this study is based on optimal control.

Many different parts of the body have been studied in musculoskeletal modelling: wrist [39], elbow [40], shoulder [11], ankle [41], and knee [19]. We chose the upper extremity for easy recording of sEMG and optical tracking. Moreover, only a limited number of muscles span the elbow joint. This simple arm model can serve as a proof of principle for the more complex models of the face, lips, and tongue.

7.2. Theoretical background

This section elaborates on the theoretical modelling background. It describes state-space modelling, inverse modelling using forward dynamics assisted data tracking, extended Kalman filtering, and optimal control.

7.2.1. State-space modelling

State-space modelling provides a general framework for describing the different approaches to forward and inverse dynamic modelling. These models are built on a state vector $\mathbf{x}(t)$ with dimension D and a control input vector $\mathbf{u}(t)$ with dimension N. In continuous time, the model is given by a system equation:

$$\dot{\mathbf{x}}(t) = \mathbf{f}\left(\mathbf{x}(t), \mathbf{u}(t)\right) \tag{7.1}$$

As an example, a model of the lower arm, simply described by a pendulum, is a 2nd order system, $D = 2$, in which $\mathbf{x}(t)$ contains an angle and an angular velocity. The control vector $\mathbf{u}(t)$ contains the activation signals of the biceps brachii and triceps brachii muscles.

In discrete time, we use a simple approximation of the continuous state-space model:

$$\begin{aligned} \mathbf{x}_{k+1} &= \mathbf{x}_k + \Delta\, \mathbf{f}\left(\mathbf{x}_k, \mathbf{u}_k\right) \\ &\overset{def}{=} \boldsymbol{\phi}\left(\mathbf{x}_k, \mathbf{u}_k\right) \end{aligned} \tag{7.2}$$

$\boldsymbol{\phi}\left(\mathbf{x}_k, \mathbf{u}_k\right)$ is the discrete time system function. Δ is the sampling period; k is the discrete time index. Note that $\mathbf{x}_k$ and $\mathbf{u}_k$ corresponds to $\mathbf{x}(t_k)$ and $\mathbf{u}(t_k)$, respectively, with $t_k = k\Delta$.

To enable state estimation, we define a measurement vector $\mathbf{z}_k$ which contains those state elements that are measured:

$$\mathbf{z}_k = \mathbf{H}\mathbf{x}_k \tag{7.3}$$

In the current study, only the angle is measured. Thus, $\mathbf{H}$ is a measurement matrix that selects this measured state element, and $\mathbf{H} = \begin{bmatrix} 1 & 0 \end{bmatrix}$.

7.2.2. Forward dynamics assisted data tracking with sEMG improvement

The static optimisation procedure described in this section uses a quadratic cost term for the state variables that are observed together with a quadratic cost term for the sEMG signals that are observed. Quadratic programming is used in each time step.

The measured state variables are represented by the vector $\mathbf{z}_k$ for which the following model holds: $\mathbf{z}_k = \mathbf{H}\mathbf{x}_k$. At step k, assuming knowledge from the previous state and control vector, i.e. $\mathbf{x}_k$ and $\mathbf{u}_k$, the measurement for $k+1$ is predicted by:

$$\hat{\mathbf{z}}_{k+1} = \mathbf{H}\boldsymbol{\phi}\left(\mathbf{x}_k, \mathbf{u}_k\right) \overset{def}{=} \mathbf{g}\left(\mathbf{x}_k, \mathbf{u}_k\right) \tag{7.4}$$

In order to formulate the inverse problem as a quadratic programming problem we apply linearisation. Assuming that we have two pivots $\bar{\bar{\mathbf{u}}}$ and $\bar{\bar{\mathbf{x}}}$, we define $\bar{\bar{\mathbf{z}}} = \mathbf{g}(\bar{\bar{\mathbf{x}}}, \bar{\bar{\mathbf{u}}})$. Applying a truncated Taylor series expansion with $\mathbf{u} = \bar{\bar{\mathbf{u}}} + \boldsymbol{\varepsilon}$ yields:

$$\mathbf{z} = \mathbf{g}(\bar{\bar{\mathbf{x}}}, \mathbf{u}) \approx \mathbf{g}(\bar{\bar{\mathbf{x}}}, \bar{\bar{\mathbf{u}}}) + \mathbf{G}(\bar{\bar{\mathbf{x}}}, \bar{\bar{\mathbf{u}}})\boldsymbol{\varepsilon} \approx \bar{\bar{\mathbf{z}}} + \mathbf{G}(\bar{\bar{\mathbf{x}}}, \bar{\bar{\mathbf{u}}})\left(\mathbf{u} - \bar{\bar{\mathbf{u}}}\right) \tag{7.5}$$

in which $\mathbf{G}(\bar{\bar{\mathbf{x}}}, \bar{\bar{\mathbf{u}}})$ is the Jacobian matrix of $\mathbf{g}(\mathbf{x}, \mathbf{u})$ evaluated at pivots $\mathbf{x} = \bar{\bar{\mathbf{x}}}$ and $\mathbf{u} = \bar{\bar{\mathbf{u}}}$. Embedding this in equation (7.2) with $\bar{\bar{\mathbf{x}}} = \mathbf{x}_k$, $\bar{\bar{\mathbf{u}}} = \mathbf{u}_{k-1}$, and $\bar{\bar{\mathbf{z}}} = \mathbf{g}(\mathbf{x}_k, \bar{\bar{\mathbf{u}}})$, we have:

$$\begin{aligned} \hat{\mathbf{z}}_{k+1} &\approx \bar{\bar{\mathbf{z}}} + \mathbf{G}(\bar{\bar{\mathbf{x}}}, \bar{\bar{\mathbf{u}}})\left(\mathbf{u}_k - \bar{\bar{\mathbf{u}}}\right) \\ &= \bar{\bar{\mathbf{z}}} + \mathbf{G}(\bar{\bar{\mathbf{x}}}, \bar{\bar{\mathbf{u}}})\boldsymbol{\varepsilon} \end{aligned} \tag{7.6}$$

The real measured state variables, denoted by $\mathbf{z}_{k+1}$, are the targets for the predicted $\hat{\mathbf{z}}_{k+1}$. The sEMG signal $\mathbf{s}_k$ are targets for the activation signals $\mathbf{u}_k$. With that, we define the cost function as follows:

$$J(\boldsymbol{\varepsilon}) = \frac{1}{2}\left(\mathbf{z}_{k+1} - \hat{\mathbf{z}}_{k+1}\right)^{\mathrm{T}} \mathbf{M}\left(\mathbf{z}_{k+1} - \hat{\mathbf{z}}_{k+1}\right) + \frac{1}{2}\mathbf{u}_k{}^{\mathrm{T}}\mathbf{A}\mathbf{u}_k + \frac{1}{2}\boldsymbol{\varepsilon}^{\mathrm{T}}\mathbf{D}\boldsymbol{\varepsilon} + \frac{1}{2}\left(\mathbf{u}_k - \mathbf{s}_k\right)^{\mathrm{T}} \mathbf{E}\left(\mathbf{u}_k - \mathbf{s}_k\right) \tag{7.7}$$

With $\mathbf{M}$, $\mathbf{A}$, $\mathbf{D}$, and $\mathbf{E}$ the penalty matrices for states, ℓ^2-regularisation term, damping term, and sEMG term, respectively. Substitution of $\mathbf{u}_k = \bar{\bar{\mathbf{u}}} + \boldsymbol{\varepsilon}$ yields:

$$\begin{aligned} J(\boldsymbol{\varepsilon}) = {} & \tfrac{1}{2}\mathbf{z}_{k+1}^T\mathbf{M}\mathbf{z}_{k+1} + \tfrac{1}{2}\hat{\mathbf{z}}_{k+1}^T\mathbf{M}\hat{\mathbf{z}}_{k+1} - \hat{\mathbf{z}}_{k+1}^T\mathbf{M}\mathbf{z}_{k+1} \\ & + \tfrac{1}{2}\bar{\bar{\mathbf{u}}}^T\mathbf{A}\bar{\bar{\mathbf{u}}} + \bar{\bar{\mathbf{u}}}^T\mathbf{A}\boldsymbol{\varepsilon} + \tfrac{1}{2}\boldsymbol{\varepsilon}^T\mathbf{A}\boldsymbol{\varepsilon} \\ & + \tfrac{1}{2}\boldsymbol{\varepsilon}^{\mathrm{T}}\mathbf{D}\boldsymbol{\varepsilon} \\ & + \tfrac{1}{2}\left(\bar{\bar{\mathbf{u}}} - \mathbf{s}_k\right)^{\mathrm{T}}\mathbf{E}\left(\bar{\bar{\mathbf{u}}} - \mathbf{s}_k\right) + \left(\bar{\bar{\mathbf{u}}} - \mathbf{s}_k\right)^{\mathrm{T}}\mathbf{E}\boldsymbol{\varepsilon} + \tfrac{1}{2}\boldsymbol{\varepsilon}^{\mathrm{T}}\mathbf{E}\boldsymbol{\varepsilon} \end{aligned} \tag{7.8}$$

Cancelling irrelevant terms, i.e. terms not depending on $\boldsymbol{\varepsilon}$, substitution of $\mathbf{G} = \mathbf{G}(\mathbf{x}_k, \mathbf{u}_{k-1})$, and rearrangement of terms of the same kind give:

$$J(\boldsymbol{\varepsilon}) = \boldsymbol{\varepsilon}^T\left(\mathbf{A}\bar{\bar{\mathbf{u}}} + \mathbf{E}\left(\bar{\bar{\mathbf{u}}} - \mathbf{s}_k\right) + \mathbf{G}^T\mathbf{M}(\bar{\bar{\mathbf{z}}} - \mathbf{z}_{k+1})\right) + \tfrac{1}{2}\boldsymbol{\varepsilon}^T\left(\mathbf{A} + \mathbf{D} + \mathbf{E} + \mathbf{G}^T\mathbf{M}\mathbf{G}\right)\boldsymbol{\varepsilon} \tag{7.9}$$

Finally, substitution of:

$$\begin{aligned}\mathbf{c} &= \mathbf{A}\bar{\bar{\mathbf{u}}} + \mathbf{E}\left(\bar{\bar{\mathbf{u}}} - \mathbf{s}_k\right) + \mathbf{G}^T\mathbf{M}(\bar{\bar{\mathbf{z}}} - \mathbf{z}_{k+1}) \\ \mathbf{R} &= \mathbf{A} + \mathbf{D} + \mathbf{E} + \mathbf{G}^T\mathbf{M}\mathbf{G}\end{aligned} \tag{7.10}$$

gives the canonical form of a quadratic programming problem:

$$J(\boldsymbol{\varepsilon}) = \boldsymbol{\varepsilon}^T\mathbf{c} + \tfrac{1}{2}\boldsymbol{\varepsilon}^T\mathbf{R}\boldsymbol{\varepsilon} \tag{7.11}$$

Without additional constraints, and assuming that the inverse of $\mathbf{R}$ exists, the solution is given by:

$$\boldsymbol{\varepsilon} = -\mathbf{R}^{-1}\mathbf{c} \tag{7.12}$$

so that the found control vector is:

$$\mathbf{u}_k = \mathbf{u}_{k-1} + \boldsymbol{\varepsilon} \tag{7.13}$$

7.2.3. Extended Kalman filtering

Kalman filtering is applied to estimate the state vectors using observations of these vectors. As spin-off, the Kalman filter can also deliver estimates of the input vectors, which can be used as a first solution for our IM problem. For this, the state-space model in equation (7.2) and (7.3) must be augmented with the unknown part $\mathbf{w}_k$ of the control vector, and with process noise $\tilde{\mathbf{w}}_k$ that drives this unknown part. We define $\mathbf{y}_k^T = \begin{bmatrix}\mathbf{x}_k^T & \mathbf{w}_k^T\end{bmatrix}$ and we define $\breve{\mathbf{u}}_k$ as the known part of the control vector, so that $\mathbf{u}_k = \breve{\mathbf{u}}_k + \mathbf{w}_k$:

$$\begin{aligned}\mathbf{y}_{k+1} &\overset{def}{=} \begin{bmatrix}\mathbf{x}_{k+1} \\ \mathbf{w}_{k+1}\end{bmatrix} = \boldsymbol{\psi}(\mathbf{y}_k, \breve{\mathbf{u}}_k) + \tilde{\mathbf{w}}_k \\ &\text{where} \quad \boldsymbol{\psi}(\mathbf{y}, \breve{\mathbf{u}}) = \begin{bmatrix}\boldsymbol{\phi}\left(\mathbf{x}, \breve{\mathbf{u}} + \mathbf{w}\right) \\ \beta\mathbf{w}\end{bmatrix} \quad \text{and} \quad \mathbf{u}_k = \breve{\mathbf{u}}_k + \mathbf{w}_k \\ \mathbf{z}_k &= \mathbf{H}\mathbf{y}_k + \mathbf{v}_k \quad \text{where } \mathbf{H} \text{ must be padded with zeros} \\ &\qquad \text{to take care of the applied augmentation}\end{aligned} \tag{7.14}$$

β is a forgetting factor which assures that $\mathbf{w}_k$ will not fluctuate wildly. $\tilde{\mathbf{w}}_k$ is the process noise, and is modelled as white noise with covariance matrix $\mathbf{C}_\mathbf{w}$. Since only the last two elements of the process noise drive $\mathbf{w}_k$, we choose $\mathbf{C}_\mathbf{w} = \text{diag}(0, 0, \sigma_1^2, \sigma_2^2)$. The measurement noise $\mathbf{v}_k$ is assumed to be white noise with covariance matrix $\mathbf{C}_\mathbf{v}$.

The sEMG vectors $\mathbf{s}_k$ are an indication of the control vectors. However, since maybe not all muscles are monitored by sEMGs, we define a binary vector $\mathbf{b}$ which indicates whether a muscle is measured. That is, $b_n = 0$ specifies that muscle n is not measured, whereas $b_n = 1$ specifies that the sEMG of that muscle is available.

With that, the known part of the control vector is:

$$\breve{\mathbf{u}}_k = \mathbf{B}\mathbf{s}_k \quad \text{with} \quad \mathbf{B} = \begin{bmatrix} b_1 & 0 & \cdots & 0 \\ 0 & b_2 & & \vdots \\ \vdots & & \ddots & 0 \\ 0 & \cdots & 0 & b_M \end{bmatrix} \tag{7.15}$$

Effectively, the elements of the control vectors that are measured by means of sEMG are replaced with the sEMG features. All other elements of the control vectors are set to zero.

The Kalman filter keeps track of the estimates $\hat{\mathbf{y}}_{k|k}$ with covariance matrices $\mathbf{C}_{k|k}$, and with the one-step-ahead predictions $\hat{\mathbf{y}}_{k+1|k}$ with covariance matrices $\mathbf{C}_{k+1|k}$. To by-pass the nonlinearity in $\boldsymbol{\psi}(\mathbf{y},\mathbf{u})$ the extended Kalman filter uses the approximation $\boldsymbol{\psi}(\mathbf{y}+\boldsymbol{\varepsilon},\mathbf{u}) \approx \boldsymbol{\psi}(\mathbf{y},\mathbf{u}) + \boldsymbol{\phi}_{\mathbf{y}}(\mathbf{y},\mathbf{u})\boldsymbol{\varepsilon}$. Starting with an initial condition $\hat{\mathbf{y}}_{-1|0} = \mathbf{x}_0$ and $\mathbf{C}_{-1|0} = \mathbf{C}_0$, the extended Kalman filter iterates as follows:

$$\begin{aligned} \mathbf{S} &= \mathbf{H}\mathbf{C}_{k|k-1}\mathbf{H}^T + \mathbf{C}_{\mathbf{v}} \\ \mathbf{K} &= \mathbf{C}_{k|k-1}\mathbf{H}^T\mathbf{S}^{-1} \\ \hat{\mathbf{y}}_{k|k} &= \hat{\mathbf{y}}_{k|k-1} + \mathbf{K}(\mathbf{z}_k - \mathbf{H}\hat{\mathbf{y}}_{k|k-1}) \\ \mathbf{C}_{k|k} &= \mathbf{C}_{k|k-1} - \mathbf{K}\mathbf{S}\mathbf{K}^T \\ \hat{\mathbf{y}}_{k+1|k} &= \boldsymbol{\psi}(\hat{\mathbf{y}}_{k|k}, \breve{\mathbf{u}}_k) \\ \mathbf{C}_{k+1|k} &= \boldsymbol{\psi}_{\mathbf{y}}(\hat{\mathbf{y}}_{k|k}, \breve{\mathbf{u}}_k)\mathbf{C}_{k|k}\boldsymbol{\psi}_{\mathbf{y}}^T(\hat{\mathbf{y}}_{k|k}, \breve{\mathbf{u}}_k) + \mathbf{C}_{\mathbf{w}} \end{aligned} \tag{7.16}$$

The final estimate of the control vectors follows from

$$\hat{\mathbf{u}}_k = \breve{\mathbf{u}}_k + \hat{\mathbf{w}}_{k|k} \tag{7.17}$$

7.2.4. Optimal Control

Instead of optimisation per time step, optimal control theory provides a framework to derive an optimal trajectory of control vectors. In continuous time, the problem is stated as follows:

Given, the initial condition, that is $\mathbf{x}(0) = \mathbf{x}_0$ at time $t = 0$, and given measurements $\mathbf{z}(t)$ and sEMG signals $\mathbf{s}(t)$ during the time period of the experiment, i.e. for $0 \le t \le T$, reconstruct the trajectory of the control vector that optimises a criterion. First, we want control vectors such that the resulting $\mathbf{x}(t)$ is most compatible with the measurement vector $\mathbf{z}(t)$. Second, we want $\mathbf{u}(t)$ to be compatible as much as possible with the sEMG signals $\mathbf{s}(t)$. For that purpose, we define the objective function:

$$J\big(\mathbf{u}(t)\big) = \int_{t=0}^{T} C\big(\mathbf{x}(t), \mathbf{u}(t)\big)\,dt \tag{7.18}$$

in which $C(,)$ is a benefit function that should be tailored to the application.

For that, we define the observed state vector $\boldsymbol{\xi}(t)$ as indicated by the measurement vector $\mathbf{z}(t)$. The observed state vector $\boldsymbol{\xi}(t)$, having the same dimension as $\mathbf{x}(t)$, contains the measured state variables at the same locations as in $\mathbf{x}(t)$, but since maybe not all state variables are measured, as indicated in the measurement matrix $\mathbf{H}$, some locations will be void. We also define a binary vector $\mathbf{p}$. The connotation of $\mathbf{p}$ is that if its element $p_d = 0$, the state variable $x_d(t)$ is not measured; whereas $p_d = 1$ specifies that that state variable is measured, and so $\xi_d(t)$ is a valid element.

$\mathbf{x}(t)$ must be consistent with $\boldsymbol{\xi}(t)$, and $\mathbf{u}(t)$ must be consistent with the sEMG vectors $\mathbf{s}(t)$. So, we define:

$$C\left(\mathbf{x}(t),\mathbf{u}(t)\right) = -\left(\mathbf{x}(t)-\mathbf{P}\boldsymbol{\xi}(t)\right)^T \mathbf{Q}\left(\mathbf{x}(t)-\mathbf{P}\boldsymbol{\xi}(t)\right) - \left(\mathbf{u}(t)-\mathbf{B}\mathbf{s}(t)\right)^T \mathbf{R}\left(\mathbf{u}(t)-\mathbf{B}\mathbf{s}(t)\right) \quad (7.19)$$

where $\mathbf{Q}$ and $\mathbf{R}$ are weighing matrices that determine the balance between the two requirements. The matrix $\mathbf{P}$ is a selection matrix that is derived from $\mathbf{p}$:

$$\mathbf{P} = \begin{bmatrix} p_1 & 0 & \cdots & 0 \\ 0 & p_2 & & \vdots \\ \vdots & & \ddots & 0 \\ 0 & \cdots & 0 & p_N \end{bmatrix} \quad (7.20)$$

The minus sign in equation (7.19) turns the quadratic cost function into a quadratic benefit function, so that the objective function needs to be maximised rather than minimised.

The objective is to determine a control signal $\mathbf{u}(t)$ $0 \le t \le T$ such that $J\left(\mathbf{u}(t)\right)$ is maximised. However, in general there maybe constraints on the solution space. In our case, each control signal must be within the range of 0 and 1.

Several strategies exist to find the solution of the optimal control problem. In biomechanical applications, the method called 'parameter optimisation' is a brute force procedure [42]. First, the problem is rephrased in discrete time so that a finite number of control vectors $\mathbf{u}_k$ with $k = 0,\cdots,K$ represents the solution. These vectors are stacked to a single $N(K+1)$ dimensional vector. This turns the dynamic optimisation problem into a parameter optimisation problem. The disadvantage is that the dimension of the parameter vector is huge, which makes the procedure impractical.

Another strategy is 'dynamic programming' [43]. By discretising not only the time, but also the control space, the optimal solution can be regarded as a path on an orthogonal lattice. Dynamic programming is an efficient algorithm to find the optimal path as the computational complexity is on the order of $(K+1)N_{\mathbf{u}}^2$, in which $N_{\mathbf{u}}$ is the number of samples in the control space. This makes this approach also impractical as, for instance, in a 2-dimensional control space that is populated with, for instance, $N_{\mathbf{u}} = 100 \times 100 = 10^4$ samples, the complexity is too large.

7.2.5. Maximum principle of Pontryagin

An elegant strategy is the application of the maximum principle of Pontryagin [43]. This principle transforms the dynamic optimisation problem also into a parameter estimation problem but unlike the 'parameter optimisation' mentioned above, the parameter vector to optimise has the same dimension as the state vector. The recipe is as follows.

First, the so-called adjoint equation is defined:

$$\dot{\boldsymbol{\lambda}}(t) = -\mathbf{f}_{\mathbf{x}}^{T}\left(\mathbf{x}(t),\mathbf{u}(t)\right)\boldsymbol{\lambda}(t) - C_{\mathbf{x}}^{T}\left(\mathbf{x}(t),\mathbf{u}(t)\right) \tag{7.21}$$

The D-dimensional vector $\boldsymbol{\lambda}(t)$ is called the adjoint vector. $\mathbf{f}_{\mathbf{x}}\left(\mathbf{x},\mathbf{u}\right)$ is the Jacobian matrix with respect to $\mathbf{x}$. $C_{\mathbf{x}}\left(\mathbf{x}(t),\mathbf{u}(t)\right)$ is the derivative of $C(,)$ with respect to the vector $\mathbf{x}$. The initial condition of the adjoint equation is not given, but instead there is a *terminal condition* at the terminal time T. In the absence of a possible cost function on $\mathbf{x}(T)$, this terminal condition is simply:

$$\boldsymbol{\lambda}(T) = \mathbf{0} \tag{7.22}$$

The maximum principle of Pontryagin states that the optimal control vector at each point in time maximises the so-called Hamiltonian function $H(\lambda(t),\mathbf{x}(t),\mathbf{u}(t))$:

$$\mathbf{u}_{opt} = \arg\max_{\mathbf{u}} H(\boldsymbol{\lambda},\mathbf{x},\mathbf{u}) \quad \text{with} \quad H(\lambda,\mathbf{x},\mathbf{u}) \overset{def}{=} \boldsymbol{\lambda}^{T}\mathbf{f}(\mathbf{x},\mathbf{u}) + C(\mathbf{x},\mathbf{u}) \tag{7.23}$$

The problem that is left, is that the initial condition $\boldsymbol{\lambda}(0)$ of the adjoint equation in equation (7.21) is not given. If it was, then we could solve the system equation and the adjoint equation simultaneously by numerical integration, and find $\mathbf{u}(t)$ for each time step by applying the principle of Pontryagin. A numerical approximation of that with Δ being the time step is:

Iterate from time step k to $k+1$

1. Maximise $H(\boldsymbol{\lambda}_k,\mathbf{x}_k,\mathbf{u}_k)$ to find the optimal control $\mathbf{u}_k = \mathbf{u}(k\Delta)$
2. $\mathbf{x}_{k+1} = \mathbf{x}_k + \Delta\mathbf{f}(\mathbf{x}_k,\mathbf{u}_k)$
3. $\boldsymbol{\lambda}_{k+1} = \boldsymbol{\lambda}_k - \Delta\left(\mathbf{f}_{\mathbf{x}}^{T}(\mathbf{x}_k,\mathbf{u}_k)\boldsymbol{\lambda}_k + C_{\mathbf{x}}^{T}(\mathbf{x}_k,\mathbf{u}_k)\right)$

(7.24)

The iteration starts at $k=0$ with $\mathbf{x}_0 = \mathbf{x}(0)$ being the (known) initial condition, and with some $\boldsymbol{\lambda}_0$ substituted for the (yet unknown) initial condition $\boldsymbol{\lambda}(0)$. The terminal time is reached when $k=K$ with $K = T/\Delta$. This yields a terminal condition $\boldsymbol{\lambda}_K$, which obviously depends on the choice of $\boldsymbol{\lambda}_0$. We therefore introduce the function $\mathbf{g}()$ as follows:

$$\boldsymbol{\lambda}_K = \mathbf{g}(\boldsymbol{\lambda}_0) \tag{7.25}$$

The numerical evaluation of $\mathbf{g}(\boldsymbol{\lambda}_0)$ is accomplished by iterating according to (7.24). Finding the optimal control boils down to finding a $\boldsymbol{\lambda}_0$ such that $\mathbf{g}(\boldsymbol{\lambda}_0) = \mathbf{0}$. This can be regarded as a parameter optimisation problem if we define an objective function $J_{pont}(\boldsymbol{\lambda}_0) = \left\|\mathbf{g}(\boldsymbol{\lambda}_0)\right\|^2$.

7.2.6. Linear quadratic control

For linear systems, and with the target set to zero, i.e. $\mathbf{z}_k = \mathbf{0}$ for all k, the optimal control problem with quadratic cost functions has an elegant feedback solution:

$$\mathbf{u}_k = -\mathbf{L}\mathbf{x}_k \tag{7.26}$$

This is called linear quadratic regulation. With a finite terminal time T, the feedback matrix $\mathbf{L}$ depends on time. However, with infinite horizon, i.e. $T \to \infty$, the matrix is constant [43]. In the current nonlinear system, a linear approximation of the system function $\boldsymbol{\phi}(\mathbf{x},\mathbf{u})$ is needed to calculate $\mathbf{L}$. Define the Jacobian matrices $\boldsymbol{\phi}_\mathbf{x}(\mathbf{x},\mathbf{u})$ and $\boldsymbol{\phi}_\mathbf{u}(\mathbf{x},\mathbf{u})$ with respect to $\mathbf{x}$ and $\mathbf{u}$, respectively. The feedback matrix $\mathbf{L}$ follows from the discrete Ricatti equation [43]:

$$\begin{aligned}
&\boldsymbol{\phi}_\mathbf{x}^T(\mathbf{x},\mathbf{u})\mathbf{S}\boldsymbol{\phi}_\mathbf{x}(\mathbf{x},\mathbf{u}) - \mathbf{S} \\
&\quad - \boldsymbol{\phi}_\mathbf{x}^T(\mathbf{x},\mathbf{u})\mathbf{S}\boldsymbol{\phi}_\mathbf{u}(\mathbf{x},\mathbf{u})\left(\boldsymbol{\phi}_\mathbf{u}^T(\mathbf{x},\mathbf{u})\mathbf{S}\boldsymbol{\phi}_\mathbf{u}(\mathbf{x},\mathbf{u}) + \mathbf{R}\right)^{-1}\boldsymbol{\phi}_\mathbf{u}^T(\mathbf{x},\mathbf{u})\mathbf{S}\boldsymbol{\phi}_\mathbf{x}(\mathbf{x},\mathbf{u}) + \mathbf{Q} = \mathbf{0} \\
&\mathbf{L} = \left(\boldsymbol{\phi}_\mathbf{u}^T(\mathbf{x},\mathbf{u})\mathbf{S}\boldsymbol{\phi}_\mathbf{u}(\mathbf{x},\mathbf{u}) + \mathbf{R}\right)^{-1}\boldsymbol{\phi}_\mathbf{u}^T(\mathbf{x},\mathbf{u})\mathbf{S}\boldsymbol{\phi}_\mathbf{x}(\mathbf{x},\mathbf{u})
\end{aligned} \tag{7.27}$$

Embedding this in the situation with a nonzero target and with knowledge of the sEMG signals is done in a feedforward-feedback framework with error correction. See Figure 7.1. The first step is the application of the extended Kalman filter, which produces an estimate $\hat{\mathbf{x}}_k$ of the state vector, as well as an estimate $\hat{\mathbf{u}}_k$ of the control vector. This allows a new state-space model for the error. Define a state-space vector $\mathbf{e}_k = \mathbf{x}_k - \hat{\mathbf{x}}_k$ with control input $\boldsymbol{\upsilon}_k = \mathbf{u}_k - \hat{\mathbf{u}}_k$, and assuming $\hat{\mathbf{x}}_{k+1} \approx \boldsymbol{\phi}(\hat{\mathbf{x}}_k, \hat{\mathbf{u}}_k)$:

$$\begin{aligned}
\mathbf{e}_{k+1} &= \mathbf{x}_{k+1} - \hat{\mathbf{x}}_{k+1} \\
&= \boldsymbol{\phi}(\mathbf{x}_k, \mathbf{u}_k) - \hat{\mathbf{x}}_{k+1} \\
&= \boldsymbol{\phi}(\hat{\mathbf{x}}_k + \mathbf{e}_k, \hat{\mathbf{u}}_k + \boldsymbol{\upsilon}_k) - \hat{\mathbf{x}}_{k+1} \\
&\approx \boldsymbol{\phi}(\hat{\mathbf{x}}_k, \hat{\mathbf{u}}_k) + \boldsymbol{\phi}_\mathbf{x}(\hat{\mathbf{x}}_k, \hat{\mathbf{u}}_k)\mathbf{e}_k + \boldsymbol{\phi}_\mathbf{u}(\hat{\mathbf{x}}_k, \hat{\mathbf{u}}_k)\boldsymbol{\upsilon}_k - \hat{\mathbf{x}}_{k+1} \\
&\approx \boldsymbol{\phi}_\mathbf{x}(\hat{\mathbf{x}}_k, \hat{\mathbf{u}}_k)\mathbf{e}_k + \boldsymbol{\phi}_\mathbf{u}(\hat{\mathbf{x}}_k, \hat{\mathbf{u}}_k)\boldsymbol{\upsilon}_k
\end{aligned} \tag{7.28}$$

Application of this linear model in equation (7.27) provides for each time step k a LQR solution for the feedback matrix $\mathbf{L}_k$ which now becomes time dependent. Note that in order to comply with the constraints on the control signal, the control inputs are limited so as to assure that it is within the allowed range, i.e. $\mathbf{u}_k = \lfloor \hat{\mathbf{u}}_k - \boldsymbol{\upsilon}_k \rfloor$.

The proposed method is an implementation of an error-correction method using LQR feedback, and with extended Kalman filtering to provide the input. This is summarised in Figure 7.1. In this diagram, the $\alpha\mathbf{s}_k$ is used instead of $\mathbf{s}_k$. This allows us to compare results with full support of the sEMG signals, $\alpha = 1$, or fully without this support $\alpha = 0$.

The strategy represented here can be considered an approximation of the solution of the optimal control problem. The approximation is done by linearisation of the system. The merit is that this linearisation is with respect to the error that is brought forth in the Kalman filter. We expect that this approximation is more accurate than a linearisation with respect to the state vector.

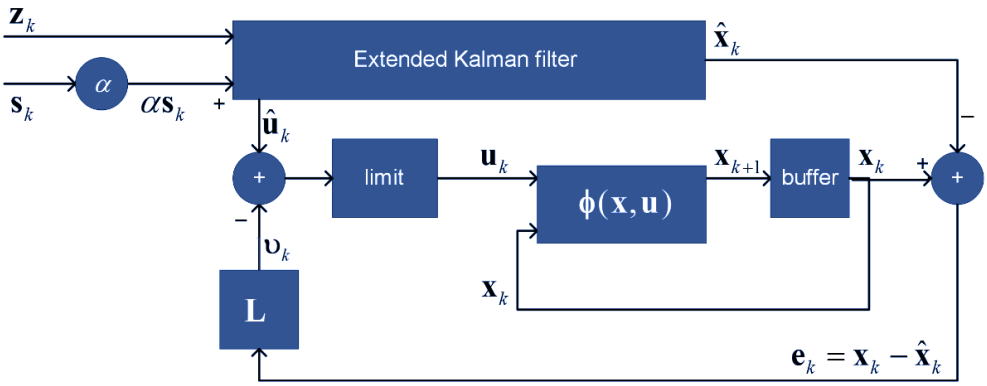

Figure 7.1 LQR feedback error correction using extended Kalman filtering as input.

7.3. Methods

7.3.1. Volunteers and data acquisition

Data of eight right-handed healthy volunteers $(k = 1, \cdots, 8)$ were acquired: four males and four females, ages ranging from 23 to 33 years ($\mu = 25.5$ and $\sigma = 2.9$). The recording sites of the skin were cleansed with NuPrep abrasive gel and alcohol to reduce skin impedance. The TMSi® Porti™ system (TMSi ®, Oldenzaal, The Netherlands) was used to record the sEMG signals. Pre-gelled disposable surface electrodes (Covidien Kendall 12 mm diameter, with shielded cables) were placed above the long head of the biceps brachii and the long head of the triceps brachii $(n = 1, \cdots, 4)$ of the right arm (see Cram et al. [44], and Figure 7.2), with an interelectrode distance of two centimetres. In addition, a common ground reference electrode was applied on the bony part of the forehead. The Polaris Spectra optical tracking system (NDI, Ontario, Canada) tracked the shoulder, elbow and wrist joints via optical markers attached to the joints. Volunteers gave their informed consent for the experiments, which were approved by the Ethics Committee of the University of Twente.

7.3.2. Instructions to volunteers

The volunteers were asked to steady their elbow by placing it against their side. The forearm was in supinated position. The range of elbow joint angle was from 0° to ~160°, fully extended to fully flexed, respectively. The tasks described below were performed in random order for 50 seconds with a predefined pace of 40 bpm (~0.67 Hz) using a metronome, resulting in eight to nine repetitions per measurement, the first eight of which were used. This was done with counterweights of 0 kg, 1 kg, 2 kg, 3, kg:

1. Normal Biceps flexion (NBF); Lifting the lower arm by focusing on contracting only the biceps.
2. Stiff Biceps flexion (SBF); Lifting the lower arm by focusing on contracting both the biceps and the triceps.

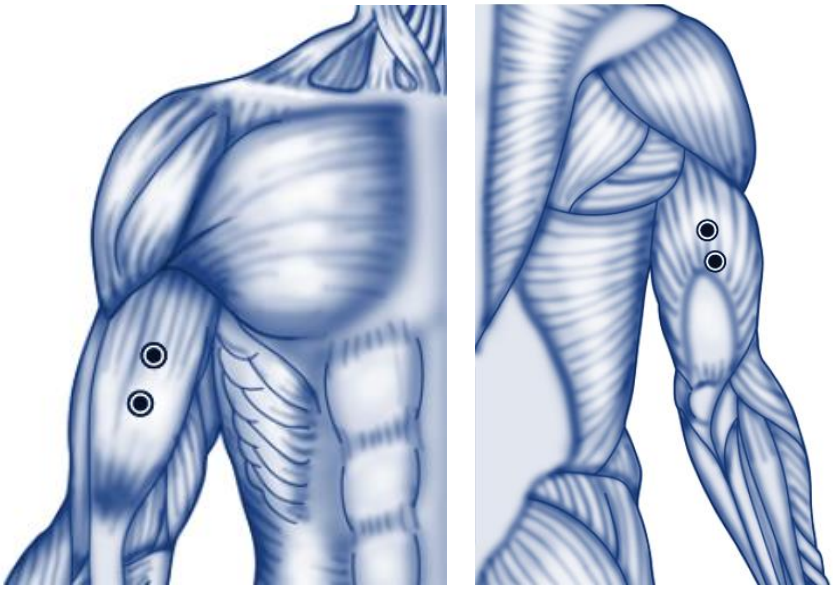

Figure 7.2 Left: bipolar electrode placement on biceps muscle, right: bipolar electrode placement on triceps muscle. Adapted from Cram et al. [45]. Original image ©2010 Jones and Bartlett Publishers, LLC.

The instructions were first demonstrated by the experimenter. Thereafter, volunteers practiced the instructions beforehand until they felt familiar with the procedures. To prevent muscle fatigue, 100 seconds of rest was given between trials. Finally, isometric maximum voluntary contraction (MVC) experiments were performed for normalising the sEMG signals. The MVC experiments were performed at an elbow joint angle of 90°.

7.3.3. Data processing and analysis

sEMG signals $s_n(t,i,r)$ were recorded in bipolar configuration with a sample frequency of 2,048 Hz. Here, t is the time index, i is the instruction, and r is the repetition number. The recorded sEMG signals were bandpass filtered with a high- and low-pass, zero-phase delay, fourth-order Butterworth filter with cut-off frequencies of 20 and 450 Hz, respectively [46]. The optical tracking position data of the shoulder $p_{shoulder}(t,i,r)$, the elbow $p_{elbow}(t,i,r)$, the wrist $p_{wrist}(t,i,r)$ were captured at a frequency of 30 Hz. The position data were filtered with a low-pass, zero-phase delay, fourth-order Butterworth filter with a cut-off frequency of 5 Hz.

Synchronisation

To synchronise the sEMG signals with the optical tracking data, both data acquisition software packages were installed on the same laptop. The recording of both software packages was started simultaneously with a script using the internal clock of the CPU as timing, resulting in a maximum synchronisation difference of 1 ms. Thereafter, the sEMG signals were resampled to 30 Hz to match the position data.

Registration

To register the different volunteers to the same generic model, the elbow joint angle θ was calculated from the smoothed position data using:

$$\theta(t) = \cos^{-1}\left(\frac{(SE(t)\cdot WE(t))}{\|SE(t)\|\|WE(t)\|}\right) \tag{7.29}$$

With SE being the vector from p_{elbow} to $p_{shoulder}$ and WE being the vector from p_{elbow} to p_{wrist}. The joint angles in time were used to calculate wrist positions $\left(p_{wrist}^{\mathrm{mod}\,el}\right)$ in time using the model's defined locations of shoulder, elbow, and wrist.

7.3.4. sEMG to muscle activation model

Buchanan et al. described the mathematical transformation from EMG via neural activation to muscle activation, and eventually muscle force [9]. Their method follows below:

$$u(t) = \alpha e(t-d) - \beta_1 u(t-1) - \beta_2 u(t-2) \tag{7.30}$$

α, β_1, and β_2 are the parameters that map processed sEMG (e), which is also full-wave rectified, to neural activation (u). The electromechanical delay d is included in the equation. There is a small time delay between sEMG activity and the corresponding muscle activation, which is called the electromechanical delay [25]. The electromechanical delay varies per subject, per muscle, and per movement. Norman et al. found different values for the biceps and triceps in concentric and eccentric conditions. We used the averaged values of 46 ms for the biceps, and 30 ms for the triceps [48]. The following is essential to form a stable equation:

$$\beta_1 = \gamma_1 + \gamma_2 \qquad \beta_2 = \gamma_1\,\gamma_2 \qquad |\gamma_1| < 1 \qquad |\gamma_2| < 1 \qquad \alpha - \beta_1 - \beta_2 = 1$$

We used the simple form, also reported in Manal et al. [49], to describe the step from neural activation to muscle activation, which incorporates the nonlinear mapping from sEMG to muscle activation:

$$a(t) = \frac{e^{Au(t)} - 1}{e^{A} - 1} \tag{7.31}$$

The Manal parameter A is the nonlinear shape factor that can vary from -3 to 0, representing highly nonlinear to linear.

7.3.5. Normalisation

The normalisation of sEMG data is still a matter of debate [50–52]. However, the processed sEMG has to be scaled between zero and one before calculating the activations according to equation (7.31).

The data in this study were normalised (e') by the peak value of processed sEMG (e) of the MVC trials, with the following equation (n indicates the muscle):

$$e'_n = \frac{e_n - \min(e_n)}{\max(e_n) - \min(e_n)} \tag{7.32}$$

7.3.6. The arm model

We used a simple upper extremity model, containing the biceps brachii and triceps brachii muscles, depicted in Figure 7.3.

The following quantities are defined:

- The lower arm length is given by ℓ .
- The mass of the lower arm is modelled as a point mass m located at the extreme end of the lower arm.
- The biceps brachii exercises a force $F_1 = u_1 F_{\max,1}$ at a point of action that is at a distance r_1 from the rotation axis of the joint.
- The triceps brachii exercises a force $F_2 = u_2 F_{\max,2}$ at a point of action that is at a distance r_2 from the rotation axis of the joint.
- The orientation of the lower arm is defined by an angle φ with respect to the vertical direction.
- The arm's moment is denoted with M

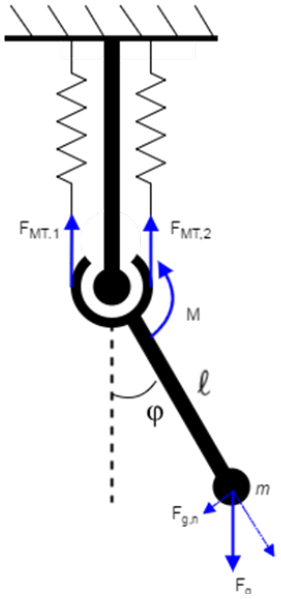

Figure 7.3 Simple arm model.

The dynamics of the system are described by the force balance according to Newton's law applied tangential to the circular trajectory of the mass:

$$\begin{aligned} ma &= -F_{gravity}\sin\varphi - F_{friction} + F_{biceps} - F_{triceps} \\ m\ell\ddot{\varphi} &= -mg\sin\varphi - \frac{D}{\ell}\dot{\varphi} + \frac{u_1 F_{\max,1} r_1}{\ell} - \frac{u_2 F_{\max,2} r_2}{\ell} \end{aligned} \tag{7.33}$$

We converted this to a state-space model by defining a state vector $\mathbf{x}(t) = \begin{bmatrix} \varphi(t) & \dot{\varphi}(t) \end{bmatrix}^T$ and a control vector $\mathbf{u}(t) = \begin{bmatrix} u_1 & u_2 \end{bmatrix}^T$:

$$\dot{\mathbf{x}}(t) = \mathbf{f}\left(\mathbf{x}(t), \mathbf{u}(t)\right) \quad \Rightarrow \quad \begin{bmatrix} \dot{x}_1 \\ \dot{x}_2 \end{bmatrix} = \begin{bmatrix} x_2 \\ -\frac{g}{\ell}\sin(x_1) - \frac{d}{m\ell^2}x_2 + \frac{F_{\max,1} r_1}{m\ell^2}u_1 - \frac{F_{\max,2} r_2}{m\ell^2}u_2 \end{bmatrix} \tag{7.34}$$

Here $\mathbf{x}(t)$ is the state vector with positions and/or velocities with dimension $D = 2$. $\mathbf{u}(t)$ is the control vector, i.e. the activation signals with dimension $N = 2$.

The activations are bounded between 0 and 1. That is, for each muscle n, we have $0 \le u_n(t) \le 1$. We used the parameters as given in Table 7.1 [24].

Table 7.1 Model parameters adopted from [24]

Parameter	Biceps ($n=1$)	Triceps ($n=2$)	Unit
d	0.2	0.2	Nms
r_n	0.03	-0.03	m
ℓ_n	0.12	0.12	m
$F_{\max,n}$	2600	2000	N

7.4. Experiments

A number of experiments were performed to compare the proposed static optimisation method with the dynamic optimisation method using LQR feedback error correction. For each run, the root mean square (RMS) error was calculated between the measured angles of the elbow and the model based estimated angles. Next, the average φ_{RMS} of these RMSs was tabulated along with its standard deviation. The same was done for the measured muscle activations, i.e. the sEMG features, and the model based estimated muscle activations, yielding e_{RMS}. Pearson's correlation coefficients were determined between the measured muscle activations and the estimated ones, and between the measured angles and estimated ones. This was done for each run, again obtaining an average ρ_e (activations) and ρ_φ (angles) and corresponding standard deviation. The last performance measure was computational time, which becomes even more important in clinical practice, where time of diagnostics to treatment should not be excessively large.

For the static optimisation the following parameters were used:

- the Jacobian step size $\alpha = 10^{-6}$
- the penalty matrix for the motion cost term $\mathbf{M} = \mathrm{diag}(1,1)$
- the penalty matrix for the activation cost term $\mathbf{A} = \mathrm{diag}(0.005, 0.005)$
- the penalty matrix for the damping cost term $\mathbf{D} = \mathrm{diag}(0.0025, 0.0025)$
- the penalty matrix for the sEMG cost term $\mathbf{E} = \mathrm{diag}(0.25, 0.25)$ or $\mathbf{E} = \mathbf{0}$ (no sEMG)

For the dynamic optimisation method using LQR feedback error correction the parameters were:

- forgetting factor of estimated control signals $\beta = 0.9$
- covariance matrix of measurement noise $\mathbf{C}_v = 0.1^2 \text{ rad}^2$
- covariance matrix of process noise $\mathbf{C}_w = \mathrm{diag}(0, 0, 10^{-2}, 10^{-2})$
- Cost matrix state vector $\mathbf{Q} = \mathrm{diag}(1000, 0)$
- Cost matrix control input $\mathbf{R} = \mathrm{diag}(1,1)$

These values were chosen in such a way, that the correlation coefficient of the biceps activities were about the same for static optimisation and dynamic optimisation.

The following experiments were conducted:

Experiment o: **Forward modelling**
The sEMG features were directly fed into the biomechanical model. To see which degree of nonlinearity performs best, this was repeated with four different instances of the Manal parameter A, that A is set to 0, -1, -2, and -3. The parameter A that performed best was used in consecutive experiments.

Experiment I: **Static optimisation without sEMG assistance**

Experiment II: **Static optimisation with sEMG assistance**

Experiment III: **Dynamic optimisation without sEMG assistance**

Experiment IV **Dynamic optimisation with sEMG assistance**

7.5. Results

In experiment o (forward only), the found RMSs of the angle were as follows:

$$A = 0 \quad \rho_{\varphi} = 0.52 \pm 0.21$$
$$A = -1 \quad \rho_{\varphi} = 0.54 \pm 0.16$$
$$A = -2 \quad \rho_{\varphi} = 0.52 \pm 0.18$$
$$A = -3 \quad \rho_{\varphi} = 0.51 \pm 0.19$$

The results do not significantly differ. Since there was a slightly higher correlation for $A = -1$, this was selected for all other experiments. We depicted the mean of the found input neural activation levels with corresponding standard deviations as well as the average and standard deviations of the found angles. This was done for experiment o (Figure 7.4 and Figure 7.5), experiment I (Figure 7.6 and Figure 7.7), experiment II (Figure 7.8 and Figure 7.9), experiment III (Figure 7.10 and Figure 7.11), and experiment IV (Figure 7.12 and Figure 7.13).

Table 7.2 denotes the results of the different algorithms, showing the mean and standard deviation of the Pearson's correlation coefficients between the measured activations and the IM calculated activations and between the measured angles and tracked angles. In the tables, the following abbreviations are used:

- FM: forward modelling
- SO: static optimisation
- DO: dynamic optimisation using Kalman filtering and LQR feedback error correction
- sEMG: sEMG-assisted approach

Table 7.1 shows the mean and standard deviation of the RMSs between the measured activations and the IM-calculated activations and between the measured angles and tracked angles. The computational effort is given in Table 7.4.

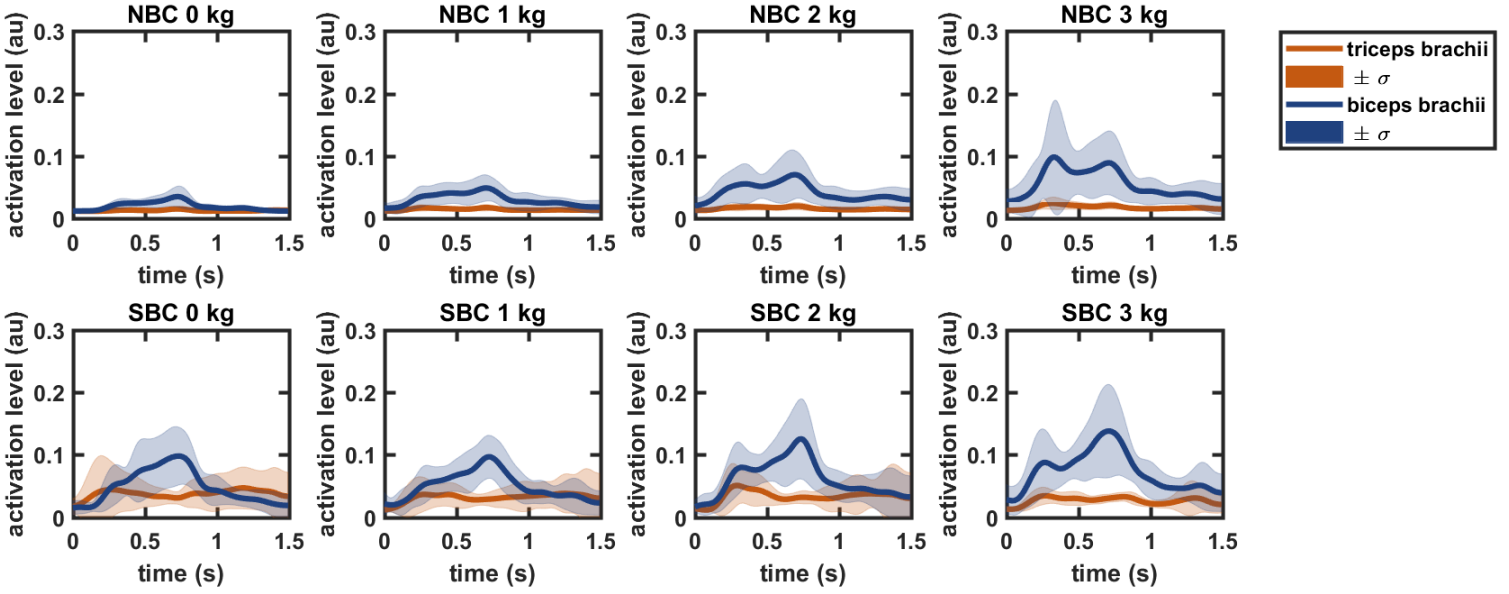

Figure 7.4 Experiment 0: The mean and standard deviation of the muscle activations found with forward modelling and with Manal parameter $A = -1$. Triceps brachii muscle activity in orange and biceps brachii muscle activity in blue.

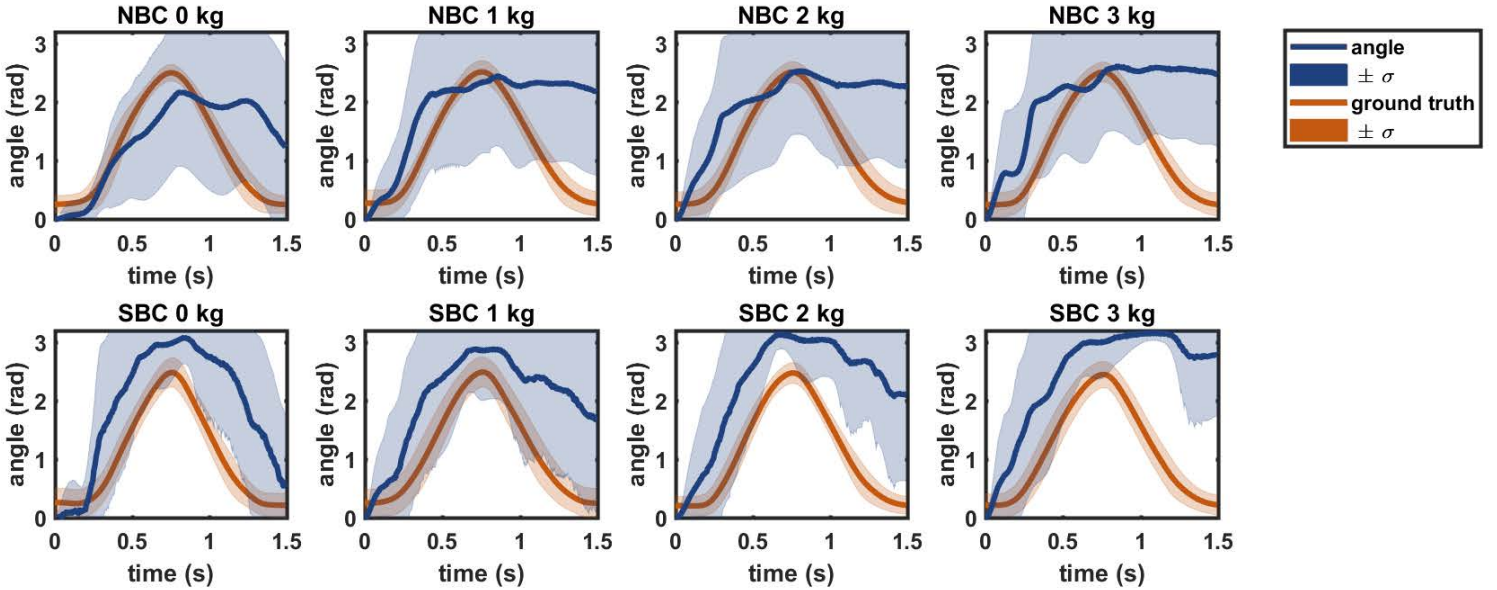

Figure 7.5 Experiment 0: The mean and standard deviation of the elbow angles found with forward modelling and with Manal parameter $A = -1$. The mean and standard deviation of the measured elbow angles are also given.

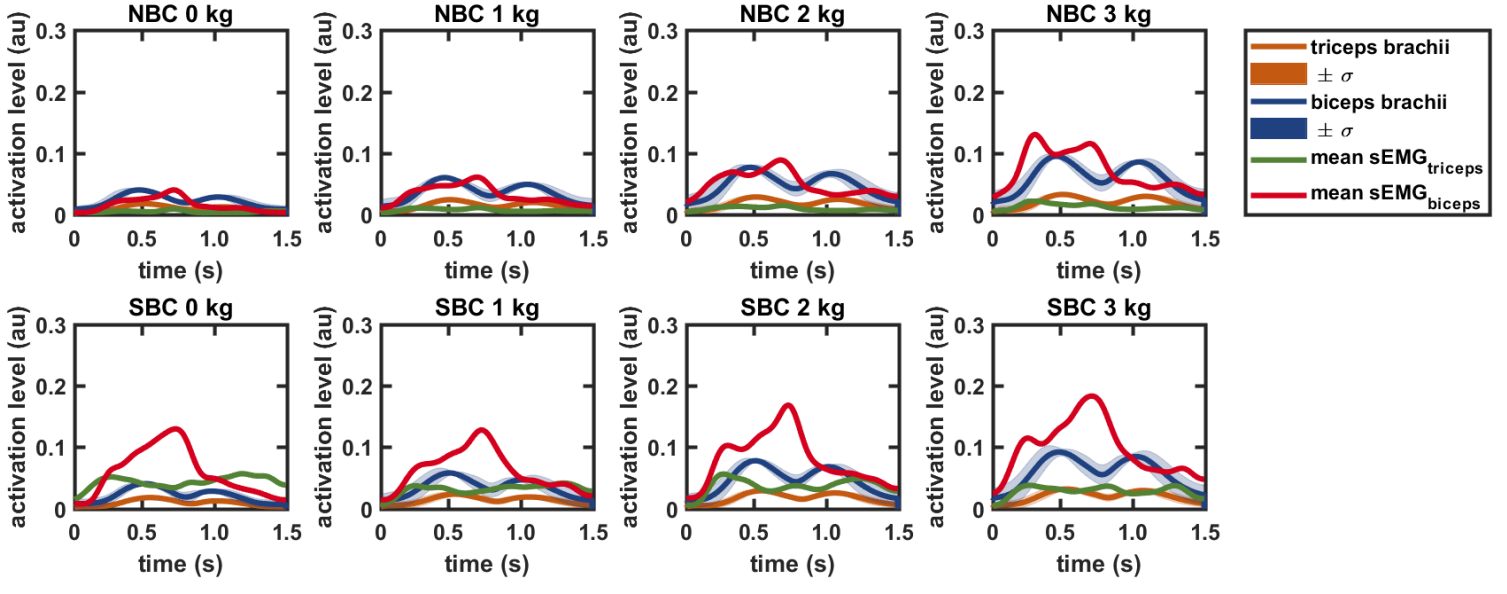

Figure 7.6 Experiment I: The means and standard deviations of the muscle activations found with static optimisation without using sEMG. The mean of the measured sEMG features (ground truth) of the triceps brachii in green and of the biceps brachii in red.

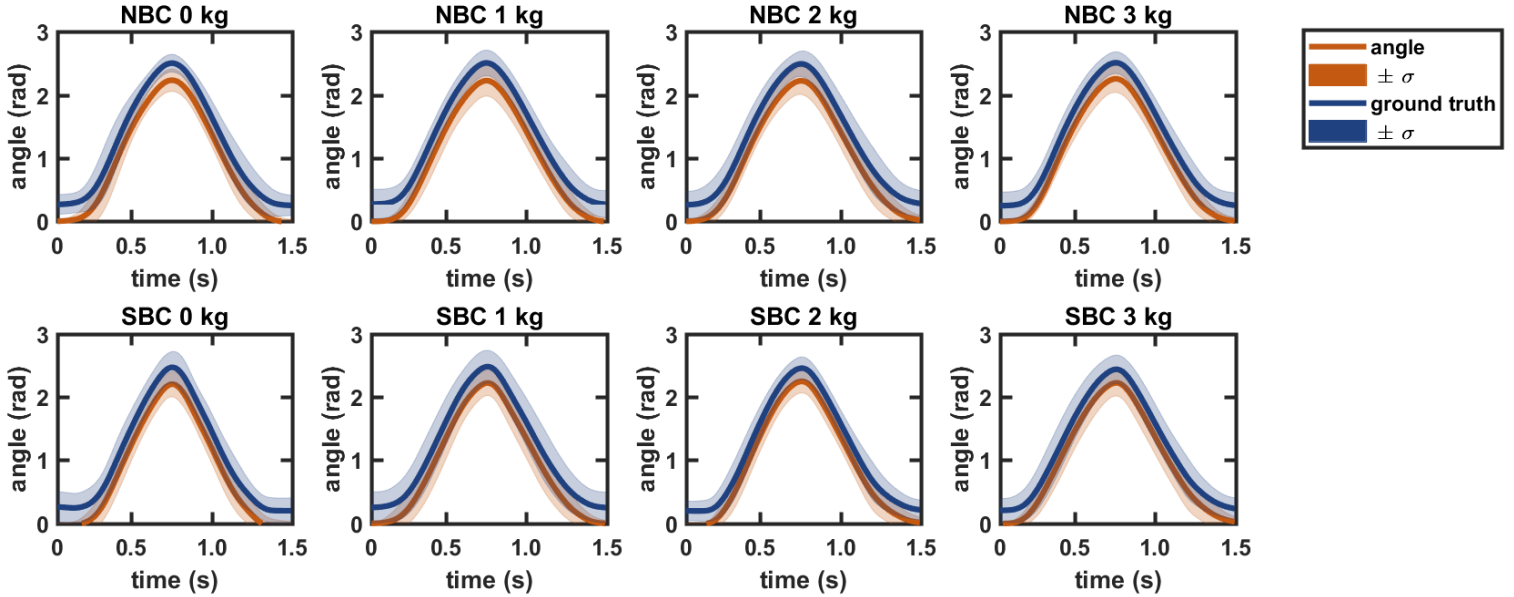

Figure 7.7 Experiment I: The mean and standard deviation of elbow angles found with static optimisation and without using sEMG in orange. The mean and standard deviation of the measured angles considered the ground truth are shown in blue.

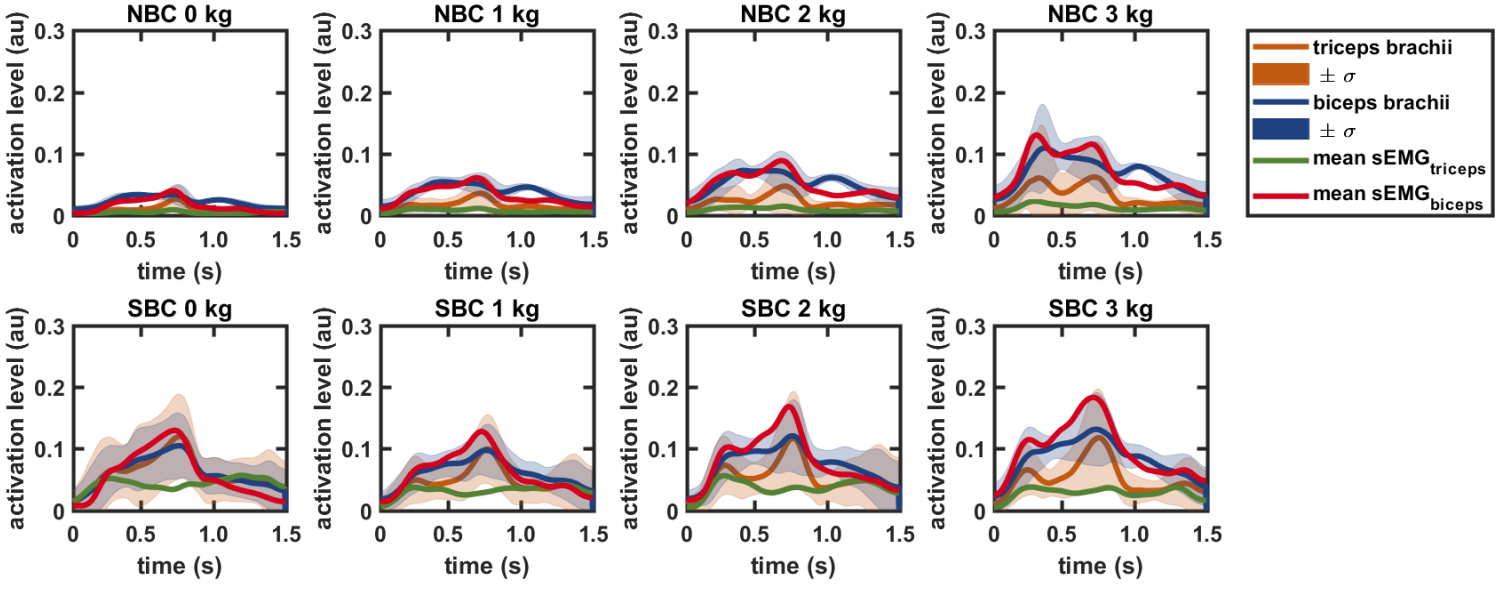

Figure 7.8 Experiment II: The means and standard deviations of the muscle activations found with static optimisation using sEMG. The mean of the measured sEMG features (ground truth) of the triceps brachii in green and of the biceps brachii in red.

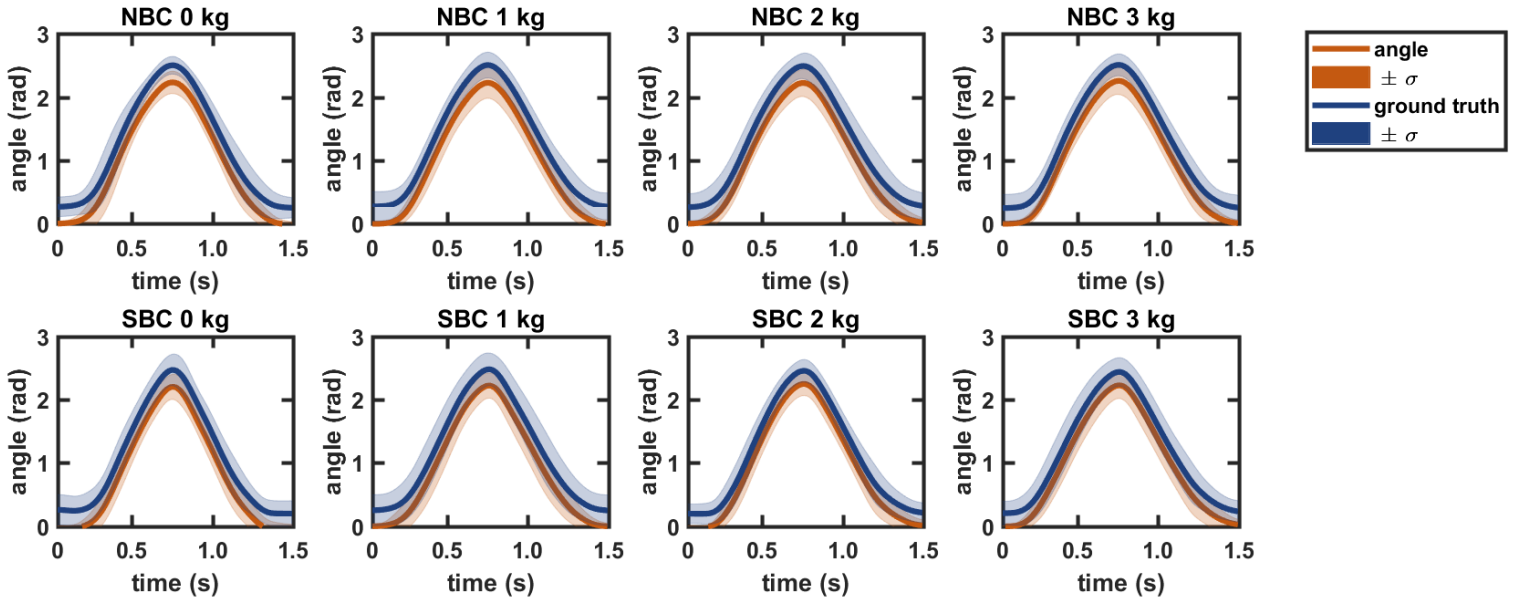

Figure 7.9 Experiment II: The mean and standard deviation of elbow angles found with static optimisation and using sEMG in orange. The mean and standard deviation of the measured angles considered the ground truth are shown in blue.

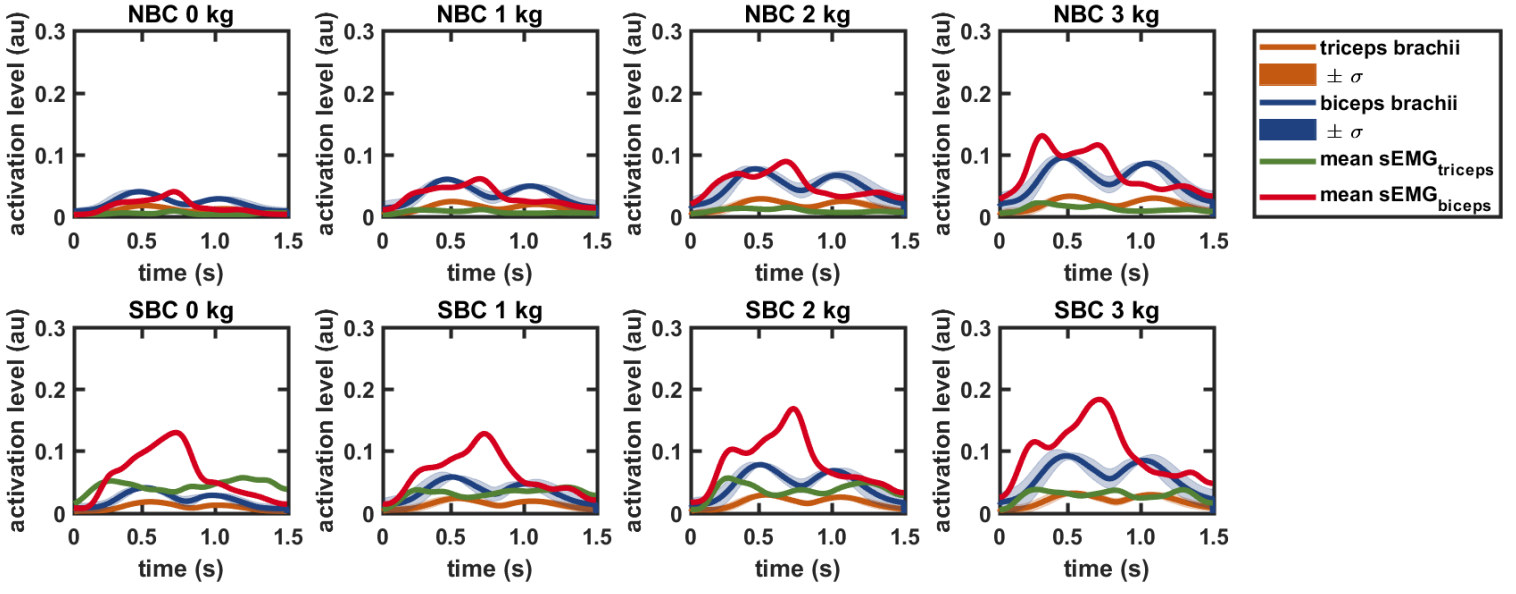

Figure 7.10 Experiment III: The means and standard deviations of the activations found with LQR feedback error correction without using sEMG. The mean of the measured sEMG features (ground truth) of the triceps brachii in green and of the biceps brachii in red.

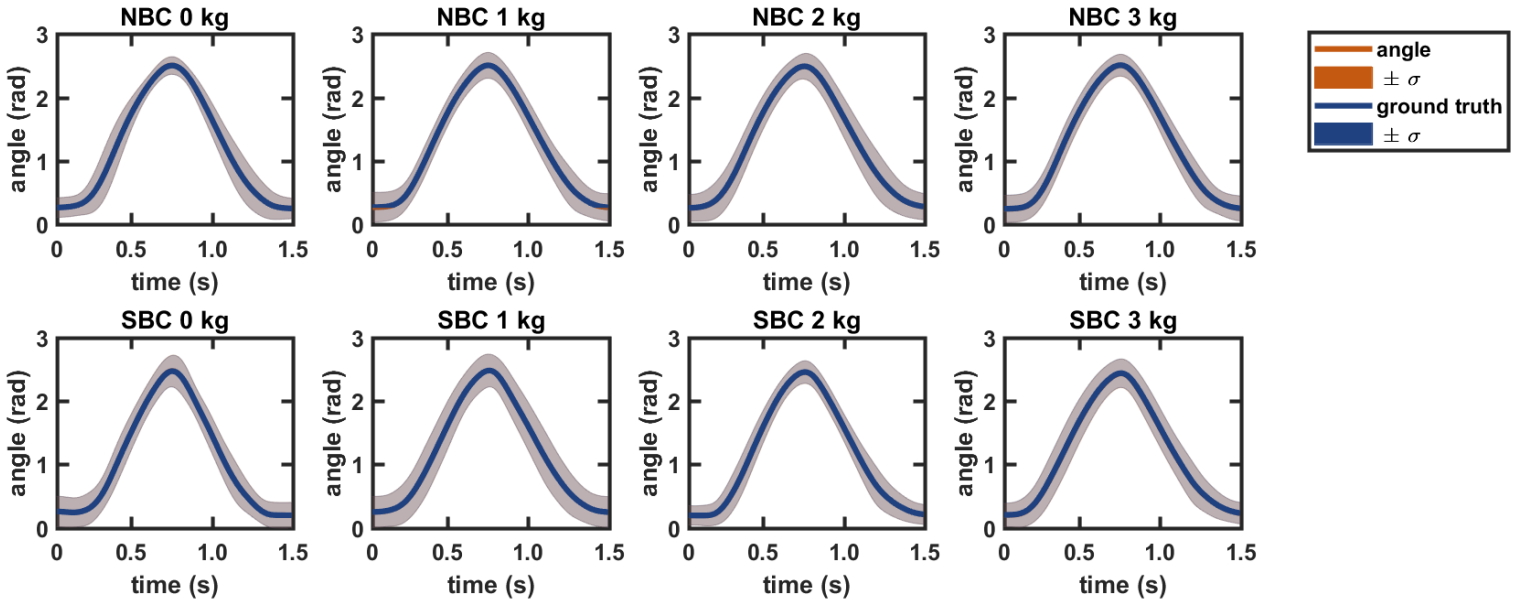

Figure 7.11 Experiment III: The mean and standard deviation of elbow angles found with LQR feedback error correction without using sEMG in orange. The mean and standard deviation of the measured angles considered the ground truth are shown in blue.

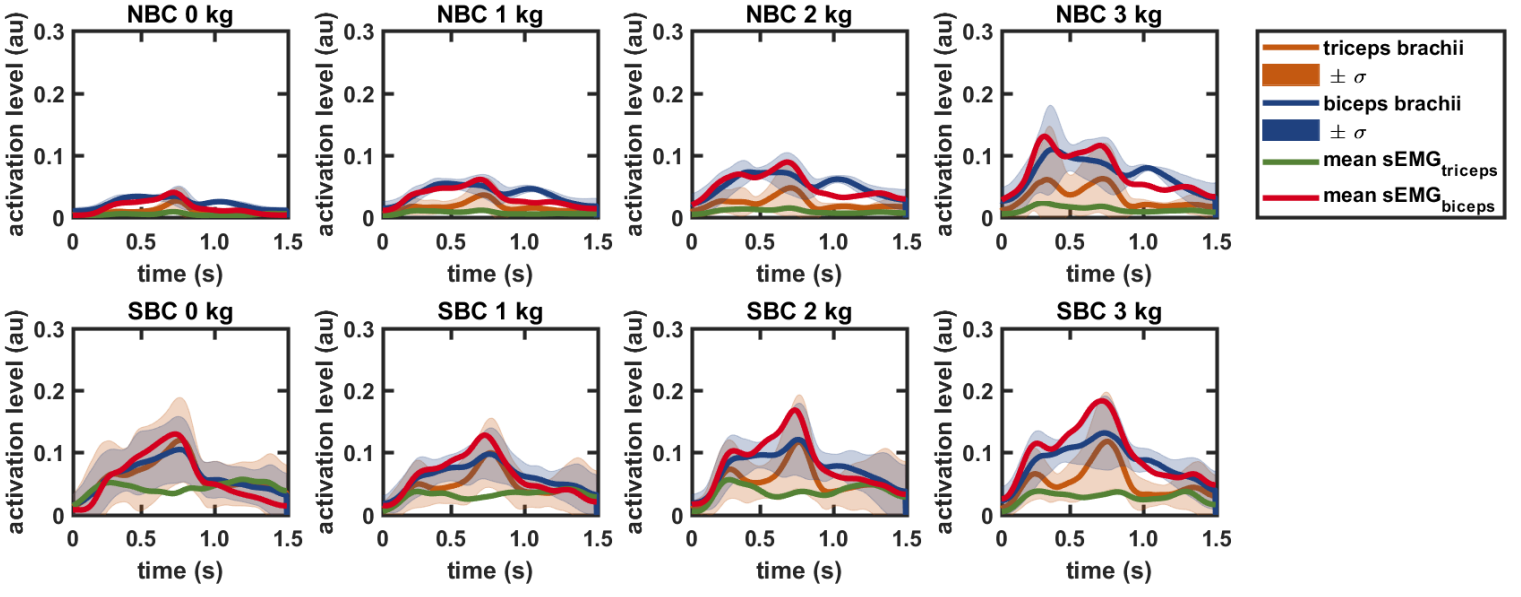

Figure 7.12 Experiment IV: The means and standard deviation of the activations found with LQR feedback error correction using sEMG. The mean of the measured sEMG features (ground truth) of the triceps brachii in green and of the biceps brachii in red.

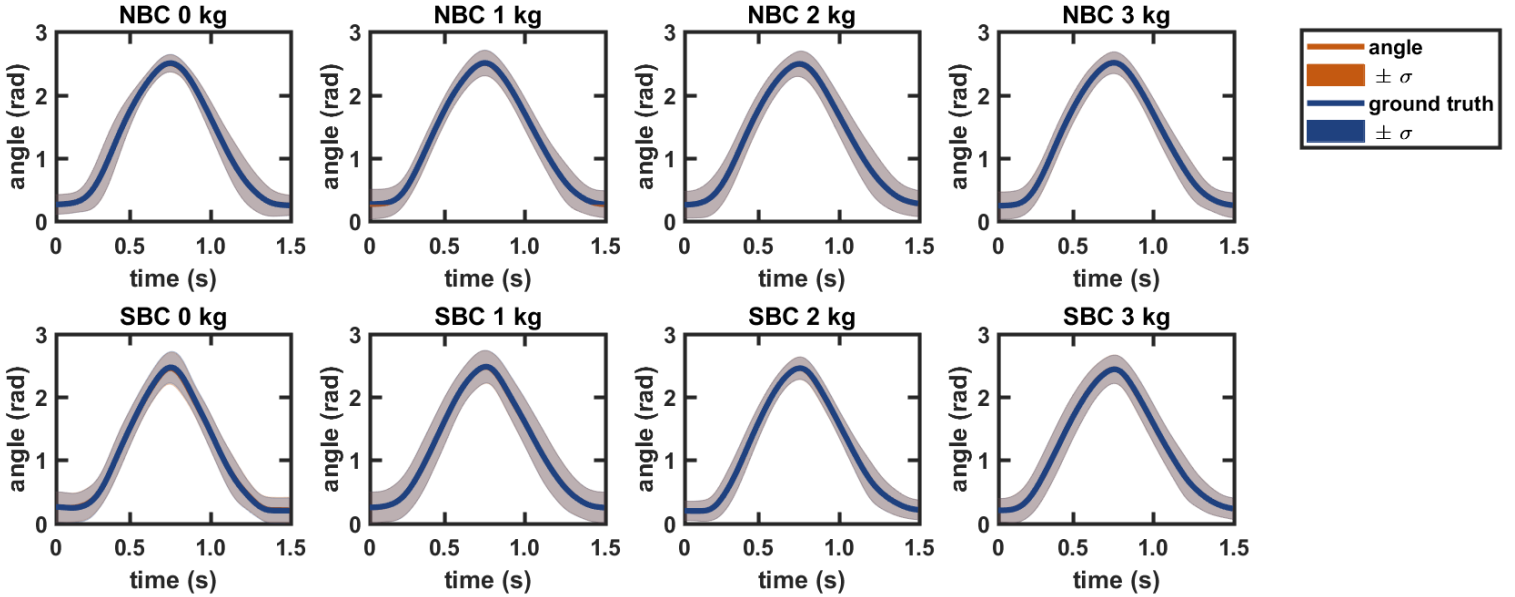

Figure 7.13 Experiment IV: The mean and standard deviation of elbow angles found with LQR feedback error correction using sEMG in orange. The mean and standard deviation of the measured angles considered the ground truth are shown in blue.

Table 7.2 Mean Pearson's correlation coefficients of activation signals and angle for the methods tested over all instructions and all volunteers. FM: forward modelling, SO: static optimisation, DO: dynamic optimisation.

	FM $\mu(\sigma)$	SO $\mu(\sigma)$	sEMG-SO $\mu(\sigma)$	DO $\mu(\sigma)$	sEMG-DO $\mu(\sigma)$
Biceps brachii ρ	~1 (~0)	0.38 (0.35)	0.79 (0.22)	0.18 (0.38)	0.72 (0.31)
Triceps brachii ρ	~1 (~0)	-0.06 (0.30)	0.72 (0.26)	-0.05 (0.36)	0.57 (0.35)
Angle ρ	0.54 (0.16)	~1 (~0)	~1 (~0)	~1 (~0)	~1 (~0)

Table 7.3 Mean e_{RMS} of activation signals and angle for the methods tested over all instructions and all volunteers. FM: forward modelling, SO: static optimisation, DO: dynamic optimisation.

	FM $\mu(\sigma)$	SO $\mu(\sigma)$	sEMG-SO $\mu(\sigma)$	DO $\mu(\sigma)$	sEMG-DO $\mu(\sigma)$
Biceps brachii	not applicable	0.05 (0.04)	0.03 (0.02)	0.05 (0.03)	0.03 (0.01)
Triceps brachii	not applicable	0.03 (0.03)	0.02 (0.02)	0.02 (0.03)	0.03 (0.03)
Angle (rad)	21.25 (25.81)	0.25 (0.21)	0.25 (0.21)	0.003 (0.002)	0.007 (0.006)

Table 7.4 Computational effort per method FM: forward modelling, SO: static optimisation, DO: dynamic optimisation.

	FM $\mu(\sigma)$	SO $\mu(\sigma)$	sEMG-SO $\mu(\sigma)$	DO $\mu(\sigma)$	sEMG-DO $\mu(\sigma)$
Time (s) (k=500)	0.017 (0.002)	4.35 (0.11)	4.34 (0.06)	0.87 (0.03)	0.87 (0.03)

7.6. Discussion

The goal of this chapter was to evaluate different methods for inverse dynamical modelling (IM) assisted by sEMG. As evaluation metrics we used: computational effort, accuracy, and physiologically realistic volunteer-specific solutions. For this test, we used a general framework based on state-space modelling. We tested two main approaches solving the IM problem: static optimisation (SO) and dynamic optimisation (DO). For both approaches, we developed a method based on the state model. We tested these models on an idealised 2nd order arm model. The dynamic variant outperformed the static one with respect to accuracy of angle tracking while in both cases the similarity between measured sEMG activity of the biceps and found activation pattern was kept to about 70%. The dynamic approach was 5 times more computationally efficient.

The forward modelling experiment with the simple model produced poor results: the average correlation was $\rho_{\varphi} = 0.54$ and the average RMS error was $\varphi_{RMS} = 1,218°$ (Figure 7.5). The input activations from sEMG (Figure 7.4) mostly resulted in inadequate outcomes (Figure 7.5). Only a few instructions of a few volunteers had some resemblance with the supposed arm movement. Most of the movements resulted in a flexed arm that ran into the upper boundary of the model. The expected relaxation to an extended arm posture did not follow because the produced forces based on sEMGs and resulting torques favoured the biceps muscle. Gravity forces and exerted triceps muscle forces could not counteract the biceps force. Consequently, the forward model performed somewhat better when cocontraction was stimulated during the stiff biceps curling (SBC) (Figure 7.5).

Without sEMG assistance, both SO and DO showed poor correlations between IM calculated activations patterns and measured activation patterns (Table 7.2). SO did not estimate cocontraction (Figure 7.7), whereas DO did (Figure 7.11). The correlation between the measured and tracked angle was high in SO, but unfortunately the φ_{RMS} was also high ($14°$). There was a systematic offset in the SO approach that apparently was not sufficiently penalised by the objective function (Figure 7.7). The DO method performed well on both measures ($\varphi_{RMS} = 0.2°$, $\rho_{\varphi} \sim 1$).

To obtain more realistic and volunteer-specific activation patterns, the sEMG-assisted approaches were introduced. Inclusion of the sEMG measurements drastically improved the correlations between measured activations and IM calculated activations, especially the biceps contribution (Table 7.2). SO triceps activations showed a reasonable ρ_e, whereas DO triceps activations were somewhat lower. Again, in SO the systematic error was present ($14°$); see Figure 7.9. When comparing DO with sEMG against DO without, the error rose to $\varphi_{RMS} = 0.4°$.

The computational time was low in both cases (Table 7.4). However, computational cost will drastically increase in the SO implementation for higher order systems because for each time step it iteratively optimises the objective function, and each iteration requires evaluating Jacobian matrices. DO has been reported to be 1000 times slower than SO [27]. In our case, this was avoided and even improved, because of the approach taken. LQR feedback is an approximation that is optimal for linear systems, and with time going to infinity, the feedback matrix becomes time invariant. Biological systems are usually nonlinear and with a finite time. Thus, our DO solution, which applies a linearisation of the system function, approximates the optimal control solution. Another advantage of the DO solution is that it is embedded in a state-space framework, thus enabling generalising capabilities e.g. enabling higher order models.

Although delivering promising results, some remarks have to be given. The influence of the design parameters of both SO and DO have not been fully optimised, e.g. by means of an extensive parameter search, and it has not been investigated how the cost matrices are optimised. This may alter the results significantly. Future research should therefore include a strategy to optimise all parameters (or perform sensitivity analysis).

The sEMG-assisted inverse modelling approaches enabled the difficult cocontraction prediction without the use of other cost terms as proposed by Forster et al. who considered joint stability an important factor aside from muscle efficiency [53]. They added a corresponding cost term. Shabani and Stavness also investigated a target joint stiffness cost term on postural stability and a short-range stiffness muscle model [54]. Another option was postulated by Raikova et al. who enforced cocontraction by allowing negative weighing factors [55]. Although both methods show cocontraction, those probably are not volunteer-specific. The approach we used may present more realistic volunteer-specific muscle activations.

The 2nd order arm model is a very simple approximation of reality. Given the forward results (Figure 7.5), it is by no means perfect in transforming sEMG features to corresponding forces and induced angles. This relationship may be improved by incorporating higher order systems, such as described by Yamasaki et al. [24]. The parameters of the arm model that we took from the literature do not represent volunteer-specific properties (Table 7.1), such as arm length, mass, muscle fibre orientations, etc. Follow-up studies may incorporate volunteer-specific data. Eventually, we aspire to implement these methods in even more complex systems, such as the face and lips, and tongue.

Also, this simple arm model contained only the long heads of the biceps and the triceps muscles. In reality, the short head of the biceps, the medial and lateral head of the triceps, the brachioradialis, and the brachialis muscle also play a role in flexion and extension of the elbow. Unloaded flexion of the arm showed low activity in triceps and biceps long head (Figure 7.4). This can be explained by the fact that unloaded elbow flexion is mainly performed by the brachialis [40,56]. Another limitation was that the shoulder joint was fixed, and so the motion was limited to the anterior-posterior and cranial-caudal axis. Enforcing a 2D plane instead of 3D movements caused an underestimation of internal loads of up to 60% in the lower extremity [57]. However, the 2D view can be used as a reasonable estimate of main movements. Unfortunately, movement of the upper extremity is more versatile and rotations of the shoulder joint lead to nonintuitive descriptions of rotational kinematics [58].

Other interesting cost terms such as optimising muscle stress or oxygen consumption were not considered here, but may add useful information. Praagman et al. suggested that oxygen consumption is the better candidate for an energy-related cost term [59]. It resulted in more realistic muscle activation patterns during inverse dynamics of a simple arm model.

The proposed sEMG-assisted inverse modelling approach can help to obtain physiologically correct and person-specific muscle activation patterns and can establish the naturally occurring cocontraction of antagonists. The work described here may now be extended to the more challenging environment of the lips, where many muscles operate to perform the various facial expressions, and thus the ambiguity problem is more apparent.

If this is successful and computational time does not exceed unacceptable limits, the last hurdle is to apply it on complex muscular structures like the tongue muscle, with its intertwining muscle fibres. Simulating orofacial structures is required for our ultimate goal of virtual head and neck surgery. Inverse modelling remains an essential component, as new activation patterns – based on physiological realistic patterns – need to be calculated after the virtual surgery on a digital model in order to estimate post-operative functional movements. Challenges, related to measuring sEMG, such as crosstalk, have to be tackled, too, in anatomical locations with many overlapping muscles, like the perioral region and face.

7.7. Conclusion

The sEMG-assisted approaches described here taking into account volunteer-specific muscle activation signals improved the estimation of muscle activations with inverse dynamics modelling in a simple arm model. The physiological cocontractions as recorded during the measurements were also seen in the sEMG-assisted inverse dynamics experiments but not in the experiments without sEMG tracking. The DO solution (LQR method) proved most feasible, with adequate results, acceptable computational time, and capability to generalise to higher-order models.

7.8. Aknowledgements

The authors gratefully acknowledge the volunteers for engaging in this project. Furthermore a word of thanks goes to the Maurits en Anna de Kock Foundation (www.mauritsenannadekockstichting.nl) for funding the Porti EMG system. Lastly, they would like to thank Jasper A. Nijkamp PhD for lending the NDI Polaris Spectra system and Martijn M. Stuiver PhD for assisting in the development of the instruction set.

7.9. Conflict of interest

The authors declare that they have no conflict of interest.

7.10. Funding

No funding was acquired for this research.

7.11. Ethical approval

The described project involved healthy human volunteers. The performed measurements were noninvasive and not stressful. There was no infringement of the (psychological) integrity of the volunteers. Therefore, no ethical approval was required. The study was performed in accordance with Dutch legislation, including the Agreement on Medical Treatment Act, Personal Data Protection Act, and the Code of Conduct for Responsible Use of the Federa (Dutch Federation of Biomedical Scientific Societies). Approval was given by the Ethics Committee of the University of Twente. Volunteers were recruited by e-mail with a short explanation about the study. They also received information on the nature of our experiment and on their rights as volunteers (including the right to opt out at any moment without any need to explain). They all gave their consent to the publication of anonymised results.

7.12. References

1. Farina D, Merletti R, Enoka RM. The extraction of neural strategies from the surface EMG. J Appl Physiol. 2004;96: 1486–1495. doi:10.1152/japplphysiol.01070.2003

2. Farina D, Merletti R, Enoka RM. The extraction of neural strategies from the surface EMG: an update. J Appl Physiol. 2014;117: 1215–1230. doi:10.1152/japplphysiol.00162.2014

3. Woods JJ, Bigland-Ritchie B. Linear and non-linear surface EMG/force relationships in human muscles. An anatomical/functional argument for the existence of both. Am J Phys Med. 1983;62: 287–99. Available: http://www.ncbi.nlm.nih.gov/pubmed/6650674

4. Lawrence JH, De Luca CJ. Myoelectric signal versus force relationship in different human muscles. J Appl Physiol. 1983;54: 1653–9. Available: http://www.ncbi.nlm.nih.gov/pubmed/6874489

5. Higginson JS, Ramsay JW, Buchanan TS. Hybrid models of the neuromusculoskeletal system improve subject-specificty. Proc Inst Mech Eng H. 2012;226: 113–119.

6. Buchanan TS, Lloyd DG, Manal K, Besier TF. Neuromusculoskeletal Modeling: Estimation of Muscle Forces and Joint Moments and Movements From Measurements of Neural Command. J Appl Biomech. 2004;20: 367–395. Available: https://www.ncbi.nlm.nih.gov/pmc/articles/PMC1357215/

7. Erdemir A, Mclean S, Herzog W, van den Bogert AJ. Model-Based Estimation of Muscle Forces Exerted During Movements. Clin Biomech. 2007;22: 131–154. doi:10.1016/j.clinbiomech.2006.09.005

8. Sartori M, Farina D, Lloyd DG. Hybrid neuromusculoskeletal modeling to best track joint moments using a balance between muscle excitations derived from electromyograms and optimization. J Biomech. 2014;47: 3613–21. doi:10.1016/j.jbiomech.2014.10.009

9. Eskes M, Balm AJM, van Alphen MJA, Smeele LE, Stavness I, van der Heijden F. Simulation of facial expressions using person-specific sEMG signals controlling a biomechanical face model. Int J Comput Assist Radiol Surg. 2017; doi:10.1007/s11548-017-1659-5

10. Eskes M, Balm AJM, van Alphen MJA, Smeele LE, Stavness I, Heijden van der F. sEMG-assisted inverse modelling of 3D lip movement: a feasibility study towards person-specific modelling. Sci Reports Nat. 2017;

11. Happee R, Van der Helm FC. The control of shoulder muscles during goal directed movements, an inverse dynamic analysis. J Biomech. 1995;28: 1179–91. Available: http://www.ncbi.nlm.nih.gov/pubmed/8550636

12. Shao Q, Bassett DN, Manal K, Buchanan TS. An EMG-driven model to estimate muscle forces and joint moments in stroke patients. Comput Biol Med. 2009;39: 1083–8. doi:10.1016/j.compbiomed.2009.09.002

13. Ding QC, Xiong a. B, Zhao XG, Han JD. A novel EMG-driven state space model for the estimation of continuous joint movements. 2011 IEEE Int Conf Syst Man, Cybern. 2011; 2891–2897. doi:10.1109/ICSMC.2011.6084104

14. Stavness I, Lloyd JE, Fels S. Automatic prediction of tongue muscle activations using a finite element model. J Biomech. 2012;45: 2841–2848. doi:10.1016/j.jbiomech.2012.08.031

15. Pitermann M, Munhall KG. An inverse dynamics approach to face animation. J Acoust Soc Am. 2001;110: 1570. doi:10.1121/1.1391240

16. Van der Helm F. a Finite Element Musculoskeletal the Shoulder Mechanism. J Biomech. 1994;27: 551–559.

17. Pizzolato C, Lloyd DG, Sartori M, Ceseracciu E, Besier TF, Fregly BJ, Reggiani M. CEINMS: A toolbox to investigate the influence of different neural control solutions on the prediction of muscle excitation and joint moments during dynamic motor tasks. J Biomech. 2015;48: 3929–3936. doi:10.1016/j.jbiomech.2015.09.021

18. Amarantini D, Martin L. A method to combine numerical optimization and EMG data for the estimation of joint moments under dynamic conditions. J Biomech. 2004;37: 1393–1404. doi:10.1016/j.jbiomech.2003.12.020

19. Lloyd DG, Besier TF. An EMG-driven musculoskeletal model to estimate muscle forces and knee joint moments in vivo. J Biomech. 2003;36: 765–776. doi:10.1016/S0021-9290(03)00010-1

20. S. Shourijeh M, Smale KB, Potvin BM, Benoit DL. A forward-muscular inverse-skeletal dynamics framework for human musculoskeletal simulations. J Biomech. 2016;49: 1718–1723. doi:10.1016/j.jbiomech.2016.04.007

21. Cholewicki J, McGill SM, Norman RW. Comparison of muscle forces and joint load from an optimization and EMG assisted lumbar spine model: Towards development of a hybrid approach. J Biomech. 1995;28: 321–331. doi:10.1016/0021-9290(94)00065-C

22. Dul J, Townsend MA, Shiavi R, Johnson GE. Muscular synergism-I. On criteria for load sharing between synergistic muscles. J Biomech. 1984;17: 663–673. doi:10.1016/0021-9290(84)90120-9

23. Dul J, Johnson GE, Shiavi R, Townsend MA. Muscular synergism-II. A minimum-fatigue criterion for load sharing between synergistic muscles. J Biomech. 1984;17: 675–684. doi:10.1016/0021-9290(84)90121-0

24. Yamasaki T, Idehara K, Xin X. Estimation of muscle activity using higher-order derivatives, static optimization, and forward-inverse dynamics. J Biomech. 2016;49: 2015–22. doi:10.1016/j.jbiomech.2016.04.024

25. Pandy MG. Computer modeling and simulation of human movement. Annu Rev Biomed Eng. 2001;3: 245–73. doi:10.1146/annurev.bioeng.3.1.245

26. Tsirakos D, Baltzopoulos V, Bartlett R. Inverse optimization: functional and physiological considerations related to the force-sharing problem. Crit Rev Biomed Eng. 1997;25: 371–407. Available: http://www.ncbi.nlm.nih.gov/pubmed/9505137

27. Anderson FC, Pandy MG. Static and dynamic optimization solutions for gait are practically equivalent. J Biomech. 2001;34: 153–61. Available: http://www.ncbi.nlm.nih.gov/pubmed/11165278

28. Morrow MM, Rankin JW, Neptune RR, Kaufman KR. A comparison of static and dynamic optimization muscle force predictions during wheelchair propulsion. J Biomech. 2014;47: 3459–3465. doi:10.1016/j.jbiomech.2014.09.013

29. Vigouroux L, Quaine F, Labarre-vila A, Amarantini D. Using EMG data to constrain optimization procedure improves finger tendon tension estimations during static fingertip force production. 2007;40: 2846–2856. doi:10.1016/j.jbiomech.2007.03.010

30. Seth A, Pandy MG. A neuromusculoskeletal tracking method for estimating individual muscle forces in human movement. J Biomech. 2007;40: 356–66. doi:10.1016/j.jbiomech.2005.12.017

31. van Alphen MJA, Eskes M, Smeele LE, Balm AJM, van der Heijden F. In vivo intraoperative hypoglossal nerve stimulation for quantitative tongue motion analysis. Comput Methods Biomech Biomed Eng Imaging Vis. 2015;1163: 1–7. doi:10.1080/21681163.2015.1072056

32. Eskes M, van Alphen MJA, Smeele LE, Brandsma D, Balm AJM, van der Heijden F. Predicting 3D lip movement using facial sEMG: a first step towards estimating functional and aesthetic outcome of oral cancer surgery. Med Biol Eng Comput. 2017;55: 573–583. doi:10.1007/s11517-016-1511-z

33. van Dijk S, van Alphen MJA, Jacobi I, Smeele LE, van der Heijden F, Balm AJM. A New Accurate 3D Measurement Tool to Assess the Range of Motion of the Tongue in Oral Cancer Patients: A Standardized Model. Dysphagia. 2016;31: 97–103. doi:10.1007/s00455-015-9665-7

34. Kreeft AM, Tan IB, Leemans CR, Balm AJM. The surgical dilemma in advanced oral and oropharyngeal cancer: how we do it. Clin Otolaryngol. 2011;36: 260–266. doi:10.1111/j.1749-4486.2011.02299.x

35. Kreeft AM, van der Molen L, Hilgers FJ, Balm AJ. Speech and swallowing after surgical treatment of advanced oral and oropharyngeal carcinoma: a systematic review of the literature. Eur Arch Otorhinolaryngol. 2009;266: 1687–1698. doi:10.1007/s00405-009-1089-2

36. van Alphen MJA, Kreeft AM, van der Heijden F, Smeele LE, Balm AJM. Towards virtual surgery in oral cancer to predict postoperative oral functions preoperatively. Br J Oral Maxillofac Surg. 2013;51: 747–751. doi:10.1016/j.bjoms.2013.06.012

37. Eskes M, van Alphen MJA, Balm AJM, Smeele LE, Brandsma D, van der Heijden F. Predicting 3D lip shapes using facial surface EMG. Zhang Y, editor. PLoS One. 2017;12: e0175025. doi:10.1371/journal.pone.0175025

38. Bélaise C, Dal Maso F, Michaud B, Mombaur K, Begon M. An EMG-marker tracking optimisation method for estimating muscle forces. Multibody Syst Dyn. 2017; doi:10.1007/s11044-017-9587-2

39. Buchanan TS, Moniz MJ, Dewald JP, Zev Rymer W. Estimation of muscle forces about the wrist joint during isometric tasks using an EMG coefficient method. J Biomech. 1993;26: 547–60. Available: http://www.ncbi.nlm.nih.gov/pubmed/8478356

40. Koo TKK, Mak AFT. Feasibility of using EMG driven neuromusculoskeletal model for prediction of dynamic movement of the elbow. J Electromyogr Kinesiol. 2005;15: 12–26. doi:10.1016/j.jelekin.2004.06.007

41. Buchanan TS, Lloyd DG, Manal K, Besier TF. Estimation of Muscle Forces and Joint Moments Using a Forward-Inverse Dynamics Model. Med Sci Sport Exerc. 2005;37: 1911–1916. doi:10.1249/01.mss.0000176684.24008.6f

42. Pandy MG, Anderson FC, Hull DG. A Parameter Optimization Approach for the Optimal Control of Large-Scale Musculoskeletal Systems. J Biomech Eng. 1992;114: 450. doi:10.1115/1.2894094

43. Luenberger DG. Introduction to Dynamic Systems: Theory, Models & Applications. 1st ed. Wiley. 1979.

44. Cram JR, Kasman GS, Holtz J. Atlas for Electrode Placement. In: Criswell E, editor. Cram's Introduction to Surface Electromyography. 2nd ed. 2011. p. 412.

45. Criswell E, editor. Cram's Introduction to Surface Electromyography. Bartlett Publishers. 2010.

46. De Luca CJ, Gilmore LD, Kuznetsov M, Roy SH. Filtering the surface EMG signal: Movement artifact and baseline noise contamination. J Biomech. 2010;43: 1573–9. doi:10.1016/j.jbiomech.2010.01.027

47. Cavanagh PR, Komi P V. Electromechanical delay in human skeletal muscle under concentric and eccentric contractions. Eur J Appl Physiol Occup Physiol. 1979;42: 159–163. doi:10.1007/BF00431022

48. Norman RW, Komi P V. Electromechanical delay in skeletal muscle under normal movement conditions. Acta Physiol Scand. 1979;106: 241–248. doi:10.1111/j.1748-1716.1979.tb06394.x

49. Manal K, Gonzalez R V, Lloyd DG, Buchanan TS. A real-time EMG-driven virtual arm. 2002;32: 25–36.

50. Burden A, Bartlett R. Normalisation of EMG amplitude: an evaluation and comparison of old and new methods. Med Eng Phys. 1999;21: 247–57. doi:10.1016/S1350-4533(99)00054-5

51. Burden A. How should we normalize electromyograms obtained from healthy participants? What we have learned from over 25 years of research. J Electromyogr Kinesiol. 2010;20: 1023–35. doi:10.1016/j.jelekin.2010.07.004

52. Halaki M, Gi K. Normalization of EMG Signals: To Normalize or Not to Normalize and What to Normalize to? Computational Intelligence in Electromyography Analysis - A Perspective on Current Applications and Future Challenges. 2012. doi:10.5772/49957

53. Forster E, Simon U, Augat P, Claes L. Extension of a state-of-the-art optimization criterion to predict co-contraction. J Biomech. 2004;37: 577–81. doi:10.1016/j.jbiomech.2003.09.003

54. Shabani M, Stavness I. Simulating the effect of muscle stiffness and co-contraction on postural stability. Comput Methods Biomech Biomed Eng Imaging Vis. 2017;1163: 1–12. doi:10.1080/21681163.2017.1332530

55. Raikova R. About weight factors in the non-linear objective functions used for solving indeterminate problems in biomechanics. 1999;32: 689–694.

56. Basmajian J V, Latif A. Integrated actions and functions of the chief flexors of the elbow: a detailed electromyographic analysis. J Bone Joint Surg Am. 1957;39–A: 1106–18. Available: http://www.ncbi.nlm.nih.gov/pubmed/13475410

57. Glitsch U, Baumann W. the Three-Dimensional Determination of Internal Loads in the Lower Extremity. J Biomech. 1997;30: 1123–1131.

58. Rau G, Disselhorst-Klug C, Schmidt R. Movement biomechanics goes upwards: From the leg to the arm. J Biomech. 2000;33: 1207–1216. doi:10.1016/S0021-9290(00)00062-2

59. Praagman M, Chadwick EKJ, Van Der Helm FCT, Veeger HEJ. The relationship between two different mechanical cost functions and muscle oxygen consumption. J Biomech. 2006;39: 758–765. doi:10.1016/j.jbiomech.2004.11.034

PART IV

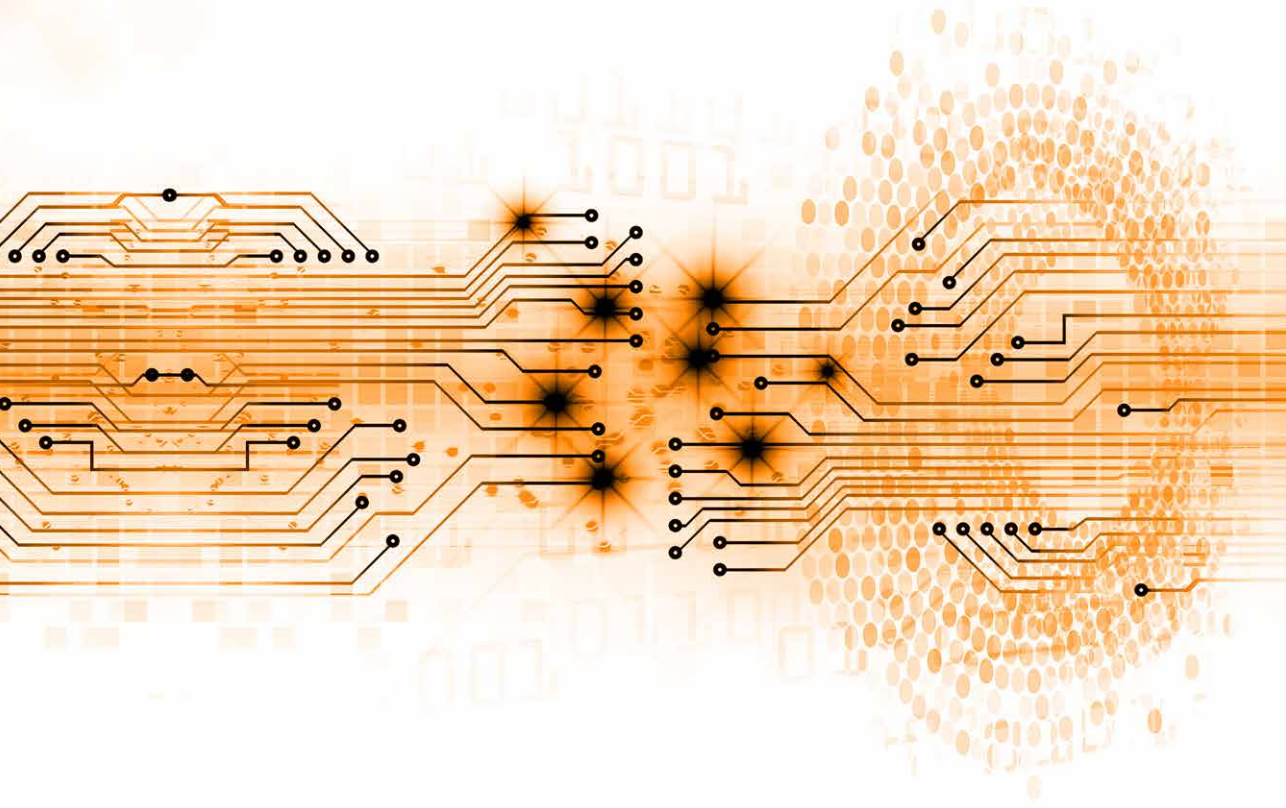

VIII

SUMMARY, CONCLUSIONS AND FUTURE PERSPECTIVES

8.1. Summary per chapter

8.1.1. Chapter I Clinical background

Chapter 1 outlines the clinical framework that has motivated the work presented in this dissertation. The term 'functional inoperability' is still relatively new, and despite its use being an upcoming trend, its exact definition – or, possibly, interpretation – is still no common ground among professionals. The fact that various advanced cases of head and neck cancer may be considered functionally inoperable by one group of professionals but operable by another illustrates that both the choice of treatment and the choice to treat or not to treat are mostly subjective. Rather than drawing on theoretical knowledge alone, clinicians largely base their decisions on personal experience. Additionally, complex patient-specific variations in anatomy, geometry and motor control tend to blur the expectations of the multidisciplinary treatment team on functional outcome.

The Virtual Therapy Group was established in 2009 and started off with an exploration into the uncultivated field of research on functional inoperability and methods to improve predictions of patient-specific functional outcome. The idea has been to create patient-specific biomechanical models, incorporating patient-specific geometry, anatomy, realistic physiology, motor control, and treatment modules. With the final creation of a digital doppelgänger, we aim to significantly improve patient counselling by showing potential aesthetic appearances as well as demonstrating synthesised pathological speech and estimating possible function loss, for instance with respect to mastication or swallowing.

8.1.2. Chapter II Technical background

Chapter 2 describes the bare technical essentials required for this dissertation, giving a short introduction of the world of muscle physiology and muscle modelling alongside the milestones in the history of electromyography (EMG). This chapter touches upon the origins of bioelectrical activity and the methods of measuring the activity of the tiny facial muscles. It then continues with a brief history of biomechanics, starting with Aristotle's "On the movement of animals," which was considered the first study in biomechanics, and finally arriving in the field of modern computational biomechanics, which, with its exponential increase of computational powers, has boosted biomechanical research.

We have explained the use of statistical models in Chapter 3 and Chapter 4. Before embarking on a journey with difficult biomechanical models that incorporate numerous adjustable parameters and require more computational power, we had to demonstrate the practical use of electromyography and the information it can convey on facial muscle activation. After all, only few studies had used facial surface electromyography (sEMG) before to predict lip shapes or movements, and they all had their drawbacks. Our successful demonstration calls for further incorporation into biomechanical models. Realistic forward modelling will be crucial to simulate movements with an adjusted model after virtual therapy, whereas inverse modelling will be vital to obtain possible muscle activation patterns that may compensate resected muscles in critical functional movements.

8.1.3. Chapter III Statistical shape modelling

In Chapter 3 we have investigated whether surface electromyography could convey enough useful information about the activations of facial muscles to establish a statistical relationship between volunteer-specific lip shapes and features calculated from measured surface electromyographic signals. The statistical models based on either principal component analysis or an extended form of the generalised regression neural network indeed demonstrated the hidden information in these sEMG features. We were able to predict 3D lip shapes with good accuracy and with an average of about 2.8 mm root mean square (RMS) error for both methods. Despite the roughly equal performance of both methods, principal component analysis proved more consistent and was better able to adapt to unknown shapes. We evaluated many features and processing parameters, such as window length, principal component analysis dimension, electrode configuration, and tuning parameters. Five volunteers participated in testing general applicability. To the best of our knowledge this is the first study that accurately predicted 3D lip shapes for an extensive set of instructions. based on patient-friendly sEMG.

8.1.4. Chapter IV Implementation of dynamics

Whereas in Chapter 3, we demonstrated the feasibility of estimating static 3D lip shapes with sEMG features, this fourth chapter builds upon the satisfactory results and incorporates dynamics. Dynamics are extremely important for functional movements. We captured 3D lip movements for all Dutch visemes (combined speech sounds that visually look the same to [expert] lip readers; e.g., /mama/ and /papa/), meaningful facial expressions, and a couple of dynamic motion transfers in five volunteers, who followed 19 different instructions four times over. Simultaneously, we recorded sixteen sEMG signals from eight muscles bilaterally, which produced a major improvement over the results described in the previous chapter. We used state-space representation to describe the relationship between 3D lip positions and sEMG features. Because the principal component analysis method had proved more consistent, as described in the previous chapter, this method was used to establish the relationship between sEMG features and 3D lip positions as the estimator in the measurement model. We used a truncated Taylor series of order two to account for potential nonlinearities. The dynamics were provided by a first-order and a second-order Kalman filter. We applied an extensive search optimisation to attain optimal fudging parameters that were used to fine-tune the system. This dynamic 3D lip model proved more accurate than the one described in Chapter 3. The first-order system resulted in a 2.43 mm RMS error and the second-order system in a 2.46 mm RMS error. These promising results will lead us further to application in biomechanical models.

8.1.5. Chapter V A step towards biomechanical models: forward modelling

After our statistical exploration had proved that there is valuable information to be had from sEMG, which may be used in predicting 3D lip shapes and 3D lip movements, we were able to take a step towards application in biomechanical face models.

The generic face model in the ArtiSynth simulation environment was adapted to meet our requirements. The finite-element face model's soft tissue was represented by three layers of 6,342 elements (6,024 linear hexahedral and 318 linear wedges), and 8,720 nodes. Twenty finite-element facial muscles were modelled. Tissue and muscle parameters were based on literature values. While six volunteers performed six different facial expressions five times over, we recorded their muscle activity using sEMG and their 3D lip movements using a high-speed triple-camera set-up. The biomechanical face model was controlled with features calculated from the sEMG signals under three different activation strategies: activation of all muscles, activation of the muscles considered relevant per instruction, and activation of the three muscles that showed the highest activity. The corresponding simulated movements were compared to the actual movement measured with 3D correlation coefficients. The median 3D correlation coefficient for the three different activation strategies were: 0.45, 0.77 and 0.78, respectively. These promising results on generic models will pave the way towards personalised biomechanical models with person-specific motor control.

8.1.6. Chapter VI Inverse dynamics and sEMG-assistance

Crucially, forward modelling of 3D lip movement proved feasible in generic models. It will be evident that inverse modelling needs to be addressed, too. Inverse modelling will be essential for estimating which muscle activation patterns may compensate if specific muscles are set inactive to simulate nerve damage, or if muscle tissue is resected virtually. It may provide insight into residual ability to perform important functional movements, and it may indicate which muscle activation patterns could still produce those elementary functions. In this Chapter, we have introduced a novel forward-dynamics-assisted data tracking approach, in which we tracked not only 3D lip movement but also muscle activity of fourteen facial muscles using calculated features from measured sEMG. To our knowledge, only Bélaise et al. came up with a similar innovative idea, around the same time as we did [1]. However, they used simulation data, whereas we used real measurements. First, to test the applicability of the inverse algorithm, we performed inverse modelling on the simulated data of the previous chapter – the forward solution. Good results were obtained with mean 3D correlation coefficients of about 0.93 for 3D lip movement. Without sEMG-tracking, mean muscle activation correlations were around 0.27, which improved to about 0.44 when we tracked all muscles, and even more when we tracked only relevant muscles: 0.84. Switching to real measurement data, mean 3D correlations of lip movement were 0.67 (without sEMG-tracking) and 0.70 (with sEMG-tracking). The mean muscle activation correlations were 0.21 and 0.60, respectively. With these satisfactory results, we have concluded that the novel idea of including a sEMG-tracking cost term in forward-dynamics assisted data tracking produces more realistic volunteer-specific muscle activations, without sacrificing accuracy in 3D movement tracking.

8.1.7. Chapter VII Feedback, optimal control and sEMG-assisted solutions for inverse modelling

The first attempt toward inverse-modelling of 3D lip movement with realistic muscle activation patterns has been described in Chapter 6. Although the first results were promising, it is not clear whether this method would be the most suited, considering computational time, accuracy, and realistic muscle activation patterns as outcomes. This chapter aims to compare two inverse modelling methods both with and without sEMG tracking to obtain realistic volunteer-specific muscle activation signals. A simplified model of the arm containing the triceps and biceps muscles was used. We recorded sEMG data of the biceps and triceps muscles from eight volunteers, who performed stiff and normal biceps curling experiments with dumbbells varying in weight: 0, 1, 2, and 3 kg. Meanwhile, the shoulder, elbow, and wrist joints were optically tracked using the NDI Aurora system. Elbow angle and angular velocity were calculated and used as motion targets. sEMG signals were transformed to muscle activation signals following the approach described by Buchanan et al. [2]. Static optimisation by means of forward-dynamics assisted data tracking was performed as described in the previous chapter. Theoretically, optimal control theory would bring the best solutions for our inverse problems [3]. However, direct application of this theory exploiting, for instance, dynamic programming or the maximum principle of Pontryagin appeared infeasible due to the computational load. The optimal control approach can be approximated with an LQR feedback regulator used for error correction and applied in an extended Kalman framework.

8.2. From generic to personalised models

Generic biomechanical models are very useful to simulate complex in vivo pathophysiological processes. However, in this era of personalised treatment, it has become increasingly important to focus on the personalisation of generic models. The virtual therapy project aims to predict the functional outcome of head and neck cancer treatment and to tailor treatment to the individual patient. This is done by acquiring lots of patient-specific data that may serve as input for generic models. These data are necessary for developing techniques to adapt generic models to the individual patients and techniques that resemble treatment effects in these models [4–11]. Ultimately, such models may be used to predict functional outcome, to simulate speech, and to simulate modified aesthetics. Increasing awareness that individuals do not only react differently to treatment but also recover differently because of compensatory mechanisms, motivational aspects, and rehabilitation efforts, creates the need for such individual approach. To estimate function loss after treatment, and consequently to determine which treatment will be most suitable for the individual patient, models require extensive personalised input information obtained from all sorts of physiological measurements. One way of personalising generic models of the head and neck region is supplying the models with person-specific motor control or, more specifically, the individual muscle activation patterns. As mentioned in this dissertation, EMG can provide an indication of which muscles are being activated and, in some way, to what extent. The use of muscle activation patterns is the central theme of this dissertation.

To avoid invasive intramuscular EMG techniques with needle or wire electrodes, we chose to use surface electrodes. The generic models used in this dissertation are controlled by personalised muscle activation patterns extracted from the signals acquired with surface EMG. This is the first step towards personalisation of biomechanical models. However, we will need to address a broad range of other personalisation parameters before we can genuinely speak of a digital doppelgänger. Among these will be gross anatomy, geometry, tissue parameters, muscle fibre orientations, nerve trajectories, and tissue mobility.

In summary, our current research has demonstrated the significant contribution of sEMG measurements (Chapter 3 and Chapter 4) to the personalisation of the generic biomechanical models (Chapter 5 and Chapter 6). To further tailor these models to the individual patient's condition, we have formulated the following future directions:

1. Improving muscle innervation estimation and electromyography techniques
2. Obtaining information on individual anatomy and geometry
3. Using sEMG as a proposed personalisation parameter
4. Improving the biomechanical models

8.2.1. Ad 1. Muscle innervation and electromyography

Limiting factors and high-density surface electromyography as a solution

To start off with a quote on electromyography by Carlo J. de Luca: "To its detriment, electromyography is too easy to use and consequently too easy to abuse" [12]. Indeed, acquiring these signals is relatively easy and can be performed without the use of invasive techniques. On the other hand, quantitative reproducibility is poor, and it gives only a crude estimate of the actual neural motor control. After all, EMG amplitudes depend on many factors, including the location of electrodes, amount of fatty tissue, amount of recruitment of motor units et cetera (Table 2.3, Chapter 2) [12,13]. To demonstrate this delicate interdependence, we performed a replacement experiment, see Figure 8.2. Even though it was the same instructor who applied the electrodes in accordance with our measurement protocol, errors arose. The first application (carrot orange) differed from the second application a week later (navy blue). The third application was performed directly after experiment two (sunset red). It seemed that even by marking the electrode locations to be able to reposition them exactly right, we could not avoid all errors if honouring the constraint that all electrodes should measure sEMG activity. The total RMS error between electrode placement at epoch = 1 and epoch = 2 was 10.95 mm. Between epoch = 1 and epoch = 3, it was 9.09 mm. Immediate replacement improved the placement accuracy to a total RMS error between epoch = 2 and epoch = 3 of 5.34 mm. The corresponding sEMG features are shown in Figure 8.1. The effect of placement and time effects on sEMG can be derived for the instruction 'voluntary smile'. Possibly, location errors could be further minimised at the expense of not measuring any signal or measuring signals with low signal-to-noise ratios.

The future use of high-density sEMG (HD-sEMG) in our experiments will require advanced processing and analytics but may neutralise the placement issue, as the whole muscle and the propagation of activation signals can be monitored [14]. Lapatki et al. demonstrated the feasibility of selecting the optimal electrode configuration and interelectrode distance on such HD-sEMG grids and proposed optimal placement of surface electrodes in the lower face region [15]. As the electrodes on an HD-sEMG grid measure the contribution of the same motor units at slightly different locations, we can deduce information on size, depth, and location of motor units [16]. Additionally, we may find out more about muscle fibre directions.

Another important aspect is the decomposition of sEMG into motor units, which has not been addressed in this dissertation because in this challenging endeavour the use of HD-sEMG is indispensable. Together with sophisticated statistical techniques such as blind source separation, fingerprints of the motor units can be statistically derived [17,18]. Figure 8.3 shows a simulated muscle cross-section with motor unit territories and the corresponding multichannel motor unit action potentials of three spatially different motor units [17]. These techniques may be extra beneficial in the complex intertwined musculature of intraoral structures like the tongue, yielding more information about muscle innervations, and together with advanced imaging techniques – which will be discussed further on – they will help in further moulding the digital models to the individual.

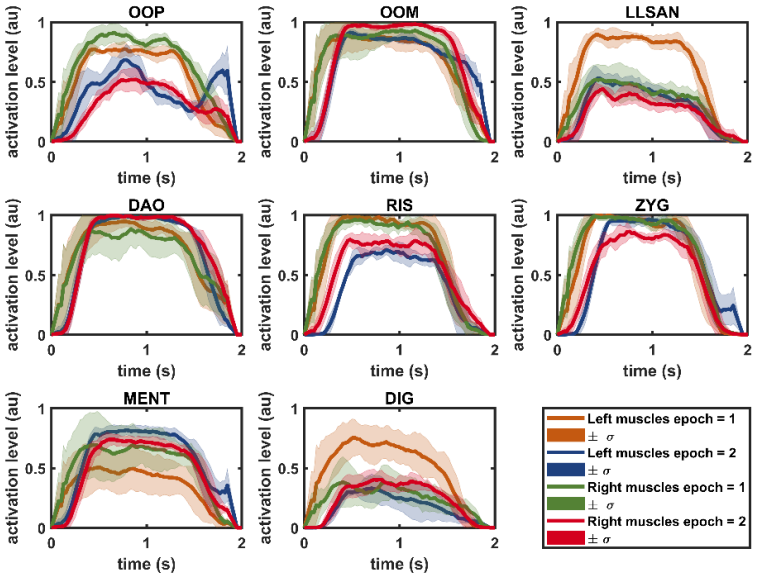

Figure 8.1 Mean muscle activations and their standard deviation of bilateral facial muscles of the same volunteer at different moments in time. The left sided muscle activations are shown in orange (epoch 1) and blue (epoch 2). The right sided muscle activations are drawn in green (epoch 1) and red (epoch 2). The measured facial muscles: orbicularis oris peripheralis (OOP), orbicularis oris marginalis (OOM), levator labii superioris alaeque nasi (LLSAN), depressor anguli oris (DAO), risorius (RIS), zygomaticus (ZYG), mentalis (MENT), and digastric muscles (DIG).

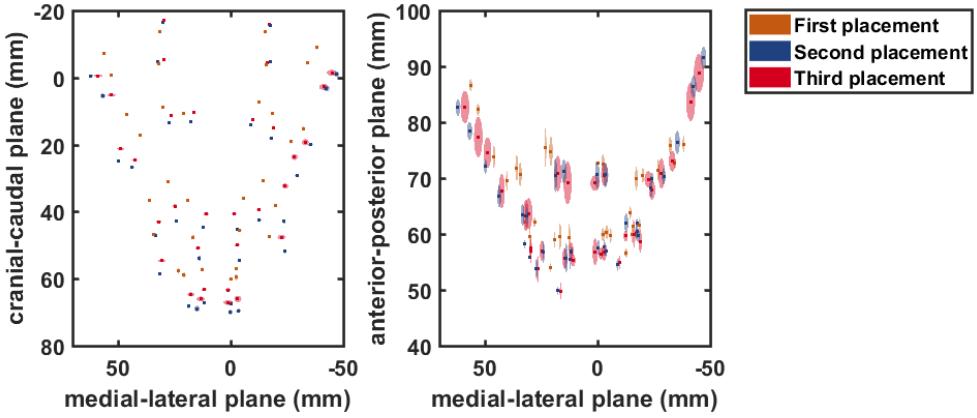

Figure 8.2 Mean locations of surface electrodes on the facial muscles for repeated measurements. The spherical cloud represents the standard deviation in electrode selection and 3D reconstruction. Clearly, the anterior-posterior reconstruction is more uncertain.

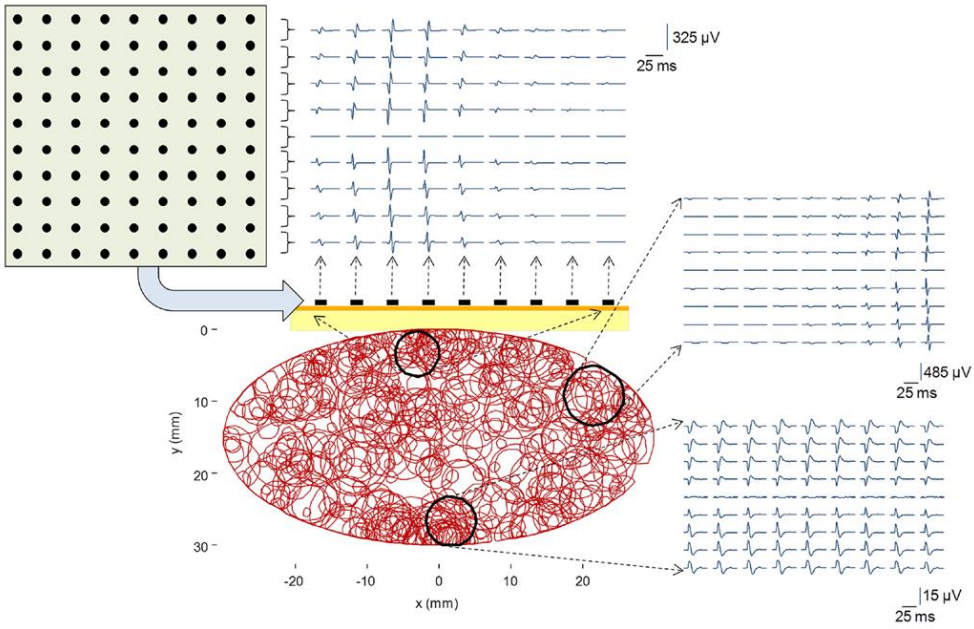

Figure 8.3 Simulated motor unit territories in a muscle cross-section (center) and multichannel motor unit action potentials (MUAPs) of three spatially distinct MUs, as detected by a grid of 10 × 9 surface electrodes (5-mm interelectrode distance in both directions) in a bipolar configuration. The grid of electrodes is depicted schematically in the upper left-hand corner. MUAPs were generated by the volume conductor model described in Farina et al. (2004c). Adopted from Holobar and Farina, Blind source identification from the multichannel surface electromyogram, Physiological measurement *[17]*. © Institute of Physics and Engineering in Medicine. Reproduced by permission of IOP Publishing. All rights reserved.

Towards auspicious epidermal electrodes

Advances in microelectronics are very interesting for our purpose of modelling muscle activation patterns of the oral cavity and perioral region. The epidermal electrodes described by Kim et al. offer wireless transmission, minuscule sEMG sensors, and superior elastic properties, which are particularly important for a complex muscle organ like the tongue [19]. More recently, Liu et al. and Jeong et al. used similar electrodes [20,21]. Liu et al. reported a new strategy, which they called 'nanopile interlocking,' to produce a high-adhesion stretchable electrode [21]. Their sensors can also measure strain and had tuneable stretchability, a high gauge factor, and good stability. They also demonstrated a similar signal-to-noise ratio compared to commercially available nonstretchable electrodes [21]. Jeong et al. systematically performed tests to establish guidelines in materials, mechanics, and geometric designs for sEMG measurements with an innovative class of epidermal sensors called epidermal electronic systems (EES) [20]. Adhesion of EES is based on the Van der Waals forces[1]. This ground-breaking new class is fundamentally different from the conventual sEMG sensors, and therefore the recommendations by the European SENIAM (Surface ElectroMyoGraphy for the NonInvasive Assessment of Muscles) project (Table 2.4, Chapter 2) cannot be extrapolated to EES [20]. Other groups, such as the Bioelectronics group in Delft[2], also focus on miniaturising the electrodes and using wireless transformation. These interesting developments could be quite beneficial to our plans for the future.

Towards essential intraoral sEMG measurements

Intraoral sEMG measurements of the tongue, in particular, pose many challenges. Adhesion is a major problem in the wet salivary intraoral environment. In our preliminary experiments, we were able to fixate microelectrodes with Fixodent denture adhesive (Figure 8.4) while other researchers used paste and hooked-wire electrodes to create bigger surface electrodes and thus more surface to bind to the tongue [22]. Some used invasive hooked-wire EMG electrodes, which stay in place better, though at the expense of comfort and interference with normal voluntary movements [23–25]. This latter problem, incidentally, occurs with most types of electrodes, apart from EES.

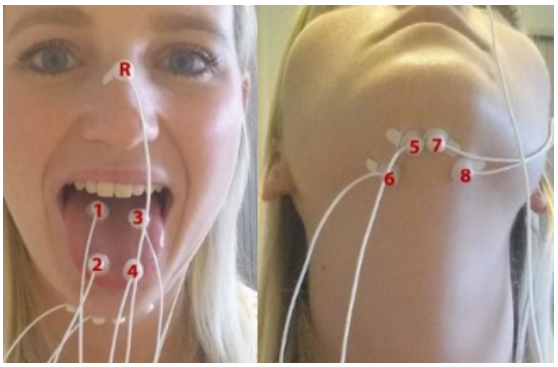

Figure 8.4 Locations of surface electrodes placed on the tongue (1, 2, 3, and 4), the digastric muscles (5, 6, 7, and 8), and the reference electrode (R) on the nasal bone.

[1] Johannes Diderik van der Waals was a Dutch theoretical physicist. The Van der Waals forces is a general term for the intermolecular forces between molecules: d*ipole-dipole, dipole-induced dipole*, and *dispersion forces* [64]

[2] http://bioelectronics.tudelft.nl

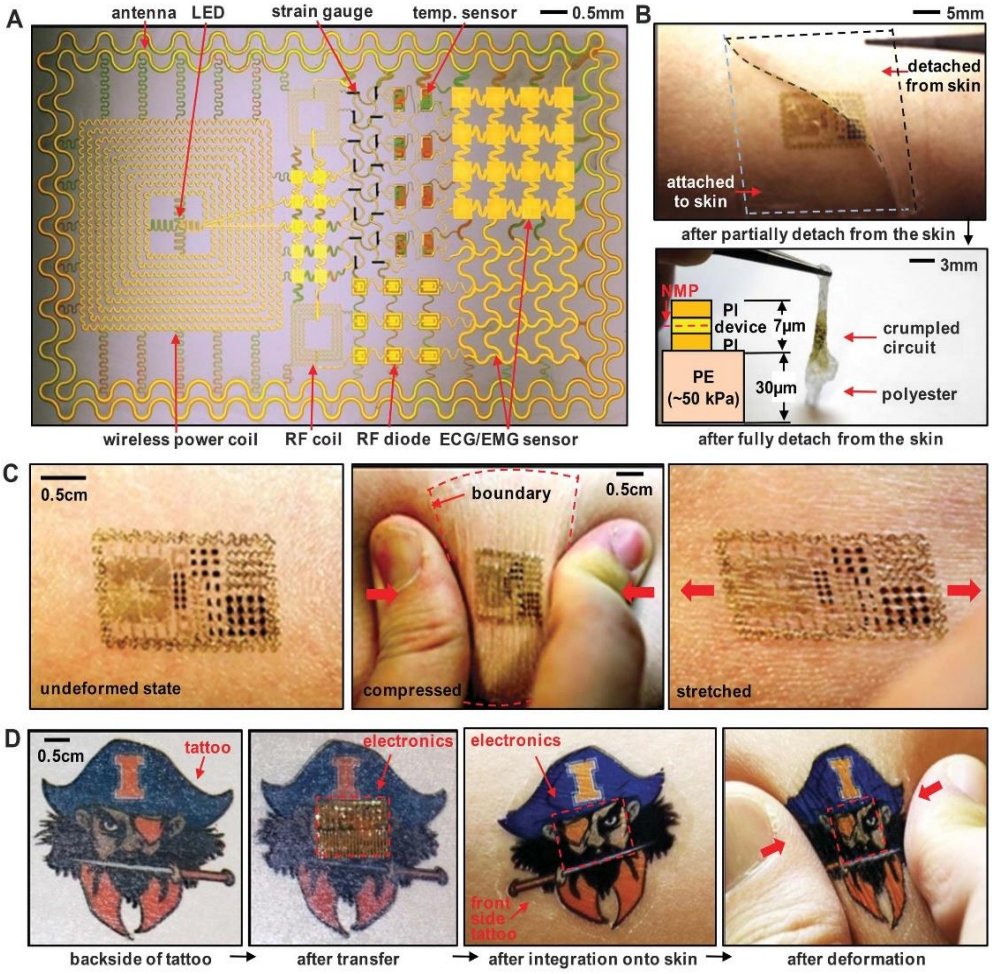

Figure 8.5 The epidermal electrode as described by Kim et al. [19]. A. The epidermal electrode. B. Application on skin, and schematic cross-section. C. Undeformed, compressed, and stretched epidermal electrode. D. application of a commercial available tattoo to disguise the epidermal electrode, again showing a deformation. Adopted from Kim et al., Epidermal Electrodes, Science [19]. Reprinted with permission from AAAS. All rights reserved.

During our initial tongue sEMG experiments, the many possible tongue movements were reduced to five standard movements as defined by van Dijk et al. and Sasaki et al. Also, a swallowing exercise was performed [4,26]:

1. reaching the left side with the tip of the tongue
2. reaching the right side with the tip of the tongue
3. protrusion of the tongue
4. elevation of the tongue: reach to the tip of the nose
5. depression of the tongue: reach to the tip of the chin
6. swallowing

Five healthy volunteers were asked to perform the six instructions four times over so that we obtained 20 repetitions for each instruction. Meanwhile, sEMG signals were recorded using the TMSi® Porti system. Four electrodes placed under the chin measured muscle activity of the suprahyoid muscles and the digastric muscle, in particular. Four other electrodes were placed on the tongue. A reference electrode was placed on the bony part of the nose (Figure 8.4). While in some volunteers intraoral fixation was good, in others it was poor because too much saliva was produced. To solve this problem, we placed intraoral medical adhesives on the opening of the parotid duct, which significantly reduced the presence of saliva in the mouth as it blocked saliva influx from the parotid gland. Notwithstanding these measures, electrodes still lost grip at some point during the experiment in all volunteers. Long-lasting experiments were deemed impossible. Nevertheless, we obtained a reasonable data set for performing some initial classification tests, with encouraging results. We used a quadratic discriminant classifier, which assumed a normal distribution per class and unequal covariance as multiple volunteers performed the instructions. A data set consisting of five volunteers performing twenty repetitions of the six instructions was available.

Table 8.1 Classification errors per individual and overall with 10-fold cross-validation. Generalisation capacity was also tested.

Classifier	QDC	SVM
Volunteer	Correctly classified (%)	Correctly classified (%)
1	87.73	90.48
2	96.17	92.87
3	83.90	81.04
4	98.08	97.65
5	91.92	92.75
Mean	91.56	90.96
Inter (generic model)	73.77	79.38

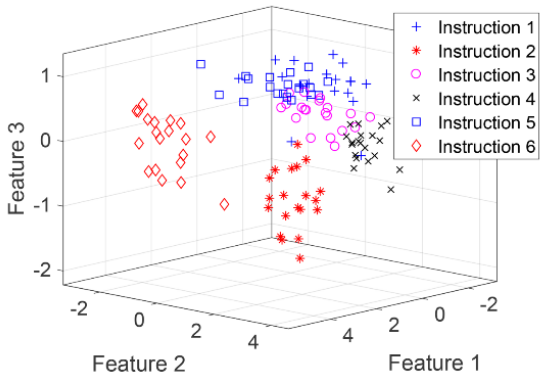

Figure 8.6 3D Scatter plot of the feature space of volunteer 1's six instructions: 1. tongue tip to the left, 2. tongue tip to the right, 3. protrude tongue, 4. tongue tip to nose, 5. tongue tip to chin, 6. swallowing. A quadratic discriminant classifier was trained to classify sEMG features in the six aforementioned instruction classes.

Although we were able to classify the aforementioned standardised tongue motions with promising accuracy (Table 8.1), we considered that four electrodes on the tongue might simply not be enough to catch the interindividual differences or individual muscle contribution. Consequently, we applied an HD-sEMG grid (Figure 8.7) to obtain more data. Unfortunately, the grid was not able to adapt entirely to the flexibility of the tongue. This led to the HD-sEMG grid losing grip on the tongue in the circumvallate papillae region. Therefore, we decided not to use the HD-sEMG grid any longer and went on a quest to find better alternatives. Electrocorticography (ECoG) electrodes used for intracranial electroencephalography (EEG) measurements may be a suitable option because these are very flexible. Preliminary experiments were promising (Figure 8.7). Apart from this option, we are currently developing flexible HD-sEMG grids with silicone and Ag/AgCl microelectrodes (Figure 8.8). The advantage of developing these grids ourselves is that we can adjust the elastic properties of the silicone as we deem fit, tailoring the flexibility of the HD-sEMG grids to our needs. However, the benefits of EES as explained above should not be overlooked.

Recently Sasaki et al. reported on the use of HD-sEMG with 22 electrodes of the suprahyoid muscles [26] because intraoral sEMG measurements are impractical for assistive devices. They obtained good classification results for the same six movements, with a mean percentage of correct classification of 95.1% against our mean percentage of 91.6% (Table 8.1). In contrast to our quadratic classifier, they used support vector machines. Therefore, we also evaluated a classification experiment with support vector machines, obtaining a value of 91.0%. One explanation for the small difference in classification percentages could be that the HD-sEMG grid with its 22 electrodes picked up more relevant information than our eight microelectrodes did. After all, it had 14 channels more with which to obtain useful information. Nevertheless, even though both classification rates are good, in the end, for our purposes, accurate classification is not enough. We aim at obtaining muscle activation patterns of the intrinsic and extrinsic tongue muscles to drive a biomechanical tongue model, just like the one for the lips described in Chapter 5.

Figure 8.8 Developed silicone grid (30 mm x 30 mm). Courtesy: Eline S. van Staveren.

Figure 8.7 Various electrodes for sEMG measurements of the tongue. From left to right: micro electrodes (10 mm x 10 mm), high density grid (25 mm x 35 mm), ECoG grid (39 mm x 51 mm).

The biomechanical tongue models have been described in literature and are available in the ArtiSynth platform [5,27,28]. Moreover, inverse modelling with tongue models as performed by Stavness et al. may benefit inclusion of muscle activation patterns similar to those described in Chapter 6 [29]. Although we are still far from our future application, these initial experiments have given us proof of the possibilities.

Concluding remarks on muscle innervation and electromyography

To conclude, many advancements are being made in the field of sEMG and microelectronics. The most promising technique for intraoral measurements involves the use of wireless HD-sEMG grids, which have great flexibility. These grids interfere with natural movement as little as possible because no bulky electrodes or wires occupy intraoral space. Additionally, their high elasticity allows HD-sEMG grids to cope with the highly irregular deformations of the tongue. Regrettably, however, the present systems are still far from ideal.

8.2.2. Ad 2. Obtaining information on patient-specific anatomy and geometry

All kinds of scans will be needed for our future clinical workflow, if we want to obtain as much information as possible on individual patients. Grossly speaking, standard magnetic resonance imaging (MRI) scans can show great detail of the soft tissues, like muscles, fatty layers, and ligaments, but the bony structures are less well depicted. Computed tomography (CT) imaging is the gold standard for depicting bony parts. Besides showing good contrast for bony areas, CT is also less affected by imaging distortions. On the other hand, because of the radiation involved, this latter imaging modality is less attractive for experimental purposes. Moreover, CT is less sensitive for detecting tumour bone infiltration and bone metastasis. A safer approach than CT, and thus ideal for experimenting, is a special MRI sequence called black bone-MRI [30–32]. Other useful special MRI sequences are diffusion-weighted-preparation MRI (D-Prep MRI) – called 'D-Prep MRN' (magnetic resonance neurography) when used for imaging the nerves – and 'diffusion tensor MRI' (DT-MRI).

Advanced magnetic resonance imaging sequences to the rescue

Allowing for better visualisation of the nervous system, D-Prep MRI is the ideal technique for imaging the peripheral nerves. It has been described by Buckle et al. for the head and neck region. They showed that this technique improved the delineation of lymph nodes and their surrounding delicate anatomical structures in the head and neck region [33]. At our institute, attempts are currently being made to visualise the facial nerve with D-Prep MRI (Figure 8.9).

DT-MRI observes the flow of water molecules based on diffusion. Diffusion is a 3D process strongly dependent on the architecture of tissues or cells, as this determines the rate of diffusion. The main field where DT-MRI is used is in Neuroscience, for creating visible tractographies to try and visualise anatomic connections between the different parts of the brain. This technique has also been used to identify possible muscle fibre orientations of the cardiac muscle [34], arms [35], legs [36], and also in the tongue [37].

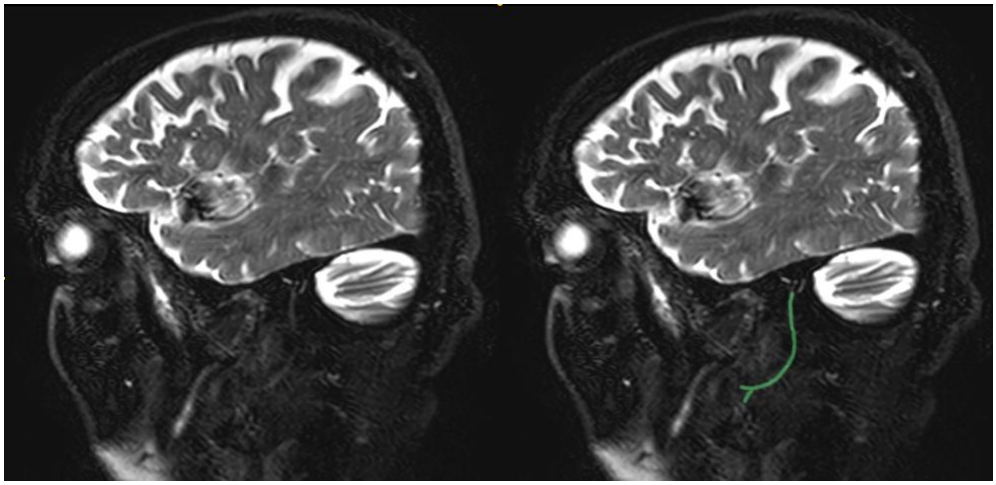

Figure 8.9 Sagittal D-Prep MRN image of one volunteer. Left: without annotation of the facial nerve. Right: highlighted facial nerve in green. Courtesy: Paula Bos.

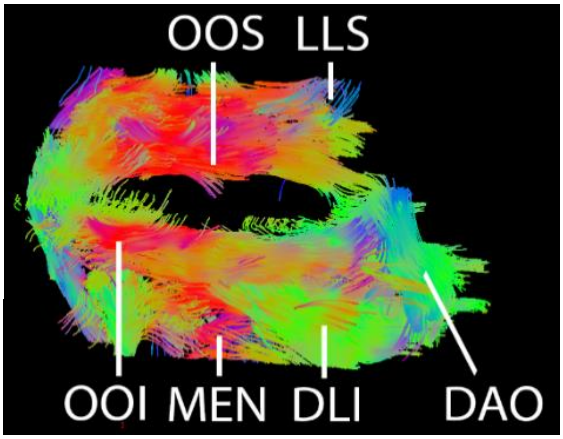

Figure 8.10 DT-MRI of the perioral region. The following muscles were identified: OOS: orbicularis oris superior, OOI: orbicularis oris inferior, MEN: mentalis, DLI: depressor labii inferior, and DAO: depressor anguli oris. Courtesy: Luuk Voskuilen.

Our group is also researching the use of DT-MRI in the head and neck region for showing the facial muscle structures and orientations (Figure 8.10), as well as for identifying the various extrinsic and intrinsic muscles of the tongue (Figure 8.11). Unfortunately, to get high-resolution images with MRI, a long acquisition time is usually necessary, which is difficult with the highly dynamic behaviour of the tongue. Recently, Burdumy et al. introduced a rapid 3D imaging method for voice research, which could observe and quantify modifications in all three dimensions [38].

To summarise, a lot of research is carried out in the field of MRI, in hopes of improving acquisition times and resolution so as to distinguish more detail and get more information on personal anatomy in relation to the extension of a tumour.

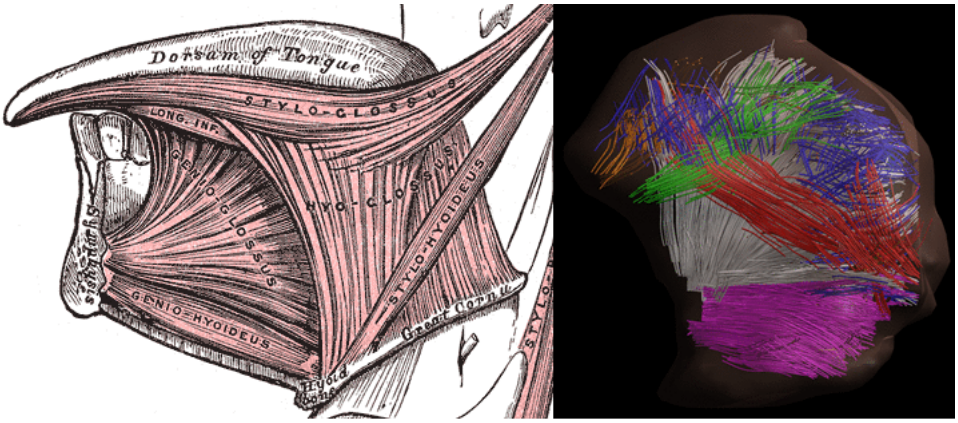

Figure 8.11 The various muscles of the tongue can be identified. Left: the anatomy image was adopted from Gray's Anatomy [39]. Right: genioglossus white; verticalis blue; transversus orange; longitudinalis inferior/styloglossus green; hyoglossus red; geniohyoideus purple. Pictures adopted from Voskuilen et al., Crossing muscle fibres in the tongue resolved using constrained spherical deconvolution, International Society of Magnetic Resonance in Medicine [40].

Optical tracking necessities

A final important imaging modality to discuss is optical tracking to acquire the outer appearance and geometry of individuals. We have developed our own 3D optical tracking system for use in clinical translational research [4,8,10]. It consists of three high-speed cameras that capture video at 100 frames per second, and four led lights to illuminate the region of interest (Figure 8.12). As we plan to measure a large group of patients in the surgical theatre, we created a smaller lightweight version with two miniature cameras that capture video at 50 frames per second and a pico-projector that can display any image or video in the region of interest (Figure 8.13). This handheld version is easy to carry to the operation theatre and even to other hospitals. One shortcoming is that both resolution and frame rate are lower. Also, with two instead of three cameras, markers can easily go out of visible range. Advanced marker tracking algorithms may reduce this problem. The incorporated beamer can display recognisable patterns with enough luminosity to allow for exact measurement of wound defects, scar tissue and conceivably also the movement itself.

On top of the challenges of acquiring high-quality images to distinguish all body structures with various imaging techniques, we will also need mathematical algorithms for optimal registration. Additionally, we will need segmentation techniques – preferably automatic segmentation algorithms – to distinguish the several organs and structures that influence the function of the oral cavity and oropharynx in the imaging data acquired with MRI and CT [41].

Figure 8.12 **Triple-camera set-up able to acquire videos at 100 frames per second. Example perioperative image during in vivo nerve stimulation, simultaneously measuring artificially induced tongue movement, as was done in van Alphen et al. [8].**

Figure 8.13 **Stereo-camera set-up able to acquire videos at 50 frames per second and project images. Developed by Ferdinand van der Heijden and Kilian D.R. Kappert.**

Towards integration of person-specific parameters

Once all this information becomes available, it should be transferred to the biomechanical models to make them patient-specific. Ultimately, the biomechanical models may be used as objective indicators of treatment effects and may incorporate personalised speech synthesis to give an impression of deformed speech sound after therapy. This ultimate goal is ambitious but does not lack vision. However, short-term results are equally important and may be beneficial to the patient and physicians in an earlier stage. One short-term advantage of D-Prep, DT-MRI, and 3D wound and scar tissue registration is at the acquisition of more information to refine tumour staging, surgical planning, and assessment of radiation-induced fibrosis. Moreover, it will enable us to research a lot of interesting processes, like 3D wound healing.

Lastly, the importance of semi-automatic segmentation algorithms cannot be overestimated – not only for our purpose of personalising our models but even more so for the disciplines of Radiology and Radiotherapy to improve the detection of anomalies and to identify and avoid vital structures. Semi-automatic segmentation will drastically decrease manual labour and eliminate the notorious intra- and inter-observer errors [41].

8.2.3. Ad 3. Using sEMG as a proposed personalisation parameter

The aforementioned imaging modalities give us anatomical, geometrical, and perhaps physiological information to personalise the generic biomechanical models. Obtaining the exact locations of muscles and nerves, however, will not be enough to describe the complex process of actuating movement. The electrical impulse pathways from the brain to the muscles involved in vital muscle functions should be further personalised, including personal muscle activation patterns via sEMG features.

For personalisation of the facial movements, the facial nerve plays a pivotal role, predominantly innervating the facial musculature. The facial nerve has six classic branching patterns [42–44]. Preoperative knowledge of the exact distribution pattern of the facial nerve is essential when performing surgery in the parotid region. During the procedure, the facial nerve is usually monitored by intraoperative nerve monitors to reduce the risk of nerve damage. However, in some cases, individual nerve branches cannot be spared – because of tumour invasion, for instance. In such situations, preoperative insight into the individual branching pattern and the innervations of the facial nerve will improve surgical planning and patient counselling. A first impression of the branching pattern can be acquired with imaging techniques such as the ones discussed above (e.g., D-Prep MRN), while sEMG might further personalise the branching patterns on a physiological level. As sEMG measures the action potentials of the depolarising sarcolemma, we can measure if a muscle becomes active and indirectly derive that the innervating nerve fibres are intact. To collect even more useful information, perioperative nerve stimulation in combination with sEMG measurements may be advantageous.

To give an impression of possible facial nerve damage simulations, we modelled nerve damage by inactivating the facial muscles on the patient's right side, corresponding to the

picture of the Bell's palsy patient in Figure 8.14. Next, we calculated the volunteer-specific activation signals from sEMG to control ArtiSynth's generic face model (see Chapters 5 and 6) using the muscles involved in voluntary smiling. We must stress that this is a simplified simulation, which does not account for other aspects, like absent muscle tone, drooping mouth corners, or drooping eyelids.

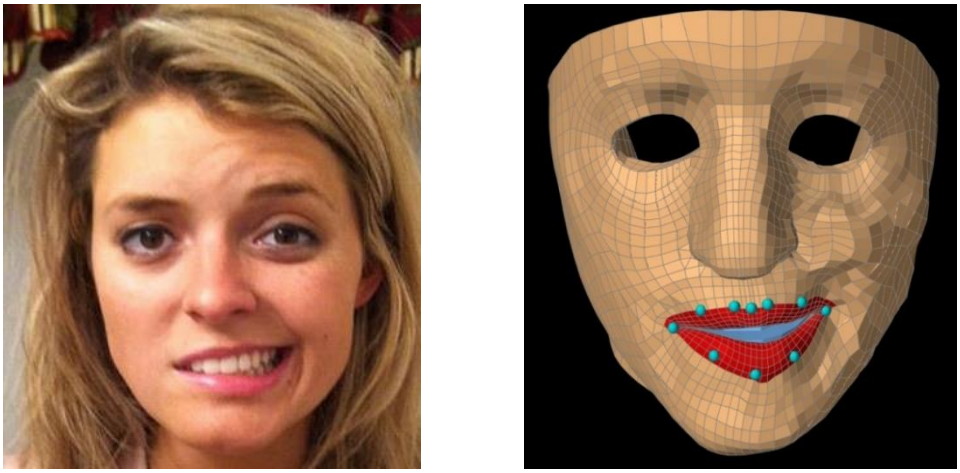

Figure 8.14 Left: Photo of a patient with facial nerve damage due to Bell's palsy (courtesy Mary King, no relationship with oncological disease). Right: Simple simulation of left-sided facial nerve damage. LLSAN, ZYG, and LAO were activated with volunteer-specific activation signals. Experiment performed by M. Eskes.

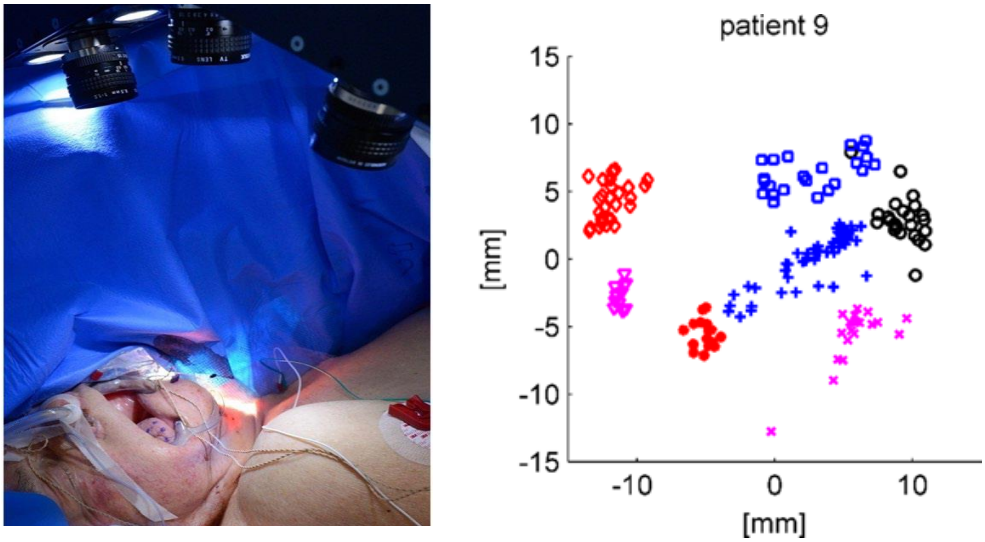

Figure 8.15 Left: perioperative data acquisition with triple-camera set-up recording at 100 frames per second. The markers on the tongue are tracked in 3D when the surgeon performs hypoglossal nerve stimulation, inducing an invoked movement of the tongue. Right: 2D scatter plot of movement clusters in a patient. The clusters correspond to different branches that were stimulated during surgery [8].

Nerve stimulation may unravel distribution patterns

Where the facial muscles are mainly innervated by the facial nerve, the tongue muscles and their innervations are mainly driven by the hypoglossal nerve, with different branching and subsequent innervation patterns. Literature suggests that there are two main types of innervation of the human tongue [45]. It will be essential to know which category a patient belongs to, as conceivably different compensatory innervations may be at play. We investigated this by stimulating the main stem of the hypoglossal nerve and subsequently its various branches perioperatively [8]. In ten patients, we found anatomically different branching patterns and were able to identify five to eight branches that could be stimulated perioperatively. By simultaneously capturing 3D trajectories of the tongue, we were able to define inter- and intra-distances of different movements corresponding to electrical nerve stimulation of the different branches in nine out of ten patients. Figure 8.15 shows the clearly distinct clusters. In this small series of patients, the above-mentioned two main branching categories [45] were not replicated.

The following step will be adding sEMG measurements to identify which muscles are innervated by the different branches and thus further personalise the branching and innervation patterns. With a priori knowledge of the stimulation pulse and with recorded sEMG signals of the response, we may be able to perform a reasonable estimation of such personalisation.

Because intraoral sEMG still has its difficulties, a good way to start will be by extraorally recording sEMG signals of the facial muscles perioperatively. During procedures such as parotidectomy, the facial nerve and its branches are exposed and can be electrically stimulated. HD-sEMG grids, ideally with wireless data transfer, will be more suited for perioperative sEMG than microelectrodes. Applying HD-grids is easier, too; instead of placing the electrodes before surgery, one could place an HD-sEMG grid while the patient is under anaesthesia. These grids have the significant advantage that the channels that actually pick up sEMG signals, can be selected afterwards, which makes perfect manual placement of the microelectrodes less relevant. As an additional advantage, there will be no more need to trouble patients with sEMG placement prior to their surgery.

A limiting factor during measurements will be the disturbance of the sEMG signals by the electrical stimulus, which will profoundly influence the acquired signals. Advanced filtering techniques may prove successful, especially if the internal workings of the stimulus device are known. Numerous techniques for stimulus artefact removal have been described in literature. These may be used in our experiments as well [46,47].

Despite the challenges described above, these innovative experiments are crucial. If we can measure 3D motions, sEMG activities, branching patterns, and the corresponding stimulus conduction pathways simultaneously in a large cohort, we will obtain valuable information on the various innervation patterns and possibly also on compensatory innervations, and the extent to which these relate to movement and sEMG.

Computed myography combining MRI, finite-element models, and electromyography

An interesting paper on computed myography by Van den Doel et al. describes how to determine both quality and quantity of the activation levels of individual muscles by performing voltage measurements and combining these with a finite-element model to simulates electrostatics. This boils down to obtaining a 3D reconstruction of motor function from sEMG and MRI data [48]. In a follow-up paper, they investigated the best suitable method to include a priori information and to design an efficient computational method for solving the involved inverse problem [49].

8.2.4. Ad 4. Improving the biomechanical models

The finite-element method is a unique way of representing physical processes and is of better use for the prediction of posttreatment function than the statistical models described in Chapters 3 and 4. However, the models described in this dissertation can be improved, not only as mentioned before by adjusting them to the patient's anatomy and geometry, but also by improving the mathematical representation, hence including tissue properties, finite-element resolution, and inverse-modelling algorithms.

Obtaining person-specific tissue parameters

An exciting way of obtaining accurate elastic tissue parameters will be the use of a robotic device – a high precision instrument, with 0.03 mm position resolution (Sensable Technologies) and a six-axis force-torque sensor with 1/1,280 N force resolution (Nano 17, ATI Industrial Automation) – that has been used to determine the tissue parameters on cadavers by applying precise displacement stimuli and recording the force responses [50]. However, in cadavers, rigor mortis sets in and alters the tissue properties significantly. Healthy, living tissue can be tested, too, as was done for various parts of the face and tongue [51–54]. Also because of rigor mortis, tumour specimens should be immediately upon resection to obtain their characteristics with maximum reliability. To ultimately get in vivo tissue properties, noninvasive techniques such as MRI – and ultrasound (US) elastography could play an important role. US elastography is currently applied in the clinic to identify or characterise suspicious lesions in the liver, the thyroid, the prostate, the breast, and in muscles in general. However, it is still an emerging field, and more evidence of clinical value is needed [55]. MR elastography has been used mainly for research purposes. Recently, this imaging modality has been promoted more extensively in the United States of America because of better results in liver elastography [56,57]. Both are interesting techniques for assessing tissue properties, not only in healthy tissues of all kinds but also in tumour and scar tissue. At our institute, we are currently validating the US technique on a couple of phantoms to correlate US values to the gold standard of dynamic mechanical shear tests (Figure 8.16).

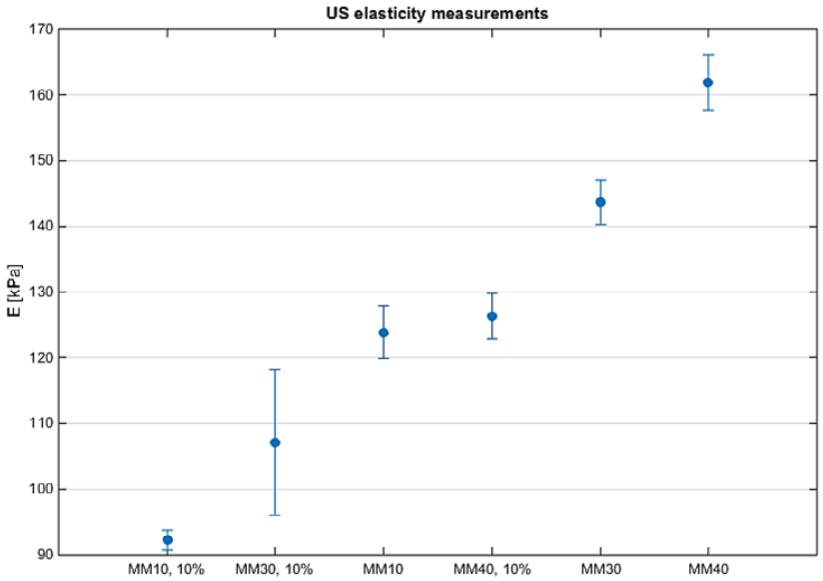

Figure 8.16 Ultrasound elasticity measurements of six test samples with known elasticity properties. On the X-axis the different samples, with increasing Young's modulus. The mean of four measurements per test sample is given with a dot. Their corresponding error bars are shown, too. Courtesy: M.A.J.M. van Erp.

Segmentation and surgical planning

At present, manual tumour delineation is still a time-consuming and rather subjective exercise. Many articles describe inconsistencies in tumour segmentation between radiologists [41]. Much research has been carried out into methods for automated segmentation of tumours, healthy tissue, and vital structures. However, all of these are still far from perfect. In the future, the existing problems will need to be addressed, not only from a time-investment perspective but also to allow for accurate tumour representation. Besides delineating tumours by using all types of imaging studies, we also plan to create a database containing all kinds of information, including preoperative tumour images and micro-CT images of the resected tumours made at our surgical theatres. Additionally, incision lengths and shapes, as well as the outer textures of the operation fields will be captured with the aforementioned handheld 3D camera (Figure 8.13).

Nowadays, static virtual surgery planning has become a routine procedure in the clinic, for instance for planning maxillofacial surgery and the required bony grafts [58,59]. Surgical time can be reduced, and precision can be improved. Planning is performed with MRI and CT digital data of the patient. In the software environment, the pertinent structures, usually the maxilla or mandibula or parts of these, are resected. Then an implant is placed, and the new bone geometry is created. The last step in the process is adjusting the outer appearance by assuming elastic soft tissue that stretches and shrinks with the bone replacement. In this way, a reasonable estimate of the patient's final appearance is made [60]. Although this static process is important and definitively needs to be addressed in

our future models, we will have to go a step further. We do not merely resect and create new bone structures, but we also resect muscles, cut or damage nerves, resect skin tissue or other soft tissues. Showing the impact of these resections will require the use of dynamics. The various facial expressions will need to be tracked by inverse algorithms to account for the adapted pathological anatomy and the damaged or interrupted innervation. Ultimately, the inverse algorithm could show us the compensatory muscle strategy that produces such facial expressions and important visemes, as mentioned in Chapter 6. These dynamic effects are far more complicated to model. The intraoral environment is even harder to grasp fully, because of its anatomical and functional complexity and the difficulties in acquiring relevant information because of impeded measurements.

Virtual therapy treatment, rehabilitation modules, and compensatory mechanisms

We are currently in the process of developing a virtual surgery tool [61]. This tool allows head and neck surgeons to adjust a virtual tongue model in the same way that real surgery would affect the patient. First, they have to create the incision on the surface of the tongue. Next, they can define the characteristics of the surgical excision (circumference, depth, width, et cetera). When the surgeon agrees upon the resected volume, which is shown with a transparent yellow colour (Figure 8.17), virtual resection is performed. The selected elements of the model including the muscle fibres are deleted. In the next step, placing sutures is simulated by applying forces on both edges of the created wound. The model brings both sides together until it reaches a steady state (Figure 8.17). The model is then rebuilt with replaced muscle fibres, and tissue parameters are adjusted to resemble scar tissue.

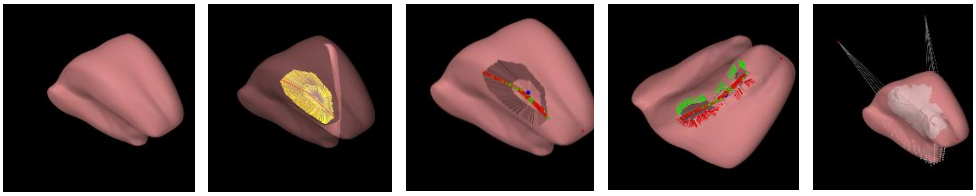

Figure 8.17 Performing virtual surgery: A. Tongue model with a tumour. B, Virtual resection. C. Placing sutures, D. Simulating the suturing procedure, E. Adjusted tongue model with scar tissue (grey area). Courtesy: K.D.R. Kappert

The second treatment module we are developing, is a radiotherapy module. In the current clinical workflow, radiotherapy planning fields have to be designed before radiotherapy is given. The distribution of radiation dose in these planning fields is calculated. Also, vital structures can be designated to set a limit on the maximum dose they are allowed to receive. These planning fields could be a true asset for our future models. If registration of the planning fields together with the patient anatomy and geometry fits perfectly in our personalised models, then an important step for this module will have been made. The next step will be to correlate the dose with stiffening of the tissue parameters. A simple first step would be to adjust the tissue parameters of the model according to MRI-elastographic data obtained from irradiated patients.

Remarkably, there will always be patients who almost fully recover their functions, regardless of the time it may take them. This may be explained in part by their compliance to essential rehabilitation exercises and in part by their compensatory mechanisms. Rehabilitation compliance will be determined by multiple factors, including the patient's persistence and the rehabilitation team's scientific level and experience. Successful compensation is a matter of sheer luck: some patients simply have better or more compensatory abilities than others, due to different nerve supply or other anatomic advantages. To unravel these compensatory contributions, we will need an extensive data set of patients with similar treatments and similar rehabilitation compliance but with different functional outcomes. Then we may to some extent add expectations of improvement with rehabilitation therapy, and possibly also predict whether specific exercises will be of any benefit for the patient. For instance, Kraaijenga et al. showed that senior volunteers could significantly improve swallowing strength and volume [62], and van der Molen et al. found a beneficial effect of preventive swallowing exercises for head and neck cancer patients who were to undergo chemoradiotherapy [63].

Inverse modelling optimisation

Two main difficulties in inverse modelling are ambiguity and high computational time. We have tried to solve the ambiguity problem by introducing the sEMG cost terms, which will also guide the algorithm in (hopefully) correctly personalising motor control. Moreover, if implemented correctly, the enormous solution space will be dramatically reduced by these constraints, which in turn will benefit the second problem of the time-consuming algorithms. Previously, we argued in favour of improving the resolution of the finite-element model by increasing the number of elements to allow for smoother transitions. Unfortunately, for inverse modelling this will be a major drawback as all these elements will introduce new possibilities, which will drastically increase computational time. To compensate for this problem, we should use simpler models for inverse modelling than we use for forward modelling. Future research may focus on the correlation of outcomes of simpler models vs. those of complex models in inverse modelling. Instead of the finite-element method, a simple mass-spring system may be used to obtain an indication of the inverse solution. We are currently experimenting with such models to obtain correct personalised activation signals (Figure 8.18).

8.3. Concluding remark

To recap, every individual is unique. Generic models can only take us so far – which is not far enough, in our opinion. The current era in medicine calls for treatments that are tailored to the needs of individual patients, since individual cancers, too, are perceived as unique, each with their own building blocks and therapeutic immunity. To address the inevitable challenges of individual responses to treatment and functional outcome, we propose generic biomechanical models that should be further personalised, incorporating as many patient-specific data as possible. In addition to gross anatomy and other tissues parameters, sEMG measurements – the crude derivatives of muscle activation levels – will be indispensable ingredients. Since most vital functions require muscle contractions, acquiring accurate sEMG data will be essential.

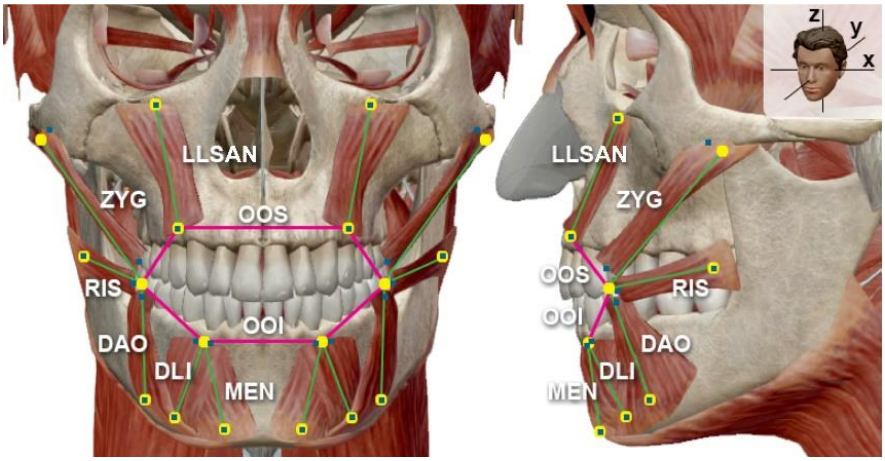

Figure 8.18 Simple mass spring system of the lips, left frontal view, right sagittal view. The facial muscles are abbreviated as follows: orbicularis oris superior (OOS), orbicularis oris inferior (OOI), depressor anguli oris (DAO), depressor labii inferior (DLI), levator labii superioris alaeque nasi (LLSAN), zygomaticus (ZYG), risorius (RIS), and mentalis (MEN).

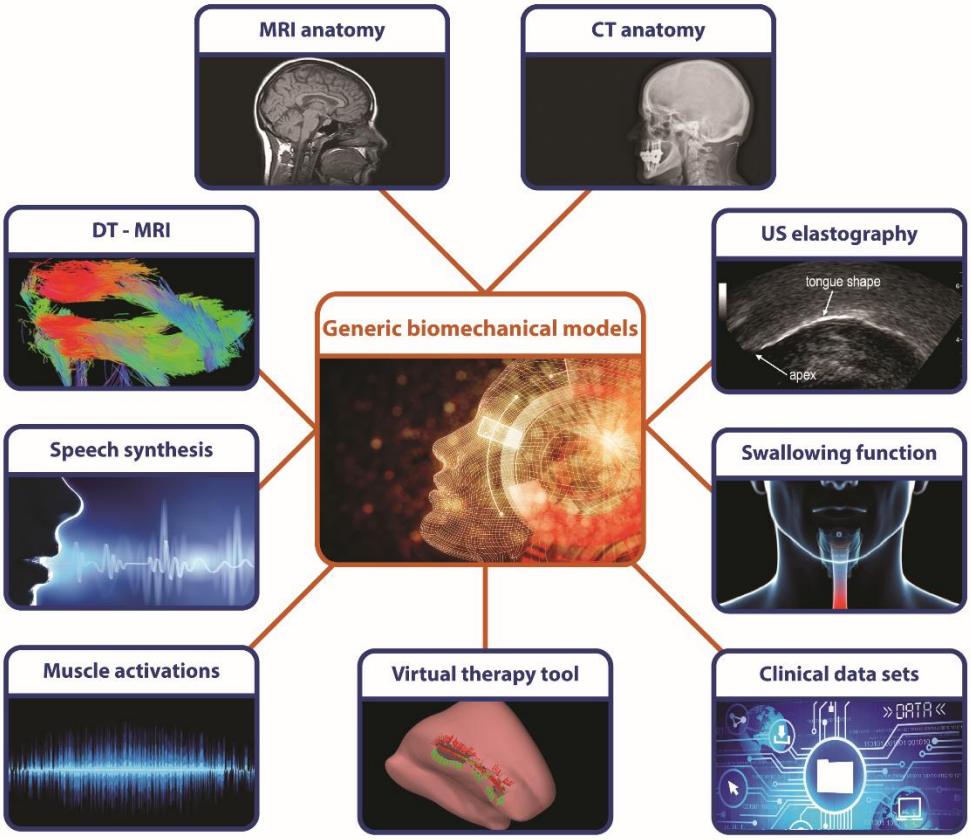

Figure 8.19 Schematic overview of fundamental aspects for personalising generic models. Input of many domains will be needed to ultimately create the perfect digital doppelgänger

8.4. References

1. Bélaise C, Dal Maso F, Michaud B, Mombaur K, Begon M. An EMG-marker tracking optimisation method for estimating muscle forces. Multibody Syst Dyn. 2017; doi:10.1007/s11044-017-9587-2

2. Buchanan TS, Lloyd DG, Manal K, Besier TF. Neuromusculoskeletal Modeling: Estimation of Muscle Forces and Joint Moments and Movements From Measurements of Neural Command. J Appl Biomech. 2004;20: 367–395. Available: https://www.ncbi.nlm.nih.gov/pmc/articles/PMC1357215/

3. Luenberger DG. Introduction to Dynamic Systems: Theory, Models & Applications. 1st ed. Wiley. 1979.

4. van Dijk S, van Alphen MJA, Jacobi I, Smeele LE, van der Heijden F, Balm AJM. A New Accurate 3D Measurement Tool to Assess the Range of Motion of the Tongue in Oral Cancer Patients: A Standardized Model. Dysphagia. 2016;31: 97–103. doi:10.1007/s00455-015-9665-7

5. van Alphen MJA, Kreeft AM, van der Heijden F, Smeele LE, Balm AJM. Towards virtual surgery in oral cancer to predict postoperative oral functions preoperatively. Br J Oral Maxillofac Surg. 2013;51: 747–751. doi:10.1016/j.bjoms.2013.06.012

6. Kreeft A, Tan IB, van den Brekel MWM, Hilgers FJ, Balm AJM. The surgical dilemma of "functional inoperability" in oral and oropharyngeal cancer: current consensus on operability with regard to functional results. Clin Otolaryngol. 2009;34: 140–6. doi:10.1111/j.1749-4486.2009.01884.x

7. Kreeft AM, Tan IB, Leemans CR, Balm AJM. The surgical dilemma in advanced oral and oropharyngeal cancer: how we do it. Clin Otolaryngol. 2011;36: 260–266. doi:10.1111/j.1749-4486.2011.02299.x

8. van Alphen MJA, Eskes M, Smeele LE, Balm AJM, van der Heijden F. In vivo intraoperative hypoglossal nerve stimulation for quantitative tongue motion analysis. Comput Methods Biomech Biomed Eng Imaging Vis. 2015;1163: 1–7. doi:10.1080/21681163.2015.1072056

9. Eskes M, van Alphen MJA, Balm AJM, Smeele LE, Brandsma D, van der Heijden F. Predicting 3D lip shapes using facial surface EMG. Zhang Y, editor. PLoS One. 2017;12: e0175025. doi:10.1371/journal.pone.0175025

10. Eskes M, van Alphen MJA, Smeele LE, Brandsma D, Balm AJM, van der Heijden F. Predicting 3D lip movement using facial sEMG: a first step towards estimating functional and aesthetic outcome of oral cancer surgery. Med Biol Eng Comput. 2017;55: 573–583. doi:10.1007/s11517-016-1511-z

11. Balm AJM, van der Heijden F. Virtual Therapy. In: Mission [Internet]. 2015 [cited 1 Sep 2017] p. 1. Available: http://www.virtualtherapy.nl/mission/

12. De Luca CJ. The Use of Surface Electromyography in Biomechanics. J Appl Biomech. 1997;13: 135–163. doi:10.1123/jab.13.2.135

13. Farina D, Merletti R, Enoka RM. The extraction of neural strategies from the surface EMG. J Appl Physiol. 2004;96: 1486–1495. doi:10.1152/japplphysiol.01070.2003

14. Lapatki BG. The Facial Musculature: Characterisation at a Motor Unit Level. Radboud University Nijmegen. 2010.

15. Lapatki BG, Oostenveld R, Van Dijk JP, Jonas IE, Zwarts MJ, Stegeman DF. Optimal placement of bipolar surface EMG electrodes in the face based on single motor unit analysis. Psychophysiology. 2010;47: 299–314. doi:10.1111/j.1469-8986.2009.00935.x

16. Stegeman DF, Kleine BU, Lapatki BG, Van Dijk JP. High-density Surface EMG: Techniques and Applications at a Motor Unit Level. Biocybern Biomed Eng. 2012;32: 3–27. doi:10.1016/S0208-5216(12)70039-6

17. Holobar A, Farina D. Blind source identification from the multichannel surface electromyogram. Physiol Meas. 2014;35: R143–R165. doi:10.1088/0967-3334/35/7/R143

18. Farina D, Holobar A. Characterization of Human Motor Units From Surface EMG Decomposition. Proc IEEE. 2016;104: 353–373. doi:10.1109/JPROC.2015.2498665

19. Kim D-H et al. Epidermal electronics. Science. 2011;333: 838–843. doi:10.1126/science.1206157

20. Jeong J-W, Yeo W-H, Akhtar A, Norton JJS, Kwack Y-J, Li S, Jung S-Y, Su Y, Lee W, Xia J, Cheng H, Huang Y, Choi W-S, Bretl T, Rogers JA. Materials and Optimized Designs for Human-Machine Interfaces Via Epidermal Electronics. Adv Mater. 2013;25: 6839–6846. doi:10.1002/adma.201301921

21. Liu Z, Wang X, Qi D, Xu C, Yu J, Liu Y, Jiang Y, Liedberg B, Chen X. High-Adhesion Stretchable Electrodes Based on Nanopile Interlocking. Adv Mater. 2017;29: 1603382. doi:10.1002/adma.201603382

22. Yoshida K, Takada K, Adachi S, Sakuda M. Clinical Science: EMG Approach to Assessing Tongue Activity Using Miniature Surface Electrodes. J Dent Res. 1982;61: 1148–1152. doi:10.1177/00220345820610100701

23. Sauerland EK, Harper RM. The human tongue during sleep: electromyographic activity of the genioglossus muscle. Exp Neurol. 1976;51: 160–70. Available: http://www.ncbi.nlm.nih.gov/pubmed/177304

24. Pittman LJ, Bailey EF. Genioglossus and Intrinsic Electromyographic Activities in Impeded and Unimpeded Protrusion Tasks. J Neurophysiol. 2008;101: 276–282. doi:10.1152/jn.91065.2008

25. Finsterer J, Fuglsang-Frederiksen A, Mamoli B. Needle EMG of the tongue: motor unit action potential versus peak ratio analysis in limb and bulbar onset amyotrophic lateral sclerosis. J Neurol Neurosurg Psychiatry. 1997;63: 175–80. Available: http://www.ncbi.nlm.nih.gov/pubmed/9285455

26. Sasaki M, Onishi K, Stefanov D, Kamata K, Nakayama A, Yoshikawa M, Obinata G. Tongue interface based on surface EMG signals of suprahyoid muscles. ROBOMECH J. 2016;3: 9. doi:10.1186/s40648-016-0048-0

27. Buchaillard S, Brix M, Perrier P, Payan Y. Simulations of the consequences of tongue surgery on tongue mobility: implications for speech production in post-surgery conditions. Int J Med Robot Comput Assist Surg. 2007;3: 252–261. doi:10.1002/rcs.142

28. Fujita S, Dang J, Suzuki N, Honda K. A Computational Tongue Model and its Clinical Application. Oral Sci Int. 2007;4: 97–109. doi:10.1016/S1348-8643(07)80004-8

29. Stavness I, Lloyd JE, Fels S. Automatic prediction of tongue muscle activations using a finite element model. J Biomech. 2012;45: 2841–8. doi:10.1016/j.jbiomech.2012.08.031

30. Eley KA, Mcintyre AG, Watt-Smith SR, Golding SJ. "Black bone" MRI: A partial flip angle technique for radiation reduction in craniofacial imaging. Br J Radiol. 2012;85: 272–278. doi:10.1259/bjr/95110289

31. Eley KA, Watt-Smith SR, Sheerin F, Golding SJ. "Black Bone" MRI: a potential alternative to CT with three-dimensional reconstruction of the craniofacial skeleton in the diagnosis of craniosynostosis. Eur Radiol. 2014;24: 2417–26. doi:10.1007/s00330-014-3286-7

32. Eley KA, Watt-Smith SR, Golding SJ. Three-Dimensional Reconstruction of the Craniofacial Skeleton With Gradient Echo Magnetic Resonance Imaging ("Black Bone"): What Is Currently Possible? J Craniofac Surg. 2017;28: 463–467. doi:10.1097/SCS.0000000000003219

33. Buckle T, KleinJan GH, Engelen T, van den Berg NS, DeRuiter MC, van der Heide U, Valdes Olmos RA, Webb A, van Buchem MA, Balm AJ, van Leeuwen FWB. Diffusion-weighted-preparation (D-prep) MRI as a future extension of SPECT/CT based surgical planning for sentinel node procedures in the head and neck area? Oral Oncol. 2016;60: 48–54. doi:10.1016/j.oraloncology.2016.06.015

34. Nielles-Vallespin S, Mekkaoui C, Gatehouse P, Reese TG, Keegan J, Ferreira PF, Collins S, Speier P, Feiweier T, de Silva R, Jackowski MP, Pennell DJ, Sosnovik DE, Firmin D. In vivo diffusion tensor MRI of the human heart: Reproducibility of breath-hold and navigator-based approaches. Magn Reson Med. 2013;70: 454–465. doi:10.1002/mrm.24488

35. Froeling M, Nederveen AJ, Heijtel DFR, Lataster A, Bos C, Nicolay K, Maas M, Drost MR, Strijkers GJ. Diffusion-tensor MRI reveals the complex muscle architecture of the human forearm. J Magn Reson Imaging. 2012;36: 237–248. doi:10.1002/jmri.23608

36. Lansdown DA, Ding Z, Wadington M, Hornberger JL, Damon BM. Quantitative diffusion tensor MRI-based fiber tracking of human skeletal muscle. J Appl Physiol. 2007;103: 673–681. doi:10.1152/japplphysiol.00290.2007

37. Gaige TA, Benner T, Wang R, Wedeen VJ, Gilbert RJ. Three dimensional myoarchitecture of the human tongue determined in vivo by diffusion tensor imaging with tractography. J Magn Reson Imaging. 2007;26: 654–661. doi:10.1002/jmri.21022

38. Burdumy M, Traser L, Burk F, Richter B, Echternach M, Korvink JG, Hennig J, Zaitsev M. One-second MRI of a three-dimensional vocal tract to measure dynamic articulator modifications. J Magn Reson Imaging. 2017;46: 94–101. doi:10.1002/jmri.25561

39. Standring S. Gray's anatomy: the anatomical basis of clinical practice. 40th ed. Churchill Livingstone. 2008.

40. Voskuilen L, Mazzoli V, Oudeman J, et al. Crossing muscle fibres in the tongue resolved using constrained spherical deconvolution. International Society of Magnetic Resonance in Medicine. 2017.

41. Teguh DN, Levendag PC, Voet PWJ, Al-Mamgani A, Han X, Wolf TK, Hibbard LS, Nowak P, Akhiat H, Dirkx MLP, Heijmen BJM, Hoogeman MS. Clinical Validation of Atlas-Based Auto-Segmentation of Multiple Target Volumes and Normal Tissue (Swallowing/Mastication) Structures in the Head and Neck. Int J Radiat Oncol. 2011;81: 950–957. doi:10.1016/j.ijrobp.2010.07.009

42. Davis RA, Anson BJ, Budinger JM, Kurth LR. Surgical anatomy of the facial nerve and parotid gland based upon a study of 350 cervicofacial halves. Surg Gynecol Obstet. 1956;102: 385.

43. Myint K, Azian AL, Khairul FA. The clinical significance of the branching pattern of the facial nerve in Malaysian subjects. Med J Malaysia. 1992;47: 114–121.

44. Khaliq BA, Nisar J, Yousuf A, Maqbool T, Ahmad R. Facial nerve branching pattern as seen in parotidectomy in Kashmiri population : our experience. 2017;3: 95–97.

45. Mu L, Sanders I. Human tongue neuroanatomy: Nerve supply and motor endplates. Clin Anat. 2010;23: 777–791. doi:10.1002/ca.21011

46. O'Keeffe DT, Lyons GM, Donnelly AE, Byrne CA. Stimulus artifact removal using a software-based two-stage peak detection algorithm. J Neurosci Methods. 2001;109: 137–145. doi:10.1016/S0165-0270(01)00407-1

47. Liu J, Li S, Li X, Klein C, Rymer WZ, Zhou P. Suppression of stimulus artifact contaminating electrically evoked electromyography. NeuroRehabilitation. 2014;34: 381–9. doi:10.3233/NRE-131045

48. van den Doel K, Ascher UM, Curt A, Steeves J, Pai DK. Computed myography (CMG): three dimensional reconstruction of motor functions from surface EMG data. Conf Proc . Annu Int Conf IEEE Eng Med Biol Soc IEEE Eng Med Biol Soc Annu Conf. 2008;2008: 550–4. doi:10.1109/IEMBS.2008.4649212

49. Doel K Van Den, Ascher UM, Pai DK. Source localization in electromyography using the inverse potential problem. 2010; 1–21.

50. Lim Y-J, Deo D, Singh TP, Jones DB, De S. In situ measurement and modeling of biomechanical response of human cadaveric soft tissues for physics-based surgical simulation. Surg Endosc. 2009;23: 1298–1307. doi:10.1007/s00464-008-0154-z

51. Schiavone P, Boudou T, Promayon E, Perrier P, Payan Y. A light sterilizable pipette device for the in vivo estimation of human soft tissues constitutive laws. 2008 30th Annual International Conference of the IEEE Engineering in Medicine and Biology Society. 2008. pp. 4298–4301. doi:10.1109/IEMBS.2008.4650160

52. Shibata A, Higashimori M, Ramirez-Alpizar IG, Kaneko M. Tongue elasticity sensing with muscle contraction monitoring. 2012 ICME International Conference on Complex Medical Engineering (CME). 2012. pp. 511–516. doi:10.1109/ICCME.2012.6275607

53. Flynn C, Taberner AJ, Nielsen PMF, Fels S. Simulating the three-dimensional deformation of in vivo facial skin. J Mech Behav Biomed Mater. 2013;28: 484–494. doi:10.1016/j.jmbbm.2013.03.004

54. Luboz V, Promayon E, Payan Y. Linear Elastic Properties of the Facial Soft Tissues Using an Aspiration Device: Towards Patient Specific Characterization. Ann Biomed Eng. 2014;42: 2369–2378. doi:10.1007/s10439-014-1098-1

55. Cosgrove D et al. EFSUMB Guidelines and Recommendations on the Clinical Use of Ultrasound Elastography.Part 2: Clinical Applications. Ultraschall der Medizin - Eur J Ultrasound. 2013;34: 238–253. doi:10.1055/s-0033-1335375

56. Imajo K, Kessoku T, Honda Y, Tomeno W, Ogawa Y, Mawatari H, Fujita K, Yoneda M, Taguri M, Hyogo H, Sumida Y, Ono M, Eguchi Y, Inoue T, Yamanaka T, Wada K, Saito S, Nakajima A. Magnetic Resonance Imaging More Accurately Classifies Steatosis and Fibrosis in Patients With Nonalcoholic Fatty Liver Disease Than Transient Elastography. Gastroenterology. 2016;150: 626–637.e7. doi:10.1053/j.gastro.2015.11.048

57. Sporea I. The Future of Liver Elastography in the Field of Hepatology. Ultrasound Int Open. 2017;3: E50–E51. doi:10.1055/s-0043-106178

58. Wang Y, Fan S, Zhang H, Lin Z, Ye J, Li J. Virtual Surgical Planning in Precise Maxillary Reconstruction With Vascularized Fibular Graft After Tumor Ablation. J Oral Maxillofac Surg. 2016;74: 1255–1264. doi:10.1016/j.joms.2016.01.010

59. Schepers RH, Kraeima J, Vissink A, Lahoda LU, Roodenburg JLN, Reintsema H, Raghoebar GM, Witjes MJ. Accuracy of secondary maxillofacial reconstruction with prefabricated fibula grafts using 3D planning and guided reconstruction. J Cranio-Maxillofacial Surg. 2016;44: 392–399. doi:10.1016/j.jcms.2015.12.008

60. Mollemans W, Schutyser F, Nadjmi N, Maes F, Suetens P. Predicting soft tissue deformations for a maxillofacial surgery planning system: from computational strategies to a complete clinical validation. Med Image Anal. 2007;11: 282–301. doi:10.1016/j.media.2007.02.003

61. Kappert KDR, van Alphen MJA, van Dijk S, Smeele LE, Balm AJM, van der Heijden F. An interactive surgical simulation tool to assess the consequences of a partial glossectomy on a biomechanical model of the tongue. Comput Methods Biomech Biomed Engin. 2017

62. Kraaijenga SAC, van der Molen L, Stuiver MM, Teertstra HJ, Hilgers FJM, van den Brekel MWM. Effects of Strengthening Exercises on Swallowing Musculature and Function in Senior Healthy Subjects: a Prospective Effectiveness and Feasibility Study. Dysphagia. 2015;30: 392–403. doi:10.1007/s00455-015-9611-8

63. van der Molen L, van Rossum MA, Rasch CRN, Smeele LE, Hilgers FJM. Two-year results of a prospective preventive swallowing rehabilitation trial in patients treated with chemoradiation for advanced head and neck cancer. Eur Arch Oto-Rhino-Laryngology. 2014;271: 1257–1270. doi:10.1007/s00405-013-2640-8

64. Chang R, Overby J. General Chemistry: The Essential Concepts. 6th ed. The McGraw-Hill Companies, Inc. 2011.

IX

SUMMARY

9. Summary

Functional inoperability (FI) is an important concept in head and neck cancer treatment. The term FI applies when surgery is not an option because the functional postoperative outcome would be too severe, with dramatic effects on speech, swallowing, and mastication. Other organ-sparing approaches, such as chemotherapy, radiotherapy or a combination of both, should then be considered as alternative treatment options.

Preoperative estimation of function loss is subjective and unreliable since it depends on the personal expertise of individual physicians. Moreover, each patient is unique and will respond differently to the various treatment options. The Virtual Therapy Group is developing tools to make this tough decision-making process easier, with personalised functional outcome expectations. The idea is to develop a digital doppelgänger. This virtual look-a-like should be able to adapt to individual patients by processing conventional imaging data (magnetic resonance imagining, computed tomography, ultrasound), as well as 3D video measurements to define mobility of anatomical structures, and surface electromyography (sEMG) to account for individual muscle activation patterns. By personalising the currently available generic models with the above data, we could create genuine digital replicas of individual patients.

The human musculoskeletal system is a redundant system: many functional movements can be generated by multiple muscle contraction patterns. Consequently, many functions have alternative control mechanisms that could be mastered to compensate for function loss.

In clinical practice, some head-and-neck patients indeed regain full function after their treatment and continue their lives with good speech and swallowing function. Others, however, do not and suffer from pathological speech and dysphagia. We think that these differences relate to variation in neural motor control and muscle innervation. Nerve anatomy differs between individuals. Some people may just have more nerve branch innervations for particular muscles than do others.

With sEMG, we can record a crude estimate of muscle activations, which will hopefully enable us to map neural motor commands. This dissertation demonstrates in Chapter 3 that with features extracted from sEMG signals, we can accurately estimate 3D static lip shapes. This promising finding shows that sEMG signals can provide sufficient information on motor control. Chapter 4 demonstrates that a statistical model can adequately predict dynamic movements – visemes (groups of speech sounds that visually look the same), facial expressions, and asymmetric movements – with signals measured from 16 facial muscles. Chapter 5 describes the step from statistical models towards biomechanical models that implement real physics. These models will be advantageous because they follow physical laws and preserve real anatomy and geometry.

In Chapter 6, we elaborate on the process of inverse modelling: calculating the input of muscle activations needed to generate specific functional outcomes – in our case, the 3D lip movements of functions such as speech. Unfortunately, this is a rather complicated procedure, and because of the aforementioned redundancy of the musculoskeletal system, it can lead to multiple solutions. However, we also demonstrate in this chapter that with sEMG we can reduce the solution-space and acquire more patient-specific data on muscle activation. Chapter 7 presents a technical elaboration on inverse modelling, investigating static and dynamic optimisation techniques with and without sEMG. Chapter 8 discusses the work and proposes future research directions on the basis of four main pillars in personalising the generic models.

To conclude, forward modelling will be elementary for driving the model with surgical adaptations and patient-specific learnt muscle-activation strategies, so it could show us the treatment effects directly after surgery. Inverse modelling, on the other hand, could show us any potential compensatory mechanisms, which may differ from patient to patient. Some patients will be able to relearn functions; others will not. With a fully operative digital doppelgänger, clinicians will be able to perform various treatment strategies and compare treatment outcomes at the multidisciplinary meeting to agree upon the best individual treatment strategies. The doppelgänger will also be helpful during counselling, to simulate the functional sequelae of treatment and to better prepare and inform the patient.

SAMENVATTING

10. Samenvatting

Functionele inoperabiliteit is een relatief nieuw begrip binnen de hoofdhals chirurgie. Het selecteert tumoren, die niet operatief verwijderd kunnen worden, omdat de postoperatieve uitkomst op functioneel gebied (spraak, slikken en kauwen) als zeer slecht wordt geschat. Andere orgaan-sparende behandelstrategieën zijn dan een optie. Helaas is het inschatten van functieverlies na behandeling subjectief en onbetrouwbaar. Immers iedere patiënt is uniek en reageert anders op verschillende behandelingen, maar ook elke arts is anders en put uit andere ervaringen. Binnen het virtuele therapie project is men bezig deze moeilijke keuze tussen behandelingen op basis van de te verwachten uitkomst te moderniseren. Zij zoeken naar een objectieve, kwantitatieve en reproduceerbare maat. Het idee is gebaseerd op het ontwikkelen van een digitale dubbelganger.

Deze digitale dubbelganger wordt opgebouwd middels patiënt-specifieke informatie verkregen via allerlei gangbare beeldvormende technieken (MRI, CT en US), maar ook met aanvullende metingen zoals mobiliteit en spieractiviteit die wordt gemeten met behulp van oppervlakte EMG. De bestaande generieke modellen kunnen met deze nieuwe informatie worden aangepast aan de patiënt, zodat er een echt digitaal evenbeeld ontstaat.

Het spierskeletstelsel van de mens is een overbepaald systeem. Dat betekent dat er meerdere mogelijkheden zijn om met behulp van de spieren de beweging van de botten aan te sturen, waardoor dezelfde functionele beweging ontstaat. Er zijn meerdere spieren die eenzelfde functie kunnen vervullen. Dit impliceert dat ook compensatoire mechanismen kunnen worden aangeleerd. Dit heeft tot gevolg dat sommige patiënten weer vrijwel normaal door het leven kunnen gaan, terwijl anderen een pathologische spraak of slikfunctie ontwikkelen.

Wij denken dat deze verschillen onder andere tot stand komen door de neurale aansturing van de spieren. De anatomie van de zenuwen verschilt per individu en de een heeft meer vertakkingen die in dezelfde spier uitmonden dan de ander. Met behulp van de oppervlakte EMG zijn wij in staat een afgeleide van de spieractiviteiten in kaart te brengen en daarmee hopelijk ook de verschillende neurale aansturingen. In dit proefschrift, in het derde hoofdstuk, laten wij zien dat met behulp van deze spieractiviteiten verschillende statische 3D lipvormen kunnen worden voorspeld. Hieruit kunnen wij mogelijk afleiden dat deze signalen genoeg informatie bevatten over de uiteindelijke spieraansturing. In het vierde hoofdstuk gebruiken wij een statistisch model om te laten zien dat wij middels de signalen van 16 gezichtsspieren dynamische bewegingen, zoals visemen (groepen woorden die er voor een liplezer hetzelfde uitzien), gezichtsuitdrukkingen en tevens asynchrone bewegingen adequaat kunnen voorspellen. Het vijfde hoofdstuk beschrijft de stap van statistische modellen naar de fysische werkelijkheid met behulp van biomechanische modellen. Deze modellen hebben als voordeel dat ze de natuurwetten volgen en de werkelijke anatomie en geometrie behouden.

In hoofdstuk zes wijden we uit over het achterwaarts modelleren. Met deze vorm van modellering kunnen wij in biomechanische modellen uitrekenen welke spieractiviteit nodig is om een bepaalde functionele beweging uit te voeren. Dit is helaas erg complex en leidt niet tot unieke oplossingen vanwege het bovengenoemde gegeven dat het spierskeletsysteem overbepaald is. Er zijn eenvoudigweg meer mogelijkheden om tot dezelfde actie te komen. We laten in dit hoofdstuk dan ook zien dat men met behulp van oppervlakte EMG de oplossingsruimte kunt verkleinen. Daarmee neemt men de patiënt-specifieke neurale aansturing in acht en komt men tot oplossingen die patiënt-specifiek zijn. Hoofdstuk zeven is een technisch uitstapje naar verschillende methoden van het achterwaarts modelleren. We beschrijven statische en dynamische optimalisatietechnieken waarbij we de uitwerking onderzochten met en zonder hulp van sEMG. Hoofdstuk acht bespreekt het werk en stelt toekomstige onderzoeksrichtingen voor gebaseerd op vier pijlers om generieke modellen te personaliseren.

Concluderend, voorwaarts modelleren is belangrijk om een model met chirurgische aanpassingen aan te sturen. Dit verschaft ons inzicht in de consequenties van zo'n behandeling direct na de ingreep, mits wij het model aansturen met de van jongs af aan geleerde patiënt-specifieke spieractivatiepatronen. Het achterwaarts modelleren geeft ons inzicht in mogelijke compensatoire mechanismen welke kunnen verschillen tussen patiënten. Sommige weten de essentiële functies opnieuw te leren, terwijl anderen daar niet toe in staat zijn. In de toekomst kunnen verschillende behandelstrategieën toegepast worden op de digitale dubbelganger. De verscheidene behandelingen en de effecten ervan kunnen dan tijdens een multidisciplinair overleg besproken worden zodat er een bewuste keuze gemaakt kan worden met inachtneming van de patiënt-specifieke factoren. Dit kan tot een optimale patiënt-specifieke behandelstrategie leiden. Tot slot biedt dit ook mogelijkheden om de voorlichting over de functionele effecten na behandeling voor de individuele patiënt te optimaliseren.

PART V

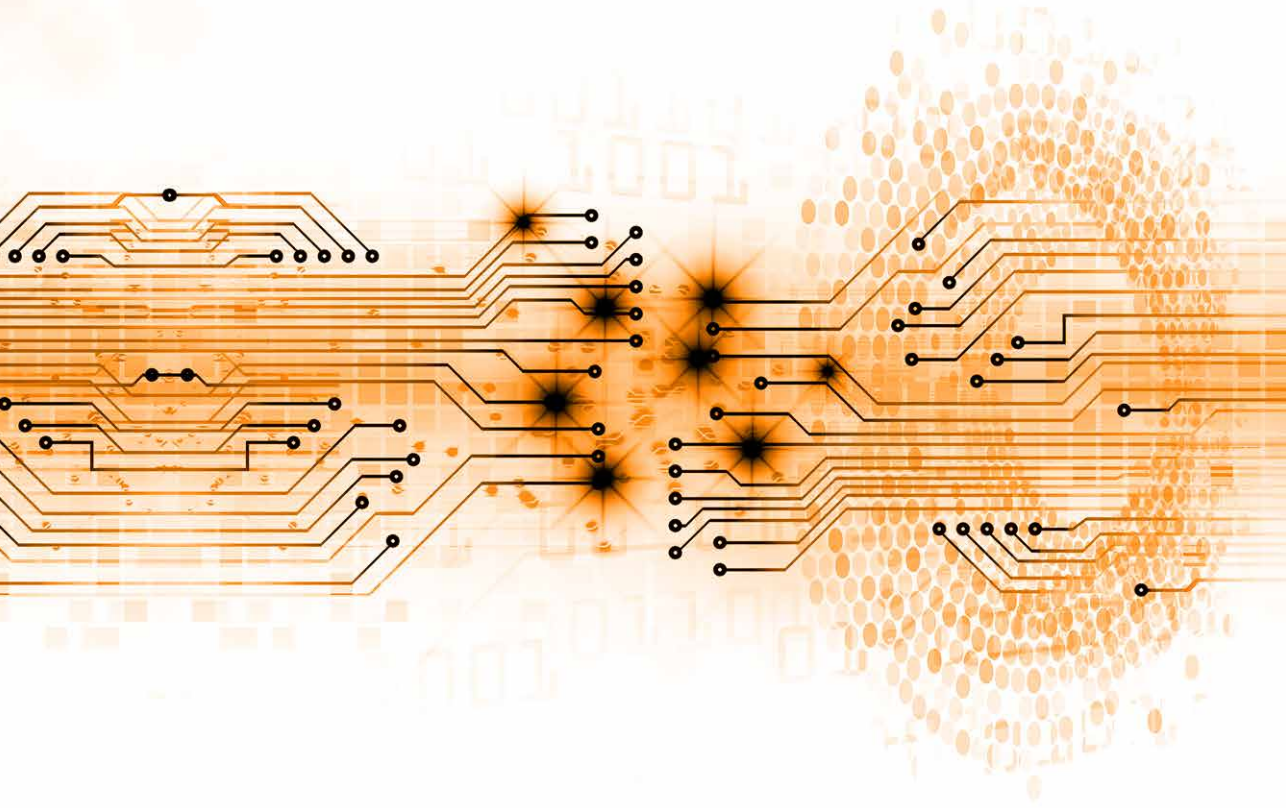

XI

ACKNOWLEDGEMENTS

11. Acknowledgements (dankwoord)

Zoals zovelen die mij op dit pad zijn voorgegaan, zal ik niet de eerste zijn die constateert dat een proefschrift niet dankzij één persoon tot stand komt, ondanks die enkele naam op de omslag. Zo ook is dit boekwerk het eindproduct van samenwerking en goed "noaberschap", de mooie Achterhoekse term voor het elkaar bijstaan in raad en daad.

Zodoende zou ik dan ook graag iedereen, die elk op zijn of haar eigen manier, direct of indirect, een steentje heeft bijgedragen (zoals de "Keienslöppers" de gigantische, ±20.000 kg wegende zwerfkei gezamenlijk naar het centrum van Lichtenvoorde hebben weten te slepen), heel hartelijk bedanken.

Om te beginnen wil ik u, de lezer, bedanken voor uw interesse in dit werk.

Volgens het gebruikelijke recept volgen mijn promotoren en copromotor.

Zeer gewaardeerde prof. dr. AJM Balm FACS FRCS, beste Fons, tijdens mijn klinische stage van drie maanden heb ik u leren kennen als een respectabel persoon, vol positiviteit en enthousiasme. Toen ik uw "*libor amicorum*" las, kon ik niet anders dan mij afvragen waar u in hemelsnaam de tijd en energie heeft gevonden om naast al uw andere activiteiten, mij te mentoren en zelfs te adviseren bij het ontwerpen van de cover (om maar iets te noemen). Het is mij nog steeds een raadsel, maar ik ben u hier zeer erkentelijk voor! Dank voor alle steun, vertrouwen, geduld en kansen die u mij gegeven heeft. Mocht u ooit weer een privéchauffeur nodig hebben, dan weet u mij te vinden.

Zeer gerespecteerde dr. ir F. van der Heijden, beste Ferdi, de afgelopen jaren hebben wij veel samengewerkt, waarbij de intensiteit van die samenwerking veelal een periodiek verloop had. Met name richting de publicatiedeadlines werden er bergen werk verzet. De vele uren in de koffiekamer in het O-gebouw alsook de uren via Skype; prachtig dat u zoveel tijd kon en wílde nemen om, naast alle andere verplichtingen, mij op ontdekkingsreis mee te nemen naar de wiskundige werelden van o.a. het *Kalman filter*, *principale componenten analyse* en *optimal control*. Dankzij u ben ik ook veel systematischer gaan werken, zo schrijf ik tegenwoordig commentaar bij mijn code en zelfs readme bestanden. Heel veel dank voor alles wat u voor mij heeft betekend!

Zeer geachte prof. dr. ir. C.H. Slump, u zou ik graag willen bedanken voor het mogelijk maken van dit promotietraject. Ik ben vereerd u als promotor te mogen hebben.

Geachte leden van de promotiecommissie: prof. dr. ir. T.T.M. Palstra,
em. prof. dr. ir. J. van Amerongen, prof. dr. ir. H.J. Hermens, prof. dr. ir. H.F.J.M. Koopman, prof. dr. ir. G.J.M. Krijnen, prof. dr. M.W.M. van den Brekel, en prof. dr. L.E. Smeele – ik wil u allen hartelijk danken voor het zitting nemen in de promotiecommissie en het vrijmaken van uw waardevolle tijd voor het beoordelen van dit proefschrift.

De coauteurs, dr. D. Brandsma en dr. M.J.A. van Alphen, dank voor jullie zeer gewaardeerde bijdrage. Maarten in het bijzonder voor het beantwoorden van mijn prangende vragen, jouw geduld en ook voor het plaatsnemen als referent in de promotiecommissie.

Ian Stavness, thank you for your time on Skype and via e-mail to help me with my ArtiSynth and inverse modelling endeavors. Also, your support in drafting the manuscripts towards publishable papers is greatly appreciated.

Maja Keizers, heel hartelijk bedankt voor het corrigeren en redigeren van de meeste stukken tekst in dit proefschrift. Hierdoor is het geheel goed leesbaar geworden.

Jeannette Alcaraz, I really appreciated your enthusiastic "YES!" on my question if you would be willing to revise parts of my dissertation. Your corrections and suggestions are gratefully acknowledged.

Mijn dank gaat ook uit naar alle betrokken collega's in het Antoni van Leeuwenhoek, de Virtual Therapy groep, de hoofdhalsafdeling, de AvL-TG-ers, de onderzoekers in het O-gebouw, met in het bijzonder mijn kamergenoten in 03.22: Charlotte, Elies, Joost, Sarah en Simone.

Dr. R.J.J.H. van Son, dank voor de vele ideeën tijdens de maandagmiddagmeeting. Veelal vanuit een ander perspectief, om zodoende toch weer een stap verder te kunnen. Zoals bijvoorbeeld de "*dynamic time warping*". Dank daarvoor.

Marion en Henny, hartelijk dank voor alle hulp omtrent praktische zaken, met name alle formaliteiten rondom nieuwe studenten.

Jolanda, vaak hebben wij elkaar niet gezien, maar veelal van alles geregeld via telefoon en e-mail. Dank voor al jouw steun vanuit de Universiteit Twente.

Vele TG studenten hebben hun kennis en kunde bij ons op het Virtual Therapy project ingebracht, waardoor het project heeft kunnen groeien en dit proefschrift tot stand heeft kunnen komen. Dank voor jullie waardevolle bijdrage en de altijd gezellige lunchwandelingen.

Om het onderzoek uit te kunnen voeren zijn vrijwillige proefpersonen noodzakelijk. Tevens moeten er voor de klinische studies patiënten bereid zijn te participeren. Bijzonder veel respect heb ik dan ook voor deze mensen die, verkerend in een moeilijke en onzekere fase, zich alsnog hiervoor beschikbaar hebben gesteld. Dank aan allen.

Graag grijp ik deze gelegenheid ook aan om alle vriendengroepen; de Tijdelijke Toppers, de Achterhoekse vrienden, de Bonobo's, de vrienden in de randstad, en de (oud-)huisgenoten, te bedanken voor hun begrip dat mijn sociale leven het afgelopen half jaar tot een minimum beperkt was. Dank voor jullie support, interesse en het geluk dat ik jullie heb leren kennen. Ik kijk ernaar uit om met jullie een goudgele pretcilinder te drinken op de succesvolle afsluiting van dit hoofdstuk en de start van een nieuwe!

Lieve (schoon)familie, dank voor de onuitputtelijke interesse en succeswensen. Ik heb me tijdens dit traject gesteund gevoeld door jullie en ik vind het ontzettend bijzonder dat zovelen van jullie de promotieplechtigheid in Enschede en/of het proosten hierop tijdens het feest in Amsterdam, met mij willen delen.

Lieve pa en ma, voor mijn dank voor jullie steun is de hele lengte van dit proefschrift natuurlijk nog te kort. De prestatie die ik heb kunnen leveren had zonder veel mensen, maar dan toch in het bijzonder zonder jullie, niet tot stand kunnen komen. Jullie oneindige vertrouwen in mijn kunnen, onvoorwaardelijke support en altijd voorhanden zijnde ouderlijk advies; wat zijn jullie toch intens betrokken en wat maken jullie veel voor ons mogelijk. Dank jullie wel.

Beste paranimfen, lieve broers, hoe tof dat jullie deze dag naast mij willen staan. Ondanks dat jullie niet echt wisten waar jullie "ja" tegen zeiden, is alles uiteindelijk "op zijn Eskes" op z'n pootjes terechtgekomen. Ontzettend trots ben ik ook op jullie dat ik eenieder van jullie de rol van oudste broer en "het grote voorbeeld" met alle bijbehorende verantwoordelijkheden, elke dag van de week kan toevertrouwen. Zodoende kan ik ook altijd voor advies bij jullie terecht. Veel dank!

Liefste Lise, allereerst heel veel dank voor jouw onvoorwaardelijke steun. Dank voor jouw luisterend oor en dat je altijd geïnteresseerd bleef, ook al waren de meeste gesprekken de afgelopen tijd gevuld met promotieperikelen. Ik ben erg blij dat we elkaar tegen het lijf zijn gelopen op de "ouderwetse manier" in een "moderne" wereld. Naast alle memorabele herinneringen kijk ik ook graag uit naar alle mooie momenten die we samen verder gaan beleven! – RAWR

Hoe zorgvuldig zo'n dankwoord ook is geschreven, het is altijd mogelijk dat er per abuis (en onbedoeld!) een belangrijke naam ontbreekt. Mocht dat bij de uwe het geval zijn, dan is er nog een plek speciaal voor u gereserveerd in deze dankbetuiging:

Beste ....., voor uw onuitputbare steun de afgelopen jaren, waardoor ik mijn promotie in goede orde heb kunnen afronden, zal ik u eeuwig dankbaar zijn.

Amsterdam – Enschede, 13 december 2017,

Merijn.

XII

AUTHOR CONTRIBUTIONS

12. Author contributions

This chapter states the author contributions according to the CRediT Taxonomy of author contributions[1] of which the definitions are given in table below.

Contributor Role	Role Definition
Conceptualisation	Ideas; formulation or evolution of overarching research goals and aims.
Data Curation	Management activities to annotate (produce metadata), scrub data and maintain research data (including software code, where it is necessary for interpreting the data itself) for initial use and later reuse.
Formal Analysis	Application of statistical, mathematical, computational, or other formal techniques to analyse or synthesise study data.
Funding Acquisition	Acquisition of the financial support for the project leading to this publication.
Investigation	Conducting a research and investigation process, specifically performing the experiments, or data/evidence collection.
Methodology	Development or design of methodology; creation of models
Project Administration	Management and coordination responsibility for the research activity planning and execution.
Resources	Provision of study materials, reagents, materials, patients, laboratory samples, animals, instrumentation, computing resources, or other analysis tools.
Software	Programming, software development; designing computer programs; implementation of the computer code and supporting algorithms; testing of existing code components.
Supervision	Oversight and leadership responsibility for the research activity planning and execution, including mentorship external to the core team.
Validation	Verification, whether as a part of the activity or separate, of the overall replication/reproducibility of results/experiments and other research outputs.
Visualisation	Preparation, creation and/or presentation of the published work, specifically visualisation/data presentation.
Writing – Original Draft Preparation	Creation and/or presentation of the published work, specifically writing the initial draft (including substantive translation).
Writing – Review & Editing	Preparation, creation and/or presentation of the published work by those from the original research group, specifically critical review, commentary or revision – including pre- or postpublication stages

[1] Brand A, Allen L, Altman M, Hlava M, Scott J. Beyond authorship: attribution, contribution, collaboration, and credit. Learned Publishing [Internet]. 2015;28(2):151-155. Doi: 10.1087/20150211

Chapter Contributor Role	I	II	III	IV	V	VI	VII	VIII
Conceptualisation	ME	ME	AB, FH, LS, DB	ME, FH, MA, AB, LS	ME, FH, AB, LS, IS, MA	ME, AB, FH	ME, FH, AB	ME
Data Curation	ME	ME	ME, MA	ME	ME	ME	ME	ME
Formal Analysis	ME	ME	ME, FH, MA	ME, FH, MA	ME	ME	ME, FH, ES	ME
Funding Acquisition	X	X	X	X	X	X	X	X
Investigation	ME	ME	ME, MA	ME	ME	ME	ME	ME
Methodology	ME	ME	FH, AB	ME, FH, MA, AB	ME, FH, MA, IS	ME, IS, FH	ME, ES, FH	ME
Project Administration	ME	ME	AB, LS	AB, LS	AB, LS, ME	AB, LS, ME	AB, FH, ME	ME
Resources	ME	ME	ME	ME	ME	ME	ME	ME
Software	ME	ME	ME, MA	ME, MA	ME	ME, IS	ME, FH, ES	ME
Supervision	AB, FH	AB, FH	AB	AB, FH	AB	AB, FH	FH	AB, FH
Validation	ME	ME	FH, ME, MA, AB	FH, ME, MA	FH, ME	ME, IS, FH	FH, ME, ES, AB	ME
Visualisation	ME	ME	ME	ME	ME	ME	ME, ES	ME
Writing – Original Draft Preparation	ME	ME	ME, MA	ME	ME	ME	ME, FH	ME
Writing – Review & Editing	ME, FH, MA, AB	ME, FH, MA, AB	AB, LS, DB, FH	ME, MA, AB, LS, DB, FH	ME, AB, MA, LS, FH, IS	ME, MA, AB, LS, FH, IS	ME, MA, AB, FH	ME, MA, AB, FH

AB – A.J.M. Balm

DB – D. Brandsma

ES – E.S. Schaft

FH – F. van der Heijden

IS – I. Stavness

LS – L.E. Smeele

MA – M.J.A. van Alphen

ME – M. Eskes

XIII

ABOUT THE AUTHOR

13. About the author

Merijn Eskes was born on the 1st of September 1987 in Winterswijk. Together with his brothers Tiemen and Jorrit he grew up in consecutively Halle and Lichtenvoorde, two small villages in the Achterhoek. In 2006 he obtained two diplomas in the disciplines of Nature & Technology and Nature & Health at the RKSG Marianum in Groenlo. After this, he started his education in Technical Medicine at the University of Twente in Enschede, where he pursued the master's specialisation "Medical Sensing and Stimulation" in 2009. After his first master's year, he was allowed to participate in a study tour to Japan, where he and his fellow students compared health care and related technology between Japan and the Netherlands. This was followed by four clinical research internships in which both research and clinical activities were the focus. He started at the Clinical Neurophysiology in the Academic Hospital Maastricht, followed by the Neonatal Intensive Care Unit at the Radboud University Medical Center in Nijmegen. During his third internship at the Head-neck oncology and surgery department at the Antoni van Leeuwenhoek in Amsterdam, he became acquainted with the Virtual Therapy project. He arranged his last internship in Mexico City at the Pediatric Oncology and Surgery department at the National Institute of Pediatrics. After living in Mexico for six months, Merijn started his clinical specialisation in December 2012; again, at the Antoni van Leeuwenhoek hospital on the Virtual Therapy project. At the end of 2013 he obtained his Master's degree in Technical Medicine. Due to his growing interest in Virtual Therapy, his PhD trajectory was formed, which ultimately resulted in the dissertation that now lies before you. During this time, he was speaker and program coordinator of the annual conference of the professional association of Technical Medicine (NVvTG). He has given presentations at various (inter) national conferences and is the author of five scientific publications.

13. Over de auteur

Merijn Eskes werd op 1 september 1987 geboren in Winterswijk. Samen met zijn broers Tiemen en Jorrit groeide hij op in achtereenvolgens Halle en Lichtenvoorde, twee kleine dorpjes in de Achterhoek. In 2006 behaalde hij zijn diploma's in de richtingen Natuur & Techniek en Natuur & Gezondheid aan het RKSG Marianum in Groenlo. Hierna startte hij met de opleiding Technische Geneeskunde aan de Universiteit Twente in Enschede, waar hij in 2009 de master specialisatie "*Medical Sensing and Stimulation"* koos. Na zijn eerste masterjaar mocht hij deelnemen aan een studiereis naar Japan, waar hij met medestudenten de gezondheidszorg en bijbehorende technologie heeft vergeleken tussen Japan en Nederland. Aansluitend volgden vier klinische onderzoeksstages waarin zowel onderzoek als het klinisch handelen centraal stonden. Hij startte op de Klinische Neurofysiologie in het Academisch Ziekenhuis Maastricht, en kwam daarna terecht op de Neonatale Intensive Care Unit in het Radboud Universitair Medisch Centrum in Nijmegen. Tijdens zijn derde stage op de Hoofdhals-oncologie en -chirurgie afdeling in het Antoni van Leeuwenhoek te Amsterdam maakte hij kennis met het Virtuele Therapie project. Zijn laatste stage die plaatsvond in Mexico-stad op de Kinderoncologie en -chirurgie afdeling in het Instituto Nacional de Pediatría heeft hij zelf opgezet. Na een half jaar in Mexico gewoond te hebben, begon Merijn zijn klinische specialisatiestage in december 2012; opnieuw in het Antoni van Leeuwenhoek ziekenhuis op het Virtuele Therapie project. Eind 2013 wist hij zijn masterdiploma "*Technical Medicine*" te behalen. Uit zijn toenemende interesse in de Virtuele Therapie ontstond zijn promotietraject, dat uiteindelijk heeft geresulteerd in het proefschrift dat nu voor u ligt. Gedurende deze tijd was hij ook sprekers- en programma-coördinator voor het jaarlijkse congres van de beroepsvereniging voor Technische Geneeskundige (NVvTG). Hij heeft presentaties gegeven op verschillende (inter)nationale congressen en is auteur van vijf wetenschappelijke publicaties.

PhD Portfolio

Graduate school Oncology Amsterdam (OOA)
Twente Graduate School Enschede (TGS)

PhD candidate:	Merijn Eskes
PhD period:	December 2013 – July 2017
PhD supervisors:	Prof. dr. ir. C.H. Slump
	Prof. dr. A.J.M. Balm FACS FRCS
	Dr. ir. F. van der Heijden

Courses

- Good Clinical Practice (Benecke) 2017
- Adobe InDesign (Gildeprint) 2016
- Writing and presenting in biomedicine (OOA) 2015
- Time Management (AVL Akademie) 2014
- Machine Learning (Coursera) 2014
- Model Thinking (Coursera) 2013
- Game Theory (Coursera) 2013
- Principles of Economics for Scientists (Coursera) 2013

(Inter)national conferences attended

- TiiM (NVvTG) Conference, Walk of Life, Amersfoort, the Netherlands 2017
- AHNS Conference, Seattle, United States of America 2016
- NVvTG Conference, Amsterdam, the Netherlands 2016
- Innovation for Health, Amsterdam, the Netherlands 2015
- OOA Retreat, Renesse, the Netherlands 2015
- CARS Conference, Barcelona, Spain 2015
- NVvTG Conference, Envision the Future, Amsterdam, the Netherlands 2015
- OOA Retreat, Renesse, the Netherlands 2014
- NVvTG Conference, Utrecht, the Netherlands 2013
- OOA Retreat, Renesse, the Netherlands 2013
- NVvTG Conference, Arnhem, the Netherlands 2012

Seminars, workshops, and master classes

- Monthly meeting of the working group for Head and Neck tumours 2013 – 2017
- Monthly seminars of the Surgical and Oncological Disciplines department 2013 – 2017
- Monthly and Quarterly Virtual Therapy group meeting 2013 – 2017
- Monthly Technical Medicine seminars 2013 – 2017
- Medical Business Masterclass, Amsterdam, the Netherlands 2016

Supervision of Technical Medicine students (master's programme)

Student	Period	Student	Period
E.S. van Staveren	2016 – 2017	M. van Erp	2015
K.D.R. Kappert	2015 – 2016	M. van den Boorn	2015
M.S. van Schie	2017	K.D.R. Kappert	2015
M.D. van der Stoel	2017	J. Vink	2015
F.M.A. van der Velden	2017	M. Tolhuisen	2015
E.V. Schaft	2017	D. Roelofs	2014
R.E.M. Bekhuis	2016	E.J. Wickering	2014
E.S. van Staveren	2016	J. Thannhauser	2014
J.G. van der Waal	2016		

Committees

- Quality committee (**BIG ambassador**), NVvTG, the Netherlands 2017
- PhD Council (**member**) Oncology Graduate School Amsterdam, NKI-AvL, Amsterdam, the Netherlands 2015 – 2016
- Lustrum conference committee (**speaker coordinator & vice president**), NVvTG, the Netherlands 2014 – 2015

Publications

- **Eskes M,** Schaft ES, Balm AJM, van der Heijden F: **sEMG-assisted inverse modelling of 2D arm movement**, *Journal of Biomechanics,* 2018 (in preparation)
- **Eskes M**, Balm AJM, van Alphen MJA, Smeele LE, Stavness I, van der Heijden F**: sEMG-assisted inverse modelling of 3D lip movement: a feasibility study towards person-specific modelling**, *Scientific Reports Nature,* 2017, (Open Access)
- **Eskes M**, Balm AJM, van Alphen MJA, Smeele LE, Stavness I, van der Heijden F: **Simulation of facial expressions using person-specific sEMG signals controlling a biomechanical face model**, *Computer Assisted Radiology and Surgery,* 2017, (Open Access), *https://doi.org/10.1007/s11548-017-1659-5*
- **Eskes M**, van Alphen MJA, Smeele LE, Brandsma D, Balm AJM, van der Heijden F: **Predicting 3D lip movement using facial sEMG: a first step towards estimating functional and aesthetic outcome of oral cancer surgery.** Medical and Biological Engineering and Computing, 2017, *55: 573* (Open Access), *https://doi.org/10.1007/s11517-016-1511-z*
- **Eskes M,** van Alphen MJA , Balm AJM, Smeele LE, van der Heijden F:**Predicting 3D lip shapes using facial surface EMG**, *Public Library of Science,* 2017, *12(4): e0175025* (Open Access), *https://doi.org/10.1371/journal.pone.0175025*
- van Alphen MJA, **Eskes M**, Smeele LE, Balm AJM, van der Heijden F: **In vivo intraoperative hypoglossal nerve stimulation for quantitative tongue motion analysis.** Computer Methods in Biomechanics and Biomedical Engineering: Imaging & Visualization, 2017, *5(6), 409-415, https://doi.org/10.1080/21681163.2015.1072056*

Presentations

- **Eskes M**, van Alphen MJA, Smeele, LE, Balm AJM, Stavness IK, van der Heijden F: **The role of virtual therapy in head and neck cancer treatment,** postgraduate education KNMT, Amsterdam, the Netherlands; 2016
- **Eskes M**, van Alphen MJA, Smeele, LE, Balm AJM, Stavness IK, van der Heijden F: **The role of virtual therapy in head and neck cancer treatment,** research symposium Head and Neck group Antoni van Leeuwenhoek, Amsterdam, the Netherlands; 2016
- **Eskes M**, van Alphen MJA, Smeele, LE, Balm AJM, Stavness IK, van der Heijden F: **Patient-specific sEMG driven models of the face and oral cavity: a first step towards prediction of post-surgical functional outcome.** In AHNS 2016, American Head & Neck Society 9th conference, Seattle, United States; 2016
- **Eskes M**, van Alphen MJA, Balm AJM, Stavness IK, van der Heijden F: **Inverse modelling: A Surface Electromyographic Signal Guidance Approach,** OOA Retreat, Renesse, the Netherlands; 2015

  Eskes M, van Alphen MJA, Balm AJM, Brandsma D, van der Heijden F: **A dynamic 3D lip shape model with facial surface EMG control.** In CARS 2015 Computer Assisted Radiology and Surgery. Barcelona, Spain; 2015
- **Eskes M**, van Alphen MJA, Balm AJM, Brandsma D, Hamburger HL, van der Heijden F: **Towards a virtual 3D lip model for head and neck cancer treatment,** postgraduate education Neurology, Amsterdam, the Netherlands; 2015
- **Eskes M**, van Alphen MJA, Balm AJM, Brandsma D, van der Heijden F: **A dynamic 3D lip shape model with facial surface EMG control,** MIRA Event. Enschede, the Netherlands; 2015
- **Eskes M**, van Alphen MJA, Balm AJM, Brandsma D, van Dijk S, Smeele LE, van der Heijden F: **Towards a Virtual 3D Lip Model,** OOA Retreat, Renesse, the Netherlands; 2014
- van Alphen MJA, **Eskes M**, Smeele LE, Balm AJM, van der Heijden F: **In vivo intraoperative hypoglossal nerve stimulation for quantitative tongue motion analysis.** PMHA Workshop 2014, Vancouver, Canada; 2014
- **Eskes M**, van Alphen MJA, Balm AJM, Smeele LE, Brandsma D, van der Heijden F: **Two methods for static lip pose prediction using facial sEMG.** NVvTG Conference 2013, Utrecht, the Netherlands; 2013
- van Alphen MJA, **Eskes M**, Smeele LE, Balm AJM, van der Heijden F: **Towards virtual therapy in oral cancer.** SEOHS 2012, Amsterdam, the Netherlands; 2012
- van Alphen MJA, **Eskes M**, Smeele LE, Balm AJM, van der Heijden F: **Towards virtual therapy in oral cancer.** NVvTG Conference 2012, Arnhem, the Netherlands; 2012